UNIVERSITY OF OKLAHOMA

GRADUATE COLLEGE

ATOM CHIP SETUP FOR COLD RYDBERG ATOM EXPERIMENTS

A DISSERTATION

SUBMITTED TO THE GRADUATE FACULTY

in partial fulfillment of the requirements for the

Degree of

DOCTOR OF PHILOSOPHY

By

ARNE SCHWETTMANN
Norman, Oklahoma
2012

Downloaded from SHAREOK. Persistent Handle URL: https://hdl.handle.net/11244/319330

ATOM CHIP SETUP FOR COLD RYDBERG ATOM EXPERIMENTS

A DISSERTATION APPROVED FOR THE
HOMER L. DODGE DEPARTMENT OF PHYSICS AND ASTRONOMY

BY

Dr. James P. Shaffer, Chair

Dr. Eric Abraham

Dr. Gregory Parker

Dr. Kieran Mullen

Dr. Wai Tak Yip

© Copyright by ARNE SCHWETTMANN 2012
All Rights Reserved.

Acknowledgements

First, I want to thank my adviser, James Shaffer, who always had the big picture in mind, and never ran out of new ideas and things to try when we thought we were stuck. Second, I want to thank Jonathon Sedlacek, who worked with me on this project since the beginning, and was a tremendous help. Working as a team and bouncing ideas back and forth made it possible to progress so much faster. Without Jon's help, the project would not be where it is today. I also want to thank Jonathan Tallant, Donald Booth, and Richard Overstreet, who all helped a lot through our constant discussions during the long hours in the lab, and made life in the lab much more bearable. I also want to thank Henry J. Neeman, director of the Oklahoma Supercomputing Center for Education & Research, for his help in parallelizing my Fortran code that I used to calculate long-range interactions between Rydberg atoms, several Monte Carlo C++ codes, and the Mathematica code used to simulate the 52-level Rydberg EIT system. Henry's weekly help sessions on cluster computing were an invaluable resource. Finally, I want to thank Paul Lett for giving me the opportunity to do post-doctoral research in his group at NIST, Gaithersburg, where I will be working on a four-wave mixing experiment with matter waves.

Table of Contents

List of Tables **ix**

List of Figures **xxi**

Abstract **xxii**

1 Introduction **1**
1.1 Overview . . . 1
1.2 Atom chips . . . 3
1.3 Rydberg atoms . . . 5
1.4 Rydberg EIT . . . 7
1.5 Outline of the thesis . . . 8

2 Theoretical basis **10**
2.1 Introduction . . . 10
2.2 Properties of ^{87}Rb . . . 10
2.2.1 Physical properties . . . 10
2.2.2 D_2 transition . . . 11
2.3 Rydberg atoms . . . 14
2.3.1 Scaling laws . . . 14
2.3.2 Energies . . . 15
2.3.3 Wavefunctions . . . 16
2.3.4 Lifetimes . . . 17
2.4 Electromagnetically induced transparency . . . 18
2.4.1 2-level atom . . . 22
2.4.2 3-level atom . . . 28
2.4.3 4-level atom . . . 34
2.4.4 52-level system . . . 38
2.4.5 Doppler shifts . . . 47
2.5 Laser cooling and trapping . . . 48
2.5.1 Laser cooling . . . 48
2.5.2 Magneto-optical trap . . . 53
2.5.3 Mirror magneto-optical trap . . . 58
2.6 Magnetic microtraps . . . 60

3 Experimental apparatus **70**
3.1 Introduction . . . 70
3.2 Vacuum system . . . 70
3.2.1 Chamber . . . 70
3.2.2 Pumps . . . 72
3.2.3 Baking cycle . . . 75
3.3 Main laser system . . . 76
3.3.1 Laser setup . . . 76
3.3.2 Saturated absorption spectroscopy . . . 79
3.4 Atom chip setup . . . 82

3.4.1 Chip design . . . 82
3.4.2 Copper z-wire . . . 83
3.4.3 Cooling solution . . . 85
3.4.4 Chip mount . . . 87
3.4.5 Heat sink . . . 89
3.4.6 Dewar . . . 89
3.4.7 Electrical systems . . . 90
3.5 Rb sources . . . 93
3.5.1 Rb dispensers . . . 93
3.5.2 Dispenser assembly . . . 93
3.5.3 Dispenser operation . . . 94
3.5.4 UV LIAD . . . 95
3.6 Magnetic field coils . . . 96
3.6.1 Coil frame design . . . 96
3.6.2 Coil electrical setup . . . 99
3.6.3 MOT coil switching circuit . . . 100
3.6.4 Bias coil switching circuits . . . 101
3.7 Rydberg excitation laser . . . 106
3.7.1 Second-harmonic generation . . . 106
3.7.2 Rydberg laser locking circuit . . . 108
3.8 Microwaves . . . 108
3.8.1 Waveguide assembly . . . 108
3.9 Imaging system . . . 109
3.9.1 Imaging setup . . . 109
3.9.2 Absorption imaging . . . 111
3.9.3 Imaging software . . . 112
3.9.4 Fluorescence imaging . . . 113
3.10 Control system . . . 115
3.10.1 NI-DAQ board setup . . . 115
3.10.2 DAQ control software . . . 115
3.10.3 Channel configuration . . . 117

4 Atom chip assembly **120**
4.1 Introduction . . . 120
4.2 Chip manufacturing . . . 120
4.2.1 Manufacturing method . . . 120
4.2.2 Choice of materials . . . 122
4.2.3 Spinning of resist . . . 124
4.2.4 Photolithography . . . 124
4.2.5 Metal evaporation . . . 128
4.2.6 Electroplating . . . 129
4.2.7 Etching . . . 130
4.3 Current atom chip . . . 130
4.4 Foil mirror manufacturing . . . 131
4.5 Rinsing . . . 133
4.6 Assembling the ceramic mount . . . 133
4.7 Gluing pins . . . 134

4.8 Wire bonding to pins . . . 136
4.9 Gluing copper z-wire . . . 137
4.10 Gluing atom chip . . . 137
4.11 Wire bonding to chip . . . 137
4.12 Gluing foil mirror . . . 137
4.13 Grounding foil mirror . . . 138
4.14 Assembling heat sink . . . 139
4.15 Electrical connections . . . 141
4.16 Insertion of atom chip into chamber . . . 143

5 Cold atoms on the chip **145**
5.1 Introduction . . . 145
5.2 Trapping setup . . . 145
5.3 Trapping potential calculations . . . 148
5.4 Heating of the atom chip . . . 154
5.5 Loading sequence . . . 156
5.6 Mirror MOT . . . 158
5.6.1 Mirror MOT parameters . . . 158
5.6.2 UV LIAD . . . 160
5.6.3 Loading curve . . . 160
5.6.4 Absorption images . . . 162
5.6.5 Temperature . . . 162
5.7 Cold MOT (CMOT) . . . 164
5.8 Optical pumping . . . 167
5.9 Macroscopic magnetic trap (z-trap) . . . 168
5.10 Compressed z-trap . . . 171
5.11 Microscopic magnetic trap (chip trap) . . . 174
5.12 Outlook . . . 176

6 Ladder-type EIT with Rydberg atoms **178**
6.1 Introduction . . . 178
6.2 Cs measurements . . . 179
6.2.1 Methods . . . 179
6.2.2 Results . . . 181
6.3 Rb measurements . . . 184
6.3.1 Methods . . . 184
6.3.2 Results . . . 186
6.3.3 Polarization effects . . . 189
6.4 Conclusion . . . 198

7 Cold Rydberg gas calculations **199**
7.1 Introduction . . . 199
7.2 Calculation of interaction potentials in a cold Rydberg gas . . . 201
7.2.1 Introduction . . . 201
7.2.2 Hamiltonian . . . 202
7.2.3 Numerical method . . . 205
7.2.4 Rotation of Hamiltonian . . . 206

7.2.5 Results . . . 209
7.3 Analysis of long-range molecular Rydberg atom - Rydberg atom potentials . 217
7.3.1 Introduction . . . 217
7.3.2 Bound states . . . 217
7.3.3 Lifetimes . . . 222
7.3.4 Lineshapes . . . 224
7.3.5 Two-photon excitation rate . . . 227
7.3.6 Conclusion . . . 229

8 Conclusion and outlook **232**

References **235**

A Field-programmable gate array based locking circuit for external cavity diode laser frequency stabilization **249**
A.1 Introduction . . . 249
A.2 Signal path . . . 251
A.3 Timing . . . 254
A.4 States . . . 255
A.5 User interface . . . 256
A.6 Compiling and using the program . . . 258
A.7 Performance . . . 263
A.8 Conclusion . . . 267

B Rydberg atom pair potential program usage **268**
B.1 Introduction . . . 268
B.2 Mathematica program CSSTARK . . . 270
B.3 Fortran program RYCOL . . . 276
B.4 Rotated Hamiltonian . . . 278
B.5 Programs and files . . . 279

C Rydberg EIT programs **283**
C.1 Introduction . . . 283
C.2 4-level Rydberg EIT notebook . . . 283
C.3 52-level Rydberg EIT notebook . . . 297

D Publications **310**
D.1 Introduction . . . 310
D.2 Publications . . . 310
D.3 Presentations . . . 311

List of Tables

2.1 Properties of ^{87}Rb from Ref. [1]. 11
2.2 Properties of the ^{87}Rb $5^2S_{1/2} \rightarrow 5^2P_{3/2}$ transition (D_2 line) from Ref. [1]. . 12
2.3 Scaling laws of alkali Rydberg atoms, together with the values for the ^{85}Rb $^2S_{1/2}$ n=100 state. 14

3.1 Summary of coil parameters. The coil separation is measured between coil centers. ID: inner diameter. 98
3.2 Digital channels used to remotely control the experiment. The operational definition column describes the effect of setting the digital channel to high. OP: optical pumping. 118
3.3 Analog channels used to remotely control the experiment. The operational definition column describes the quantitative effect of the voltage output, V_c, of each channel. 119

5.1 Parameters of the magnetic traps. Applied bias fields for the magnetic traps are given in the (x, y, z) coordinate system. The calculated and experimentally optimized bias field values are shown. The discrepancy is most probably due to stray magnetic fields in the chamber. 153
5.2 Loading sequence of the atom chip trap. w_0 is the distance to the lowest chip mount surface, 80 μm away from the chip wire surface. Errors are standard deviations obtained by taking multiple absorption images. 157

A.1 Files needed to compile the LockBox FPGA program. 259
A.2 Files needed to compile the LockBoxControlWin Windows program. 260
A.3 Filetypes used in the LockBoxControlWin and LockBox projects. 261

B.1 Program filenames for Rydberg pair potential calculations. 280
B.2 Output filenames of CSSTARK program. All files are space-delimited ASCII files. 281
B.3 Output filenames of RADIAL, RYCOL and SHROT programs. All files are space-delimited ASCII files. 282

List of Figures

1.1 A typical atom chip device consists of a vacuum chamber in which the atom chip is mounted upside down. A typical size of an atom chip is 1 cm × 2 cm. The chip is seated in a mount that has standard electrical connectors on the back. The mount is attached to a heat sink. The atom chip surface consists of microscopic wire structures that are used to magnetically trap or otherwise manipulate a cloud of cold atoms that hovers ∼ 100 μm below the chip surface (the cloud is not drawn to scale). The atom chip surface is also used to reflect cooling laser beams for initial laser cooling and trapping of the atoms in a magneto-optical trap. For clarity, the external bias coils, the source of atoms, and the cooling laser beams are not shown. 4

2.1 Level diagram of the Rubidium D_2 line with some of the relevant frequencies used in the experiment. 13

2.2 Two alkali three-level systems that exhibit EIT. The hyperfine EIT system shown in a) is a λ-system in which two hyperfine levels of the ground state are coupled to an excited state by two radiation fields. The ground states are stable or metastable. A strong coupling beam and a weak probe beam couple the short-lived excited state to the energetically higher and lower ground state, respectively. EIT arises from a dark state that forms in the presence of both laser beams. The dark state consists of a coherent superposition of both ground states. The Rydberg EIT system shown in b) is a Ξ-system consisting of a ground state, the first excited state, and a Rydberg level. The ground and Rydberg levels are long-lived. Here, the strong coupling beam and weak probe beam couple the excited state to the ground and the Rydberg level, respectively. In this case, the dark state is formed between the Rydberg level and the ground state. 19

2.3 Four-level system investigated in this thesis. A three-level Rydberg EIT system is coupled to a second close-lying Rydberg state via microwave radiation. 21

2.4 The two-level system. Two energy levels $|1\rangle$, and $|2\rangle$, with energies $\hbar\omega_1$ and $\hbar\omega_2$ are coupled by laser radiation of frequency ω, Rabi frequency Ω, and detuning Δ. 23

2.5 Three-level system subject to two laser fields. 28

2.6 Transmission ($\propto \mathrm{Im}\{\rho_{21}\}$) and Dispersion ($\propto \mathrm{Re}\{\rho_{21}\}$) in the three-level system, in the weak probe limit, as given by Eq. 2.37 and Eq. 2.38. The functions are plotted against the probe detuning Δ_1, for the two coupling Rabi frequencies $\Omega_c = 2\pi \times 1$ MHz (solid lines) and $\Omega_c = 0$ (dotted lines). The other parameters are $\Omega_p = 2\pi \times 1$ kHz, $\gamma_2 = 2\pi \times 6.12$ MHz, and $\Delta_2 = \gamma_3 = 0$. 31

2.7 Light shifts in the three-level system. a) In the uncoupled basis of atom+field states, the energy levels are separated by the laser detunings. Shown is the case of positive (blue) detuning of both laser beams. In the notation $|\alpha, \beta, \gamma\rangle$, α refers to the atomic energy level, and β and γ refer to the photon numbers of the probe and coupling fields, respectively. b) At zero detuning, the uncoupled states are degenerate. In the basis of coupled atom+field states $|a\rangle$, $|b\rangle$, $|c\rangle$ (dressed state basis), the effect of the off-diagonal coupling terms in the Hamiltonian is to split the energy levels by the light shift $\hbar\Omega'/2$. In the dressed state basis, the Hamiltonian is diagonal. 33
2.8 Four-level system subject to two laser fields and microwave radiation. . . . 34
2.9 Calculated probe absorption spectrum in the Cs 4-level system when turning on a) only the probe laser, b) both probe and coupling laser, and c) probe laser, coupling laser, and microwaves. When the Rydberg states are resonantly coupled by the microwave radiation, a narrow dip of opacity appears in the center of the EIT peak. The parameters used are $\Gamma_{21} = 2\pi \times 5.2$ MHz, $\Gamma_{32} = 2\pi \times 2$ kHz, $\Gamma_{43} = 2\pi \times 2.33$ kHz, $\Omega_p = 2\pi \times 100$ kHz, $\Omega_c = 2\pi \times 1$ MHz, $\Omega_{\rm rf} = 2\pi \times 157$ kHz. Note that the energy level diagrams are not drawn to scale. 36
2.10 Dependence of the calculated probe absorption spectrum in the Cs 4-level system on a) Ω_p, b) Ω_c, c) $\Omega_{\rm rf}$, and d) Γ_{32} (assuming $\Gamma_{43} = \Gamma_{32} = \gamma_{\rm Ry}$). The other parameters are the same as in Fig. 2.9. 37
2.11 The four-level systems explored in this thesis. a) Cs system, b) ^{87}Rb system. In the Rb system, the polarization dependence of the absorption spectrum is measured. 38
2.12 The 52-level system used to reproduce the measured absorption lineshapes in Rb Rydberg EIT. The magnetic sublevels of each hyperfine state are separated horizontally. Only a few of all the possible transitions are shown. Double-headed arrows are used to denote polarization-dependent couplings for one specific combination of polarizations. Dashed arrows denote spontaneous decay channels of the excited state. Couplings between Rydberg levels are omitted for clarity. The model accounts naturally for optical pumping effects. The Rabi frequency between two specific magnetic sublevels becomes Ω_{ij} (see text), changes for different laser or microwave polarizations, and depends on the specific sublevels involved. The numbers in the figure are the values of the Rabi frequencies $|\Omega_{ij}|$ in units of MHz for a probe field amplitude of $E_p = 0.5$ V cm^{-1} and a coupling field amplitude of $E_c = 50$ V cm^{-1}. Values are rounded two two significant digits for clarity. 40
2.13 Scattering force due to red-detuned counterpropagating beams of light along one dimension. The total scattering force F_s (solid) is the sum of the scattering force from the beam in the positive direction, F_+ (dashed) and the beam in the negative direction, F_- (dotted). Parameters used are $\Delta = -\Gamma$, and $I/I_s = 0.5$. For the D_2 line of ^{87}Rb, a velocity of one would correspond to $\Gamma/k = 4.7$ m s^{-1}, and a force of one would correspond to an acceleration of $\hbar k \Gamma M^{-1} = 2.24 \times 10^5$ m s^{-2}, respectively. 51

2.14 Restoring force in a MOT along the quadrupole coil center axis, z. The z-axis is chosen as quantization axis. The magnetic field increases linearly along z and creates a Zeeman shift for the excited states. The Zeeman shift results in position dependent detunings Δ_+ and Δ_- for the σ^+ and σ^- beams, respectively. Atoms located at positive position z' are closer to resonance with the σ^- beam that pushes them in the negative z-direction. Atoms located at negative position -z' experience a Zeeman shift that brings them closer to resonance with the σ^+ beam which pushes them in the positive z-direction. The net effect is that the atoms experience a restoring force that pushes them toward the trap center. Note that along the longitudinal quadrupole axis, both beams need to be RHC polarized. This is different from the lateral axes, where both beams need to be LHC polarized (see Fig. 2.15). 55
2.15 Restoring force in a MOT along the x-axis, perpendicular to the quadrupole center axis z. The x-axis is chosen as quantization axis. The same principle applies as for the z-axis (see Fig. 2.14). However, compared with Fig. 2.14, the magnetic field slope is reversed and the field now decreases through the trap center. The role of $m' = +1$ and $m' = -1$ is therefore reversed. As result, the laser beams along the x- or y-axis have to be LHC polarized in order to create the desired restoring force. 56
2.16 Sketch of a MOT setup. The pumping system and the source of atoms is not shown. Six laser beams, counterpropagating along the Cartesian axes, overlap at the zero of a quadrupole magnetic field that is generated by Anti-Helmholtz coils. The zero of the magnetic field is the location where a cold cloud of atoms forms, with a radial size of typically a few hundred microns and a temperature of $\sim 100\ \mu$K. 57
2.17 Sketch of a mirror MOT setup. The pumping system and the source of atoms is not shown. In a mirror MOT, the zero of the magnetic field is located a few mm away from a mirror surface. In the region where the incoming, beams overlap with the reflected beams, the atoms are subject to the same configuration of laser beams as in a regular MOT. Note that the quadrupole coils have to be oriented along one of the reflected beams, due to the change of polarization upon reflection off the mirror surface. 59
2.18 Atomic guide formed by an infinitely long wire. The wire is along the x-axis. Parameters are $I = 1\ A$ and $\mathbf{B}_{\text{bias}} = (0, 10\ \text{G}, 0)^{\text{T}}$ 63
2.19 The z-wire geometry leads to a Ioffe-Pritchard type trap. The top view of the wire is shown in a), and the front view is shown in b). The trap minimum forms just above the center segment, where the external bias field $\boldsymbol{B}_{\text{bias}}$ cancels the field $\boldsymbol{B}_2$, created by current density $\boldsymbol{j}_2$. The side segments of the wire, current densities $\boldsymbol{j}_1$ and $\boldsymbol{j}_3$, create two additional fields at the trap minimum, $\boldsymbol{B}_1$ and $\boldsymbol{B}_3$. The larger vertical components of those fields cancel, but a small component pointing horizontally remains. This remaining field $\boldsymbol{B}_{\text{Ioffe}} = \boldsymbol{B}_1 + \boldsymbol{B}_2 + \boldsymbol{B}_3 + \boldsymbol{B}_{\text{bias}}$ is the Ioffe field. It prevents Majorana losses at the trap minimum. 64

2.20 The z-wire magnetic microtrap on the atom chip. 3D current densities were calculated using the finite element method. The current enters the wire in the positive y-direction. The wire is made of Au. It is 100 μm wide and approximately 9 μm high. In a), the Joule heating of the wire surface, proportional to I^2, is plotted as a color gradient. This illustrates the complicated current flow across the corners that leads to heating. In b), c), and d), the magnetic field magnitude along the three Cartesian axes through the trap minimum is shown. Note that the field is non-zero at the trap center. This is due to the Ioffe field produced by the two side segments of the z wire, and prevents Majorana losses. Along the z direction, the trap is highly anharmonic. Parameters are $I = 1.86$ A and $\mathbf{B}_{\text{bias}} = (0, 30\text{ G}, 0)^{\text{T}}$. 66
2.21 Adiabatic trapping potentials calculated for ^{87}Rb F=2 ground state atoms in the microtrap from Fig. 2.20 (solid lines), together with the harmonic approximation for the $m_F = 2$ state atoms (dotted lines) and corresponding trap frequencies ω. The plots a), b) and c) correspond to cross sections through the trap minimum along the three Cartesian axes x, y and z respectively. Both WFS, $m_F = 2$ and $m_F = 1$, are trapped. Atoms in the $m_F = 2$ state experience the largest restoring forces, characterized by the trap frequencies shown. Trap parameters are the same as for Fig. 2.20. 68

3.1 Sketch of the vacuum system. The experimental chamber that houses the atom chip is shown in red. The pumps are attached to the dark blue colored parts as labeled. Other parts such as the rubidium sources connect to the system as labeled. Flexible bellows, labeled "bellows" (yellow) in the diagram, are used to isolate the chamber from vibrations. The MOT and imaging beams are also depicted (dark and light purple), as is the gate valve used to isolate the chamber (orange). 71
3.2 Schematic of the pump setup. Four pumps are pumping on the experimental chamber in the configuration shown. Multiple valves allow the user to isolate the chamber and/or tee, and select whether to pump on the atom chip dewar or not. The pressure in the chamber and in the tee is measured with Bayard-Alpert ionization gauges (IG). The roughing line pressure and the pressure on the small turbo pump exhaust is monitored with thermocouple gauges (T/C). A pneumatic valve can be used to purge the chamber with nitrogen during a controlled loss of vacuum. The nitrogen purge pressure is controlled via a manual needle valve. Here, solid lines denote CF components, and dashed lines denote KF components. 73

3.3 Schematic of the main laser system. Both external cavity diode lasers are locked to the side of a hyperfine transition of ^{87}Rb using the saturated absorption spectroscopy setups shown. The cooling (repumping) laser frequency is adjusted with accousto-optic modulator 2 (4). The optical pumping and imaging beams are derived from the main cooling laser via accousto-optic modulators 1 and 3, respectively, before they are fiber coupled. The repumping light is overlapped with the +X MOT beam before entering the chamber. PBS: Polarizing beamsplitter cube, BS: non-polarizing beamsplitter cube, L: focussing lens, Q: quarter-wave plate, H: half-wave plate, AOM: accousto-optic modulator, FC: fiber collimator, CS: collimation stage, M: mirror, PD: photodiode, VC: Rb vapor cell. 77
3.4 Relevant atomic transitions and laser frequencies in the MOT setup. C: cooling beams, I: imaging beam, OP: optical pumping beam, R: repumping beam. The lock points of the cooling laser (left) and repumping laser (right) are shown as dotted horizontal lines. The laser frequencies denoted by solid vertical arrows are derived from the locked lasers via four AOMs as described in the text. The detuning δ of the MOT beams is -17 MHz during the MOT loading phase. Hyperfine splittings are taken from Ref. [2] and Ref. [3]. . . 78
3.5 Saturated absorption spectrum obtained by scanning the cooling laser piezo and current to cover a large frequency range $\sim$ 9 GHz. The cooling and repumping transitions are highlighted. The voltages are negative because an offset was applied. 80
3.6 Saturated absorption spectrum of the $F = 2 \rightarrow F'$ transitions and crossover peaks, including the $F = 2 \rightarrow F' = 3$ cooling transition. The frequency axis was calibrated using the $F' = 2$ to $F' = 3$ hyperfine splitting. Vertical lines denote the expected peak positions, calculated from the known hyperfine splittings [2]. The cooling laser lock point is highlighted by a red cross. . . . 81
3.7 Saturated absorption spectrum of the $F = 1 \rightarrow F'$ transitions and crossover peaks, including the $F = 1 \rightarrow F' = 2$ repumping transition. The frequency axis was calibrated using the $F' = 1$ to $F' = 2$ hyperfine splitting. Vertical lines denote the expected peak positions, calculated from the known hyperfine splittings [2]. The repumping laser lock point is highlighted by a red cross. . 82
3.8 Photolithography mask design for the atom chip. Wires are defined by 40 μm gaps in the gold surface. The mirror plane covering almost all of the chip surface is omitted to highlight the actual wire traces. a) overview, b) close-up view of the center region. Lengths are specified in μm. 84
3.9 Photo of the atom chip received from AFRL. 85
3.10 Sketch of the atom chip assembly mounted in the chamber. Two sections are shown: a section through a plane parallel to the MOT X-beam (a) and a section through a plane perpendicular to the MOT X-beam (b). The MOT beams are depicted in purple. 86
3.11 Photo of the atom chip assembly just before insertion into the vacuum chamber. 87
3.12 Sketch of the atom chip mount. 88
3.13 Photo of the aluminum heat sink. 90

3.14 Photos of the cooling dewar and cup. Shown are a) dewar and cup mounted on high power electrical feedthrough, b) view into the cup from above when it is mounted on the high power electrical feedthrough, and c) bottom of dewar showing protruding sockets that slide onto cold fingers. 91
3.15 Simplified schematic of the macroscopic copper z-wire electrical system. The high power IGBT (1.2 kV, 125 A) switches the large currents in 2 μs, and a dummy coil slows down this switching to 234 μs (590 μs) for the off (on) switching when switching a current of 34.4 A. 92
3.16 Photo of the source assembly prior to insertion into the chamber. Three pairs of sources are attached to the six alumel conductors of an electrical feedthrough. Each pair is connected in parallel with push/crimp BeCu connectors. 94
3.17 Photo of a mounted UV LED array used for UV LIAD. 96
3.18 Sketch of the coil setup. 97
3.19 Sketch (a) and photo (b) of the coil setup assembled around the chamber. . 99
3.20 MOT coil switching circuit. The circuit switches the MOT coils off in 450 μs. It is based on a high power IGBT and a series of high power transient voltage suppressing diodes. When the IGBT opens, the coil current decreases according to $\dot{I} = -V_Z/L$, where V_Z is the breakdown voltage of the diode array. The IGBT gate driving circuit is not shown. 101
3.21 X-bias coil switching circuit. The circuit switches the bias coil pair quickly on and off. It also allows to quickly switch between current values. Fast on switching is done by discharging a high voltage capacitor into the coils. The capacitor is discharged by applying a pulse to the silicon-controlled rectifier diode (SCR). Fast off switching is done through IGBTs and TVS diodes. Switching between currents is done by switching between two capacitors and two different power supplies. 102
3.22 Solid state crossover relay used to switch current direction on the y-bias coil. Depending on a TTL control signal, either input "+" is connected to output 1 and input "-" to output 2, or the connections are flipped so that input "+" is connected to output 2 and input "-" to output 1. With this relay, the unipolar fast switching circuitry can be used with arbitrary coil current directions. The relay requires three 15 V DC power supplies, two of which are floating to different (small) voltages during operation. We use cheap off-the-shelf regulated brick supplies for this purpose. 105
3.23 Second-Harmonic-Generation system for Rydberg excitation. Following the light path, the labels are DL: external-cavity diode laser, AL: aspheric lens, G: grating, P: piezo-electric transducer, L: spherical lens, OI: optical isolator, AO: accousto-optic modulator, H: half-wave plate, F: polarization-maintaining single-mode optical fiber, TA: tapered amplifier, CL: cylindrical lens, PPLN: periodically poled lithium-niobate waveguide crystal, CO: crystal oven, BF: bandpass filter, G: glass slide, RC: reference cavity, PD: photodiode. 106
3.24 User interface of the imaging software written in C++. 113
3.25 User interface of the pulse sequencing software written in C++. 116

4.1 Sketch of atom chip manufacturing steps. a) a metallic seed layer is deposited on the insulating substrate, b) photoresist is spun on, c) the photoresist is exposed and developed, d) the seed layer is grown to a thickness of ~ 7 μm in-between the resist via electroplating, e) the resist is removed, f) the remaining seed layer is etched away. 121
4.2 Cutting dimensions of the AlN wafer. Two atom chips can be patterned on one piece of cut substrate. Approximately 5 mm clearance is provided at the edges of each piece to account for the edge bead created during the spin-on of photoresist. Dimensions are in inches. 123
4.3 Design of the photolithography mask that contains two of our atom chip designs (lower right corner), along with other circuit designs of the local SPM group. The mask consists of a chrome layer on glass. The blue area denotes the chrome layer. 125
4.4 Demonstration how an edge bead can create poor contact between the mask and resist, limiting the resolution of the photolithography. 126
4.5 Comparison of lithography results on AlN substrate with (a) poor mask contact resulting from edge bead and (b) with edge bead removed. It is clear the lithography resolution is higher when the edge bead is removed. 126
4.6 Chip design on AlN. The darker blue is the negative photoresist while the lighter blue is the AlN substrate. 127
4.7 Chip design on Au seed layer. Dark gold color is resist. Lighter area is the seed layer where the wires will be electroplated in. 128
4.8 Setup used for electroplating. The anode penetrates into the electroplating solution to a distance of 4.8 cm away from the cathode. The cathode current is controlled with a power supply (Keithley Sourcemeter 2400, not shown). . 129
4.9 Microscope image of the atom chip. a) whole chip, b) magnified view of the center region. 131
4.10 Photos of the ceramic mount after various steps of the chip mount assembly. The mount is shown after gluing the pins and wire bonding to the pins (a), after bending up the wires and gluing the z wire (b), after gluing in the atom chip (c), after wire bonding to the chip pads (d), and after attaching and grounding the foil mirror (e). 134
4.11 Setup used to glue the pins into the ceramic mount. The pins are inserted into the mount, and the mount is fastened upside down onto an aluminum block covered with a layer of Teflon and Kapton foil. The flexible Teflon pushes on the pin heads and forces the pins into their correct positions. Epoxy is then applied to the backside of the pins. 135
4.12 Sketch of the assembled atom chip mount showing the positions of gold wires and the designations of the contact pads. 136
4.13 Microscope image of some of the finished silver epoxy wire bonds on the chip mount. The conductive bridge used to ground the foil mirror surface is shown. Next to the conductive bridge, one of the four drops of non-conductive epoxy can be seen, used to attach the foil mirror to the atom chip. 139

4.14 Sketch of the heat sink assembly steps. Dashed red arrows denote the joining of parts and solid red arrows denote the insertion positions of fasteners. a) The aluminum heat sink is slid onto the copper cold fingers. b) The heat sink is secured to the cold fingers by compressing the saw cut with six screws, and extension rods are attached to the current-carrying copper rods with barrel connectors. c) The lower two set screws on the barrel connectors are tightened, and the atom chip mount is lowered onto the heat sink. d) The atom chip mount is secured with four screws, and the upper two set screws on the barrel connectors are tightened. 140
4.15 Sketch illustrating the electrical connections between the chip mount and the 9-pin low power electrical feedthrough. The pairs of pins U1_out-U2_in, U2_out-U3_in, U3_out-U4_in are connected directly using short wires to ensure correct in-series operation of the microscopic u-wires. The other pins are then connected to the 9-pin feedthrough as shown. 142
4.16 Photos of the chip setup after all electrical connections are made. a) overview, b) close-up of the chip mount. 143
4.17 Photo of the atom chip assembly after it was inserted into the vacuum chamber. 144

5.1 Atom trap setup. a) top view, b) side view. Note that positive currents through the x-, y-, and z-bias coil pairs (not shown) create uniform magnetic fields in the positive x-, y-, and z-directions, respectively. The x-, y- and z-directions are indicated by arrows in b). The coordinate system (u, v, w) is used when referring to absorption images. The u-, v- and w-directions are indicated by arrows in a) and b). Q: Quarter-wave plate, H: half-wave plate, PBS: polarizing beamsplitter cube, BS: non-polarizing beamsplitter cube. . 146
5.2 Current density distribution and magnetic fields calculated for the macroscopic copper wire. The wire is 2 mm high. a) Joule heating in the wire. Black (white) corresponds to the minimum (maximum) current density. In b), c) and d), the magnetic fields from the finite-element currents (solid) are compared to a simpler model (dashed). The current and bias fields parameters are $I = 30$ A, $B_v = 16.2$ G, $B_u = 27.64$ G, and $B_w = 2.72$ G. Note that w points into the page in a). 149
5.3 Magnetic fields calculated for the three magnetic traps employed during the loading sequence. The z-trap (solid), compressed z-trap (dashed), and chip trap (dotted) are shown. The fields along the three perpendicular axes w, u and v are shown. Each curve in c), d), e) and f) is evaluated at the w coordinate of the respective trap minimum. 151
5.4 Measured heating of the atom chip z-wire. a) Time dependence of the heating for applied currents up to 4 A, b) Temperature increase within 10 ms as a function of applied current. 155
5.5 Fluorescence image of the cold atoms in the mirror MOT, hovering 1.5 mm below the chip. 159
5.6 Loading curves of the MOT for various durations of LIAD pulses. The UV LEDs are pulsed on together with the MOT magnetic field at time zero. The LEDs are turned off after various delays. Each curve is labeled on the right by the delay used. 160

5.7 Loading curve of the MOT after installation of the foil mirror. During this measurement, the MOT was 3 mm away from the chip surface, just as during the LIAD measurements. The foil mirror increased the atom number by a factor of 3.5. 161
5.8 Absorption image of the MOT, taken while the MOT was on. 163
5.9 Time-of-flight temperature measurement of the MOT. 164
5.10 Absorption image of the cold MOT, taken at delay $\tau = 200$ μs. The atom number deduced from this image is $N = 2.64 \times 10^6$. 165
5.11 Time-of-flight temperature measurement of the cold MOT (a), and vertical center-of-mass position of the cloud (b). 166
5.12 Absorption image of the z-trap, taken at delay $\tau = 500$ μs. The z-trap was loaded for 133 ms. The atom number deduced from this image is $N = 1.02 \times 10^6$. 169
5.13 Time-of-flight temperature measurement of the z-trap (a), and vertical center-of-mass position of the cloud (b). 170
5.14 Absorption image of the compressed z-trap, taken at delay $\tau = 500$ μs. The atom number deduced from this image is $N = 1.04 \times 10^6$. 172
5.15 Time-of-flight temperature measurement of the compressed z-trap (a), and vertical center-of-mass position of the cloud (b). 173
5.16 Absorption image of the chip trap while it is on. The atom number deduced from this image is $N = 5.8 \times 10^5$. 175
5.17 Time-of-flight temperature measurement of the chip trap. 176

6.1 Cs Rydberg EIT setup. a) Excitation scheme, b) experimental setup. CM: cold mirror, C: chopper wheel, VC: Cs vapor cell, DM: dichroic mirror, PD: photodiode, A: microwave horn antenna. 180
6.2 Measured EIT in Cs. Shown is the probe transmission vs. detuning of the coupling beam. a) low microwave powers, b) high microwave powers. The microwaves cause a broadening and splitting of the EIT peak. 182
6.3 Effect of detuning the microwaves in the Cs system, measured at a microwave-power of 14 μW. 184
6.4 Rb EIT setup. a) Excitation scheme, b) experimental setup. H: half-wave plate, PBS: polarizing beamsplitter cube, H/Q: half-wave plate or quarter-wave plate, I: iris, O: oven, VC: Rb vapor cell, CM: cold mirror, AO: accousto-optic modulator, PD: photodiode. 185
6.5 Rb EIT measurements. Probe transmission vs. coupling beam detuning. The effect of increasing the microwave power is to split and broaden the EIT peak. a) Experiment, b) 4-level theory with no adjustable parameters. . . . 187
6.6 Effect of detuning the microwaves in Rb, measured at a microwave power of 1.4 μW. 189
6.7 Sketch of polarization effects for σ^+ beam polarization and transverse linear microwaves. a) Schematic of all magnetic sublevels in the system. For clarity, the 54P level is drawn energetically above the 53D level instead of below. Transitions deemed most important are highlighted by solid arrows (absorption/stimulated emission) and dashed arrows (spontaneous decay). b) Geometric configuration of the fields and antenna. c) Resulting EIT lineshape. Optical pumping preferentially populates a 53D sublevel that is coupled to the 54P state by the microwaves. 191

6.8 Sketch of polarization effects for σ^+ beam polarization and longitudinal linear microwaves. a) Schematic of all magnetic sublevels in the system. For clarity, the 54P level is drawn energetically above the 53D level instead of below. Transitions deemed most important are highlighted by solid arrows (absorption/stimulated emission) and dashed arrows (spontaneous decay). b) Geometric configuration of the fields and antenna. c) Resulting EIT lineshape. Optical pumping preferentially populates a 53D sublevel that is not coupled to by the microwaves, denoted by the red X. The effect of the microwaves is reduced. 192
6.9 Polarization effects for linear beam polarization and longitudinal linear microwaves. a) Schematic of all magnetic sublevels in the system. For clarity, the 54P level is drawn energetically above the 53D level instead of below. Transitions deemed most important are highlighted by solid arrows (absorption/stimulated emission) and dashed arrows (spontaneous decay). b) Geometric configuration of the fields and antenna. c) Resulting EIT lineshape. Both coupled and uncoupled (denoted by red crosses) Rydberg sublevels are populated. The uncoupled sublevels are denoted by red crosses. 193
6.10 Polarization effects in calculated probe transmission spectra at $T = 0$ K. The density matrix evolution in the 52-level system was solved numerically for different polarizations. a) All fields linearly polarized along x, b) beams along x and microwaves along z (π-polarization), c) beams circular (σ^+-polarization) and microwaves along x, d) beams circular and microwaves along z. 194
6.11 Effect of dephasing terms due to finite laser linewidths on the calculated probe transmission spectra. The calculation was done for $T = 85$ °C, including all 52-levels and the average over thermal velocities. The laser beams are σ^+ polarized and the microwaves linearly along x. 195
6.12 Polarization effects on the probe transmission in Rb EIT. a) Experimental results, b) 52-level theory with no adjustable parameters. 197

7.1 Two Rydberg atoms interact via electric multipole interactions over a long internuclear distance R of several μm. A small applied electric field $\sim \mathrm{mV\,cm^{-1}}$ along the internuclear axis is denoted by $\boldsymbol{\epsilon}$. 203
7.2 Calculated single atom Stark energies for Cs 89D and adjacent states. . . . 206
7.3 Overview of the pair potentials of the 89D89D and surrounding states for zero background E-field. Labels are zero-field labels. The 89D89D potentials are circled. 209
7.4 Comparison of pair potentials calculated via matrix diagonalization (solid black) to those from Ref. [4] calculated via perturbation theory (dashed red). Potentials for all M are plotted. The background field is zero. Note that the perturbative calculations did not include the fine-structure and therefore converge asymptotically to a single energy. For ease of comparison, the asymptotic energy of the perturbative potentials is chosen to be the $89D_{5/2}89D_{5/2}$ pair. 210

7.5 Pair potentials of the 89D89D and surrounding states for $M = 2$ for a background E-field of 28 mV cm^{-1}. Pairs of numbers below a given label are the respective j_1, j_2 combinations. The exclamation mark denotes the splitting of degenerate states caused by the E-field and the quadrupole-quadrupole interaction. For small R, the manifold of Stark fan pairs appears that can lead to large energy transfer and eventual ionization. 211
7.6 Pair potentials of the 89D89D and surrounding states for $M = 3$ for a background E-field of 28 mV cm^{-1}. Some avoided crossings are circled. 212
7.7 Pair potentials of the 89D89D and surrounding states for $M = 3$ obtained by matrix diagonalization for different background E-field magnitudes: a) 28 mV cm^{-1} and b) 120 mV cm^{-1}. 214
7.8 Pair potentials of the 23P23P and surrounding states for $0 \leq M \leq 5$, obtained by matrix diagonalization for a background E-field magnitude of 60 mV cm^{-1}. Note the change of scales compared to the $n \sim 89$ potentials. Labels in parentheses denote the (j_1, j_2) quantum numbers of the respective pair. 215
7.9 Long-range wells in the pair potentials of the Cs 89D89D and surrounding states for $M = 3$ for a background E-field of a) 0 mV cm^{-1}, b) 30 mV cm^{-1}, c) 60 mV cm^{-1}, and d) 120 mV cm^{-1}. Potential wells C1 and C2 in b) and C1' and C2' in c) are circled. Pairs of numbers below a given label are the respective j_1, j_2 combinations. Labels for small fields are asymptotic zero-field quantum numbers. At larger fields, c) and d), even the asymptotic ($R \to \infty$) states begin to mix. The zero field quantum numbers become meaningless, apart from M. 219
7.10 Detail of the potential wells that are circled in Fig. 7.9: a) C1, b) C2, c) C1', and d) C2'. The bound vibrational ($J = 0$) wavefunctions for ν=0, 99, and 199 and corresponding eigenvalues are indicated. The energy axis is the atom-pair energy. The energetic zero is chosen as the asymptotic ($R \to \infty$) pair energy of the state correlating at zero field to $89D_{5/2}89D_{5/2}$ ($M = 3$) for C1, C1' and $88D_{5/2}90D_{5/2}$ ($M = 3$) for C2, C2'. The kink in the potential curve at $R = 5$ μm in a) is due to an additional avoided crossing with a very small gap size of 2 MHz. It is further discussed in the text. 220
7.11 Vibrational ($J = 0$) energy spacings vs. vibrational quantum number ν for the potential wells circled in Fig. 7.9. Upper vibrational states in these wells form an effective continuum, with spacings on the order of kHz. The kink in a) results from the kink in Fig. 7.10a) at $R = 5$ μm. 221
7.12 Effective thermally averaged Franck-Condon overlap factors $\overline{FC}$ vs. binding energy for the transition of a pair of 6P atoms into the crossings circled in Fig. 7.9. The main plots of a), b), c), and d) show the values of $\overline{FC}$ convoluted with a 1 MHz laser linewidth for the wells C1, C2, C1' and C2', respectively. The insets show the unconvoluted values of $\overline{FC}$ for the same wells. The energetic zero is chosen as the asymptotic ($R \to \infty$) pair energy of the state correlating at zero field to $89D_{5/2}89D_{5/2}$ ($M = 3$) for C1, C1' and $88D_{5/2}90D_{5/2}$ ($M = 3$) for C2, C2'. 226

7.13 Schematic of the two-photon excitation into the well C1. The two possible choices for the intermediate state are shown. Due to the large R between the atoms in the final state, each of the two atoms will interact mostly with one of the two photons, and the pair transition dipole moments reduce to the atomic ones. Thus the left arrow is a transition taking place mostly on atom 1, the right arrow is a transition taking place mostly on atom 2. 228

A.1 Schematic of the internal signal path on the FPGA. Insets denote parameters controlled by the user interface. SM: pictorial representation of the state machine that switches between lock and scan states (debug state not shown). 252
A.2 Screenshots of the user interface that controls the FPGA loop, scan, filter, and debugging parameters. Shown are the main lock panel (top left), the menu options (top right), the scan control panel (bottom left), the filter settings panel (bottom right), and the debugging panel (center right). Mouse clicks on the ±-buttons or key presses of the up arrow or down arrow keys smoothly change the currently active parameter. The order of magnitude of change depends on the digit that the cursor is positioned over. 257
A.3 Electromagnetically induced transparency to measure the linewidth of the locked laser. a) Ladder-type excitation scheme (Rydberg EIT). b) Rydberg EIT setup with counter-propagating probe and coupling beams. Labels are H: half-wave plate, PBS: polarizing beamsplitter cube, I: iris, VC: rubidium vapor cell, CM: cold mirror, PD: photodiode, AO: accousto-optic modulator. 264
A.4 EIT measurement. The probe transmission photodiode signal is plotted vs. the coupling laser detuning. The coupling laser frequency is swept by slowly ramping the reference cavity piezo voltage while the ECDL is locked to the red side of the cavity peak. The EIT peak has a width of 2.58 MHz. This corresponds to a frequency range of 1.29 MHz for the ECDL light, and gives an upper limit on the locked ECDL linewidth. 266

B.1 Flow chart of the Rydberg pair potential calculation. Dashed boxes enclose lists of data filenames. 269
B.2 Screenshot of the folded view of CSSTARK as it appears after opening the notebook in Mathematica. The headlines of the major sections of the program are shown. 270

Abstract

The design, construction and characterization of an atom chip apparatus for cold Rydberg atom experiments with ^{87}Rb is presented. The apparatus is designed to investigate interactions between Rydberg atoms and the nearby chip surface, as well as the dynamics of Rydberg atoms in a double well. The proposed interrogation scheme is Rydberg electromagnetically induced transparency (Rydberg EIT). Magnetic trapping potentials used to load the chip with atoms are calculated. The atom number and temperature during various phases of the loading sequence are measured using absorption imaging. The room-temperature 4-level ladder-type Rydberg EIT system, in which the 3-level Rydberg EIT system is coupled via microwaves to a second Rydberg state, is investigated experimentally. EIT transmission spectra for different microwave powers and different polarizations of optical fields and microwaves are presented. It is shown that, to explain the observed polarization effects in the probe transmission lineshape, all magnetic sublevels, including the hyperfine structure of both Rydberg levels, have to be taken into account. The corresponding 52-level theory is discussed. Calculations of long-range multipolar Rydberg-atom Rydberg-atom interaction potentials are also presented and discussed.

Chapter 1

Introduction

This chapter begins with a general overview, continues with brief specific introductions to the topics of atom chips, Rydberg atoms, and Rydberg EIT, and concludes with an outline of the thesis.

1.1 Overview

In this thesis, an atom chip setup is described that provides unique opportunities to study the physics of cold ^{87}Rb Rydberg atoms. The system is designed to investigate the interactions of cold Rydberg atoms with surfaces as well as the dynamics of cold Rydberg atoms in a double well potential.

Rydberg atoms are promising candidates to use as qubits for the realization of a functioning quantum computer, due to their strong long-range interactions and their long lifetimes. Rydberg atoms are used as the basis for quantum gates in several proposed quantum computing schemes [5, 6, 7, 8]. One can envision a scalable quantum computer, in which a microchip is used to interface with cold Rydberg atoms. The atoms could be held in arrays of multiple magnetic traps close to the chip surface. In order to understand such future devices, we first need to understand how the interactions between Rydberg atoms and nearby surfaces affect the coherent control of the atoms. In a recent study of coherent excitation of Rydberg atoms in vapor cells, the authors stressed the importance of interactions between Rydberg atoms and surface polaritons in the cell walls [9]. Rydberg atoms close to a microchip surface were recently studied, and the authors observed a shift of the Rydberg energy levels due to atoms that were adsorbed onto the nearby surface [10]. More work needs to be done in the ultracold regime to fully understand the interactions between

Rydberg atoms and surface excitations such as polaritons and plasmons. With the setup presented here, we will be able to look at such interactions in detail and measure the Rydberg energy level shifts and dephasing rates as a function of the distance to the nearby surface at high spectroscopic resolution.

In addition to the interactions of Rydberg atoms with a microchip surface, the interactions between Rydberg atoms themselves will also be important for future devices. When Rydberg atoms are excited in arrays of microscopic magnetic traps close to a microchip, the distances between trapped clouds are on the order of several μm. At these distances, the long-range interactions between Rydberg atoms play an important role in the dynamics and coherence properties of the trapped atoms [4, 11]. With our atom chip, we will be able to trap atoms in a microscopic double well, where two clouds of cold atoms are separated by a small distance < 10 μm [12]. At these separations, the long-range dipole-dipole interactions between Rydberg atoms in each of the two clouds will become observable as shifts of the Rydberg energy levels.

In order to better understand the dynamics of cold interacting Rydberg atoms, we calculated the Rydberg atom pair interaction potentials. The calculations included, for the first time, the fine-structure of the Rydberg levels and a small background electric field. We found that the interaction potentials are very sensitive to the background electric field, and support very long-range Rydberg atom-Rydberg atom molecules, bound at internuclear distances of several μm. The results of the calculations are presented in this thesis.

In order to probe Rydberg atoms on the atom chip, we investigated Rydberg electromagnetically induced transparency (Rydberg EIT), a direct nondestructive coherent probe of Rydberg energy levels [13]. This method is attractive, because it will allow us to detect changes of the Rydberg energy levels and the Rydberg dephasing rates even when they are much smaller than the natural linewidth of the

first excited state, which limits traditional detection schemes based on direct two-photon excitation and subsequent ionization. We performed measurements on the room-temperature Rydberg EIT system perturbed by microwaves. We found that the measured transmission spectra are extremely sensitive to changes in the microwave power and to polarization effects.

In the following, brief introductions to atom chips, Rydberg atoms, and Rydberg EIT are given, followed by an outline of the remainder of the thesis.

1.2 Atom chips

An atom chip [14] is a microchip that is used to manipulate cold atoms. A typical atom chip device is shown in Fig. 1.1. The cold atoms usually hover 100 μm or less in front of the surface of the atom chip. Typically, an atom chip consists of microscopic wire structures patterned on a planar substrate. The simplest use of the wires is to generate three-dimensional constant magnetic fields to guide or trap the atoms [15]. Extremely large magnetic field gradients can be generated with moderate currents, due to the close distance of the atoms to the wires. This led to the first observations of Bose-Einstein Condensation (BEC) on atom chips in 2001 [16, 17], and, recently, to the first observation of Bose-Einstein condensation in microgravity [18], where an atom chip apparatus was dropped from the drop tower in Bremen, Germany.

Atom chip setups bridge the gap between atomic physics and solid-state physics. The manufacturing of atom chips involves well-developed microfabrication techniques from solid-state physics such as photolithography, electroplating, and etching [19]. Due to the advancements of microchip fabrication techniques, almost any imaginable microscopic wire pattern can be constructed, and elaborate micromanipulation of atoms can be performed on atom chips. Combinations of DC and AC electromagnetic fields on atom chips have been used to create cold-atom devices such as

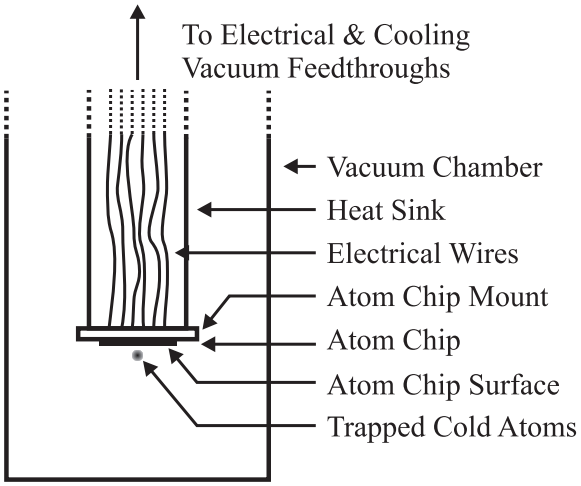

Figure 1.1: A typical atom chip device consists of a vacuum chamber in which the atom chip is mounted upside down. A typical size of an atom chip is 1 cm $\times$ 2 cm. The chip is seated in a mount that has standard electrical connectors on the back. The mount is attached to a heat sink. The atom chip surface consists of microscopic wire structures that are used to magnetically trap or otherwise manipulate a cloud of cold atoms that hovers $\sim$ 100 μm below the chip surface (the cloud is not drawn to scale). The atom chip surface is also used to reflect cooling laser beams for initial laser cooling and trapping of the atoms in a magneto-optical trap. For clarity, the external bias coils, the source of atoms, and the cooling laser beams are not shown.

the atomic conveyor belt [20], matter-wave interferometers [21, 22], integrated single atom detectors [23], and atom chip based atomic clocks [24, 25]. The close proximity of a microscopic cloud of atoms to the solid surface of the chip is also ideal to investigate atom-surface interactions [26, 27, 28].

Atom chips are loaded with cold atoms using laser cooling and trapping methods that were developed during the "race for BEC" in the 1980s and 1990s [29]. In our atom chip setup, an initial cloud of cold atoms is collected in a variant of the magneto-optical trap (MOT, Ref. [30]) called the mirror MOT, which was conceived in 1999 [31, 32]. The atom chip surface is used as a mirror to reflect two of four cooling laser

beams. The initial cloud of atoms in the mirror MOT is a few mm away from the chip. The atoms are then moved closer to the chip surface through a sequence of magnetic trapping potentials. The magnetic potentials are created using the wires on the chip, wires behind the chip, and external magnetic field coils. Once the atoms are trapped close to the atom chip surface, the coherent transitions to Rydberg states, including any level shifts or line shape changes due to the nearby surface, can be probed using Rydberg EIT [13].

1.3 Rydberg atoms

Rydberg atoms [33] are atoms in states of high principal quantum number n. Technically, an atom is labeled a Rydberg atom if n is larger than the valence number of the ground state atom. However, in this thesis, the term Rydberg atom is taken to refer only to much larger n, $n > 30$. Because the Rydberg electron is far away from the core, Rydberg atoms exist on the border between classical and quantum physics [34]. Rydberg atoms have exotic properties such as large radii $\sim \mu$m, large transition dipole moments to nearby states $\sim 10^{-26}$ C m, and long lifetimes ~ 100 μs. Pairs of Rydberg atoms also have strong long-range electrical dipole interactions in the range of several MHz over several μm. Rydberg states have been known since 1885 due to Balmer's formula for the transition wavelengths in Hydrogen. They are named after J. R. Rydberg, who unraveled some of the early mysteries of the spectral lines of the alkali atoms in the late 19th century [35]. In the early 20th century, experiments on pressure shifts due to rare gas atoms [36] led to Fermi's potential for scattering of Rydberg electrons from ground state atoms [37]. Rydberg atoms have been studied more extensively since the invention of tunable dye lasers in the 1970s [38], which made the wavelengths and laser linewidths needed to excite specific Rydberg levels more easily accessible. It was found that the long-range interactions between Rydberg

atoms [39] can cause an excitation suppression known as dipole blockade [40]. The excitation of one Rydberg atom prohibits the excitation of a second Rydberg atom close to it, if the long-range pair interaction shifts the pair energy out of resonance with the excitation laser [41]. The region around the Rydberg atom where excitations of other Rydberg atoms are prohibited is known as the blockade sphere, and can have a radius of > 10 μm for $n \sim 80$ [41]. Due to the dipole blockade, the excitation of the second atom is conditional. Several schemes for quantum information with Rydberg atoms have been proposed on the basis of this conditional excitation [6, 7, 5]. It has been shown recently that the excitation of a Rydberg atom is also collective. The single Rydberg excitation is shared between all the atoms within the blockade sphere in an entangled state. The N atoms within the blockade sphere behave as one large atom, sometimes called a superatom, with new properties such as an enhanced Rabi frequency $\Omega' = \sqrt{N}\,\Omega$ [42, 43]. Rydberg atom interactions play an important part in the evolution to ultracold plasmas [44], and, when tuned with an electric field, can lead to resonant energy transfer between Rydberg atoms [45]. The interactions between Rydberg atoms also lead to the observation of exotic states such as ultralong-range Rydberg-Rydberg molecules [46, 47]. In this thesis, large-scale calculations of long-range Rydberg pair interaction potentials are presented that include fine structure and small background electric fields.

Because the Rydberg electron spends a large amount of time far away from the core, Rydberg atoms are also highly sensitive to electric fields and other external perturbations. This makes Rydberg atoms attractive candidates to use in high-sensitivity electric or magnetic field sensors. In Rydberg EIT, Rydberg atoms are setup as quantum interferometers coupled coherently to two light fields. The method is extremely sensitive to perturbations such as external electric fields.

1.4 Rydberg EIT

Electromagnetically induced transparency (EIT), first observed in 1991 [48], is a coherent nonlinear excitation scheme that involves the coupling of two light fields to three atomic energy levels. A medium which is normally opaque to a single light field can be made transparent by application of a second light field of the right frequency and intensity. The transparency is due to a coherent quantum interference effect. The transmission window can be orders of magnitude more spectrally narrow than the natural linewidth of the excited state [49]. Rydberg atom EIT is a variant of EIT, in which a 3-level cascade scheme is used, where the highest of the energy levels is a Rydberg state. In the context of Rydberg atom-surface interactions, Rydberg EIT was used recently to probe surface polaritons in vapor cells [9], to perform electrometry near a dielectric surface [50], and to measure the effects of atoms adsorbed onto an atom chip surface [10]. In the context of Rydberg atom-Rydberg atom interactions, Rydberg EIT was used recently to investigate the interactions between Rydberg atoms through trap loss [51] and an optical nonlinearity [52]. Due to the narrow linewidth and high sensitivity to external fields, Rydberg EIT is the ideal Rydberg atom excitation and detection scheme for our atom chip setup [13].

We will use Rydberg EIT to study the interactions of Rydberg atoms with nearby surfaces in the microscopic atom chip trap and to study the long-range interactions between Rydberg atoms trapped in a double well potential. For atom-surface interactions, the external electric fields will be the polariton and plasmon fields created above the surface that couple to the Rydberg atoms. Due to their large polarizability, Rydberg atoms are very sensitive to external fields. Since EIT is a coherent probing scheme that relies on quantum interference, it will enable us to detect decay or dephasing of Rydberg atom excitations with high sensitivity, as line broadenings, shifts and attenuations in the EIT spectrum. For Rydberg atom-Rydberg atom interactions,

the long-range interactions shift the Rydberg energies, and will cause a corresponding shift of the EIT line.

In this thesis, model Rydberg EIT measurements in room temperature vapor cells are described, where we use microwave AC electric fields to coherently couple two Rydberg levels in a 4-level cascade scheme. The microwaves are used to simulate the effect of coupling of Rydberg atoms to surface excitations or other Rydberg atoms in future experiments on the atom chip. We measure for the first time the polarization effects in transmission lineshapes in the 4-level Rydberg EIT scheme. We present theoretical calculations that take into account all magnetic sublevels and explain the measured EIT lineshapes both qualitatively and quantitatively.

1.5 Outline of the thesis

The thesis is organized as follows. In Chapter 2, the relevant theory is summarized, including the properties of ^{87}Rb, the properties of Rydberg atoms, the theory of laser cooling and trapping, the theory of EIT and the theory of magnetic wire traps. In Chapter 3, each part of the experimental apparatus is described in detail. This includes the vacuum system, the atom chip, the laser systems, the magnetic coils, the electrical systems, the imaging system and the control software. In Chapter 4, the manufacturing and assembly of the atom chip is described in detail. This includes the mounting of the chip onto the heat sink, the assembly of the heat sink, the electrical connections to the chip and the insertion of the chip into the vacuum chamber. In Chapter 5, the loading sequence of the atom chip is described, and the atom number and temperature at various stages during the loading is measured using time-of-flight absorption imaging. In Chapter 6, measurements on the room temperature 4-level Rydberg EIT system are presented and compared to theory. These measurements serve as a model for future measurements on the atom chip. In Chapter 7, large-scale

calculations of pair interaction potentials in the cold Rydberg gas are presented. The thesis closes with conclusions and an outlook on future measurements. Appendix A describes the field programmable gate array-based feedback circuit that was used to frequency stabilize our diode lasers. Appendix B describes how to use our Rydberg atom interaction code base. In Appendix C, the Mathematica code for numerical simulation of Rydberg EIT spectra is reproduced. Finally, Appendix D contains a list of the publications and presentations that I have been involved in during my stay at the University of Oklahoma.

Chapter 2

Theoretical basis

2.1 Introduction

In this chapter, the basic theory that is necessary to understand the work presented in this thesis is discussed. First, the properties of the isotope ^{87}Rb are summarized. Then, some of the theory of alkali Rydberg atoms is presented, including the numerical methods used to compute the radial wavefunctions of Cs and Rb Rydberg atoms. Next, the theory of electromagnetically induced transparency (EIT) is presented, including numerical methods that allow us to simulate polarization effects in Rydberg EIT spectra. The theory of laser cooling and magneto-optical traps is then discussed in some detail. The chapter concludes with the theory of magnetic wire traps.

2.2 Properties of ^{87}Rb

Most experiments described in this thesis are done with the isotope ^{87}Rb. In this section, the properties of the isotope and the relevant transitions are discussed.

2.2.1 Physical properties

Table 2.1 lists some of the relevant properties of ^{87}Rb, reproduced from Ref. [1]. Further properties of rubidium, such as the vapor pressure at different temperatures, will be introduced as they become relevant in later chapters. The energy level structure of rubidium is the topic of the next sections.

Table 2.1: Properties of ^{87}Rb from Ref. [1].

Quantity	Value
Atomic Number	37
Total Nucleons	87
Nuclear Spin	3/2
Atomic Mass	86.909 180 520(15) u
Relative Natural Abundance	27.83(2) %
Nuclear Lifetime	4.88×10^{10} yr
Vapor Pressure at 25 °C	$3.92(20) \times 10^{-7}$ torr
Ionization Limit	4.177 127 06(10) eV

2.2.2 D_2 transition

With the exception of a few EIT measurements done on Cs, all of the experiments presented in this thesis involve the different hyperfine levels of the transition ^{87}Rb $5^2S_{1/2} \rightarrow 5^2P_{3/2}$ known as D_2 line. Some of the relevant properties of the D_2 line are reproduced in Table 2.2 [1]. A level diagram of the transition is reproduced in Fig. 2.1, together with the laser transitions used in the experiments. The detunings of the laser beams are omitted from Fig. 2.1 for clarity. They can be found in Fig. 3.4. Apart from coupling the ground state to the first excited state via the D_2 line, atoms were also coupled to highly excited states for the EIT measurements, which is the topic of the next section.

Table 2.2: Properties of the ^{87}Rb $5^2S_{1/2} \rightarrow 5^2P_{3/2}$ transition (D_2 line) from Ref. [1].

Quantity	Value
Wavelength in Vacuum	780.241 209 686(13) nm
Lifetime	26.2348(12) ns
Natural Line Width (FWHM)	$2\pi \times 6.0666(18)$ MHz
Recoil Temperature	361.96 nK
Doppler Temperature	145.57 μK
Reduced Matrix Element[†] $\langle J = 1/2 \|\| e\boldsymbol{r} \|\| J' = 3/2 \rangle$	$\sqrt{2} \times 4.227\,52(87)\ e\,a_0$
Saturation Intensity $\|F = 2, m_F = 2\rangle \rightarrow \|F = 3', m'_F = 3\rangle$	1.669 33(35) mW cm^{-2}

[†] I use the convention of Refs. [53, 54] for the definition of reduced matrix elements which differs from Ref. [1] by a pre-factor $\sqrt{2J+1}$ as shown here.

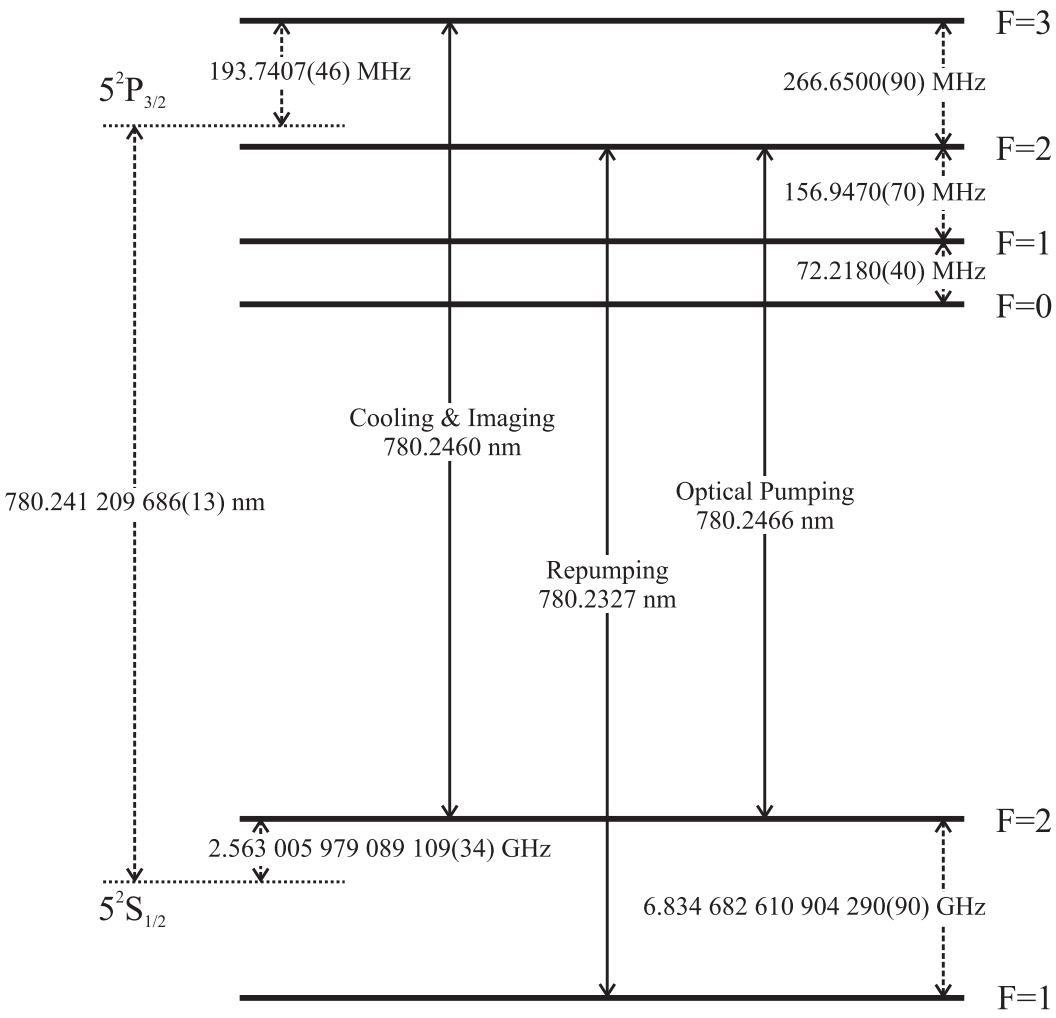

Figure 2.1: Level diagram of the Rubidium D_2 line with some of the relevant frequencies used in the experiment.

2.3 Rydberg atoms

Rydberg atoms are atoms in highly excited electronic states [33]. In this section, some of the properties of alkali metal Rydberg atoms are detailed.

2.3.1 Scaling laws

Rydberg atoms have exaggerated properties. For example, pairs of ultracold Cs atoms in high-lying Rydberg states ($n \sim 66$) can have such strong electric dipole interactions that they bind at internuclear distances of several micrometers [55, 56, 47]. Rydberg atoms are also highly sensitive to external electric fields [57]. This makes them promising for electrometry applications, especially when combined with a coherent detection scheme such as EIT [50].

The properties of Rydberg atoms generally scale with principal quantum number, n [33]. Some of the relevant scaling laws are shown in Table 2.3. In the context of using Rydberg atoms in multi-level coherent sensing schemes, the scaling laws are beneficial. The scaling of the polarizability and the transition dipole moment mean

Table 2.3: Scaling laws of alkali Rydberg atoms, together with the values for the ^{85}Rb $^2S_{1/2}$ n=100 state.

Quantity	Symbol	Scaling	Rb 100S	Ref.
Radius	$\langle r \rangle$	n^2	0.7 μm	[4]
Transition Dipole	$\langle nl\|er\|nl' \rangle$	n^2	0.5 $\mu\text{m} \cdot e$	[5]
Polarizability	α	n^7	3.8 μm^3	[58]
Van der Waals Interaction	C_6	n^{11}	-3.90×10^{23} (a.u.)†	[4]
Radiative Lifetime	τ	n^3	1.2 ms	[59]

† Corresponds to an energy shift of 56 MHz at internuclear distance $R = 10$ μm.

that the sensitivity of Rydberg atoms to external fields can be increased by many orders of magnitude by going to higher n Rydberg states. The scaling of the lifetime means that high-lying Rydberg atoms have narrow natural linewidths < 100 kHz. When the atom is driven into a superposition of ground state and Rydberg state by coherent excitation, the atoms can then form a dark state with a narrow linewidth in the absorption spectrum. This makes it possible to probe any perturbation caused by external fields at high resolution. The scaling of the Van der Waals interaction leads to such diverse phenomena as ultralong-range Rydberg atom pair interactions [4], dipole blockade and collective excitations [7], quantum computing with Rydberg atoms [5], and exotic states formed by pairs of Rydberg atoms, such as photo-initiated collisions [60] and macrodimers [47]. Pair interactions and macrodimers are the subject of Chapter 7 of this thesis.

2.3.2 Energies

The energies of alkali metal Rydberg atoms are calculated using quantum defect theory [33]. The inner electrons and the nucleus of the atom together constitute the ionic core. The ionic core behaves like an effective nucleus for the valence electron. The Rydberg atom is then treated as a perturbed Hydrogen atom. The differences between a Hydrogen atom and an alkali Rydberg atom are that the alkali core can be polarized because it contains many electrons, and the alkali core has a larger size and a larger mass. The alkali electron can penetrate the core more frequently. The result is that the energies of alkali Rydberg atoms follow a Rydberg-like formula known as the modified Rydberg-Ritz formula [33],

$$E_{nlj} = \mathrm{IP} - \frac{\mathrm{Ry}_{\mathrm{alk}}}{(n - \delta_{nlj})^2} \tag{2.1}$$

where IP is the ionization potential, $\mathrm{Ry}_{\mathrm{alk}}$ is the Rydberg constant for the alkali species, n is the principal quantum number, and δ_{nlj} is called the quantum defect.

Quantum defects are determined empirically to high accuracy by high-resolution spectroscopy, which makes it possible to predict energies with accuracy of ≤ 1 MHz using Eq. 2.1. The quantum defects are related to the phase shift of the radial wave function of the Rydberg atom due to the presence of the ionic core [33]. The quantum defects are non-zero due to core polarization and core penetration by the valence electron, which shift the energy of the state (to lower energy) when compared to Hydrogen. As the angular momentum l increases, the wavefunction of the valence electron becomes more and more circular, and the probability to find it close to or inside the core becomes less and less. Therefore, the quantum defect is largest for low l states and goes to zero as l increases. The quantum defect of a Rydberg state, quantum numbers $\{n, l, j\}$, is given by the power series,

$$\delta_{nlj} = \delta_0^{(lj)} + \frac{\delta_2^{(lj)}}{\left(n - \delta_0^{(lj)}\right)^2} + \frac{\delta_4^{(lj)}}{\left(n - \delta_0^{(lj)}\right)^4} + \frac{\delta_6^{(lj)}}{\left(n - \delta_0^{(lj)}\right)^6} + \frac{\delta_8^{(lj)}}{\left(n - \delta_0^{(lj)}\right)^8}, \cdots, \quad (2.2)$$

where $\delta_k^{(lj)}$ is the quantum defect parameter of order k for the quantum numbers $\{l, j\}$.

The quantum defect parameters for Rb used in this work are taken from Ref. [61] (nS and nD states), Ref. [62] (nF states), and Ref. [63] (nP states). The defect parameters for Cs are taken from Ref. [64] and are supplemented with the fine structure splittings from Ref. [65]. For states with $l \geq 4$, hydrogenic wavefunctions are used.

2.3.3 Wavefunctions

We calculate Rydberg atom wavefunctions from the l-dependent parametric model potential with a core polarization term, given in Ref. [66] as

$$V_l(r) = -\frac{Z_l(r)}{r} - \frac{\alpha_c}{2\,r^4}\left[1 - e^{-(r/r_c)^6}\right], \quad (2.3)$$

where α_c is the static dipole polarizability of the ionic core, and $Z_l(r)$ is the radial charge, given as

$$Z_l(r) = 1 + (z-1)\, e^{-a_1 r} - r\,(a_3 + a_4 r)\, e^{-a_2 r}. \tag{2.4}$$

Here, z is the nuclear charge of the atom and r_c is a cutoff radius to truncate the unphysical short-range part of the core polarization term. In Ref. [66], the energies determined from $V_l(r)$ were fit to the empirically determined Rydberg state energies to find optimized values of the fit parameters $a_1 \ldots a_5$ for each alkali species, and the results were tabulated. Using those optimized fit parameters, we programmed the potential $V_l(r)$ into the program RADIAL [67] to numerically solve the 1D Schrödinger equation and compute the radial wavefunctions of the Rydberg states of interest. The radial wavefunctions are highly oscillatory in space near the origin, and less oscillatory near the outer turning point. To accurately represent every oscillation, a non-uniform logarithmic grid is used in RADIAL for the wavefunction and the potential.[1] Wavefunctions around $n = 60$ are typically calculated using a grid of 1000 points with initial points spaced 10^{-7} a_0 apart at $r = 0$ and final points spaced 10 a_0 apart at $r \approx 8500$ a_0. A wavefunction can be calculated in a few seconds on a desktop level 3 GHz Pentium D PC using RADIAL.

2.3.4 Lifetimes

The effective lifetime of a Rydberg state is caused by two processes: radiative decay and black body decay. Radiative decay is due to spontaneous emission. Spontaneous emission depopulates the Rydberg state via transitions into the ground state and other low n states. The associated rate is $(\tau_{\text{rad}})^{-1}$ where τ_{rad} is called the radiative lifetime or lifetime at zero Kelvin. Black body decay, on the other hand, is due to the

[1]The potential grid parameters used in RADIAL are RATIO=1.15D0, RNN=1000.0D0, NV=100000, STEP=RNN/(NV-150.0D0), the radial wavefunction grid parameters are RN=6.0D5, NGP=50000, Ratio=1.15D0, STEP=RN/(NGP-200.0D0)

interaction of the Rydberg atom with the broadband thermal background radiation. The thermal radiation can be resonant or near-resonant with transitions to other close-lying Rydberg states. The resulting stimulated emission and absorption processes cause a depopulation of the Rydberg state at a rate of $(\tau_{\rm bb})^{-1}$, which is temperature dependent and goes to zero at 0 K. The effective lifetime is calculated from the sum of the two rates.

$$\tau_{\rm eff} = \left(\frac{1}{\tau_{\rm rad}} + \frac{1}{\tau_{\rm bb}} \right)^{-1} \tag{2.5}$$

The radiative and black body lifetimes used in this thesis are calculated with the empirical expressions from Ref. [59]

$$\tau_{\rm rad} = \tau_s \, n_{\rm eff}^{\delta} \tag{2.6}$$

$$\tau_{\rm bb} = \frac{A}{n_{\rm eff}^{D}} \frac{2.14 \times 10^{10}}{\exp\left(315780 \, B/n_{\rm eff}^{C} \times T/K\right) - 1}, \tag{2.7}$$

where τ_s, δ, A, B, C, and D are optimized parameters that depend on the alkali species and the quantum numbers l and j of the Rydberg state, $n_{\rm eff} = n - \delta$ is the effective quantum number where δ is the quantum defect, and T is the temperature of the thermal background. The optimized parameters are tabulated in Ref. [59]. The empirical expressions were verified experimentally to be correct for Rb [68, 69] and Cs [70].

2.4 Electromagnetically induced transparency

In this section, the theory of the experiments presented in Chapter 6 is detailed.

EIT is the phenomenon where a medium, usually an atomic vapor, that would normally be opaque to light of a certain frequency, called the probe light, can be rendered transparent in the presence of intense light of a different frequency, called the coupling light [71, 49, 48, 72]. EIT takes place in the three-level system. Two example systems are shown in Fig. 2.2. An energy level, usually a short-lived excited

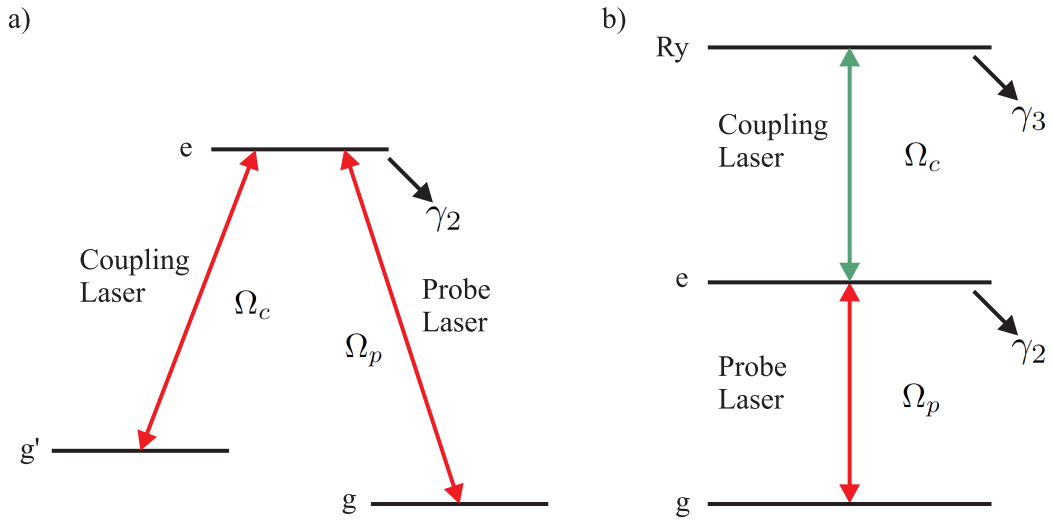

Figure 2.2: Two alkali three-level systems that exhibit EIT. The hyperfine EIT system shown in a) is a λ-system in which two hyperfine levels of the ground state are coupled to an excited state by two radiation fields. The ground states are stable or metastable. A strong coupling beam and a weak probe beam couple the short-lived excited state to the energetically higher and lower ground state, respectively. EIT arises from a dark state that forms in the presence of both laser beams. The dark state consists of a coherent superposition of both ground states. The Rydberg EIT system shown in b) is a Ξ-system consisting of a ground state, the first excited state, and a Rydberg level. The ground and Rydberg levels are long-lived. Here, the strong coupling beam and weak probe beam couple the excited state to the ground and the Rydberg level, respectively. In this case, the dark state is formed between the Rydberg level and the ground state.

state, is coherently coupled to two long-lived energy levels by two light fields. EIT is a coherent nonlinear effect that is due to the destructive interference of a three-photon process with a single-photon process. The three-photon process consists of absorption of one photon from the probe and two photons from the coupling light. The single-photon process consists of absorption of a single photon from the probe light. The destructive interference is strongest when the coupling light Rabi frequency is much

larger than the probe Rabi frequency, which is sometimes called the EIT condition. To satisfy the EIT condition, the coupling beam typically has to be much more intense than the probe beam.

Closely related to EIT is coherent population trapping [73]: in the presence of both coupling and probe laser beams, the atoms are transferred into a dark state. A dark state is a quantum mechanical superposition of field-free eigenstates that is not coupled to other states by the laser fields anymore.

Due to its coherent nature, the window of transparency created via EIT can be orders of magnitude narrower in frequency than the natural linewidth of the probe transition. The width of the peak is not determined by the spontaneous decay of the short-lived excited state, but by the coherence relaxation rate between two stable or meta-stable atomic states. For example, using noise correlation spectroscopy, EIT linewidths of less than 1 kHz have been measured on a transition that has a natural linewidth of 6 MHz, in a vapor cell filled with ^{87}Rb [74]. The narrow linewidth makes EIT a valuable tool for high-resolution spectroscopy and sensitive frequency measurements. For example, EIT can be used to precisely lock lasers to an absolute frequency reference [75]. Associated with the narrow EIT transmission peak is a large dispersion, which has been exploited to create slow light [76, 77]. EIT has also been used to create lasing without inversion [78], and recently, EIT with single atoms in a cavity was demonstrated [79].

A system in which EIT is frequently studied is the λ-system, shown in Fig. 2.2a, where the common level is the short-lived first excited state and the two long-lived levels are two hyperfine components of the ground state of an alkali atom. EIT in this system is sometimes called hyperfine EIT [74]. Here, we will focus on ladder-type systems, or Ξ-systems, where one of the long-lived levels is a high-lying Rydberg state ($n \sim 40$). One such system is shown in Fig. 2.2b. EIT in such a system is

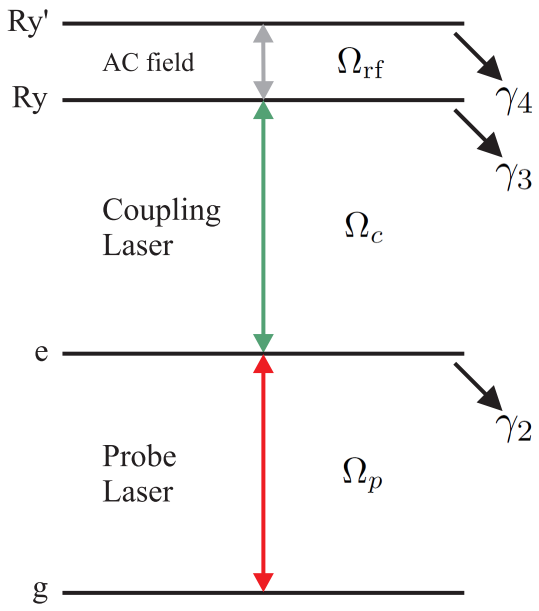

Figure 2.3: Four-level system investigated in this thesis. A three-level Rydberg EIT system is coupled to a second close-lying Rydberg state via microwave radiation.

sometimes called Rydberg EIT [50]. Due to the high sensitivity of Rydberg atoms to external fields, Rydberg EIT can be used for precise sensing such as electrometry or magnetometry, among other applications. For example, three-level Rydberg EIT has been used recently to demonstrate a giant DC Kerr effect [80], to probe surface polaritons in microscopic vapor cells [9], to measure small DC electric fields close to surfaces [10], and to detect cooperative atom-light interactions in an ultracold Rydberg gas [52].

If a three-level EIT system is coupled to a fourth level, the lineshape of the transmission peak can change dramatically, depending on the strength of the coupling. The absorption spectrum in this system can be quite rich [81, 82, 83, 84, 85]. In this thesis, the four-level Ξ-system with two Rydberg states, shown schematically in Fig. 2.3, is investigated. In this setup, a Rydberg state is coupled to a second close-lying Rydberg state by microwave radiation, and the Rydberg atoms are probed using EIT. This system can be used for electrometry. EIT is used to setup the atoms as

interferometers to perform quantum assisted sensing of applied AC electric fields. Because of the large transition dipole moment between nearby Rydberg states, a small AC electric field amplitude on the order of 100 μV cm^{-1} is converted into a large Rabi frequency on the order of MHz that couples the two Rydberg states together. This coupling changes the amplitude and lineshape of the EIT peak observed on the probe transition, which can be resolved to frequencies much smaller than the natural linewidth, and allows for the detection of very small electric field amplitudes $< \mu$V cm^{-1}, using standard diode laser technology in a room temperature vapor cell. Using narrow linewidth lasers and high-lying Rydberg states ($n \sim 100$), the EIT peak can become as narrow as $\sim 2\pi \times 2$ kHz, and the corresponding sensitivity becomes < 10 nV cm^{-1}. Rydberg atoms can, in principle, provide the most sensitive electric field sensors to date. In addition, a detector based on atoms has the benefit over semiconductor devices that it is linked to the atomic parameters and therefore inherently traceable. This is because atoms are always the same, while solid state devices are all slightly different, show aging, and need re-calibration.

In the following sections, the basic theory that is relevant for the EIT experiments described in this thesis is presented.

2.4.1 2-level atom

To understand EIT, we first consider the 2-level system shown in Fig. 2.4, subject to laser radiation with frequency ω. The field-free states $|1\rangle$ and $|2\rangle$ have energies $\hbar\omega_1$ and $\hbar\omega_2$, separated in energy by $\hbar\omega_0 = \hbar\omega_2 - \hbar\omega_1$. Making the dipole approximation and treating the field classically, the Hamiltonian is

$$H = \hbar\,\omega_2\,|2\rangle\langle 2| + \hbar\,\omega_1\,|1\rangle\langle 1| - \langle 2|\boldsymbol{\mu}\cdot\mathbf{E}|1\rangle\,|2\rangle\langle 1| - \langle 1|\boldsymbol{\mu}\cdot\mathbf{E}|2\rangle\,|1\rangle\langle 2|, \tag{2.8}$$

where $\mu = -e\,\mathbf{r}$ is the electric dipole operator, $\mathbf{r}$ is the position of the electron, and $\mathbf{E}$ the electric field. Here e denotes the positive elementary charge, e.g. $e = |e|$. The

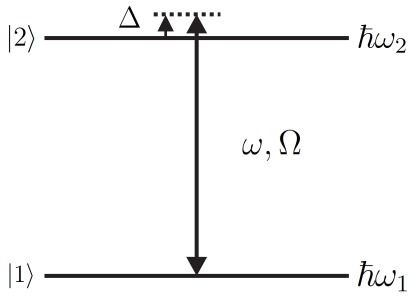

Figure 2.4: The two-level system. Two energy levels $|1\rangle$, and $|2\rangle$, with energies $\hbar\omega_1$ and $\hbar\omega_2$ are coupled by laser radiation of frequency ω, Rabi frequency Ω, and detuning Δ.

electric field is given by

$$\mathbf{E} = \mathrm{Re}\left\{E_0\,\boldsymbol{\epsilon}\,e^{i\omega t}\right\} = \frac{1}{2}E_0\left(\boldsymbol{\epsilon}\,e^{i\omega t} + \boldsymbol{\epsilon}^*\,e^{-i\omega t}\right), \tag{2.9}$$

where E_0 is the real electric field amplitude, and $\boldsymbol{\epsilon}$ is the complex polarization unit vector.

Since it will be of importance in the later treatment of polarization effects in the multi-level system, the significance of polarization will be discussed here. Let $\hat{x}, \hat{y}$, and $\hat{z}$ be the unit vectors of a right handed Cartesian coordinate system. For right-handed circularly polarized (RHC) light propagating in the z-direction, $\boldsymbol{\epsilon}_{\mathrm{RHC}} = \frac{1}{\sqrt{2}}(\hat{x} - i\,\hat{y})$, for left-handed circularly polarized (LHC) light propagating in the z-direction, $\boldsymbol{\epsilon}_{\mathrm{LHC}} = \frac{1}{\sqrt{2}}(\hat{x} + i\,\hat{y})$, and for light linearly polarized along the z-direction, $\boldsymbol{\epsilon}_z = \hat{z}$. If we choose z as the quantization axis, and the atomic basis $|n, L, J, F, m_F\rangle$,[2] where then RHC light corresponds to σ^+ light that drives $\Delta m_F = +1$ transitions, LHC light corresponds to σ^- light that drives $\Delta m_F = -1$ transitions, and light polarized along the z-axis corresponds to π polarized light that drives $\Delta m_F = 0$ transitions. We see that linearly polarized light along the x-axis corresponds to a polarization vector $\boldsymbol{\epsilon}_{\mathrm{x}} = \frac{1}{\sqrt{2}}(\boldsymbol{\epsilon}_{\mathrm{RHC}} + \boldsymbol{\epsilon}_{\mathrm{LHC}})$, and linearly polarized light along the y-axis corresponds to

[2]Here and in the rest of the thesis, $\boldsymbol{F} = \boldsymbol{J} + \boldsymbol{I}$ denotes the total atomic angular momentum, $\boldsymbol{J} = \boldsymbol{L} + \boldsymbol{S}$ is the total electronic angular momentum, $\boldsymbol{I}$ is the nuclear angular momentum, $\boldsymbol{L}$ is the electronic orbital angular momentum, and $\boldsymbol{S}$ denotes the electronic spin.

$\boldsymbol{\epsilon}_{\rm y} = \frac{1}{i\sqrt{2}}(\boldsymbol{\epsilon}_{\rm RHC} + \boldsymbol{\epsilon}_{\rm LHC})$.

The spherical components of the dipole operator in this frame of reference are

$$r_{+1} = -\frac{1}{\sqrt{2}}(x + i\,y) \tag{2.10}$$

$$r_0 = z \tag{2.11}$$

$$r_{-1} = \frac{1}{\sqrt{2}}(x - i\,y)\,. \tag{2.12}$$

Any complex polarization vector can also be expressed in terms of its spherical components. The dot products $\boldsymbol{\epsilon}\cdot\mathbf{r}$ in the interaction Hamiltonian then gives rise to terms involving sums over the spherical components of the dipole operator, which can be evaluated conveniently in the atomic basis $|n, L, J, F, m_F\rangle$ using the Wigner-Eckart theorem [53, 54].

For example, if we assume for a moment that $|2\rangle$ is an $m_{\rm F} = 1$ magnetic sublevel of an electronically excited state, and $|1\rangle$ is an $m_{\rm F} = 0$ magnetic sublevel of an electronic ground state, we can see that σ^+ light gives rise to non-zero elements both above and below the diagonal of the Hamiltonian. This is because, for σ^+ light, from Eq. 2.9, we not only get a term in the Hamiltonian that is proportional to $\boldsymbol{\epsilon}\cdot\mathbf{r} = \frac{1}{\sqrt{2}}(x - i\,y) = r_-$, but the electric field also gives rise to a term proportional to $\boldsymbol{\epsilon}^*\cdot\mathbf{r} = \frac{1}{\sqrt{2}}(x + i\,y) = -r_+$. The evaluation of those two terms using the Wigner-Eckart theorem shows that $(-1)\langle 2|\,r_+|1\rangle = \langle 1|r_-|2\rangle$, a general property that ensures that the Hamiltonian remains Hermitian even in the case of circularly polarized light. To illustrate this further, the Hamiltonian in matrix notation is

$$H = \hbar \begin{pmatrix} \omega_1 & \langle 1|\frac{1}{2}E_0\, e\,(\mathbf{r}\cdot\boldsymbol{\epsilon}\, e^{i\omega t} + \mathbf{r}\cdot\boldsymbol{\epsilon}^*\, e^{-i\omega t})\,|2\rangle \\ \langle 2|\frac{1}{2}E_0\, e\,(\mathbf{r}\cdot\boldsymbol{\epsilon}\, e^{i\omega t} + \mathbf{r}\cdot\boldsymbol{\epsilon}^*\, e^{-i\omega t})\,|1\rangle & \omega_b \end{pmatrix} \tag{2.13}$$

which becomes for σ^+ light, where $\boldsymbol{\epsilon} = \frac{1}{\sqrt{2}}(\hat{x} - i\,\hat{y})$

$$H_{\sigma^+} = \hbar \begin{pmatrix} \omega_1 & \frac{1}{2}(\Omega_- e^{i\omega t} + 0\, e^{-i\omega t}) \\ \frac{1}{2}(0\, e^{i\omega t} - \Omega_+ e^{-i\omega t}) & \omega_2 \end{pmatrix}, \tag{2.14}$$

where the Rabi frequencies $\Omega_- = E_0\, e\, \hbar^{-1} \langle 1|r_-|2\rangle$ and $\Omega_+ = E_0\, e\, \hbar^{-1} \langle 2|r_+|1\rangle$ are both real quantities. Note that the zeros enter because $\langle 2|r_-|1\rangle = \langle 1|r_+|2\rangle = 0$, since $r_\pm$ couples only $\Delta m = \pm 1$. Because $\Omega_+ = -\Omega_-$, we get

$$H_{\sigma^+} = \hbar \begin{pmatrix} \omega_1 & -\frac{1}{2}\Omega_+ e^{i\omega t} \\ -\frac{1}{2}\Omega_+ e^{-i\omega t} & \omega_2 \end{pmatrix}. \tag{2.15}$$

Incidentally, this particular choice of polarization has eliminated the counter-rotating terms in the Hamiltonian that would normally be neglected as part of the rotating wave approximation (RWA) [86].

In the following, we assume the light is linearly polarized along z, $\boldsymbol{\epsilon} = \hat{z}$, and the field couples two states $|1\rangle$ and $|2\rangle$ with a Rabi frequency $\Omega = -\mu\, E_0\, \hbar^{-1}$, where $\mu = -e\,\langle 2|\mathbf{r}\cdot\boldsymbol{\epsilon}|1\rangle$. Since the polarization vector is real, the Hamiltonian becomes

$$H = \hbar \begin{pmatrix} \omega_1 & \frac{1}{2}\Omega\ (e^{i\omega t} + e^{-i\omega t}) \\ \frac{1}{2}\Omega\ (e^{i\omega t} + e^{-i\omega t}) & \omega_2 \end{pmatrix}. \tag{2.16}$$

This Hamiltonian is time-dependent. By a sequence of unitary transformations, it can be put into a time-independent form [87]. First, we go to the interaction picture with the following unitary transformation

$$U = \begin{pmatrix} e^{-i\omega_1 t} & 0 \\ 0 & e^{-i\omega_2 t} \end{pmatrix}. \tag{2.17}$$

In the interaction picture, the wavefunction is $\psi_I = U^\dagger \psi_S$. After this unitary transformation, the Hamiltonian in the new frame is $H_I = i\hbar \frac{dU^\dagger}{dt} U + U^\dagger H U$ [88], which is

$$H_1 = \frac{\hbar}{2} \begin{pmatrix} 0 & \Omega\, e^{i\Delta t}\,(e^{-2i\omega t} + 1) \\ \Omega\, e^{-i\Delta t}\,(1 + e^{2i\omega t}) & 0 \end{pmatrix}. \tag{2.18}$$

Here, the detuning is defined as $\Delta = \omega - (\omega_2 - \omega_1)$. To remove the time dependent factors involving the detuning, we transform into a rotating frame using the unitary transformation

$$U_2 = \begin{pmatrix} e^{i\frac{\Delta}{2}t} & 0 \\ 0 & e^{-i\frac{\Delta}{2}t} \end{pmatrix}. \tag{2.19}$$

The Hamiltonian in this rotating frame becomes

$$H_2 = \frac{\hbar}{2} \begin{pmatrix} \Delta & \Omega\left(1 + e^{-2i\omega t}\right) \\ \Omega\left(1 + e^{2i\omega t}\right) & -\Delta \end{pmatrix}. \tag{2.20}$$

Then, we perform a shift in energy, using the unitary transformation

$$U_3 = \begin{pmatrix} e^{-i\frac{\Delta}{2}t} & 0 \\ 0 & e^{-i\frac{\Delta}{2}t} \end{pmatrix}. \tag{2.21}$$

The Hamiltonian becomes

$$H_3 = \frac{\hbar}{2} \begin{pmatrix} 0 & \Omega\left(1 + e^{-2i\omega t}\right) \\ \Omega\left(1 + e^{2i\omega t}\right) & -2\Delta \end{pmatrix}. \tag{2.22}$$

Finally, we make the rotating wave approximation (RWA), ignoring the terms that rotate at twice the laser frequency in the off-diagonal, to get the canonical two-level Hamiltonian

$$H_{\mathrm{RWA}} = \frac{\hbar}{2} \begin{pmatrix} 0 & \Omega \\ \Omega & -2\Delta \end{pmatrix}. \tag{2.23}$$

The basis that diagonalizes this Hamiltonian is the dressed state basis, which consists of coupled states of the atom plus laser field. In the two-level system, there is an infinite number of multiplicities of atom plus laser field states. One pair of states $\{|1, n\rangle, |2, n-1\rangle\}$ exists for each possible photon number n in the laser mode [89]. However, as long as we ignore spontaneous emission and stay within the RWA, the system is confined within one of the multiplicities. The pair of coupled dressed states

is then given by [89]

$$|a\rangle = \sin(\theta)|1\rangle + \cos(\theta)|2\rangle \tag{2.24}$$

$$|b\rangle = \cos(\theta)|1\rangle - \sin(\theta)|2\rangle, \tag{2.25}$$

where θ is an effective mixing angle for which $0 \leq \theta < \pi/2$ and

$$\tan(2\theta) = -\frac{\Omega}{\Delta}. \tag{2.26}$$

The eigenvalues are $-\hbar/2\left(\Delta \pm \sqrt{\Delta^2 + \Omega^2}\right)$. The dressed states are split in energy by $\hbar\,\Omega_1 = \hbar\sqrt{\Delta^2 + \Omega^2}$, where Ω_1 is sometimes referred to as the generalized Rabi frequency. The light changes the atomic energy levels from their zero-field values. This shift is called the light shift. It has a magnitude of $\hbar/2 \times \Omega_1$. Explicitly, the pre-factors in Eqs. 2.24 and 2.25 can be written as

$$\sin(\theta) = \frac{\Omega}{\sqrt{2\,(\Omega_1^2 - \Delta\,\Omega_1)}} \tag{2.27}$$

$$\cos(\theta) = \frac{\Omega_1 - \Delta}{\sqrt{2\,(\Omega_1^2 - \Delta\,\Omega_1)}}. \tag{2.28}$$

For zero detuning, the dressed states become

$$|a(\Delta = 0)\rangle = \frac{1}{\sqrt{2}}\left(|1\rangle + |2\rangle\right) \tag{2.29}$$

$$|b(\Delta = 0)\rangle = \frac{1}{\sqrt{2}}\left(|1\rangle - |2\rangle\right). \tag{2.30}$$

and the splitting is given by the Rabi frequency Ω.

The dressed state basis allows us to gain intuitive insight into the absorption spectrum that obtains when probing the two-level system on a transition involving a third level $|3\rangle$, using a weak probe $\Omega_p \ll \Omega$ that couples for example $|3\rangle$ and $|2\rangle$. Since each of the dressed states has a component parallel to $|2\rangle$, the probe can couple to each of the dressed states, which are both shifted in energy. We therefore expect that two absorption lines will appear, split by the generalized Rabi frequency Ω_1. This

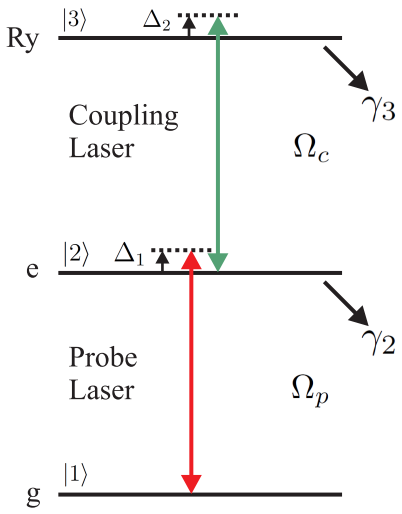

Figure 2.5: Three-level system subject to two laser fields.

is the well-known Autler-Townes effect [90]. The dressed state basis of the two-level system gives intuitive insight into the three-level system when the probe laser is weak enough to not perturb the eigenvectors.

2.4.2 3-level atom

To understand the 3-level ladder system subject to two fields shown in Fig. 2.5, we first derive the Hamiltonian as in the two-level system. After making the dipole approximation, going to the interaction picture, and making the RWA, we get

$$H = \frac{\hbar}{2}\begin{pmatrix} 0 & \Omega_p & 0 \\ \Omega_p & -2\Delta_1 & \Omega_c \\ 0 & \Omega_c & -2\left(\Delta_1+\Delta_2\right) \end{pmatrix}. \tag{2.31}$$

The evolution of the system can be calculated using the density matrix formalism. In this formalism, semi-classical decay and decoherence operators are used to account for spontaneous emission and dephasing due to finite laser linewidths [89]. The time evolution of the density matrix operator ρ is given by the master equation

$$\dot{\rho} = -\frac{i}{\hbar}\left[H,\rho\right] + L_{32} + L_{21} + L_d, \tag{2.32}$$

with the decay and decoherence operators [49]

$$L_{ij} = \frac{\Gamma_{ij}}{2} \left(2\,\sigma_{ji}\,\rho\,\sigma_{ij} - \sigma_{ii}\,\rho - \rho\,\sigma_{ii} \right). \tag{2.33}$$

where Γ_{ij} is the spontaneous decay rate from energy level i to energy level j, and $\sigma_{ij} = |i\rangle\langle j|$ are projection operators. The total decay rate of a level due to spontaneous emission is $\gamma_i = \sum_j \Gamma_{ij} = (\tau_i)^{-1}$, where τ_i is the e^{-1} lifetime of state i. The total dephasing rate of a level due to spontaneous emission is $\gamma_{ij} = (\gamma_i + \gamma_j)/2$. The case of equal indices on a decay operator corresponds to an additional dephasing process, affecting only the coherences but not the populations. Such additional dephasing could be due to collisions, laser phase jitter or other sources of decoherence and are neglected here. The decay of the Rydberg level $|3\rangle$ can usually be neglected on the grounds of its extremely long lifetime ($\tau \sim 100$ μs for $n \sim 50$ in Cs and Rb), but is included here for completeness. L_d is a dephasing operator that can be used to add dephasing due to finite laser linewidth. Its definition is $L_d = \sum_{ij} \left(-\gamma^L\right)_{ij} \rho_{ij}\,|i\rangle\langle j|$ where $\left(\gamma^L\right)_{ij}$ is the sum of the linewidths of all lasers coupling the levels $i \leftrightarrow j$ [91].

Ignoring dephasing due to finite laser linewidths, the differential equations for the density matrix elements are

$$\begin{aligned}
\dot{\rho}_{11} &= \gamma_2\rho_{22} - i\frac{\Omega_p}{2}(\rho_{21} - \rho_{12}) \\
\dot{\rho}_{22} &= -\gamma_2\rho_{22} + \gamma_3\rho_{33} + i\frac{\Omega_p}{2}(\rho_{21} - \rho_{12}) - i\frac{\Omega_c}{2}(\rho_{32} - \rho_{23}) \\
\dot{\rho}_{33} &= -\gamma_3\rho_{33} + i\frac{\Omega_c}{2}(\rho_{32} - \rho_{23})) \\
\dot{\rho}_{21} &= -(\gamma_{21} - i\Delta_1)\rho_{21} + i\frac{\Omega_p}{2}(\rho_{22} - \rho_{11}) - i\frac{\Omega_c}{2}\rho_{31} \\
\dot{\rho}_{32} &= -(\gamma_{32} - i\Delta_2)\rho_{32} + i\frac{\Omega_c}{2}(\rho_{33} - \rho_{22}) + i\frac{\Omega_p}{2}\rho_{31} \\
\dot{\rho}_{31} &= -(\gamma_{31} - i(\Delta_1 + \Delta_2))\rho_{31} - i\frac{\Omega_c}{2}\rho_{21} + i\frac{\Omega_p}{2}\rho_{32}
\end{aligned} \tag{2.34}$$

The complex susceptibility at the probe frequency is given by [92]

$$\chi = -4\frac{\hbar^2\,\Omega_p\,N}{\epsilon_0\,(E_p)^2}\,\rho_{21}, \tag{2.35}$$

where ϵ_0 is the permittivity of free space, N is the density of atoms and E_p is the electric field amplitude of the probe field. The probe absorption is therefore proportional to $\mathrm{Im}\,\{\rho_{21}\}$, and the dispersion is proportional to $\mathrm{Re}\,\{\rho_{21}\}$ [49]. Solving the above equations in steady state and setting γ_3 to zero, ρ_{21} becomes, to first order in Ω_p (weak probe limit),

$$\rho_{21} = -\frac{(\Delta_1+\Delta_2)\,\Omega_p}{-2\Delta_1^2 - 2\Delta_1\Delta_2 + \frac{\Omega_c^2}{2} - i(\Delta_1+\Delta_2)\gamma_2} + O(\Omega_p^2). \tag{2.36}$$

With the coupling laser on resonance, $\Delta_2 = 0$, the probe absorption and dispersion in the weak probe limit are then proportional to

$$\mathrm{Im}\,\{\rho_{21}\} = -\frac{\gamma_2}{\left(-2\Delta_1 + \frac{\Omega_c^2}{2\Delta_1}\right)^2 + \gamma_2^2}\,\Omega_p + O(\Omega_p^2) \tag{2.37}$$

$$\mathrm{Re}\,\{\rho_{21}\} = -\frac{\frac{\Omega_c^2}{2\Delta_1} - 2\Delta 1}{\left(\frac{\Omega_c^2}{2\Delta_1} - 2\Delta_1\right)^2 + \gamma_2^2}\,\Omega_p + O(\Omega_p^2). \tag{2.38}$$

Plots of the transmission and dispersion versus probe detuning, Δ_1, are shown in Fig. 2.6, for $\Omega_c = 2\pi\ \times 1.0$ MHz and $\Omega_c = 0$. The EIT peak appears as a narrow window of transparency on top of the absorption peak, and is associated with a high dispersion.

Some intuitive insight can be gained from considering the eigenvectors of the Hamiltonian, which are the dressed states within one multiplicity. For simplicity, we assume the detunings to be zero so that both lasers are on resonance. Following Ref. [82], we begin by realizing that

$$|v\rangle = -\frac{\Omega_c}{\Omega'}|1\rangle + \frac{\Omega_p}{\Omega'}|3\rangle, \tag{2.39}$$

with

$$\Omega' = \sqrt{\Omega_p^2 + \Omega_c^2}, \tag{2.40}$$

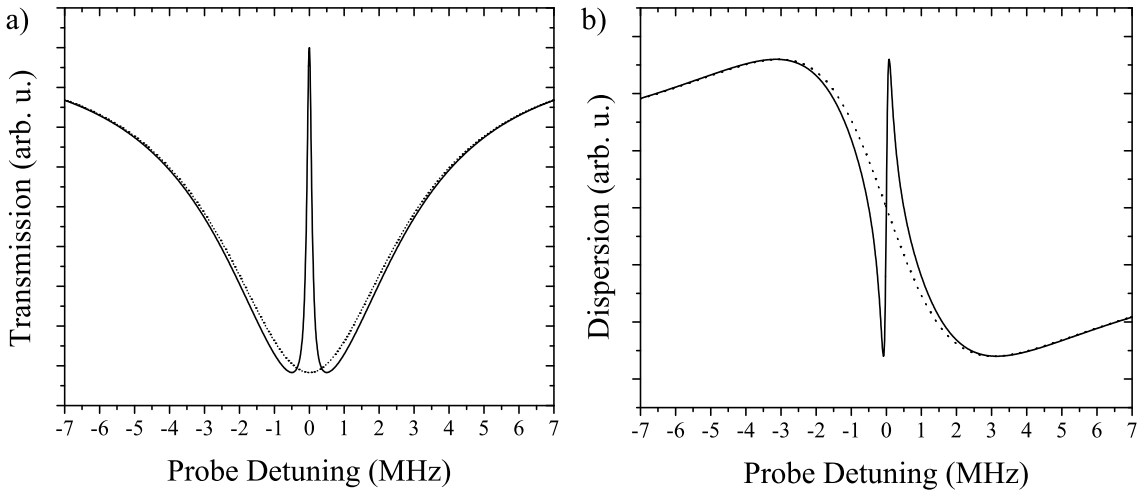

Figure 2.6: Transmission ($\propto \mathrm{Im}\{\rho_{21}\}$) and Dispersion ($\propto \mathrm{Re}\{\rho_{21}\}$) in the three-level system, in the weak probe limit, as given by Eq. 2.37 and Eq. 2.38. The functions are plotted against the probe detuning Δ_1, for the two coupling Rabi frequencies $\Omega_c = 2\pi \times 1$ MHz (solid lines) and $\Omega_c = 0$ (dotted lines). The other parameters are $\Omega_p = 2\pi \times 1$ kHz, $\gamma_2 = 2\pi \times 6.12$ MHz, and $\Delta_2 = \gamma_3 = 0$.

is an eigenvector corresponding to eigenvalue zero. $|v\rangle$ is not coupled by the Hamiltonian to state $|2\rangle$. Even though the laser fields couple $|1\rangle$ and $|3\rangle$ to $|2\rangle$, the contributions in the superposition $|v\rangle$ cancel exactly:

$$\langle 2|H|v\rangle = \langle 2|H|1\rangle\frac{\Omega_c}{\Omega'} - \langle 2|H|3\rangle\frac{\Omega_p}{\Omega'} = \frac{1}{\Omega'}\left(\Omega_p\Omega_c - \Omega_p\Omega_c\right) = 0 \tag{2.41}$$

When both laser fields are on, depending on the initial conditions, atoms are either adiabatically transferred into the dark state $|v\rangle$ or reach it via spontaneous emission. Once in the dark state, the atoms will not absorb the probe light anymore, making the medium transparent. Both $|1\rangle$ and $|2\rangle$ need to be long-lived states in order to prevent the dark state from decaying.

The other eigenvectors can be found by realizing that

$$|u\rangle = \frac{\Omega_p}{\Omega'}|1\rangle + \frac{\Omega_c}{\Omega'}|3\rangle. \tag{2.42}$$

is a superposition of only $|1\rangle$ and $|3\rangle$ that is orthogonal to $|v\rangle$. In the basis spanned by $|u\rangle$, $|v\rangle$, and $|2\rangle$, H is block diagonal: $|v\rangle$ is not coupled to the other states, but $|u\rangle$ is coupled to $|2\rangle$ with Rabi frequency Ω'. The remaining two dressed state eigenvectors are thus obtained by diagonalizing a 2×2 matrix, to obtain

$$|a\rangle = -\frac{1}{\sqrt{2}}\left(|2\rangle + \frac{\Omega_p}{\Omega'}|1\rangle + \frac{\Omega_c}{\Omega'}|3\rangle\right) \tag{2.43}$$

$$|b\rangle = -\frac{\Omega_c}{\Omega'}|1\rangle + \frac{\Omega_p}{\Omega'}|3\rangle, \tag{2.44}$$

$$|c\rangle = -\frac{1}{\sqrt{2}}\left(-|2\rangle + \frac{\Omega_p}{\Omega'}|1\rangle + \frac{\Omega_c}{\Omega'}|3\rangle\right), \tag{2.45}$$

with eigenvalues

$$\lambda_a = +\frac{\hbar}{2}\Omega' \tag{2.46}$$

$$\lambda_b = 0 \tag{2.47}$$

$$\lambda_c = -\frac{\hbar}{2}\Omega', \tag{2.48}$$

as depicted in Fig. 2.7. The form of the dressed states of the three-level system $\{|a\rangle, |b\rangle, |c\rangle\}$ reveals some of the expected features of the absorption spectrum that should obtain when Ω_p is not small, and the system is instead probed from a fourth level, $|4\rangle$ [82]. The dressed states retain their form as long as the additional probe laser is weak enough to not perturb the eigenvectors. If this is the case, and this new probe laser couples $|4\rangle$ to $|1\rangle$, we expect to see three absorption lines, split by $\hbar\,\Omega'/2$. When the new probe laser couples $|4\rangle$ to $|3\rangle$, we should obtain a similar spectrum. However, when coupling $|4\rangle$ to $|2\rangle$, only two lines should appear, because the dark state $|b\rangle$ is not coupled (it has no $|2\rangle$ component).

The four-level system will be analyzed in more detail in the following section.

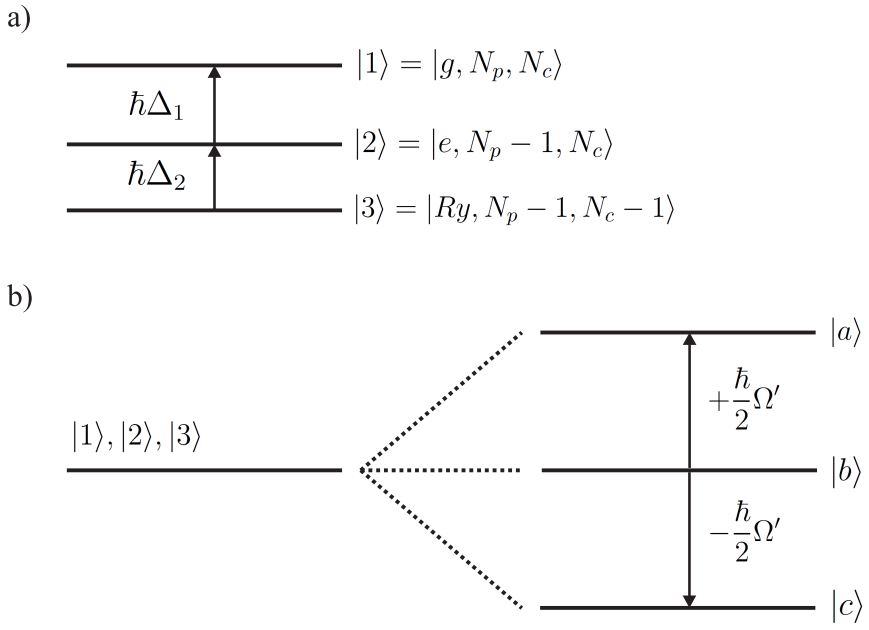

Figure 2.7: Light shifts in the three-level system. a) In the uncoupled basis of atom+field states, the energy levels are separated by the laser detunings. Shown is the case of positive (blue) detuning of both laser beams. In the notation $|\alpha, \beta, \gamma\rangle$, α refers to the atomic energy level, and β and γ refer to the photon numbers of the probe and coupling fields, respectively. b) At zero detuning, the uncoupled states are degenerate. In the basis of coupled atom+field states $|a\rangle$, $|b\rangle$, $|c\rangle$ (dressed state basis), the effect of the off-diagonal coupling terms in the Hamiltonian is to split the energy levels by the light shift $\hbar\Omega'/2$. In the dressed state basis, the Hamiltonian is diagonal.

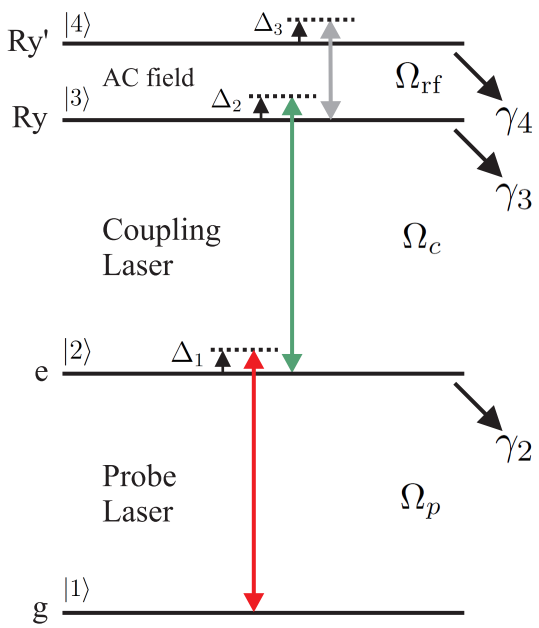

Figure 2.8: Four-level system subject to two laser fields and microwave radiation.

2.4.3 4-level atom

The 4-level ladder system with two Rydberg states, subject to two laser fields and microwave radiation is investigated experimentally in Chapter 6. The system is shown in Fig. 2.8. The Hamiltonian is derived analogous to the 2-level and 3-level systems. It is

$$H = \frac{\hbar}{2}\begin{pmatrix} 0 & \Omega_p & 0 & 0 \\ \Omega_p & -2\Delta_1 & \Omega_c & 0 \\ 0 & \Omega_c & -2(\Delta_1+\Delta_2) & \Omega_{\mathrm{rf}} \\ 0 & 0 & \Omega_{\mathrm{rf}} & -2(\Delta_1+\Delta_2+\Delta_3) \end{pmatrix}. \tag{2.49}$$

The master equation becomes

$$\dot{\rho} = -\frac{i}{\hbar}[H,\rho] + L_{43} + L_{32} + L_{21}, \tag{2.50}$$

where the decay and decoherence operators are defined as in Eq. 2.33. Using the same notation as in the last section, the density matrix equations become

$$
\begin{aligned}
\dot{\rho}_{11} &= \gamma_2\rho_{22} - i\frac{\Omega_p}{2}(\rho_{21} - \rho_{12}) \\
\dot{\rho}_{22} &= -\gamma_2\rho_{22} + \gamma_3\rho_{33} + i\frac{\Omega_p}{2}(\rho_{21} - \rho_{12}) - i\frac{\Omega_c}{2}(\rho_{32} - \rho_{23}) \\
\dot{\rho}_{33} &= -\gamma_3\rho_{33} + \gamma_4\rho_{44} + i\frac{\Omega_c}{2}(\rho_{32} - \rho_{23}) - i\frac{\Omega_{\mathrm{rf}}}{2}(\rho_{43} - \rho_{34}) \\
\dot{\rho}_{44} &= -\gamma_4\rho_{44} + i\frac{\Omega_{\mathrm{rf}}}{2}(\rho_{43} - \rho_{34}) \\
\dot{\rho}_{21} &= -(\gamma_{21} - i\Delta_1)\rho_{21} + i\frac{\Omega_p}{2}(\rho_{22} - \rho_{11}) - i\frac{\Omega_c}{2}\rho_{31} \\
\dot{\rho}_{32} &= -(\gamma_{32} - i\Delta_2)\rho_{32} + i\frac{\Omega_c}{2}(\rho_{33} - \rho_{22}) + i\frac{\Omega_p}{2}\rho_{31} - i\frac{\Omega_{\mathrm{rf}}}{2}\rho_{42} \\
\dot{\rho}_{31} &= -(\gamma_{31} - i(\Delta_1 + \Delta_2))\rho_{31} - i\frac{\Omega_c}{2}\rho_{21} + i\frac{\Omega_p}{2}\rho_{32} - i\frac{\Omega_{\mathrm{rf}}}{2}\rho_{41} \\
\dot{\rho}_{41} &= -(\gamma_{41} - i(\Delta_1 + \Delta_2 + \Delta_3))\rho_{41} - i\frac{\Omega_{\mathrm{rf}}}{2}\rho_{31} + i\frac{\Omega_p}{2}\rho_{42} \\
\dot{\rho}_{42} &= -(\gamma_{42} - i(\Delta_2 + \Delta_3))\rho_{42} - i\frac{\Omega_{\mathrm{rf}}}{2}\rho_{32} + i\frac{\Omega_c}{2}\rho_{43} + i\frac{\Omega_p}{2}\rho_{41} \\
\dot{\rho}_{43} &= -(\gamma_{43} - i\Delta_3)\rho_{43} - i\frac{\Omega_{\mathrm{rf}}}{2}(\rho_{33} - \rho_{44}) + i\frac{\Omega_c}{2}\rho_{42}
\end{aligned}
\tag{2.51}
$$

This system of ordinary differential equations can be solved numerically. The result is that, although the microwaves couple two Rydberg levels that are both uncoupled by the probe laser, the probe absorption spectrum changes drastically. In the presence of the microwaves, a narrow dip of opacity appears in the center of the EIT peak, with a width determined by Ω_{rf}.

Fig. 2.9 shows calculated absorption spectra of the Cs 4-level system, obtained by numerically solving Eqs. 2.51 in steady state. To illustrate the differences between the 2-level, the 3-level, and the 4-level system, the spectrum is calculated in the presence of one laser, two lasers, and all three radiation fields. The dependence of the absorption spectrum on the Rabi frequencies of the three lasers and the Rydberg lifetime is shown in Fig. 2.10.

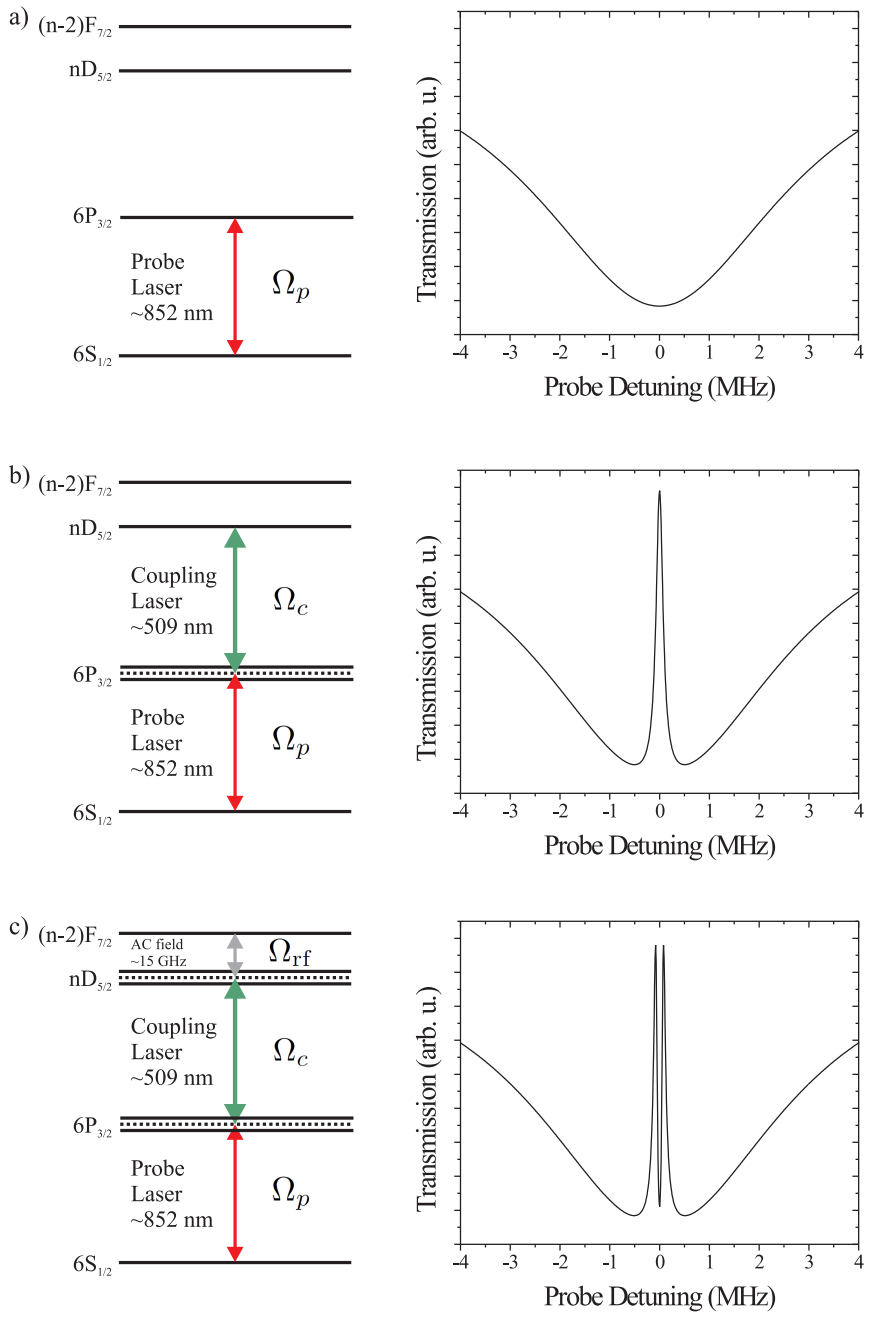

Figure 2.9: Calculated probe absorption spectrum in the Cs 4-level system when turning on a) only the probe laser, b) both probe and coupling laser, and c) probe laser, coupling laser, and microwaves. When the Rydberg states are resonantly coupled by the microwave radiation, a narrow dip of opacity appears in the center of the EIT peak. The parameters used are $\Gamma_{21} = 2\pi \times 5.2$ MHz, $\Gamma_{32} = 2\pi \times 2$ kHz, $\Gamma_{43} = 2\pi \times 2.33$ kHz, $\Omega_p = 2\pi \times 100$ kHz, $\Omega_c = 2\pi \times 1$ MHz, $\Omega_{\mathrm{rf}} = 2\pi \times 157$ kHz. Note that the energy level diagrams are not drawn to scale.

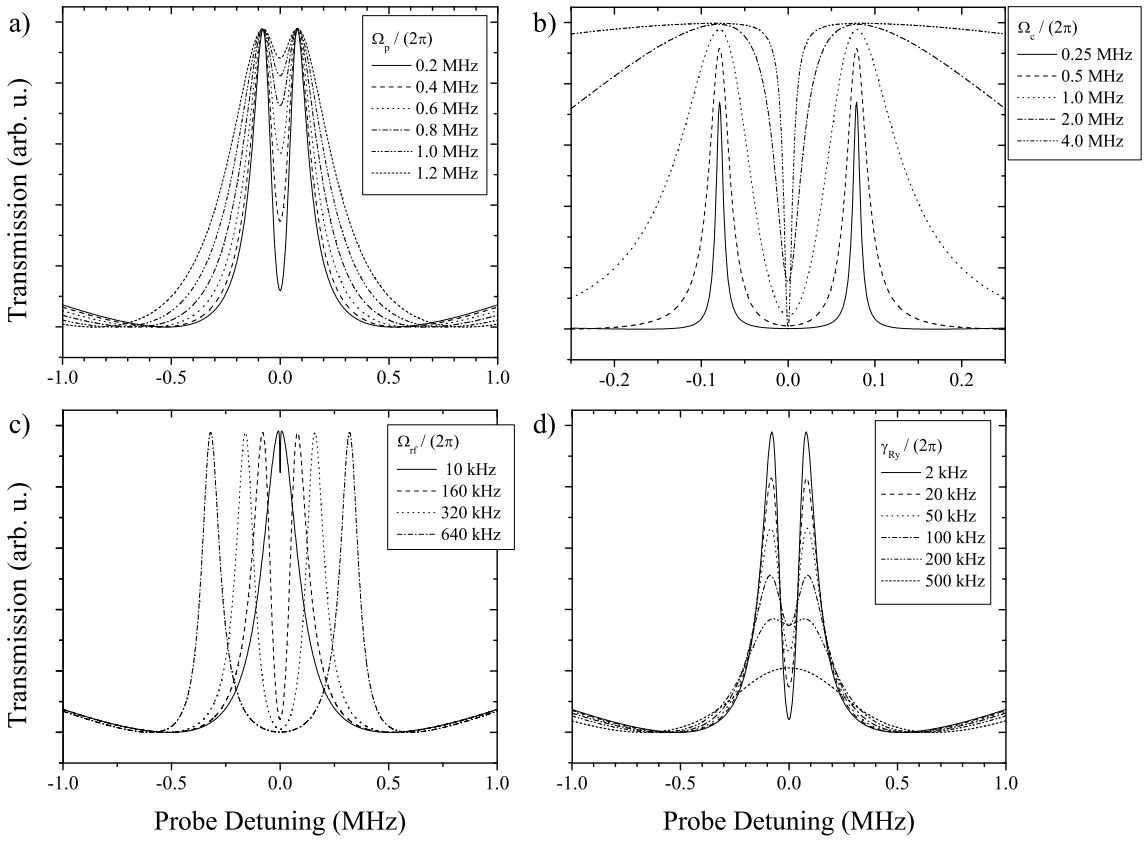

Figure 2.10: Dependence of the calculated probe absorption spectrum in the Cs 4-level system on a) Ω_p, b) Ω_c, c) $\Omega_{\rm rf}$, and d) Γ_{32} (assuming $\Gamma_{43} = \Gamma_{32} = \gamma_{\rm Ry}$). The other parameters are the same as in Fig. 2.9.

Because the microwaves couple two close-lying Rydberg states which have a large transition dipole moment, $\Omega_{\rm rf}$ can be large ($\sim$ 1 MHz) even when the microwave radiation is extremely weak. As an example, consider the ^{87}Rb $55D \rightarrow 54F$ transition, which is in the K band of microwaves and has a frequency of 13.9 GHz. Only 1 nW in a 15 cm diameter beam, corresponding to an intensity of only 5 fW/cm^2 and an AC Field amplitude of only 64 μV/cm is enough for $\Omega_{\rm rf}$ to be 1 MHz, leading to an opacity peak that is broad enough to be easily observed in the probe absorption spectrum.

The four-level systems measured in the course of this thesis work are shown in

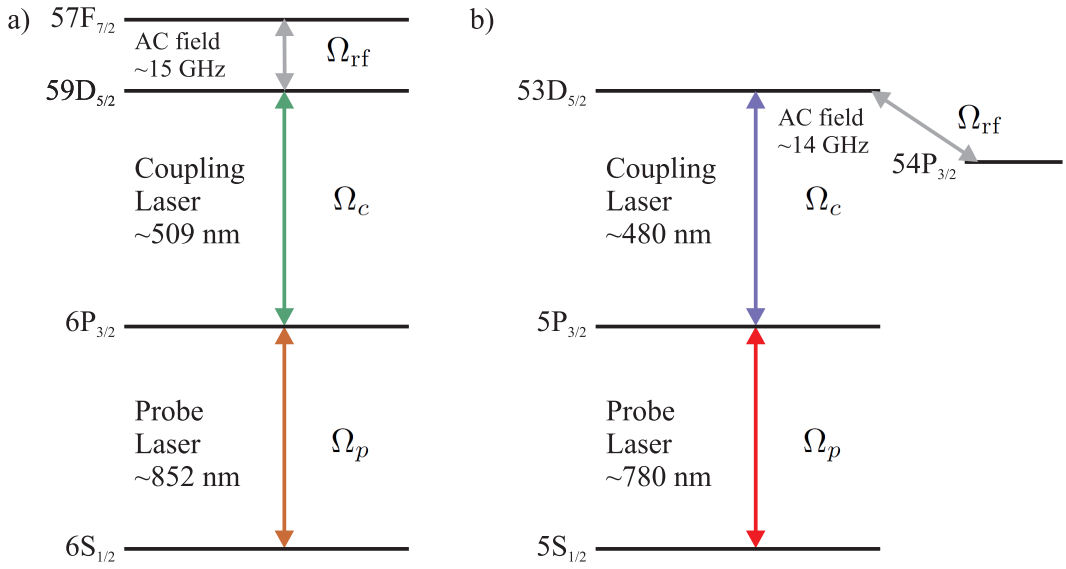

Figure 2.11: The four-level systems explored in this thesis. a) Cs system, b) ^{87}Rb system. In the Rb system, the polarization dependence of the absorption spectrum is measured.

Fig. 2.11. For the Rb system shown in Fig. 2.11b, the polarization effects on EIT are investigated. The polarization of the microwaves, probe and coupling laser is found to significantly change the absorption spectrum of the system. In the following section, the theory used to model the polarization effects is detailed.

2.4.4 52-level system

To accurately reproduce the polarization dependence of the measured probe absorption lineshapes in the 4-level Rydberg EIT system shown in 2.11b, it turns out that it is necessary to include the degenerate hyperfine levels of both Rydberg states, including all the magnetic sublevels that are coupled by the radiation fields.

The hyperfine levels of high-lying Rydberg states with $l > 1$ are effectively degenerate, because the Rydberg electron is so far away from the nucleus that the interaction with the nuclear spin is usually negligible in experiments. For example, the hyperfine interval between the $F = 1$ and $F = 2$ states of the ^{87}Rb $54P_{1/2}$ state is ~ 55 kHz,

estimated from the measurements of Ref. [63] using the reported $(n-\delta)^{-3}$ scaling. The hyperfine interval between the $F = 2$ and $F = 3$ levels of the $53D_{3/2}$ state is ~ 1.5 kHz, estimated by scaling the splitting of the $4D_{3/2}$ state reported in Ref. [93].

Taking the hyperfine levels into account, the idealized system of Fig. 2.11b becomes the more realistic system of figure Fig. 2.12. The Rb system measured in the experiment consists of 52 magnetic sublevels that are each coupled differently by the different possible combinations of laser and microwave polarizations.

To model this system, the states are first numbered so that $|i\rangle = |n_i, L_i, J_i, F_i, m_i\rangle$, where m_i is the m_F quantum number of state number i, and i ranges from 1 to 52. The Rabi frequencies, the Hamiltonian, the decay and decoherence operators, the laser dephasing operator, and the evolution equations are then constructed algorithmically. The coordinate system is chosen so that the quantization axis, the z-axis, is pointing along the propagation direction of the probe laser, the x-axis is pointing horizontally, and the y-axis is pointing vertically up away from the optics table.

The Hamiltonian is constructed according to

$$\langle i|H|j\rangle = \frac{\hbar}{2}\left(-2\,\delta_{ij}\Delta_{ii} + \Omega_{ij}\,(1-\delta_{ij})\right) \qquad i,j = 1\ldots 52. \tag{2.52}$$

The detunings in the diagonal are given by

$$\Delta_{ii} = \begin{cases} 0 & : n_i L_i = 5S \\ \Delta_1 & : n_i L_i = 5P \\ \Delta_1 + \Delta_2 & : n_i L_i = 53D \\ \Delta_1 + \Delta_2 - \Delta_3 & : n_i L_i = 54P. \end{cases} \tag{2.53}$$

$\Delta_1 = \omega_p - (\omega_{5P} - \omega_{5S})$ is the detuning of the probe laser from the $5S_{1/2}, F = 2 \rightarrow 5P_{3/2}, F = 3$ transition, $\Delta_2 = \omega_p - (\omega_{53D} - \omega_{5P})$ is the detuning of the coupling laser from the $5P_{3/2}, F = 3 \rightarrow 53D_{5/2}$ transition, and $\Delta_3 = \omega_{\mathrm{RF}} - (\omega_{53D} - \omega_{54P})$ is the detuning of the microwave source from the $54P_{3/2} \rightarrow 53D_{5/2}$ transition. The negative

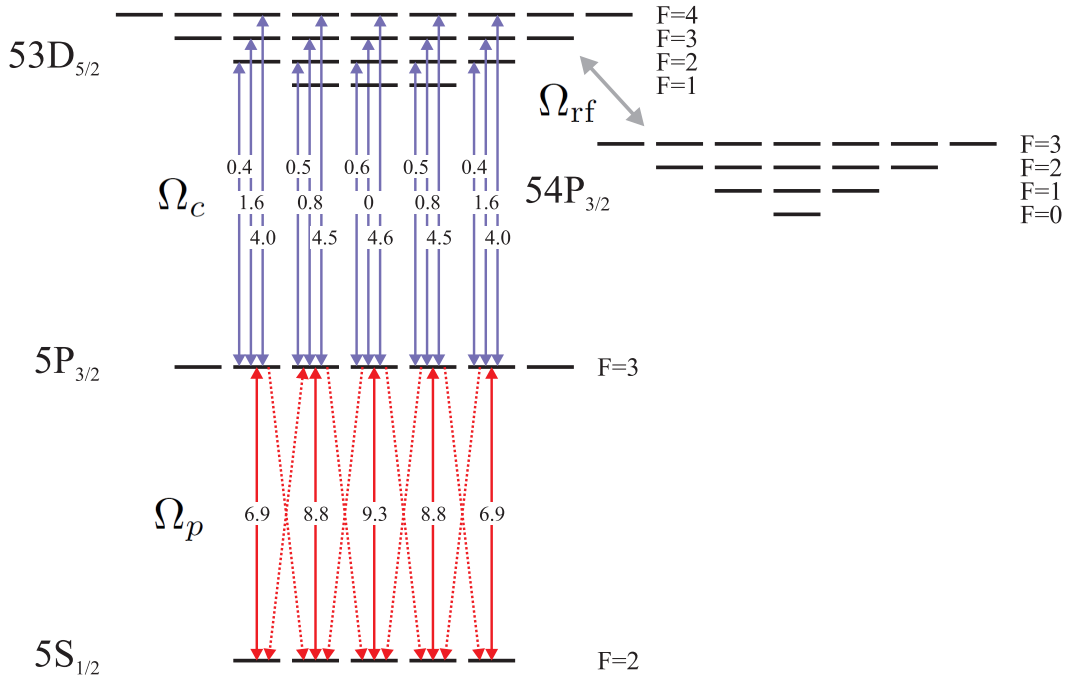

Figure 2.12: The 52-level system used to reproduce the measured absorption lineshapes in Rb Rydberg EIT. The magnetic sublevels of each hyperfine state are separated horizontally. Only a few of all the possible transitions are shown. Double-headed arrows are used to denote polarization-dependent couplings for one specific combination of polarizations. Dashed arrows denote spontaneous decay channels of the excited state. Couplings between Rydberg levels are omitted for clarity. The model accounts naturally for optical pumping effects. The Rabi frequency between two specific magnetic sublevels becomes Ω_{ij} (see text), changes for different laser or microwave polarizations, and depends on the specific sublevels involved. The numbers in the figure are the values of the Rabi frequencies $|\Omega_{ij}|$ in units of MHz for a probe field amplitude of $E_p = 0.5$ Vcm^{-1} and a coupling field amplitude of $E_c = 50$ V cm^{-1}. Values are rounded two two significant digits for clarity.

sign in front of Δ_3 in the Hamiltonian arises from the fact that the 54P Rydberg level is energetically below the 53D level.

The Rabi frequencies between different magnetic sublevels are

$$\Omega_{ij} = \Omega^0_{(n_iL_i,n_jL_j)} \sum_{q=-1}^{q=1} \left(\epsilon_{(n_iL_i,n_jL_j)}\right)_q \langle n_iL_iJ_iF_im_i|n_q|n_jL_jJ_jF_jm_j\rangle. \tag{2.54}$$

In this expression,

$$\Omega^0_{(nL,n'L')} = \frac{|e|\,\zeta_{(nL,n'L')}}{\hbar} \times \begin{cases} E_p & : (nL,n'L') = (5P,5S) \text{ or } (5S,5P) \\ E_c & : (nL,n'L') = (53D,5P) \text{ or } (5P,53D) \\ E_{\rm rf} & : (nL,n'L') = (53D,54P) \text{ or } (54P,53D) \\ 0 & : \text{else,} \end{cases} \tag{2.55}$$

is a bare Rabi frequency calculated using only the radial matrix elements of the operator r, $\zeta_{(nL,n'L')} = \int_0^\infty R_{nL}(r) r R_{n'L'}(r)\, r^2 dr$, and the electric field amplitude of the radiation that couples the two levels. Here, R_{nL} is the radial part of the electronic wavefunction, defined from the product expansion in spherical coordinates $\psi_i(r,\theta,\phi) = R_{n_iL_i}(r)Q_i(\theta,\phi)$, and E_p, E_c, and $E_{\rm rf}$ are the real field amplitudes of the probe, coupling and microwave radiation, respectively. $\left(\epsilon_{(nL,n'L')}\right)_q$ are the spherical components of the complex polarization vector of the radiation field that couples the two states with principal quantum number n and n',

$$\boldsymbol{\epsilon}_{(nL,n'L')} = \begin{cases} \boldsymbol{\epsilon}_p & : (nL,n'L') = (5P,5S) \\ \boldsymbol{\epsilon}_p{}^* & : (nL,n'L') = (5S,5P) \\ \boldsymbol{\epsilon}_c & : (nL,n'L') = (53D,5P) \\ \boldsymbol{\epsilon}_c{}^* & : (nL,n'L') = (5P,53D) \\ \boldsymbol{\epsilon}_{\rm rf} & : (nL,n'L') = (53D,54P) \\ \boldsymbol{\epsilon}_{\rm rf}{}^* & : (nL,n'L') = (54P,53D) \\ 0 & : \text{else,} \end{cases} \tag{2.56}$$

and n_q are the spherical components of the unit vector $\vec{r}/\,|\vec{r}|$. Just as in the derivation of the two-level Hamiltonian, the complex conjugates arise naturally from casting the

electric field as the real part of a complex expression

$$\mathbf{E} = \mathrm{Re}\left\{E_0\,\boldsymbol{\epsilon}\,e^{i\omega t}\right\} = \frac{1}{2}E_0\left(\boldsymbol{\epsilon}\,e^{i\omega t} + \boldsymbol{\epsilon}^*\,e^{-i\omega t}\right), \tag{2.57}$$

and ensure that the Hamiltonian remains Hermitian even in the presence of circular polarization. For example, for linear probe polarization in the x-direction,

$$\boldsymbol{\epsilon}_{(5\,1,5\,0)} = \boldsymbol{\epsilon}_p = \hat{x} = \frac{1}{\sqrt{2}}\left(\hat{n}_{-1} + \hat{n}_{+1}\right), \tag{2.58}$$

and thus for this polarization

$$\left(\epsilon_{(5\,1,5\,0)}\right)_{-1} = \frac{1}{\sqrt{2}} \tag{2.59}$$

$$\left(\epsilon_{(5\,1,5\,0)}\right)_{0} = 0 \tag{2.60}$$

$$\left(\epsilon_{(5\,1,5\,0)}\right)_{+1} = \frac{1}{\sqrt{2}}. \tag{2.61}$$

The matrix element of the spherical components of the unit vector,

$\langle nLJFm_F|n_q|n'L'J'F'm_F{}'\rangle$, can be evaluated using the Wigner-Eckart theorem [53],

$$\langle \alpha F m_F|n_q|\alpha' F' m'_F\rangle = (-1)^{F-m_F}\begin{pmatrix} F & 1 & F' \\ -m_F & q & m'_F\end{pmatrix}\langle \alpha F||n||\alpha' F'\rangle \tag{2.62}$$

$$\begin{aligned}\langle \alpha F||n||\alpha' F'\rangle &= \langle \beta JIF||n||\beta' J'I'F'\rangle \\ &= \delta_{II'}(-1)^{J+I+F'+1}\sqrt{(2F'+1)(2F+1)}\begin{Bmatrix} J & F & I \\ F' & J' & 1\end{Bmatrix}\langle \beta J||n||\beta' J'\rangle\end{aligned} \tag{2.63}$$

$$\begin{aligned}\langle \beta J||n||\beta' J'\rangle &= \langle \gamma LSJ||n||\gamma' L'S'J'\rangle \\ &= \delta_{SS'}(-1)^{L+S+J'+1}\sqrt{(2J'+1)(2J+1)}\begin{Bmatrix} L & J & S \\ J' & L' & 1\end{Bmatrix}\langle \gamma L||n||\gamma' L'\rangle\end{aligned} \tag{2.64}$$

$$\begin{aligned}\langle \gamma L||n||\gamma' L'\rangle &= \sqrt{\frac{4\pi}{3}}\langle L||Y^1||L'\rangle \\ &= (-1)^L\sqrt{(2L+1)(2L'+1)}\begin{pmatrix} L & 1 & L' \\ 0 & 0 & 0\end{pmatrix}.\end{aligned} \tag{2.65}$$

Here α, β, and γ denote remaining quantum numbers, the curly braces denote 6-j symbols, the parentheses denote 3-j symbols, and $\langle \cdot||\cdot||\cdot\rangle$ denotes a reduced matrix element. The definition of the reduced matrix element and the 6-j and 3-j symbols are those of Refs. [53, 94].

Setting $I = 3/2$ and $S = 1/2$ for ^{87}Rb, substituting Eqs. 2.63, 2.64, and 2.65 into

Eq. 2.62, and reordering, gives the expression

$$\begin{aligned}
&\langle nLJFm_F|n_q|n'L'J'F'm'_F\rangle = \\
&\quad (-1)^{J+F'+J'+F+m_F}\sqrt{(2F'+1)(2F+1)(2J'+1)(2J+1)(2L'+1)}\times \\
&\quad \times\sqrt{(2L+1)}\begin{Bmatrix} J & F & 3/2 \\ F' & J' & 1 \end{Bmatrix}\begin{Bmatrix} L & J & 1/2 \\ J' & L' & 1 \end{Bmatrix}\begin{pmatrix} L & 1 & L' \\ 0 & 0 & 0 \end{pmatrix}\begin{pmatrix} F & 1 & F' \\ -m_F & q & {m_F}' \end{pmatrix}.
\end{aligned} \tag{2.66}$$

It is clear that the Rabi frequencies in the off-diagonal terms of the Hamiltonian depend on the polarization and specific magnetic sublevels coupled by the radiation.

The master equation is given by

$$\dot{\rho} = -\frac{i}{\hbar}[H,\rho] + L + L_d, \tag{2.67}$$

where L is a decay and decoherence operator, and L_d is a pure dephasing operator that accounts for dephasing due to finite laser linewidth. L is given by

$$L = \sum_{i=1}^{52}\sum_{j=1}^{52} L_{ij}, \tag{2.68}$$

where L_{ij} is defined as in Eq. 2.33 to be [49]

$$L_{ij} = \frac{\Gamma_{ij}}{2}\left(2\,\sigma_{ji}\,\rho\,\sigma_{ij} - \sigma_{ii}\,\rho - \rho\,\sigma_{ii}\right). \tag{2.69}$$

Since Γ_{ij} is the decay rate due to spontaneous emission from state i to state j, it is nonzero for any two states i and j that are coupled by the dipole operator. For unequal indices i and j

$$\Gamma_{ij} = B_{(J_iF_im_i,J_jF_jm_j)} \times \gamma_{(n_iL_i,n_jL_j)} \qquad : i \neq j, \tag{2.70}$$

$\gamma_{(n_iL_i,n_jL_j)}$ is the total radiative decay rate from a single upper state into a lower

hyperfine manifold, given by

$$\gamma_{(n'L',nL)} = \begin{cases} (\tau_{5P})^{-1} & : (n'L', nL) = (5P, 5S) \\ (\tau_{53D})^{-1} & : (n'L', nL) = (53D, 5P) \\ (\tau_{54P})^{-1} & : (n'L', nL) = (54P, 5S) \\ (\tau_{BB})^{-1} & : (n'L', nL) = (53D, 54P) \\ 0 & : \text{else} \end{cases} , \tag{2.71}$$

B is the branching ratio for the decay into a specific lower magnetic sublevel, given by [1][3]

$$B_{(J'F'm_{F'},JFm_F)} = \left| \sqrt{(2J'+1)(2F'+1)(2F+1)} \begin{pmatrix} F & 1 & F' \\ -m_F & m_F - m_{F'} & m_{F'} \end{pmatrix} \begin{Bmatrix} J & F & 3/2 \\ F' & J' & 1 \end{Bmatrix} \right|^2 . \tag{2.72}$$

B follows the sum rule

$$\sum_{F\,q} B_{(J'F'm_{F'},JF(m_F=m_{F'}+q))} = 1 \tag{2.73}$$

for allowed transitions from a single upper state with quantum numbers $(J', F', m_{F'})$ to a lower hyperfine manifold with quantum number J. For the decay of the $5P_{3/2}$, $F = 3$ state, the decay rate is given exactly by the known lifetime. For the spontaneous decays of the Rydberg states, the rates are approximated by the known radiative [59, 95] and black body lifetimes [59, 96], ignoring any decays out of the 52 level system.

[3] Care has to be taken when comparing Ref. [1] to the expressions in this thesis, since Steck uses a definition of the reduced matrix elements that differs from the convention of Refs. [53, 54] that is used here: $\langle \beta J||A||\beta' J'\rangle_{\text{This Thesis}} = \sqrt{2J+1}\langle \beta J||A||\beta' J'\rangle_{\text{Steck}}$

To account for a dephasing of the Rydberg levels, we set

$$\Gamma_{ii} = \begin{cases} 2\,\gamma_{\mathrm{Ry}} & : n_i L_i = 53D \\ 2\,\gamma_{\mathrm{Ry}} & : n_i L_i = 54P \\ 0 & : \text{else} \end{cases} . \tag{2.74}$$

γ_{Ry} is a phenomenological pure dephasing rate of the Rydberg states with respect to the other states. It could be due to collisions, Rydberg atom interactions, or fluctuating electric or magnetic fields.

The pure dephasing operator due to the finite laser linewidths, L_d, is given by

$$L_d = \sum_{ij} -\left(\gamma^L\right)_{ij} \rho_{ij} \, |i\rangle\langle j|. \tag{2.75}$$

Here $\left(\gamma^L\right)_{ij}$ is the sum of the FWHM linewidths of the radiation field coupling the levels $i \leftrightarrow j$, explicitly

$$\left(\gamma^L\right)_{ij} = \begin{cases} \gamma_p \left(1 - \delta_{0\,\Omega_{ij}}\right) & : (n_i L_i, n_j L_j) = (5P, 5S) \text{ or } (5S, 5P) \\ \gamma_c \left(1 - \delta_{0\,\Omega_{ij}}\right) & : (n_i L_i, n_j L_J) = (53D, 5P) \text{ or } (5P, 53D) \\ \gamma_{\mathrm{rf}} \left(1 - \delta_{0\,\Omega_{ij}}\right) & : (n_i L_i, n_j L_j) = (54P, 53D) \text{ or } (53D, 54P) \\ \gamma_p + \gamma_c & : (n_i L_i, n_j L_j) = (53D, 5S) \text{ or } (5S, 53D) \\ \gamma_c + \gamma_{\mathrm{rf}} & : (n_i L_i, n_j L_j) = (54P, 5P) \text{ or } (5P, 54P) \\ \gamma_p + \gamma_c + \gamma_{\mathrm{rf}} & : (n_i L_i, n_j L_j) = (54P, 5S) \text{ or } (5S, 54P) \\ 0 & : \text{else} \end{cases} . \tag{2.76}$$

In the above expressions, the polarization dependence of the laser dephasing terms is approximated by the Kronecker delta, $\delta_{0\,\Omega_{ij}}$, which accounts for the fact that γ^L is zero for a transition that is not coupled by the laser polarizations.

After the differential equations for the density matrix elements are built algorithmically, they can be solved numerically. Due to the large number of over 2000 variables, an algebraic or numerical steady state solution is computationally more involved than a numerical integration of the differential equations using Runge-Kutta methods. We use the 4th order explicit Runge-Kutta routine found in Mathematica.

To calculate the absorption spectrum, the initial conditions are set to an equal distribution of populations in the magnetic sublevels of the five $5S_{1/2}, F = 2$ ground state sublevels, and all other matrix elements are initialized to zero. The numerical integration is then run to a time of $t_1 = 64\ \mu$s for each probe detuning. t_1 is chosen to be long enough to reach the steady state, e.g.

$$t_1 \gg \tau_{5\mathrm{P}} \tag{2.77}$$

$$t_1 \gg \left(\Omega^0_{(n_i L_i, n_j L_j)}\right)^{-1}, \tag{2.78}$$

for all Ω^0 that are non-zero.

The probe absorption is proportional to the weighted sum over all off-diagonal elements between states that are coupled to by the probe light [92]

$$A \propto -\sum_{ij} \Omega_{ij}\, \mathrm{Im}\left\{\rho_{ij}(t)\,|_{t=t_1}\right\}\, \delta_{n_j\,5}\, \delta_{L_j\,0} \times \left(1 - \delta_{\Omega_{ij}\,0}\right). \tag{2.79}$$

Here the Kronecker symbols are used to pick out only the off-diagonal density matrix elements between states that are coupled by the polarization of the probe laser light.

2.4.5 Doppler shifts

In a thermal vapor, the atoms experience velocity dependent Doppler shifts of the radiation fields. To incorporate thermal motion of the atoms into the theory, the detunings in the Hamiltonian are modified via $\Delta \to \Delta - \boldsymbol{k}\cdot\boldsymbol{v}$. $\boldsymbol{k}$ is the wavevector of the laser light and $\boldsymbol{v}$ is the atomic velocity vector. In the case of counter-propagating probe and coupling laser beams, the detunings become

$$\Delta_1 \to \Delta_1 + k_p\, v_z \tag{2.80}$$

$$\Delta_2 \to \Delta_2 - k_c\, v_z, \tag{2.81}$$

where $k_{p,c} = 2\pi\ (\lambda_{p,c})^{-1}$. Δ_3 is not modified, because the maximum Doppler shift of the microwave field is negligible (< 15 kHz), due to the much longer wavelength of the microwaves (~ 2 cm).

The solutions of the master equation are numerically integrated over the Maxwell-Boltzmann distribution of the v_z velocity component. The Doppler averaged probe transmission is then

$$A_{\mathrm{D}} = \int_{-\infty}^{\infty} A(v_z)\, f(v_z)\, dv_z, \tag{2.82}$$

where

$$f(v_z) = \frac{1}{u\sqrt{\pi}}\, e^{-v^2/u^2}, \tag{2.83}$$

and $u = \sqrt{\frac{2\,k_b\,T}{M}}$ is the rms velocity at temperature T. Eq. 2.82 is integrated numerically for each probe detuning, using velocity steps of $\Delta v_z = 1\ \mathrm{m\,s^{-1}}$ and a velocity range of $(-600 \ldots 600)\ \mathrm{m\,s^{-1}}$. At each velocity value, the density matrix equations are numerically integrated as described in the last section, to obtain the Doppler averaged transmission spectrum.

2.5 Laser cooling and trapping

In this section, the basic theory describing laser cooling and the mirror magneto-optical trap is presented.

2.5.1 Laser cooling

The idea of laser cooling is to use laser light to exert a velocity dependent force on atoms to cool them down.

When an atom absorbs a photon from a laser beam, the photon momentum $\hbar\boldsymbol{k}$ is transferred to the atom, and the atom changes its velocity by a small amount ($0.6\ \mathrm{cm\,s^{-1}}$ for Rb and light resonant on the D_2 line). After this primary momentum kick due to absorption, the atom re-emits a photon and receives a secondary momentum kick due to spontaneous emission. Since spontaneous emission occurs in a random direction, the secondary momentum kicks average to zero over the course of

multiple absorptions, while the primary momentum kicks all add up. The laser beam thus exerts a net force on the atoms that points in the direction of the beam. This force is the scattering force. The rate of photons hitting the atoms is proportional to the intensity of the laser beam. For a two-level atom, in steady state, the scattering rate from a single beam is given by $\gamma_s = \Gamma\,\rho_{22}$, where ρ_{22} is the population in the excited state. This is because, in steady state, the excitation rate must equal the decay rate which is given by $\Gamma\rho_{22}$. Solving the optical Bloch equations of the two-level system results in the expression for the scattering rate

$$\gamma_s = \frac{\Gamma}{2}\,\frac{I/I_s}{1 + I/I_s + (2\Delta/\Gamma)^2}, \tag{2.84}$$

where $\Delta = \omega - \omega_0$ is the laser detuning, Γ is the spontaneous decay rate of the excited state, I is the beam intensity, and I_s is the saturation intensity. The ratio I/I_s is related to the Rabi frequency Ω through $\Omega = \Gamma\,\sqrt{I/(2I_s)}$. For low intensities, the rate of absorption is proportional to the laser intensity. As the intensity approaches the saturation intensity, stimulated emission processes start to compete with spontaneous emission processes. In stimulated emission, the photon emission is in the direction of the beam, and the corresponding momentum change of the atom is in the opposite direction of the laser beam. The competition of spontaneous and stimulated processes results in a saturation of the scattering force at large intensities. On resonance, for zero velocity atoms, the scattering force for large intensities $I \gg I_s$ saturates at $\hbar\,k\,\Gamma/2$ [29].

To cool atoms, a velocity dependent force is necessary. Due to the Lorentzian absorption lineshape, the scattering force already depends strongly on the frequency of the laser beam. For moving atoms, this frequency dependence is translated into a velocity dependence by the Doppler shift. For an atom with velocity $\boldsymbol{v}$, the laser light in the co-moving frame has the Doppler-shifted frequency $\omega' = \omega - \boldsymbol{k}\cdot\boldsymbol{v}$. If the laser beam is red-detuned from the resonance, atoms moving toward the light beam are

closer to resonance than atoms moving away from the light beam. The atoms moving toward the beam feel a larger scattering force and are pushed back stronger than the atoms moving away from the beam. The net effect is that the atoms moving toward the beam are selectively slowed down. Using two counter-propagating red-detuned laser beams, the scattering force is the sum of the forces from each beam. In one dimension, the scattering force becomes [29]

$$\boldsymbol{F_s} = \boldsymbol{F}_+ + \boldsymbol{F}_- \tag{2.85}$$

$$\boldsymbol{F}_\pm = \pm\frac{\hbar\,\boldsymbol{k}\,\Gamma}{2}\,\frac{I/I_s}{1 + I/I_s + (2(\Delta \mp \boldsymbol{k}\cdot\boldsymbol{v})/\Gamma)^2}, \tag{2.86}$$

where Δ is the detuning of the light from resonance, $\boldsymbol{k}$ is the wavevector of the beam labeled +, pointing in the positive direction, and stimulated emission was neglected (low intensity regime). The form of this sum of two Lorentzian curves is shown in Fig. 2.13. We see that the scattering force becomes a pure damping force $F_s = -\beta\,\boldsymbol{v}$, equivalent to friction, for a range of velocities around zero. The friction coefficient is obtained by expanding Eq. 2.85 in a power series around zero for small Doppler shifts $\boldsymbol{k}\cdot\boldsymbol{v} \ll \Gamma$

$$\boldsymbol{F_s} = -\beta\,\boldsymbol{v} = \frac{8\,\hbar\,k^2\,\Delta\,I/I_s}{\Gamma\left(1 + I/I_s + (2\Delta/\Gamma)^2\right)^2}\,\boldsymbol{v} + O\left((\boldsymbol{k}\cdot\boldsymbol{v}/\Gamma)^3\right). \tag{2.87}$$

This configuration cools atoms in one dimension and is called one-dimensional optical molasses. By using six crossed counterpropagating beams in a configuration where each pair of beams is along one of the Cartesian axes, atoms can be laser cooled in three dimensions. In the overlap region of the beams, a three dimensional optical molasses is formed.

The spontaneous emissions cause the atoms to perform a random walk in momentum space with discrete step size $\hbar\,k$. The minimum temperature associated with this random walk is known as the Doppler temperature, T_D. It was originally believed to be the lowest temperature achievable within an optical molasses. The frequency

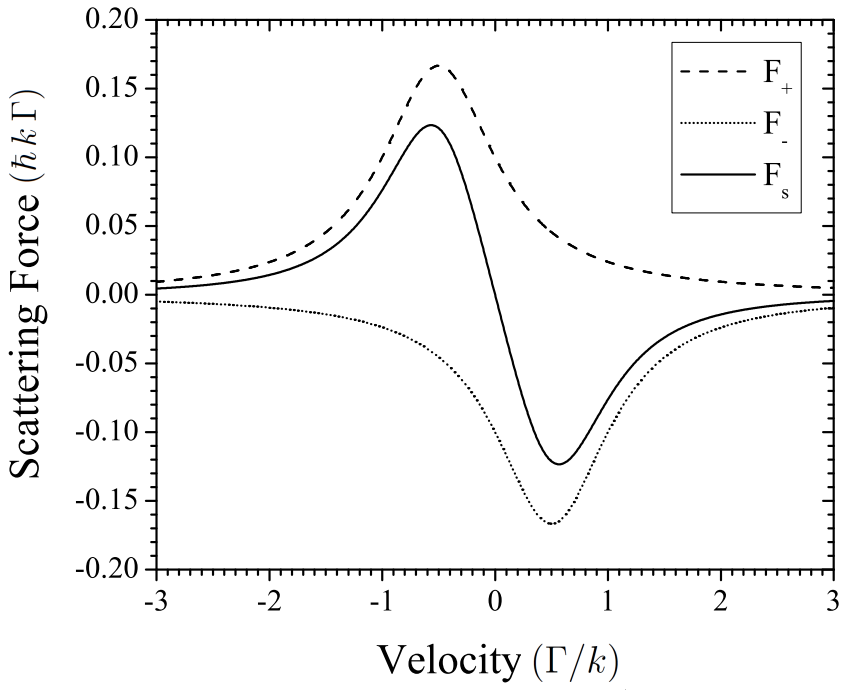

Figure 2.13: Scattering force due to red-detuned counterpropagating beams of light along one dimension. The total scattering force F_s (solid) is the sum of the scattering force from the beam in the positive direction, F_+ (dashed) and the beam in the negative direction, F_- (dotted). Parameters used are $\Delta = -\Gamma$, and $I/I_s = 0.5$. For the D_2 line of ^{87}Rb, a velocity of one would correspond to $\Gamma/k = 4.7\ \mathrm{m\,s^{-1}}$, and a force of one would correspond to an acceleration of $\hbar\,k\,\Gamma\,M^{-1} = 2.24 \times 10^5\ \mathrm{m\,s^{-2}}$, respectively.

of random walk steps is given by the scattering rate multiplied by the number of incident beams. In one dimension an optical molasses has two beams, and the step frequency is $2\,\gamma_s$. The random walk causes a diffusion in momentum space with a diffusion coefficient $D = 2\,(\Delta p)^2/\Delta t = 4\,\gamma_s\,(\hbar\,k)^2$, related to a minimum steady state temperature $T_D = \hbar\,\Gamma\,(2\,k_B)^{-1}$ [29]. The minimum temperature is achieved at a detuning $\Delta = -\Gamma/2$ [29].

The Doppler temperature can also be derived from energetic considerations [29]. Since the momentum changes by $\hbar\,k$ during each absorption and spontaneous emis-

sion, the atoms emit photons at lower frequency than they absorb. In one dimension, the situation is simplified. When an atom absorbs a photon, the recoil energy $\hbar\,\omega_r = (1/2)\,\hbar^2\,k^2/M$ is taken away from the photon energy, which must therefore be $\hbar\,(\omega_0 + \omega_r)$. Here, M is the atomic mass. When an atom emits a photon, the recoil energy is missing from the photon energy, which must therefore be $\hbar\,(\omega_0 - \omega_r)$. The difference in energy between an absorbed and emitted photon in one dimension is thus given by twice the recoil energy, $2\,\hbar\,\omega_r$. From the two beams, photons are absorbed at the rate $2\,\gamma_s$. In steady state, the magnitude of energy lost from the light field is $|\boldsymbol{F}\cdot\boldsymbol{v}|$ and must be equal to the magnitude of energy emitted by the atom $|4\,\gamma_s\,\hbar\,\omega_r|$. Using Eqs. 2.87 and 2.84 to equate those expressions in the low intensity limit, we get an expression for the steady state atomic energy in the 1D optical molasses

$$E_{\mathrm{OM}} = \frac{1}{2}\,M\,v^2 = \frac{\hbar\,\Gamma}{8}\left(\frac{\Gamma}{2\,|\Delta|} + \frac{2\,|\Delta|}{\Gamma}\right) \tag{2.88}$$

which has a minimum at $\Delta = -\Gamma/2$. The corresponding temperature is again the Doppler temperature $T_D = 2\,E_{\mathrm{OM}}/k_b = \hbar\,\Gamma\,(2\,k_B)^{-1}$.

For ^{87}Rb, the Doppler temperature is 145 μK. In early experiments on laser cooling, it was found that, in a real optical molasses, temperatures can be significantly lower than the Doppler temperature [97]. The responsible mechanism for this sub-Doppler cooling was identified soon after the experiments and is called Sisyphus-cooling or polarization-gradient cooling [98, 99]. In an optical molasses, the overlapping light fields lead to polarization gradients. Due to the polarization gradients, the atoms move in spatially dependent periodic light-shift potentials that have hills and valleys. It turns out that for red-detuned laser beams, the atoms are optically pumped by the laser light preferentially into the valleys, from which they climb up the hills. As the atoms climb up the potential hills that are due to the light shift, they lose kinetic energy and cool down. Temperatures in optical molasses can therefore be as low as a few μK [100]. This is close to the recoil limit $T_{\mathrm{rec}} = \hbar^2\,k^2\,(k_B\,M)^{-1}$, the tem-

perature associated with a single photon recoil energy. For ^{87}Rb, $T_{\rm rec} = 362$ nK. Due to sub-Doppler cooling effects, the temperature in an optical molasses is proportional to the light shift parameter

$$\Lambda = \frac{\Omega^2}{|\delta|\Gamma} \tag{2.89}$$

via [29]

$$T = T_0 + 2C_\sigma\, T_D\, \Lambda, \tag{2.90}$$

where T_0 is a temperature intercept, and C_σ is a dimensionless constant that depends only the beam configuration (1D vs. 3D) and the atomic parameters. Note that in this definition $\Omega = \Gamma\sqrt{I/(2I_s)}$ is the Rabi frequency of one of the beams. Most theory is done in 1D [29], but the constant C_σ has been determined experimentally for ^{87}Rb in a magneto-optical trap to be $C_\sigma = 0.52 \pm 0.03$ with a temperature intercept of ~ 5 μK [101].[4] Note that in the experiments of Ref. [101], temperatures for ^{87}Rb as low as 10 μK have been observed in a magneto-optical trap.

2.5.2 Magneto-optical trap

An optical molasses cools the atoms down, but does not trap them, because there is a damping force, but no restoring force. The magneto-optical trap (MOT) fixes this shortcoming. In a MOT, a magnetic quadrupole field is applied that is zero at the center of the molasses and linearly increases in magnitude away from the center. The atomic energies are shifted by the magnetic field due to the Zeeman shift, and the scattering force becomes position dependent. The polarization of the laser beams is then chosen so that atoms away from the center are shifted into resonance with those beams that push them back towards the center. The atomic selection rules are taken advantage of to ensure atoms absorb light from the correct directions.

[4] It should be noted that C_σ in Ref. [101] was fit using older values of the constants, namely $T_D = 141$ μK, $I_s = 1.6$ mW and $\Gamma = 2\pi \times 5.32$ MHz, which differ slightly from the most recent numbers used in this thesis

The principle of the MOT is illustrated in Fig. 2.14. For simplicity, a $F = 0 \rightarrow F' = 1$ cooling transition is assumed. The z-axis is the longitudinal axis of the quadrupole coils. For atoms located at positive z coordinates, the magnetic field points in the positive z-direction. Due to the Zeeman shift, the $m = -1$ sublevel of the excited state is shifted closer to resonance with the laser beams. Only the σ^- beam can excite atoms into this sublevel because of the selection rule $\Delta m = -1$. Thus, the atoms preferentially absorb light from the σ^- beam and are pushed back to the center. For atoms located at negative z coordinate, the magnetic field points in the negative z-direction. Here, the $m = +1$ sublevel of the excited state is shifted closer to resonance with the laser beams. These atoms preferentially absorb photons from the σ^+ beam and are also pushed towards the center. The polarization of the beams is correct when both beams are right-handed circularly polarized (RHC).

The same principle also works along the x- and y-axes, in directions perpendicular to the quadrupole symmetry axis. The only difference is that the magnetic field direction is reversed and the light polarization of both beams now has to be left-handed circularly polarized (LHC) instead of RHC, as illustrated in Fig. 2.15.

A typical MOT setup uses anti-Helmholtz coils to create the quadrupole field, wrapped on the outside or inside of the vacuum chamber. The laser beams can be retro-reflected. A quarter-wave plate in front of each retro-reflecting mirror is used to enforce the correct circular polarization of the retro-reflected beams. This setup requires three incident beams. There is a small inherent imbalance between the incident and retro-reflected beams due to losses in the windows and absorption of light by the atoms, which can be detrimental to the atom number and symmetry of the MOT. For more control over the exact beam balancing, a setup with six incident beams can be used, where each beam is balanced separately. The six-beam MOT is our preferred method, because it allows us to optimize the MOT shape and atom

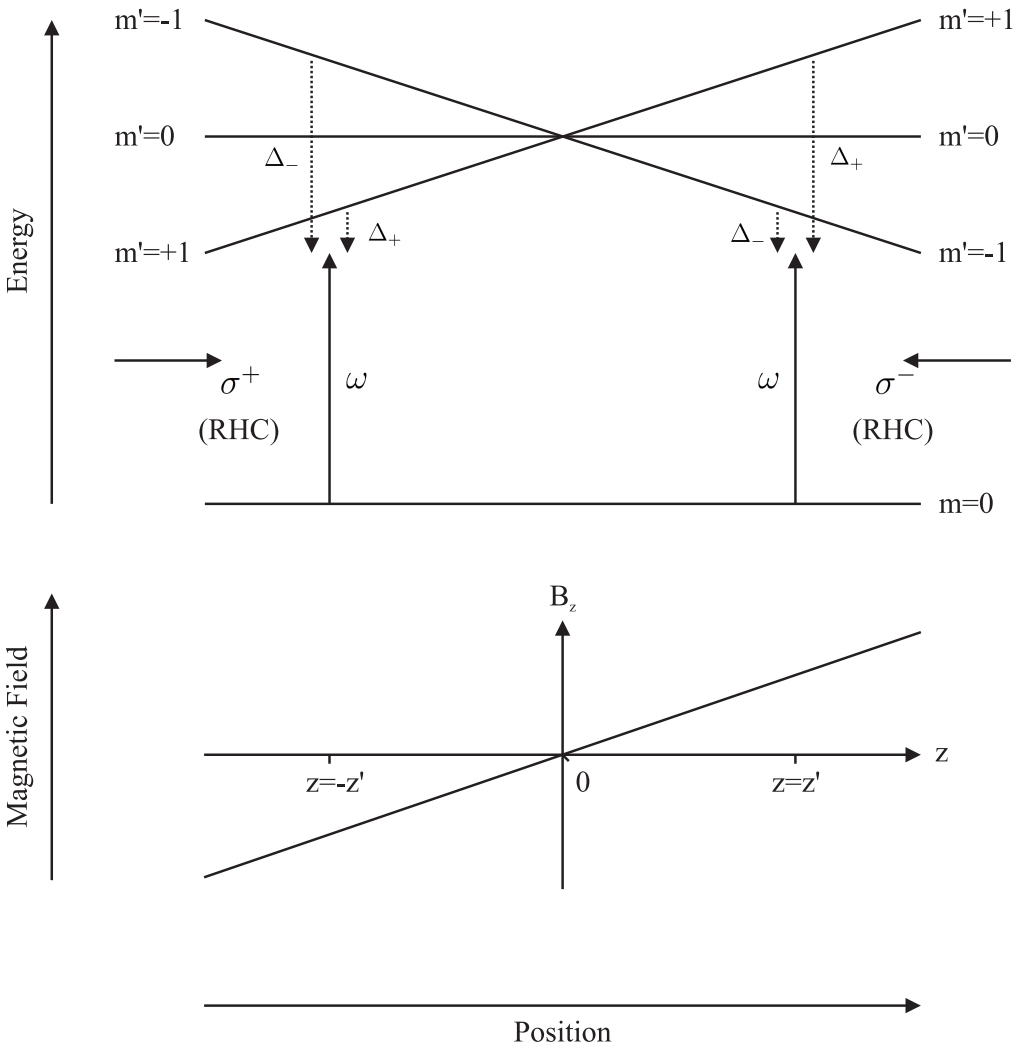

Figure 2.14: Restoring force in a MOT along the quadrupole coil center axis, z. The z-axis is chosen as quantization axis. The magnetic field increases linearly along z and creates a Zeeman shift for the excited states. The Zeeman shift results in position dependent detunings Δ_+ and Δ_- for the σ^+ and σ^- beams, respectively. Atoms located at positive position z' are closer to resonance with the σ^- beam that pushes them in the negative z-direction. Atoms located at negative position -z' experience a Zeeman shift that brings them closer to resonance with the σ^+ beam which pushes them in the positive z-direction. The net effect is that the atoms experience a restoring force that pushes them toward the trap center. Note that along the longitudinal quadrupole axis, both beams need to be RHC polarized. This is different from the lateral axes, where both beams need to be LHC polarized (see Fig. 2.15).

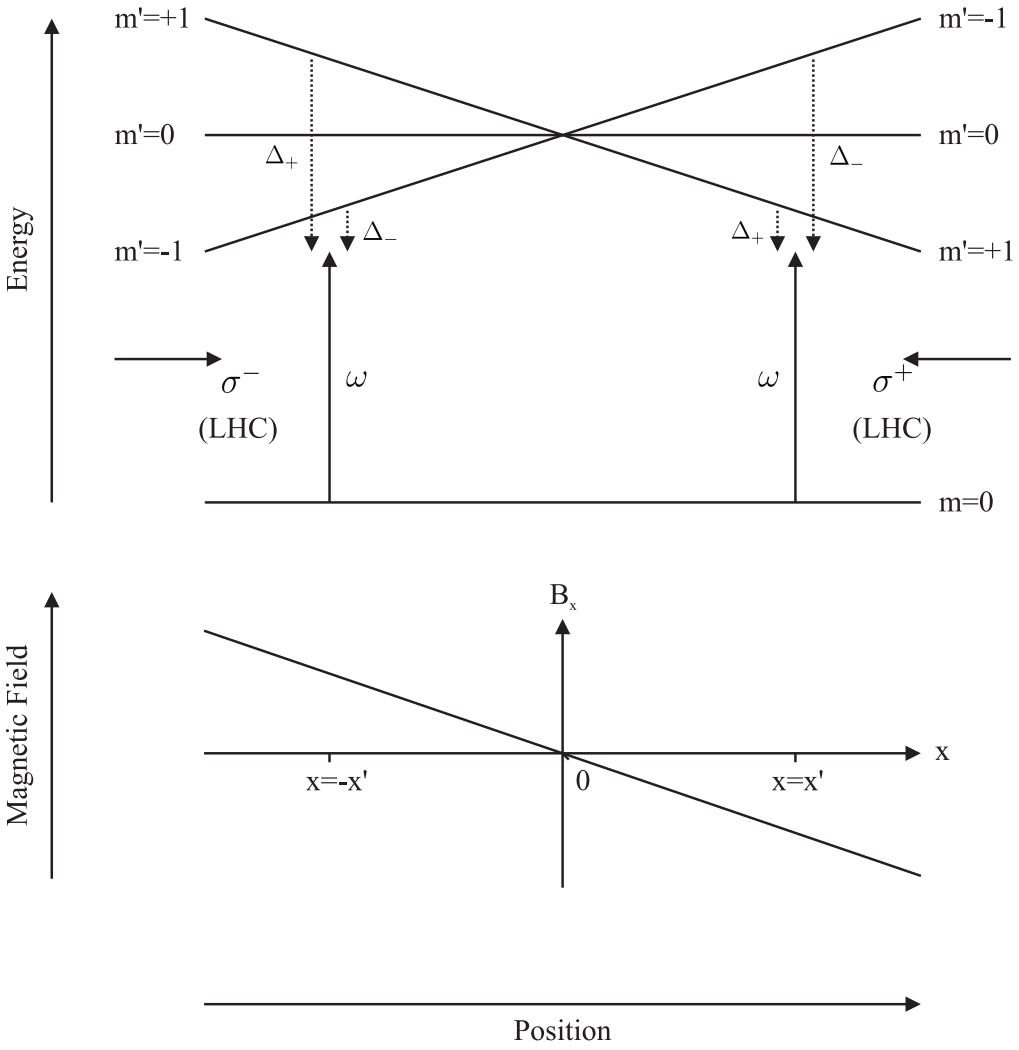

Figure 2.15: Restoring force in a MOT along the x-axis, perpendicular to the quadrupole center axis z. The x-axis is chosen as quantization axis. The same principle applies as for the z-axis (see Fig. 2.14). However, compared with Fig. 2.14, the magnetic field slope is reversed and the field now decreases through the trap center. The role of $m' = +1$ and $m' = -1$ is therefore reversed. As result, the laser beams along the x- or y-axis have to be LHC polarized in order to create the desired restoring force.

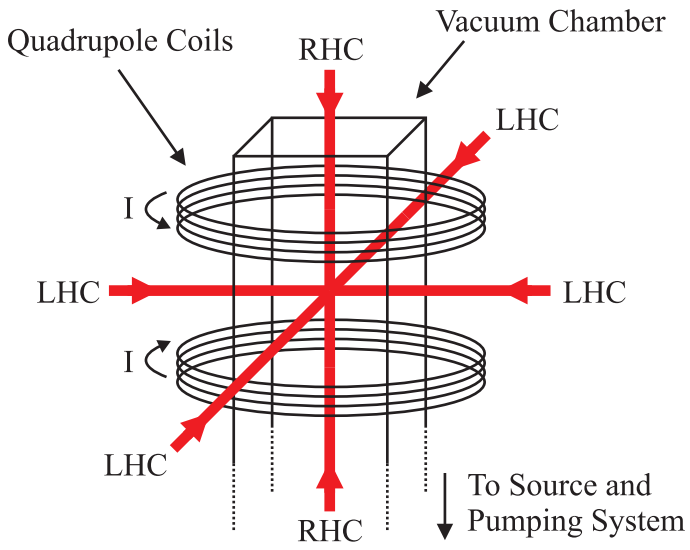

Figure 2.16: Sketch of a MOT setup. The pumping system and the source of atoms is not shown. Six laser beams, counterpropagating along the Cartesian axes, overlap at the zero of a quadrupole magnetic field that is generated by Anti-Helmholtz coils. The zero of the magnetic field is the location where a cold cloud of atoms forms, with a radial size of typically a few hundred microns and a temperature of $\sim 100\ \mu$K.

number more precisely than the setup with retro-reflections. A schematic of a typical MOT setup is shown in Fig. 2.16.

Using the one-dimensional model of Fig. 2.14 with two counter-propagating beams along the z-direction, the detuning from the $\sigma^{\pm}$ beam in the MOT is $\Delta_{\pm} = \Delta \mp (\boldsymbol{k} \cdot \boldsymbol{v} \mp \mu B/\hbar)$, where $\boldsymbol{k}$ is the wavevector of the σ^{+} beam that points in the positive z-direction, and μ is the (positive) effective dipole moment of the $\Delta m = +1$ transition. The scattering force due to the two beams can be written using Eq. 2.85, making the replacement $\boldsymbol{k} \cdot \boldsymbol{v} \rightarrow \boldsymbol{k} \cdot \boldsymbol{v} + \mu\, B/\hbar$. If both the Zeeman shift and the Doppler shift are small compared to Γ, we can expand the force in orders of the parameter $\alpha = (\boldsymbol{k} \cdot \boldsymbol{v} + \mu\, B/\hbar)\,/\Gamma$ to see that

$$F_s = -\beta\, \boldsymbol{v} - \kappa\, \boldsymbol{r} + O\left(\alpha^2\right), \tag{2.91}$$

where β is the friction coefficient defined as before, and $\kappa = (\hbar\, k)^{-1}\, \mu\, \beta\, dB/dz$. We

see that a restoring force appeared in addition to the damping force of the optical molasses. The spring constant of the restoring force is κ.

As an example, for a magnetic field gradient $dB/dz = 10$ Gcm^{-1}, single beam laser intensity $I = 0.5\, I_s$, detuning $\Delta = 1\ \Gamma$, and magnetic moment $\mu \approx 2\,\pi \times 1.39$ MHzG^{-1} for the Rb D_2 $F = 2, m_F = 2 \rightarrow F = 3, m_F = 3$ transition, the trap frequency is $\omega_{\mathrm{MOT}} = \sqrt{\kappa/M} = 2.6$ kHz, the damping rate is $\gamma_{\mathrm{MOT}} = \beta/M = 6.4$ kHz, the motion is overdamped with a damping ratio of $\beta\, 2^{-1}\, M^{-1}\, \omega_{\mathrm{MOT}}^{-1} = 1.2$, and the restoring time to the center is $\tau_r = 2\,\beta\, M^{-1}\, \omega_{\mathrm{MOT}}^{-2} = 1.8$ ms.

In real alkali metal atoms, there are more than two hyperfine levels. Even when using a closed transition such as the ^{87}Rb $F = 2 \rightarrow F' = 3$ cooling transition, there is a small probability of off-resonant excitation of the closest hyperfine level, $F' = 2$. From the $F' = 2$ level, atoms can then decay into the uncoupled $F = 1$ ground state. Once in the $F = 1$ ground state, atoms would be lost from the MOT. A repumping beam is therefore used to recycle atoms out of the $F = 1$ ground state back into the cooling transition. In our case, this is accomplished by overlapping a weak repumping beam, resonant with the $F = 1 \rightarrow F' = 2$ transition, with the cooling beam along the x-axis. Considering the magnetic sublevel populations in real systems, the circular light polarization in the laser fields tends to optically pump the atoms into the stretched Zeeman sublevels and the MOT operation is generally not hindered by the complicated magnetic sublevel structure of real systems [1].

2.5.3 Mirror magneto-optical trap

The mirror MOT, first demonstrated in 2001 [32], is a variant of the MOT in which atoms are trapped a few mm away from a mirror surface. In a mirror MOT, two beams are reflected off a mirror at 45°, and two other counter-propagating beams are passed perpendicular to the reflected beams as shown in Fig. 2.17. In the region of

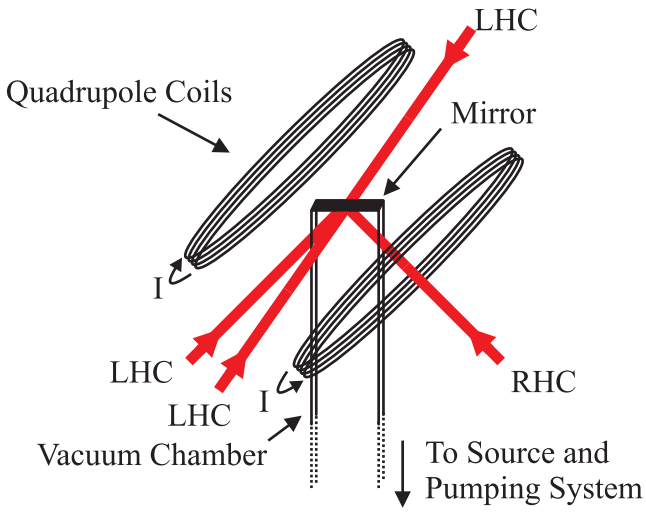

Figure 2.17: Sketch of a mirror MOT setup. The pumping system and the source of atoms is not shown. In a mirror MOT, the zero of the magnetic field is located a few mm away from a mirror surface. In the region where the incoming, beams overlap with the reflected beams, the atoms are subject to the same configuration of laser beams as in a regular MOT. Note that the quadrupole coils have to be oriented along one of the reflected beams, due to the change of polarization upon reflection off the mirror surface.

overlap of all beams just in front of the mirror surface, the atoms are subject to the same beams and the same magnetic field gradients as in the regular MOT. To ensure the correct circular polarizations of reflected and incident beams, the longitudinal axis of the quadrupole coils must be aligned with one of the reflected beams and cannot be aligned with the straight beams. This is because of the polarization change from RHC to LHC upon reflection.

The mirror MOT is the initial trap of choice in atom chip experiments, because an atom chip represents a natural surface that can be made into a highly reflecting mirror. From the initial cold atom cloud, trapped in the mirror MOT, further magnetic traps can then be loaded. Such purely magnetic traps are the topic of the next section.

2.6 Magnetic microtraps

In this section, the theory behind the technique of magnetic wire traps and magnetic microtraps is detailed.

Magnetic trapping of neutral atoms relies on the Zeeman shift. The atomic energy states in a magnetic field are split due to the interaction of the atomic angular momentum with the magnetic field

$$\begin{aligned} H_B = \mu \cdot \mathbf{B} &= \frac{\mu_B}{\hbar} \left(g_S \, \mathbf{S} + g_L \, \mathbf{L} + g_I \, \mathbf{I} \right) \cdot \mathbf{B} \\ &= \frac{\mu_B \, g_F}{\hbar} \, \mathbf{F} \cdot \mathbf{B} \\ &= \frac{\mu_B \, g_F}{\hbar} \, F_z \, B_z, \end{aligned}$$

where μ_B is the Bohr magneton, and the g are the various Landé g factors. S, L, I, and F are the spin, orbital, nuclear, and total angular momentum operators. In the last step, we chose the quantization axis z to coincide with the magnetic field axis.

If the splitting due to the magnetic field is smaller than the hyperfine splitting, F_z and $|F|$ are good quantum numbers, and we can label the resulting potential energy curves by F and m_F. A first-order approximation of the energy shifts for such weak fields is then

$$\Delta E(F, m_F) = \mu_B \, g_F \, m_F \, B_z, \tag{2.92}$$

For larger fields, when the energy shifts are on the order of the hyperfine splitting, the diagonalization of H_B is more complicated. For the ground state of ^{87}Rb, this regime corresponds to fields of a few thousand Gauss. An analytical solution for the Zeeman shifts is then given by the Breit-Rabi formula [102]:

$$E_{|J=1/2, m_j, I, m_I>} = -\frac{\Delta E_{hfs}}{2(2\,I+1)} + g_I \, \mu_B \, m \, B \pm \frac{\Delta E_{\text{hfs}}}{2} \left(\frac{1 + 4\,m\,x}{2\,I+1} + x^2 \right)^{1/2}, \tag{2.93}$$

where ΔE_{hfs} is the hyperfine splitting, $m = m_I \pm m_J$, and $x = (g_J - g_I) \, \mu_B \, B / \Delta E_{\text{hfs}}$. The atomic energy states can be divided into weak-field seeking states (WFS) and high-field seeking states (HFS), depending on the sign of the slope $\partial E / \partial B$.

To determine the atomic motion in a given magnetic field, in the case of adiabatic motion, the trapping potentials can be determined by evaluating the eigenenergies of H_B at each point in space for the magnetic field present at that point. This leads to potential energy curves that depend on the position of the atomic nucleus. The nuclear motion can then be treated as if it was confined to one of those potential curves under the assumption that there are no transitions between potential curves. This is similar to the Born-Oppenheimer approximation for molecules [103] in so far as any coupling between internal energy and the motion of the nucleus is ignored, e. g. the center of mass motion of the atom is assumed to be slow compared to the motion of the electron. A magnetic field gradient then leads to forces on the nuclei that allow trapping of WFS in a local minimum. For a two-state system with constant field direction, the criterion for the adiabatic approximation is given by the Landau-Zener parameter [104],

$$\frac{(\delta E(\mathbf{r}_0))^2}{\hbar \left(\nabla \left(\delta E\right)\right)_{\mathbf{r}=\mathbf{r}_0} \cdot \mathbf{v}(\mathbf{r}_0)} \gg 1 \tag{2.94}$$

here $\delta E(\mathbf{r}_0)$ is the energy difference between two potential curves, evaluated at a point in space $\mathbf{r}_0$, and $\mathbf{v}(\mathbf{r}_0)$ is the velocity of the atom as it passes through $\mathbf{r}_0$. If the magnetic field direction is constant in space and time, the interaction potential becomes scalar in nature. Assuming the magnetic field points along the z-direction everywhere, the above expression becomes

$$\frac{(g_F\ \mu_B\ B_z(\mathbf{r}_0))^2}{\hbar\ g_F\ \mu_B\ (\nabla B_z)_{\mathbf{r}=\mathbf{r}_0} \cdot \mathbf{v}(\mathbf{r}_0)} \gg 1. \tag{2.95}$$

In real traps, the magnetic field direction usually varies in space. The criterion for an effectively scalar potential in the presence of a spatially varying magnetic field direction is given by

$$\omega_B \ll \omega_L, \tag{2.96}$$

where the Larmor frequency $\omega_L = \mu B/\hbar$ is the splitting between neighboring potential curves, and $\omega_B = \mathbf{v} \cdot \nabla \left(\mathbf{B}/B\right)$ is the apparent rate of change of direction of the

magnetic field as seen in the rest frame of the atom. Then, it is $|B|$ instead of the vector $\mathbf{B}$ that governs the atomic motion. Strictly speaking, the above criteria are not valid for systems with more than two states. However, numerical and experimental results suggest that the Landau-Zener parameter is a rather robust estimate and remains valid even in more complicated systems [105, 106]. If in doubt, the time-dependent Schrödinger equation can be solved numerically in a truncated basis to determine the validity of the adiabatic approximation.

The above Born-Oppenheimer type approximation breaks down when the motion becomes nonadiabatic. From the Landau-Zener parameter, we can see that this happens when the potential curves come close enough to each other, and/or the atomic velocity is large enough to induce nonadiabatic transitions between Zeeman levels. During a nonadiabatic transition, atoms change their internal energy state. The largest Landau-Zener parameters are obtained at the trap center. At the trap center, the field has a minimum and the Zeeman splitting is therefore close to zero. In addition, the atomic velocities are also largest there. If the minimum is at zero magnetic field, atoms can change states from WFS to HFS with high probabilities and consequently be ejected from the trap in large quantities. This is a trap loss mechanism due to nonadiabatic change of magnetic dipole moments and is known as Majorana flopping [107, 108]. To prevent Majorana flopping in a Ioffe-Pritchard type magnetic trap, a small homogenous offset field of a few Gauss, called the Ioffe field, is applied in a perpendicular direction to the main trapping field. The small offset field ensures a splitting of potential curves even at the trap minimum.

While the original Ioffe-Pritchard magnetic trap employed multiple coils [109], a Ioffe-Pritchard type trap can be created by a simple z-shaped current-carrying wire combined with an external homogenous offset field [110]. First, consider the field of

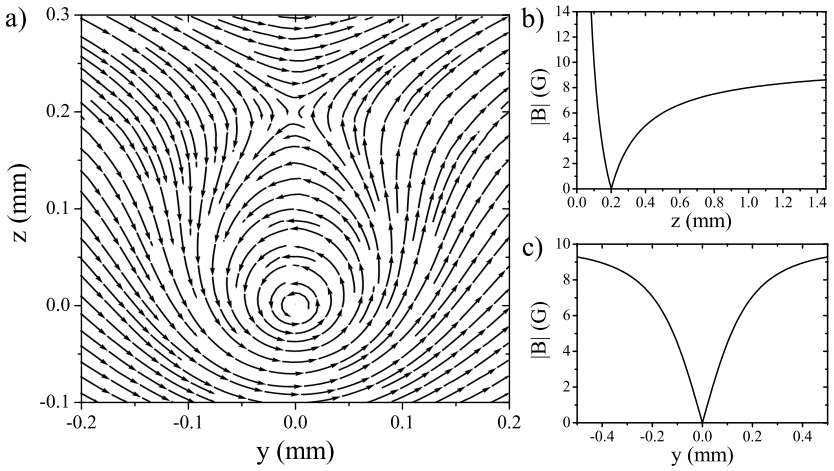

Figure 2.18: Atomic guide formed by an infinitely long wire. The wire is along the x-axis. Parameters are $I = 1\ A$ and $\mathbf{B}_{\text{bias}} = (0, 10\ \text{G}, 0)^{\text{T}}$

an infinitely long wire aligned with the x-axis

$$B(z) = \frac{\mu_0\, I}{2\pi}\, \frac{1}{z}\, \mathbf{e}_\phi, \tag{2.97}$$

where z is the distance to the wire which is assumed infinitely thin, and $\mathbf{e}_\phi$ is the unit vector in the direction of the azimuthal angle with respect to rotation about the x-axis. A homogenous offset field B_{bias}, directed perpendicular to the wire direction will create a minimum with zero magnetic field at a distance

$$z_0 = \frac{\mu_0\, I}{2\pi}\, \frac{1}{B_{\text{bias}}} \tag{2.98}$$

away from the wire. This configuration, shown in Fig. 2.18, can be used as an atomic guide [111]. Assume B_{bias} points in the +y-direction. The guide is then closed to form a Ioffe-Pritchard type trap by making the central wire finite in length and adding two segments parallel to the y-axis to give the wire a shape in the form of a "Z". The added segments close the trap along the x-axis and create a Ioffe field at the trap minimum. This is illustrated in Fig. 2.19. At the trap minimum, which forms just above the central segment, the field from the first side segment mostly points in the -z-direction,

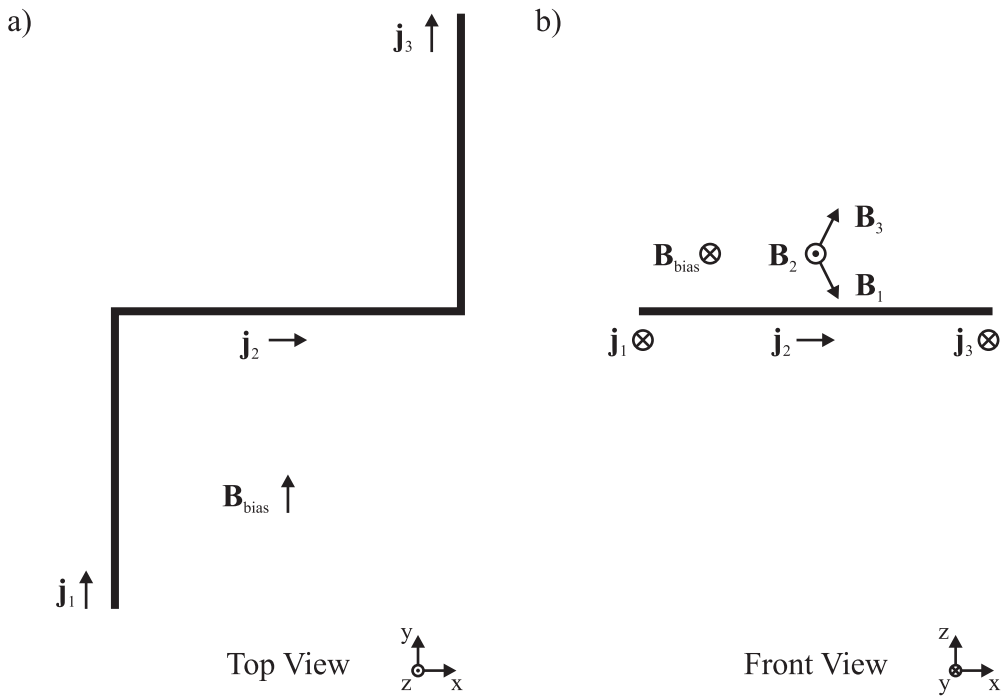

Figure 2.19: The z-wire geometry leads to a Ioffe-Pritchard type trap. The top view of the wire is shown in a), and the front view is shown in b). The trap minimum forms just above the center segment, where the external bias field $\boldsymbol{B}_{\text{bias}}$ cancels the field $\boldsymbol{B}_2$, created by current density $\boldsymbol{j}_2$. The side segments of the wire, current densities $\boldsymbol{j}_1$ and $\boldsymbol{j}_3$, create two additional fields at the trap minimum, $\boldsymbol{B}_1$ and $\boldsymbol{B}_3$. The larger vertical components of those fields cancel, but a small component pointing horizontally remains. This remaining field $\boldsymbol{B}_{\text{Ioffe}} = \boldsymbol{B}_1 + \boldsymbol{B}_2 + \boldsymbol{B}_3 + \boldsymbol{B}_{\text{bias}}$ is the Ioffe field. It prevents Majorana losses at the trap minimum.

towards the central wire segment, but also has a small component in the +x-direction. The field from the second side segment mostly points in the +z-direction, away from the central wire segment, but also has a small component in the +x-direction. The large z-components of those segments cancel exactly at the trap center, but a small x-component remains. Since the trapping field created by the center segment points along the $\pm y$ direction, this small x-component is the Ioffe field.

To calculate the actual fields of the z-shaped wire, numerical integration of the Biot-Savart law is necessary. For real wires with non-zero cross sections, the current flows around the wire corners in a non-trivial way. We therefore perform a finite element simulation using the open-source software Elmer [112] to obtain accurate current density elements for all of our Biot-Savart calculations. The current density is calculated on a nonuniform volume mesh that consists of roughly 30000 elements. The density data is imported into Mathematica and used to calculate the magnetic field vectors on a uniform, three-dimensional grid. Fig. 2.20 shows the results of such a calculation for our microscopic atom chip z-wire. Impurities and roughness of the wires are not included in our calculations. The role of microscopic wire imperfections due to the manufacturing process was studied experimentally in Ref. [113] and shown to cause a potential roughness of $< 1\ \mu\mathrm{KA}^{-1}$ for atoms trapped at distances $\geq 100\ \mu$m from the imperfect wire surface. For the measurements presented in this thesis, this roughness is two orders of magnitude smaller than the energies of the trapped atoms, and can therefore be neglected in the calculations.

A magnetic trap can be characterized by the trap frequencies ω_x, ω_y and ω_z, corresponding to the frequencies of oscillation of a trapped atom when it is displaced a small distance from the trap center along the x-, y- and z-directions, respectively. The trap frequencies are obtained by approximating the trapping potential with that of a 3D harmonic oscillator with resonance frequencies $\omega_x, \omega_y, \omega_z$ around the trap

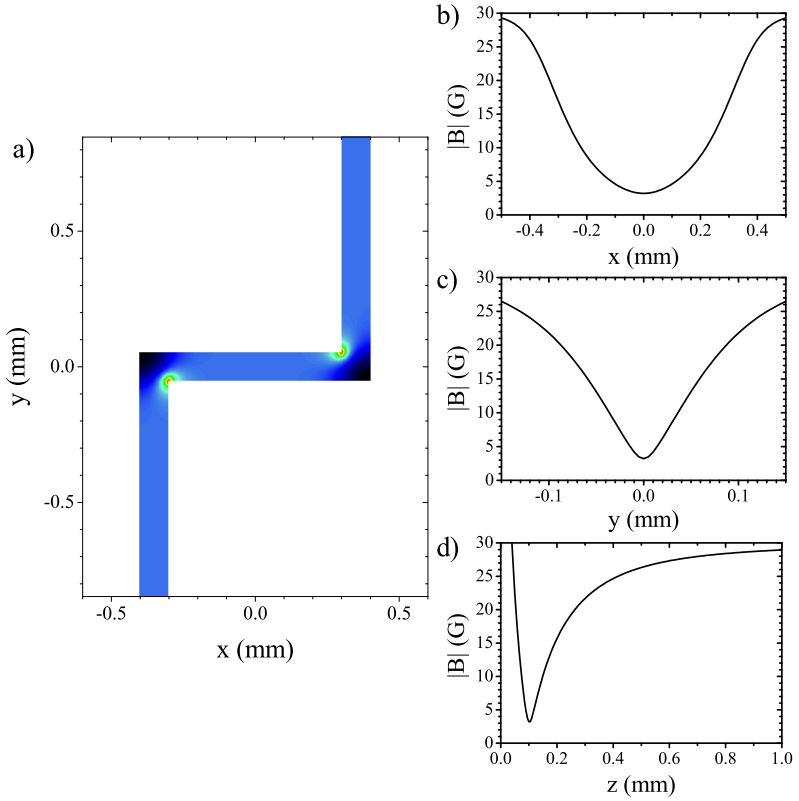

Figure 2.20: The z-wire magnetic microtrap on the atom chip. 3D current densities were calculated using the finite element method. The current enters the wire in the positive y-direction. The wire is made of Au. It is 100 μm wide and approximately 9 μm high. In a), the Joule heating of the wire surface, proportional to I^2, is plotted as a color gradient. This illustrates the complicated current flow across the corners that leads to heating. In b), c), and d), the magnetic field magnitude along the three Cartesian axes through the trap minimum is shown. Note that the field is non-zero at the trap center. This is due to the Ioffe field produced by the two side segments of the z wire, and prevents Majorana losses. Along the z direction, the trap is highly anharmonic. Parameters are $I = 1.86$ A and $\mathbf{B}_{\text{bias}} = (0, 30\text{ G}, 0)^{\text{T}}$.

minimum,

$$\Delta E(\mathbf{r}-\mathbf{r}_0) = \frac{1}{2}\, m\, \omega_x^2\, (x-x_0)^2 + \frac{1}{2}\, m\, \omega_y^2\, (y-y_0)^2 + \frac{1}{2}\, m\, \omega_z^2\, (z-z_0)^2 + \mathrm{O}(|\mathbf{r}-\mathbf{r}_0|^3), \tag{2.99}$$

where $\mathrm{O}(x^i)$ denotes terms of order i or higher in x. Once the trapping potential and minimum is found, a simple Taylor expansion to second order in the displacement will reveal the trap frequencies, which are proportional to the curvatures of B along the Cartesian directions. As an example, Fig. 2.21 shows the trapping potentials for $^{87}\mathrm{Rb}, F = 2$ ground state atoms in the fields of the microtrap from Fig. 2.20, together with the harmonic approximations and corresponding trap frequencies. To calculate potential curves, the adiabatic approximation and Eq. 2.93 was used.

As long as r_0 is shorter than the length of the central segment, the following approximate scaling laws can aid in the design process of magnetic z-wire traps [110],

$$B_0 \sim \frac{I^2}{B_{\mathrm{bias}}\, L^2} \tag{2.100}$$

$$\frac{d^2B}{dz^2} \sim \frac{d^2B}{dy^2} \sim \frac{B_{\mathrm{bias}}^5\, L^2}{I^4} \tag{2.101}$$

$$\frac{d^2B}{dx^2} \sim \frac{B_{\mathrm{bias}}}{L^2}, \tag{2.102}$$

where L is the length of the central segment. By increasing B_{bias} or decreasing I, the trap minimum can be moved closer to the wire. This also compresses the trap because the trapping frequencies increase according to

$$\omega_z \sim \omega_y \sim \frac{B_{\mathrm{bias}}^{2.5}}{I^2} \tag{2.103}$$

$$\omega_x \sim B_{\mathrm{bias}}^{0.5}, \tag{2.104}$$

obtained from Eqs. 2.101, 2.102 and Eq. 2.99 under the assumption of a linear Zeeman shift. For $z \leq 200\ \mu$m, extremely large magnetic field gradients on the order of several $\mathrm{kG\,cm^{-1}}$ can be obtained with moderate currents of a few Ampere and bias fields of only a few tens of Gauss. This corresponds to very tight magnetic microtraps with

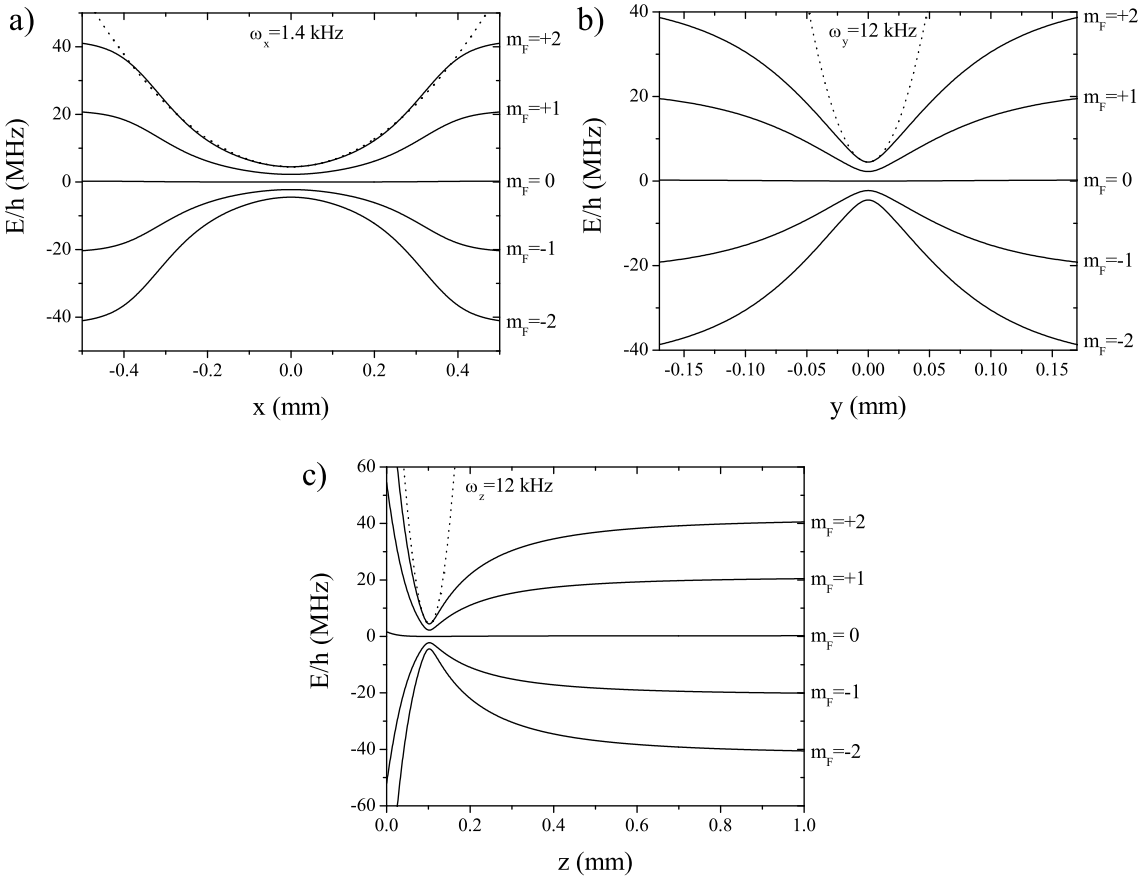

Figure 2.21: Adiabatic trapping potentials calculated for ^{87}Rb F=2 ground state atoms in the microtrap from Fig. 2.20 (solid lines), together with the harmonic approximation for the $m_F = 2$ state atoms (dotted lines) and corresponding trap frequencies ω. The plots a), b) and c) correspond to cross sections through the trap minimum along the three Cartesian axes x, y and z respectively. Both WFS, $m_F = 2$ and $m_F = 1$, are trapped. Atoms in the $m_F = 2$ state experience the largest restoring forces, characterized by the trap frequencies shown. Trap parameters are the same as for Fig. 2.20.

large trapping frequencies in the range of kHz. A high atomic density results due to the large compression of the atom cloud. In addition, this is a setup that lends itself naturally to miniaturization [114]. Using well-understood technologies from the microchip industry such as photolithography and electroplating, one can create almost arbitrary microscopic wire patterns [19, 115, 116]. Such atom chips have been used not only to create magnetic z-wire microtraps but also other wire patterns that allow further manipulation and experiments with the trapped atoms, such as the atomic conveyor belt [20] and many others [15, 117]. Wire traps on atom chips have been used to implement BEC interferometry [118], and Rydberg experiments on high-density ultracold samples [10], using relatively small experimental setups.

Chapter 3

Experimental apparatus

3.1 Introduction

In this chapter, the experimental apparatus is described in detail. This includes the vacuum system, the laser systems, the atom chip mount and cooling setup, the Rb sources, the various magnetic field coils and coil switching electronics, the microwave setup, and the imaging system. The remote control system used to switch coil currents, laser detunings and other experimental parameters in pre-defined sequences is also described.

3.2 Vacuum system

3.2.1 Chamber

An overview of the vacuum system is shown in Fig. 3.1. The main vacuum chamber that houses the atom chip is a stainless steel 6" spherical octagon (Kimball Physics MCF600-SphOct-F2C8). It has eight 2.75" and two 6" CF ports. It is mounted such that a 2.75" viewport faces the optical table surface. This viewport is used for imaging the trapped atoms from below. The atom chip mount is inserted through the topmost 2.75" port, allowing the atom chip to hang upside down, centered in the chamber. The Rb sources are situated in a 2.75" nipple on the port facing diagonally away from the optical table at an angle of 45°. The other top diagonal facing port is blanked off. Two diagonal facing viewports on the bottom are used for two of the four mirror magneto-optical trap (MOT) cooling beams that reflect off the chip surface. Two smaller horizontally facing viewports, one directly on the chamber and one on the far end of a 2.75" tee that is connected to the chamber, are used for absorption

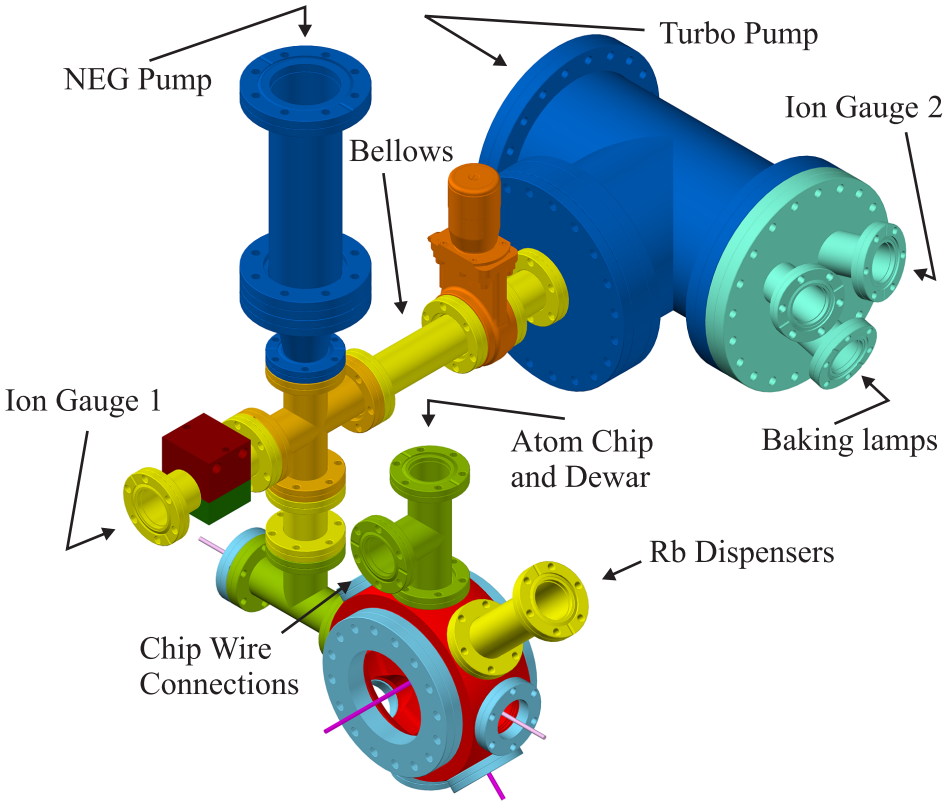

Figure 3.1: Sketch of the vacuum system. The experimental chamber that houses the atom chip is shown in red. The pumps are attached to the dark blue colored parts as labeled. Other parts such as the rubidium sources connect to the system as labeled. Flexible bellows, labeled "bellows" (yellow) in the diagram, are used to isolate the chamber from vibrations. The MOT and imaging beams are also depicted (dark and light purple), as is the gate valve used to isolate the chamber (orange).

imaging and optical pumping. The two larger 6" viewports on the side are used for the two remaining counterpropagating mirror MOT beams. The 6" viewports are also used for light from the UV LEDs for light induced atomic desorption (UV LIAD), for microwave radiation, for sideways imaging of the MOT, and to mount the x-bias coils to the chamber.

The bottom viewport of the chamber is 6" above the table surface. The vacuum system is held in place by clamps (not shown). Three clamps support the chamber. Four clamps that rest on two layers of Sorbothane and lead support the large tee and turbo pump. The Sorbothane is used to isolate the table from vibrations caused by the turbo pumps.

3.2.2 Pumps

The pumping setup is shown schematically in Fig. 3.2. The chamber is pumped out through the top port of a 2.75" tee that is mounted on the horizontally facing small viewport on the back. Following the tee is a four way cross that connects to an ion gauge on the side, and a non-evaporable getter pump (SAES Getters Capacitorr D-400 2) on the top. The other side of the cross connects via flexible bellows to a manual gate valve (VAT 1032). The flexible bellows are used to isolate the chamber from vibrations due to the turbo pumps. The gate valve can be used to isolate the chamber vacuum. Behind the gate valve is an 8" tee that houses two baking lamps and another ion gauge which are attached via two ports of a three-way multiplexer on the side of the tee. The third multiplexer port is blanked off. Connected to the other side of the tee are the pumps. They are attached in series, starting with a large turbo pump (Leybold TVAC 340), followed by a small turbo pump (Leybold TVAC 50), a pneumatic isolation valve, a backing hose, a manual angle valve, a longer backing hose that leads into the mechanical pump room, and finally a mechanical backing

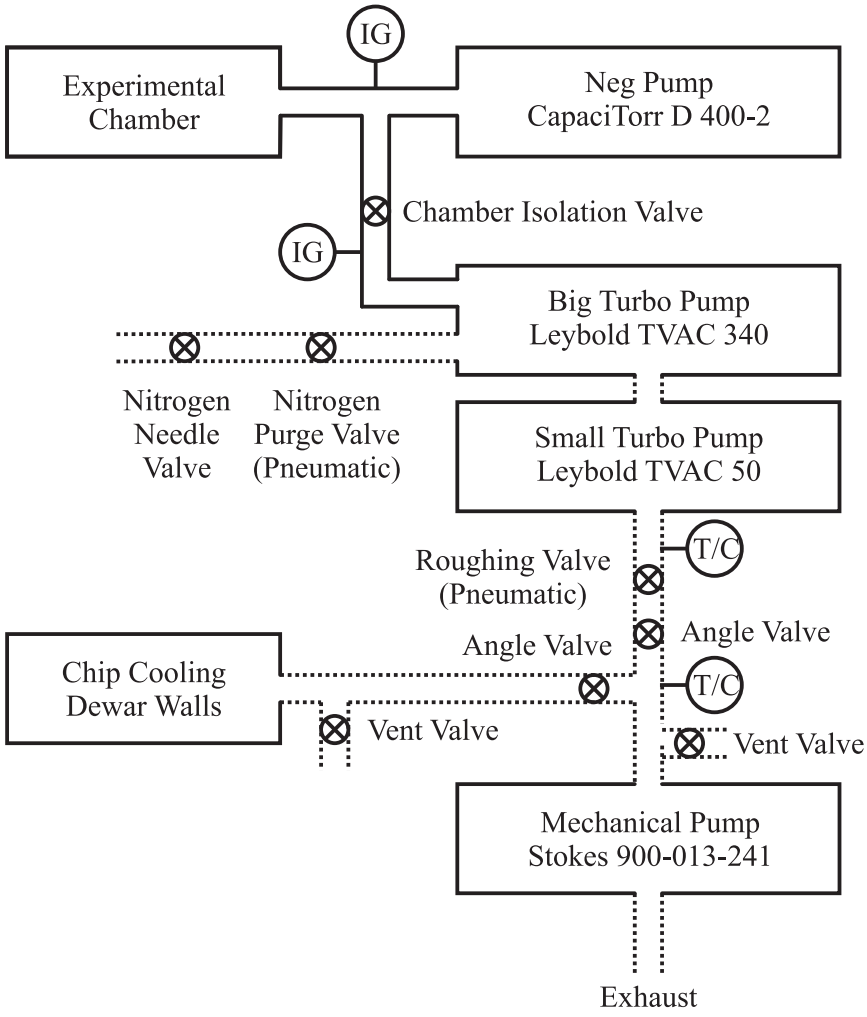

Figure 3.2: Schematic of the pump setup. Four pumps are pumping on the experimental chamber in the configuration shown. Multiple valves allow the user to isolate the chamber and/or tee, and select whether to pump on the atom chip dewar or not. The pressure in the chamber and in the tee is measured with Bayard-Alpert ionization gauges (IG). The roughing line pressure and the pressure on the small turbo pump exhaust is monitored with thermocouple gauges (T/C). A pneumatic valve can be used to purge the chamber with nitrogen during a controlled loss of vacuum. The nitrogen purge pressure is controlled via a manual needle valve. Here, solid lines denote CF components, and dashed lines denote KF components.

pump (Stokes 900-013-241) that exhausts into the air. The atom chip cooling dewar is pumped out by the same mechanical pump through a second manual angle valve and a roughing hose. The turbo pumps, the mechanical pump and the pneumatic valve are interlocked to prevent the chamber from filling with air in case of a loss of power. They are controlled by a programmable-logic circuit (PLC, DirectLogic 105) that is equipped with a push-button interface.

To pump the chamber out after it has been up to air, the push-buttons on the PLC circuit are pushed in sequence from left to right, while the pressure gauges are monitored to ensure leak-free operation. The first push-button turns on the mechanical pump. The roughing line pressure can be read off the first thermocouple gauge. The second push-button opens the pneumatic isolation valve behind the small turbo pump, allowing the mechanical pump to pump on the chamber. The pressure at the turbo pump exhaust can be read off the second thermocouple gauge. The third push-button turns on the small turbo pump. The fourth push-button then turns on the big turbo pump. At this point the tee and experimental chamber pressures can be monitored with the two ion gauges.

The PLC circuit is programmed to not allow pumps to be switched on or off out of sequence, and to automatically shut off the turbo pumps when the pressure in the backing line rises above a setpoint of 10^{-2} Torr.

A separate manual switch controls the pneumatic nitrogen purge valve. This valve can be used to purge the chamber with nitrogen in case of a controlled loss of vacuum. Purging the chamber with nitrogen at a pressure slightly above 1 atm instead of exposing it to room air reduces the amount of water accumulating on the chamber walls. In addition, the constant flow during purging mechanically hinders small particles from blowing into the chamber when one of the viewports is removed to perform maintenance on the chamber. The nitrogen purge pressure is controlled

by a manual needle valve.

The NEG pump is passive, but should be (re-)activated after it has come up to atmospheric pressure. The NEG pump can only be activated in a vacuum environment and should be activated during bake-out. In order to activate the NEG pump, a voltage of 16 V is applied to its internal heater for a duration of 60 min.

3.2.3 Baking cycle

A bake-out is performed by first covering the chamber and all vacuum parts apart from the dewar in a layer of aluminum foil, wrapping the foil with heating tape (Omegalux STH-101-060), and covering the tape with another layer of aluminum foil. The two layers of aluminum foil ensure even heating. While the turbo pumps and mechanical pumps are pumping on the system, the chamber is then heated up to 150 °C with the heating tape. The other parts of the vacuum system are heated up to 120 °C with the heating tape and by turning on the baking lamps in the tee. The pressure is monitored and recorded with the ion gauges until it is not dropping anymore. A bake-out usually takes 1-2 weeks. If the system has been up to air before baking, the NEG pump is activated a few days into the bake-out cycle while baking. Care has to be taken to never subject the NEG pump to atmospheric pressure during baking. The getter material will burn when it gets into contact with air while it is hot. This can destroy the pump. At the end of the bake out, all heating tapes and baking lamps are switched off or turned down, making sure that the chamber is cooling down slower than the rest of the system. This method of bake-out consistently leads to an ultimate pressure of $< 10^{-10}$ Torr as measured by the ion gauge closest to the main chamber.

3.3 Main laser system

3.3.1 Laser setup

The main laser system that generates the cooling, repumping, imaging and optical pumping light from two commercial external cavity diode lasers (ECDL, Toptica DL100) is shown in Fig. 3.3. Each ECDL is mounted on an aluminum block that functions as a heat sink. Each mounting block rests on a layer of Sorbothane, to isolate the ECDL from table vibrations caused by the turbo pumps and cooling water lines. Using an accelerometer (Wilcoxon Research 731A), we verified that mounting the lasers on Sorbothane reduces the dominant component of vibrational noise, at 860 Hz, by 42 dB. As a consequence, the frequency stability of the ECDLs is significantly improved.

Four accousto-optic modulators (AOM) are used to fix the frequencies of the cooling, repumping, imaging and optical pumping beams. The frequencies are summarized in Fig. 3.4. The optical pumping beam is derived from the cooling laser via the minus one order of a 40 MHz fixed frequency AOM (Isomet 1201E-2, driver 221A-2, labeled by nr. 1 in Fig. 3.3). The imaging beam is derived from the cooling laser via the first order of a tunable AOM (Crystal Technologies AOM 3110-140, driver 1110-AF-AEF0-1.5, nr. 3) in double-pass configuration. The detuning of the imaging beam AOM is set to bring the beam on resonance with the $F = 2 \rightarrow F' = 3$ transition and is then optimized empirically by maximizing the optical density of the atomic cloud to account for stray magnetic fields. Imaging and optical pumping beams are each fiber coupled into a polarization maintaining fiber before entering the chamber. The MOT cooling light is derived from the cooling laser via the first order of a tunable AOM (same model as imaging AOM, nr. 2), also in double-pass configuration. The frequency of the cooling beam AOM is set so that the detuning δ from the $F = 2 \rightarrow F' = 3$ resonance is -17 MHz during the loading phase of the

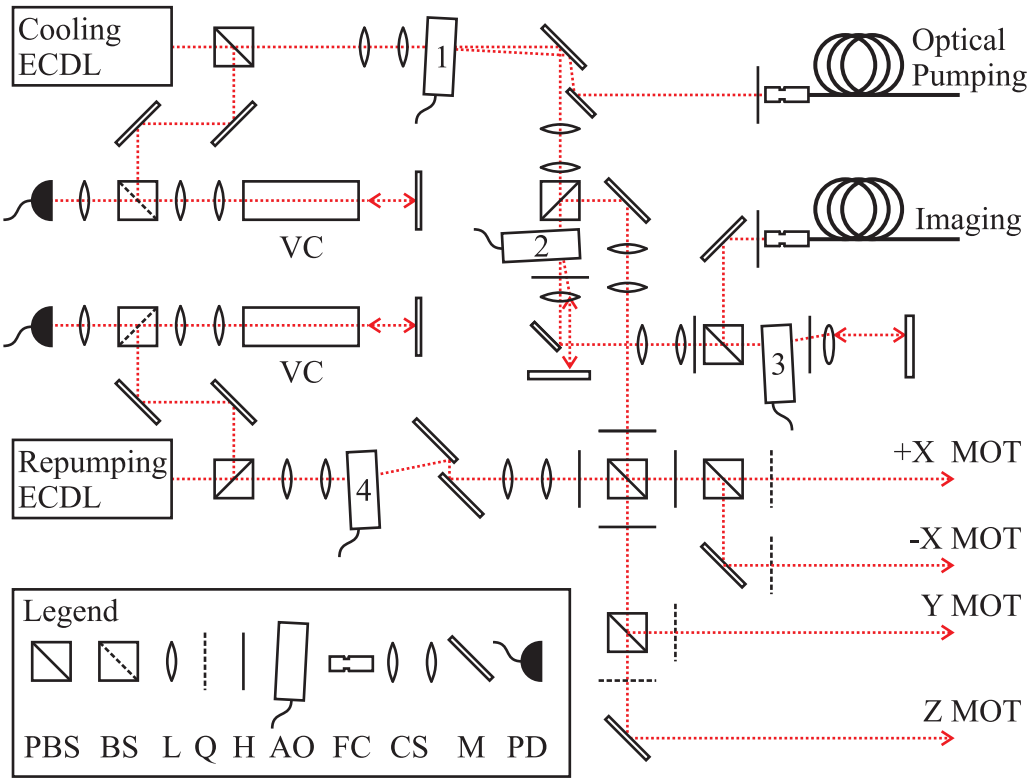

Figure 3.3: Schematic of the main laser system. Both external cavity diode lasers are locked to the side of a hyperfine transition of ^{87}Rb using the saturated absorption spectroscopy setups shown. The cooling (repumping) laser frequency is adjusted with accousto-optic modulator 2 (4). The optical pumping and imaging beams are derived from the main cooling laser via accousto-optic modulators 1 and 3, respectively, before they are fiber coupled. The repumping light is overlapped with the +X MOT beam before entering the chamber. PBS: Polarizing beamsplitter cube, BS: non-polarizing beamsplitter cube, L: focussing lens, Q: quarter-wave plate, H: half-wave plate, AOM: accousto-optic modulator, FC: fiber collimator, CS: collimation stage, M: mirror, PD: photodiode, VC: Rb vapor cell.

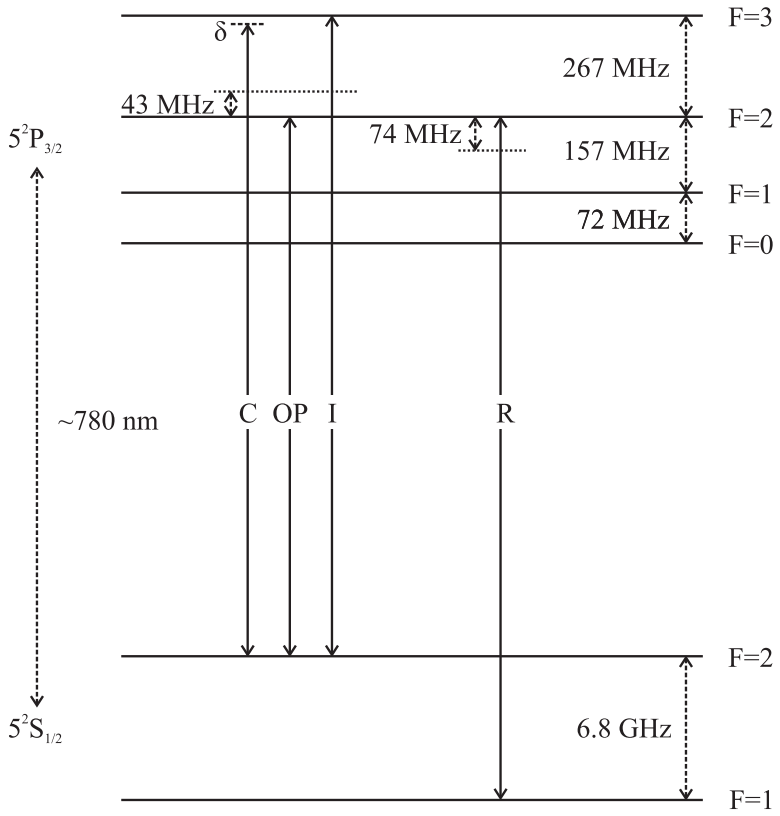

Figure 3.4: Relevant atomic transitions and laser frequencies in the MOT setup. C: cooling beams, I: imaging beam, OP: optical pumping beam, R: repumping beam. The lock points of the cooling laser (left) and repumping laser (right) are shown as dotted horizontal lines. The laser frequencies denoted by solid vertical arrows are derived from the locked lasers via four AOMs as described in the text. The detuning δ of the MOT beams is -17 MHz during the MOT loading phase. Hyperfine splittings are taken from Ref. [2] and Ref. [3].

MOT. The MOT light is then up-collimated to a FWHM of ~ 1 cm and split via polarizing beamsplitter cubes into four separate cooling beams, labeled +X, -X, Y, and Z. The mirror MOT is operated with these four dedicated beams instead of two retro-reflected beams. Retro-reflected beams are always power-imbalanced, because the reflected beam makes additional passes through lossy windows and experiences further losses upon reflection before it hits the atoms again. This imbalance turned out to be detrimental to the atom number and shape of our mirror MOT, and we were able to increase the atom number by a factor of 2 by balancing each of the four beams separately. The beam balancing is done for each pair of beams by rotating a half-wave plate in front of a beamsplitter cube. The beam balancing is done empirically every day to maximized the atom number in the MOT. The optimum beam balance is achieved at an intensity of $\sim 4 - 5$ mW cm^{-2} per beam. The polarization of each MOT beam is changed into circular polarization by a quarter-wave plate.

The repumping light is shifted by 74 MHz via the first order of an AOM (Isomet 1205C-1, driver D322B-788, nr. 4) to bring it into resonance with the $F = 1 \rightarrow F' = 2$ repumping transition. It is then up-collimated to the same size as the cooling beams and overlapped with the +X cooling beam via a polarizing beamsplitter cube. The repumping light is attenuated and has a power of ~ 1 mW entering the chamber.

3.3.2 Saturated absorption spectroscopy

Each laser is locked via saturated absorption spectroscopy to the side of a crossover Lamb dip between two hyperfine transitions of ^{87}Rb. The necessary piezo and current feedback signals are generated by a commercial digital locking circuit (Toptica Digilock). Both locking circuits are controlled from the experimental computer, a desktop PC running Windows XP. The saturated absorption spectroscopy is performed with standard 10 cm long Rb vapor cells, heated up to ~ 45 °C. The saturated absorption

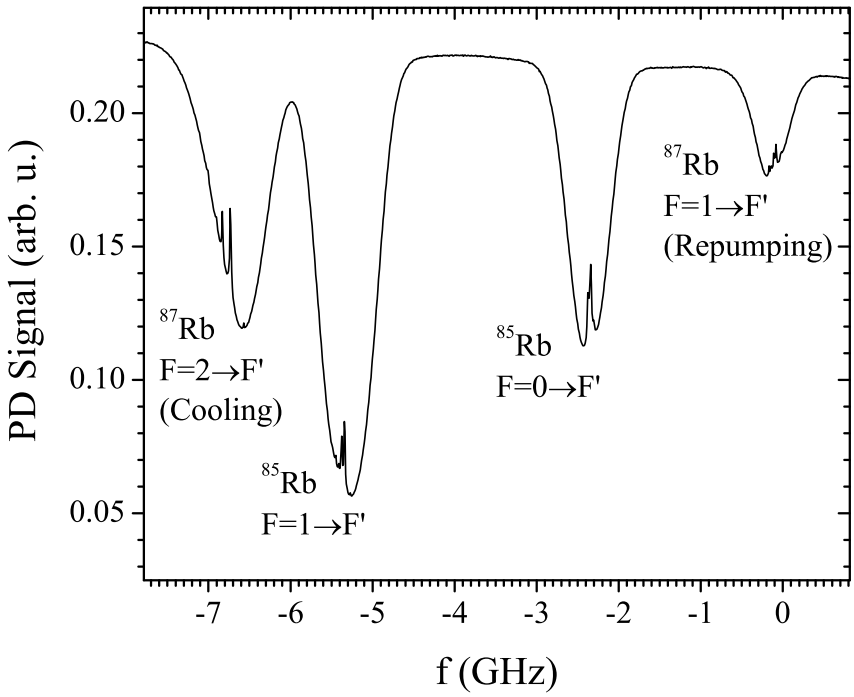

Figure 3.5: Saturated absorption spectrum obtained by scanning the cooling laser piezo and current to cover a large frequency range $\sim$ 9 GHz. The cooling and repumping transitions are highlighted. The voltages are negative because an offset was applied.

beams are up-collimated to match the size of the vapor cell windows before entering the vapor cell. This decreases the intensity and allows us to use larger probe powers while minimizing the power-broadening of the Lamb dips. Using larger probe powers increases the signal-to-noise ratio in the saturated absorption signal and therefore increases the quality of the lock. The cooling laser is locked to the red side of the $F = 2 \rightarrow F' = 1, 3$ crossover peak, and the repumping laser is locked to the blue side of the $F = 1 \rightarrow F' = 1, 2$ crossover peak. Increasing the signal-to-noise ratio is especially useful on the repumping transition, since it is a weaker transition than the cooling transition and proved difficult to lock to in the beginning. Typical saturated absorption spectra taken with this setup are shown in Fig. 3.5, Fig. 3.6 and Fig.3.7.

As an overview, Fig. 3.5 shows a scan over the ground state hyperfine splitting of

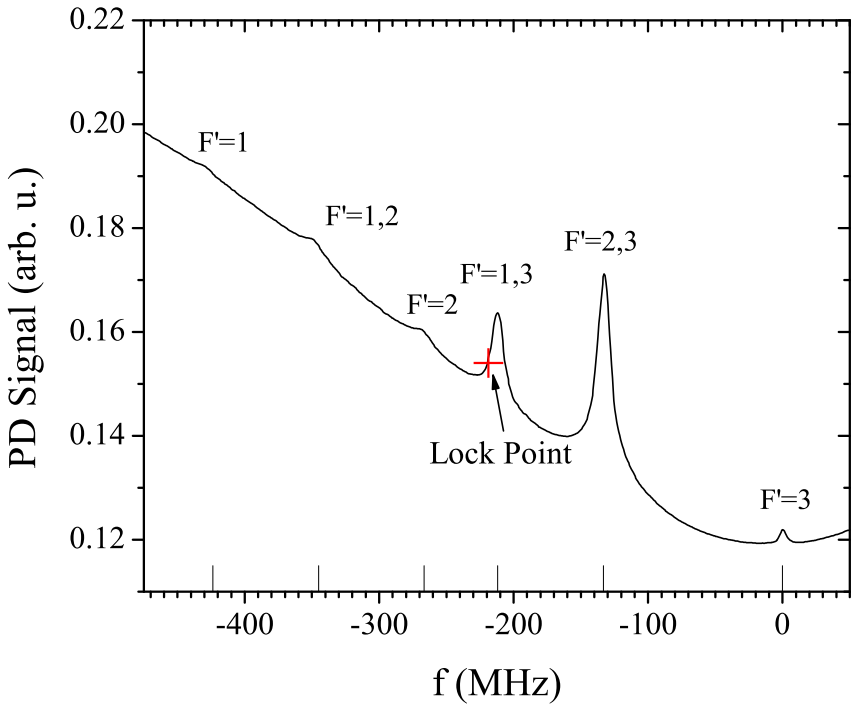

Figure 3.6: Saturated absorption spectrum of the $F = 2 \rightarrow F'$ transitions and crossover peaks, including the $F = 2 \rightarrow F' = 3$ cooling transition. The frequency axis was calibrated using the $F' = 2$ to $F' = 3$ hyperfine splitting. Vertical lines denote the expected peak positions, calculated from the known hyperfine splittings [2]. The cooling laser lock point is highlighted by a red cross.

^{87}Rb, which spans 6.8 GHz. Fig. 3.6 depicts the saturated absorption spectrum for frequencies close to the $F = 2 \rightarrow F' = 3$ cooling transition. The lock point of the cooling laser is highlighted. Fig. 3.7 shows a similar spectrum for frequencies close to the repumping transition, where the lock point of the repumping laser is highlighted. The spectra were taken with the cooling laser by scanning the grating piezo and diode current simultaneously, using the scan mode of the locking circuit. They are typical spectra, displayed in realtime everyday by the locking software. The repumping laser gives equivalent results.

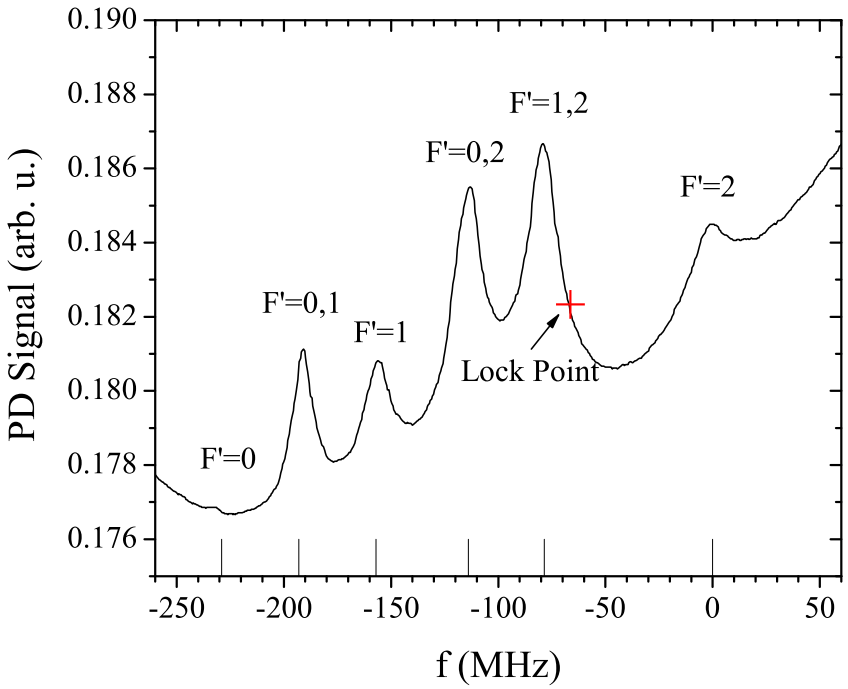

Figure 3.7: Saturated absorption spectrum of the $F = 1 \rightarrow F'$ transitions and crossover peaks, including the $F = 1 \rightarrow F' = 2$ repumping transition. The frequency axis was calibrated using the $F' = 1$ to $F' = 2$ hyperfine splitting. Vertical lines denote the expected peak positions, calculated from the known hyperfine splittings [2]. The repumping laser lock point is highlighted by a red cross.

3.4 Atom chip setup

3.4.1 Chip design

The atom chip was manufactured for us by Steve Miller's research group at Air Force Research Laboratories (AFRL). It consists of a 9 μm thick Au layer on a Si substrate. The wires are defined by 40 μm wide gaps in the gold layer that are patterned according to our chip design. The chip size is 0.86" $\times$ 0.53" and it is $\sim$ 400 μm thick.

A picture of the mask design is shown in Fig. 3.8, and a photo of the atom chip

as received from AFRL is shown in Fig. 3.9.

The atom chip wire pattern contains a central z-shaped wire that is used to create the main Ioffe Pritchard type magnetic microtrap. The chip contains four u-shaped wires that can be used to increase longitudinal confinement of the z-trap for experiments that require a smaller trap aspect ratio. There are also two wires for application of RF currents that can be used to smoothly change the trapping potential from a single well into a double well using RF adiabatic potentials [119] for atom interferometry experiments.

3.4.2 Copper z-wire

While the MOT is located about 2 mm away from the chip surface, the chip trap minimum is located at closer distances ~ 100 μm. Thus, a transfer is necessary to bring the atoms from the MOT closer to the chip surface before the they can be loaded into the microtrap. For this purpose, an intermediate, macroscopic, magnetic trap is loaded from the MOT. It is used to move the atoms closer to the chip surface and is generated by a macroscopic z-shaped copper wire that is mounted behind the chip. The macroscopic wire is 1 mm thick, and it can withstand DC currents of $I_z > 40$ A. The macroscopic magnetic trap formed by this wire is chosen so that it initially overlaps with the MOT. After the macroscopic trap is fully loaded with atoms from the MOT, it is then compressed by ramping up the x-bias field. As the trap is compressed, the trap minimum moves closer to the atom chip. The trapped atoms follow the trapping potential adiabatically if the ramp is slow enough. At distances of < 1 mm from the atom chip the ramp is stopped, and atoms can then be transferred into the microscopic chip trap.

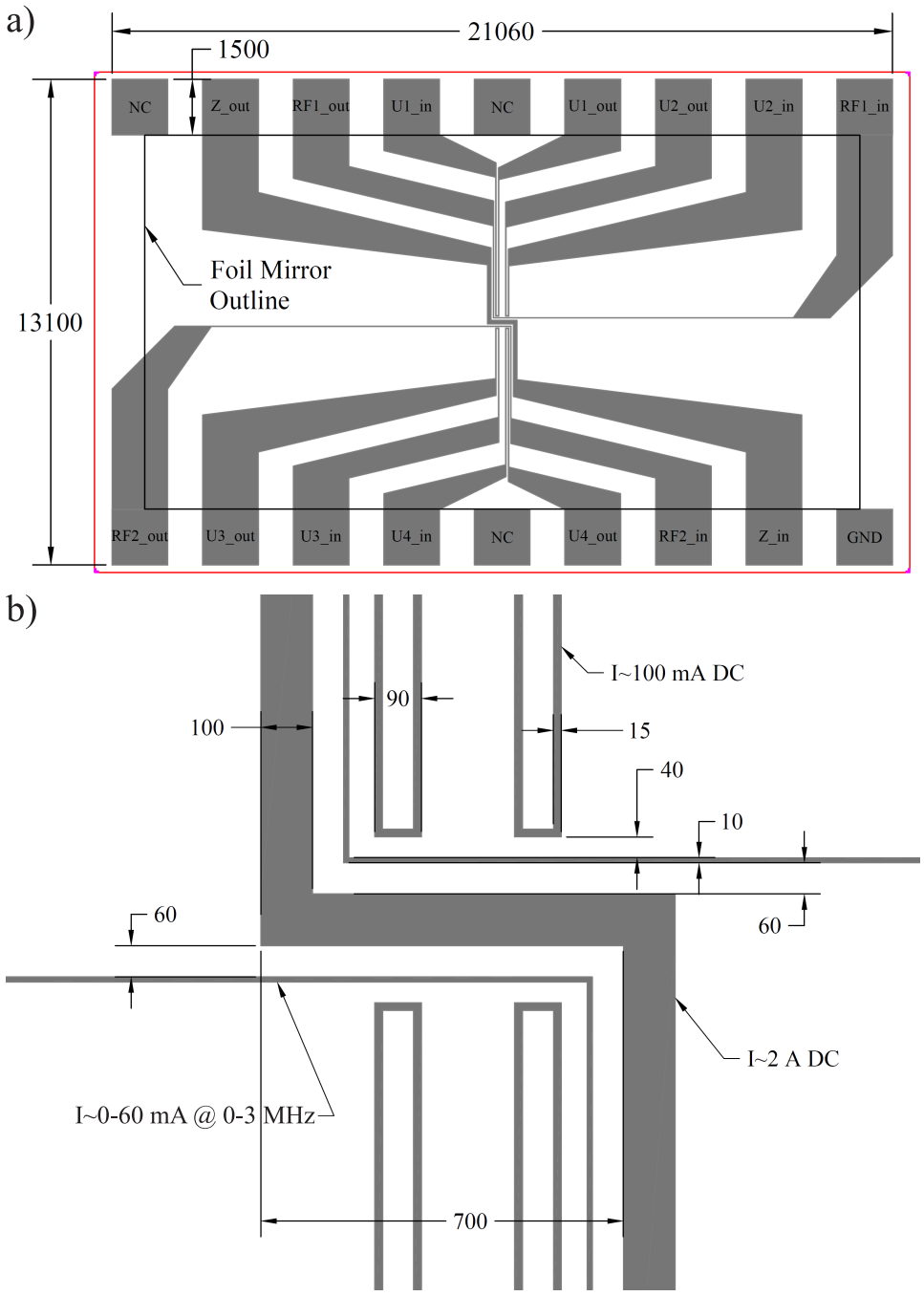

Figure 3.8: Photolithography mask design for the atom chip. Wires are defined by 40 μm gaps in the gold surface. The mirror plane covering almost all of the chip surface is omitted to highlight the actual wire traces. a) overview, b) close-up view of the center region. Lengths are specified in μm.

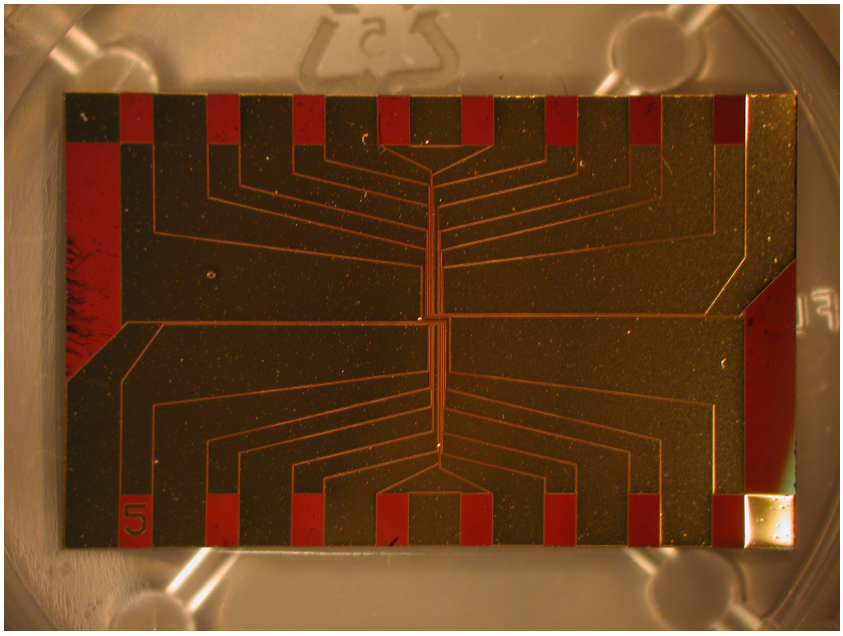

Figure 3.9: Photo of the atom chip received from AFRL.

3.4.3 Cooling solution

The microscopic z-wire on the atom chip must withstand currents up to 3 A for hundreds of ms to create useful trapping potentials with trap depths $\sim$ 1 mK at distances a few hundred μm away from the chip surface. Similarly, the copper z-wire has to withstand currents up to 60 A for hundreds of ms. To protect the chip from damage due to the associated Joule heating, it has to be cooled to dissipate the heat.

A sketch of the complete cooling assembly mounted in the chamber is shown in Fig. 3.10. A photo of a cooling assembly just before insertion into the chamber is shown in Fig. 3.11.

The atom chip heat sink hangs from a high power electrical feedthrough (Lesker EFT0543253) that has four 0.25" diameter copper rods thick enough to provide mechanical stability. Two of the copper rods serve as conductors for the copper z-wire currents. The other two copper rods are used as cold fingers to cool and support an aluminum heat sink on which the atom chip mount rests. On the air side of the

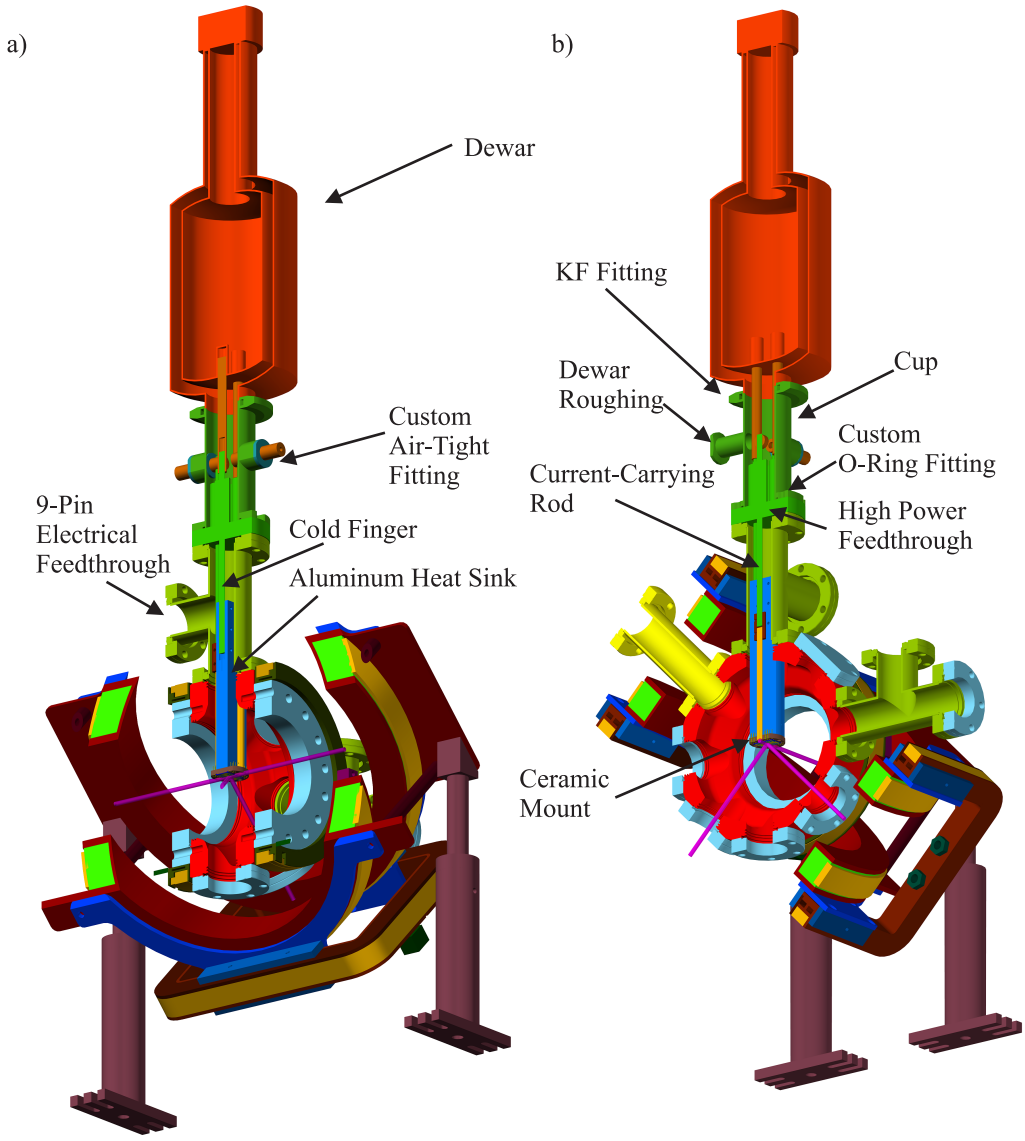

Figure 3.10: Sketch of the atom chip assembly mounted in the chamber. Two sections are shown: a section through a plane parallel to the MOT X-beam (a) and a section through a plane perpendicular to the MOT X-beam (b). The MOT beams are depicted in purple.

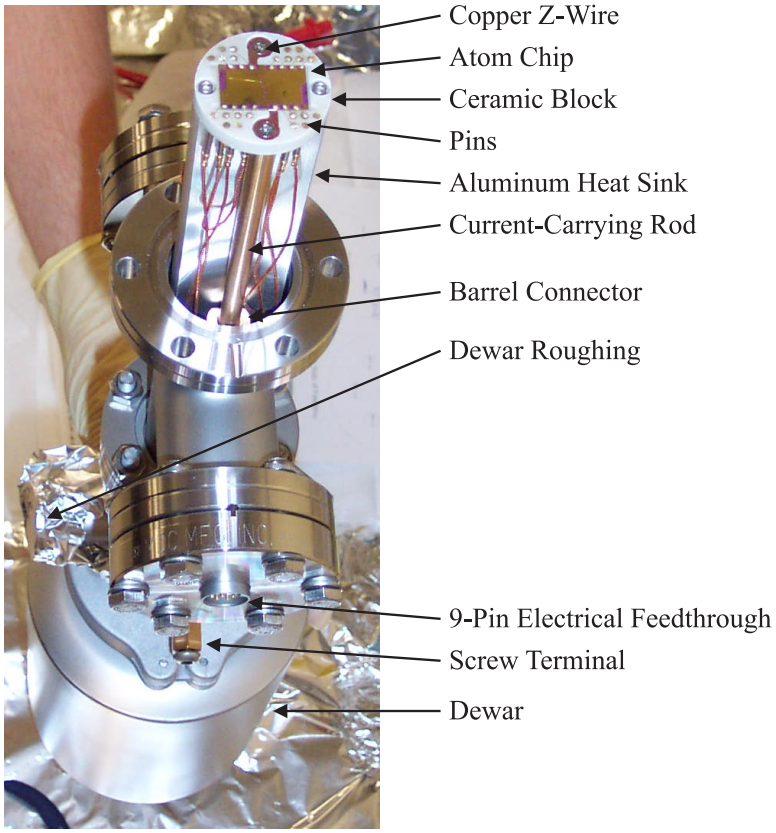

Figure 3.11: Photo of the atom chip assembly just before insertion into the vacuum chamber.

feedthrough, the two cold fingers reach into a home-made dewar mounted on top of the vacuum chamber. The dewar can be filled with LN_2, dry ice or ice water. The two other copper rods are connected to the current supply for the macroscopic z-wire (Agilent 6672A).

3.4.4 Chip mount

A close-up sketch of the chip mount on the Al heat sink is shown in Fig. 3.12. The chip is mounted on a small circular ceramic block (AlN) together with the copper z-wire and the pins used to make electrical connections to the chip. The ceramic block has a diameter of 1.3" and a thickness of 0.18". All parts are glued to the

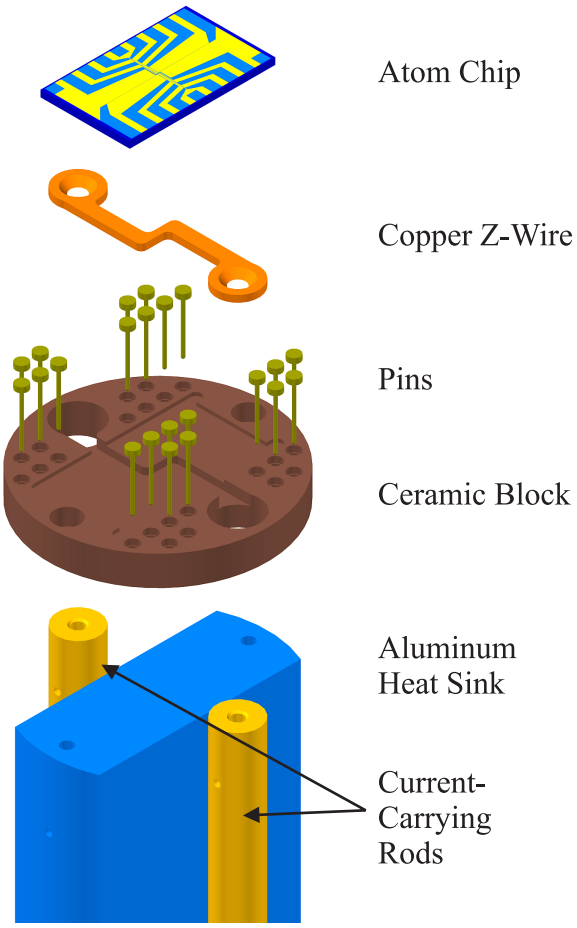

Figure 3.12: Sketch of the atom chip mount.

mount with UHV compatible nonconducting Epoxy (Epotek H77). Alunit (AlN) ceramic was chosen as the material for the mount because of its insulating qualities, high thermal conductivity, and UHV compatibility. The ceramic block has engraved keys for the copper wire and the chip, to ensure that they are mounted with good thermal contact to the AlN block and are aligned and positioned properly within the vacuum chamber. The pins are filed-down UHV compatible male sub-d type pins (Lesker FTADPEEK-M). The pins around the atom chip are connected on the back to Kapton-coated UHV compatible copper wires (MDC KAP2 22 AWG) equipped with female sockets (Lesker, FTADPEEK). The wires are connected to the outside world

via an electrical 9-pin type C instrumentation feedthrough (MDC 9152005) using the same female sockets. The connections to the contact pads on the chip from the front of the pins are made with 5 mil gold wire that is glued on with UHV silver epoxy (Epotek H20E-175). Two 0.25" diameter current-carrying copper rods are attached to the copper z-wire with two vented screws. The copper rods are connected with home-made barrel-connectors to the two copper rods of the high power electrical feedthrough that are used to supply current to the copper wire.

3.4.5 Heat sink

The AlN block is connected with two vented screws directly to the aluminum heat sink. The thermal conductance of the ceramic block is 32 $\mathrm{W\,K^{-1}}$. Fig. 3.13 shows a photo of the heat sink mounted onto the high power feedthrough. The heat sink has a saw cut on its back and two holes to slide it onto to the two copper rods of the high power electrical feedthrough that are used as cold fingers. Once it is slid onto the cold fingers, the saw cut is compressed from the side by six screws. This establishes firm thermal contact between the heat sink and the cold fingers and gives additional mechanical stability to the setup.

3.4.6 Dewar

The dewar, volume 1.2 l, is mounted via a KF fitting onto a specially designed cup that rests on top of the air side of the high power electrical feedthrough, as shown in Fig. 3.14. The cup has two custom air-tight fittings on the sides with screw terminal connections for the wires that connect to the current carrying rods. The cup mounts on top of the high power electrical feedthrough via a custom o-ring fitting. The dewar has two protruding female copper sockets that slide onto the two cold fingers and connect them to a copper plate in the bottom of the inner dewar wall. The

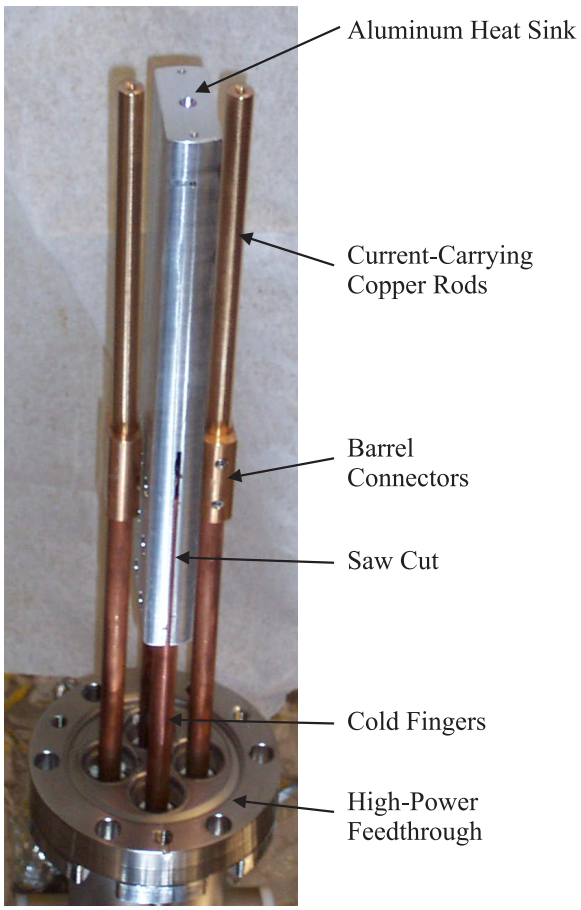

Figure 3.13: Photo of the aluminum heat sink.

dewar wall and cooling cup can be evacuated via a roughing connection on the front of the cooling cup. The pressure achieved in this volume by the mechanical pump is $< 10^{-3}$ Torr and insulates the dewar satisfactorily.

3.4.7 Electrical systems

The macroscopic copper z-wire requires currents in the range $30 - 60$ A to approximately mode match the magnetic trap to the MOT. The ultra-low noise z-wire current supply (Agilent 6672A, 20V 100A), in external programming mode, turned out to be too slow when switching the z-wire current off and on. The switching time was over 10 ms. In order to transfer atoms in and out of the copper z-trap without excessive

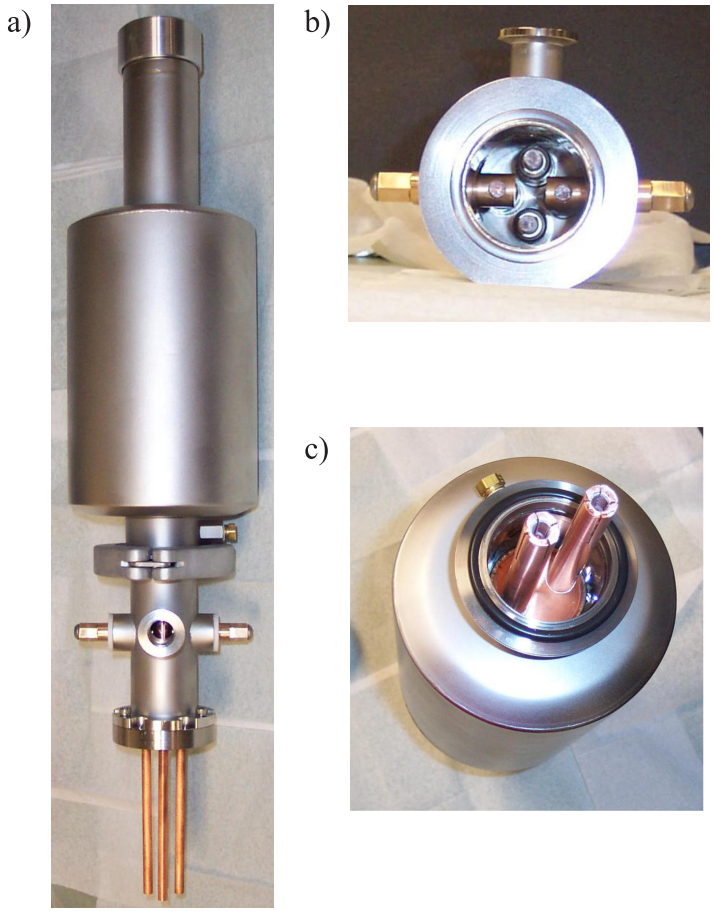

Figure 3.14: Photos of the cooling dewar and cup. Shown are a) dewar and cup mounted on high power electrical feedthrough, b) view into the cup from above when it is mounted on the high power electrical feedthrough, and c) bottom of dewar showing protruding sockets that slide onto cold fingers.

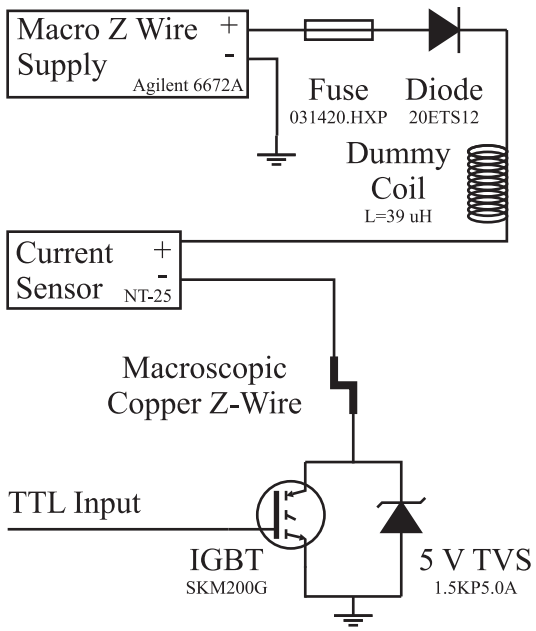

Figure 3.15: Simplified schematic of the macroscopic copper z-wire electrical system. The high power IGBT (1.2 kV, 125 A) switches the large currents in 2 μs, and a dummy coil slows down this switching to 234 μs (590 μs) for the off (on) switching when switching a current of 34.4 A.

losses, the switching time has to be on the order of a ms or less. The switching time should also be matched to the switching time of the bias coils. The electrical system used to accomplish this is shown in Fig. 3.15. The supply is operated in constant voltage mode. The voltage is chosen on the front-controls of the supply to match the desired copper z-wire current. The current can be verified with a magneto-resistive current sensor that is permanently present in the setup (Bell NT-25). An IGBT is used to switch the load on and off within 2 μs, and a dummy coil is used to slow down this switching time to $\sim 200 - 500$ μs to match the switching times of the bias coils.

The atom chip z-wire current supply is an ultrastable supply with a current range from -3 A to 3 A (High Finesse BCS3/12). It is controlled remotely in current

programming mode. In the microtrap, small fluctuations in current can cause large fluctuations in the trap center position which result in heating of the atoms. To ensure the most stable z-wire current, the programming voltage that enters the supply is isolated from the remote control system by an opto-coupler (HCNR200/01) to eliminate ground loops.

3.5 Rb sources

3.5.1 Rb dispensers

The chamber is filled with Rb by applying current to two of six Rb dispensers (SAES Getters Rb/NF/4.5/12/FT10+10) that are mounted close to the atom chip on an electrical feedthrough. The dispensers are trapezoidal metal containers with a slit that allows evaporation of Rb vapor. The containers have an active length of 12 mm and come pre-fitted with 1 cm long terminals on each side. The containers are filled with a Rb generating material, a mixture of Rb chromate and a reducing agent (St101 alloy Zr 84%-Al 16%). When the dispenser is resistively heated to a suitable temperature ($550 - 850$ °C) under vacuum, a reduction reaction is initiated between the chromate and the St101 alloy and free alkali metal is evaporated. At the same time, the St101 getter alloy also sorbs chemically active gases produced during the reduction, which keeps the Rb vapor pure.

3.5.2 Dispenser assembly

A picture of the dispenser assembly is shown in Fig. 3.16. The dispensers are mounted on a 6-pin alumel conductor electrical feedthrough (Lesker IFTAG065103) that is attached to one of the top diagonal ports on the chamber. The sides of each dispenser terminal are first clipped with scissors to make them fit into the previously flattened crimp side of a BeCu push/crimp connector (Lesker FTAPC062). The clipped termi-

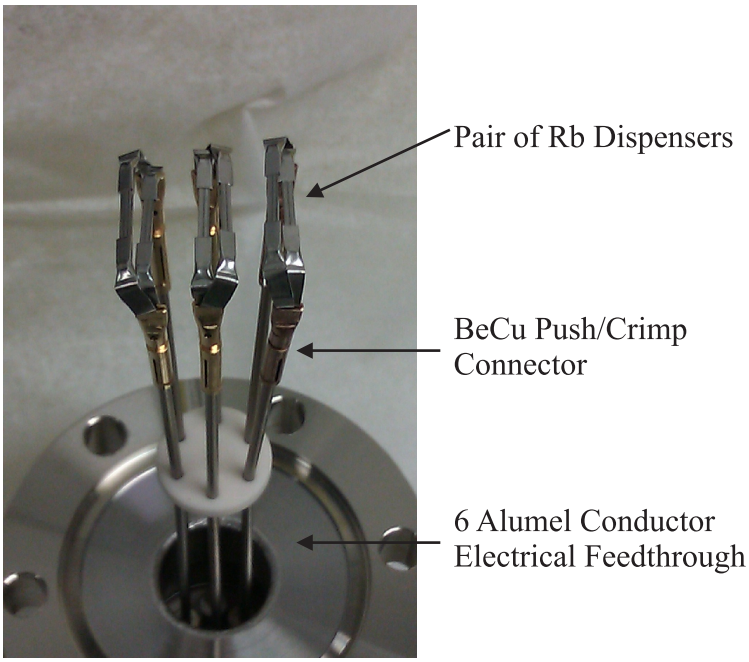

Figure 3.16: Photo of the source assembly prior to insertion into the chamber. Three pairs of sources are attached to the six alumel conductors of an electrical feedthrough. Each pair is connected in parallel with push/crimp BeCu connectors.

nals from two sources are inserted into the crimp side of one connector at the same time and crimped with needle-nose pliers. The sources are then attached with the push sides of the connectors onto the alumel conductors so that, upon insertion of the feedthrough into the chamber port, they point roughly into the chamber center with their long axis oriented parallel to the atom chip surface.

3.5.3 Dispenser operation

Before use, a pair of dispensers is activated under vacuum by applying five successive pulses of 20 A with a duration of 5 s per pulse. We leave enough time for the pressure to decrease back to $< 10^{-9}$ Torr between pulses. During the last two activation pulses, the fluorescence due to the cooling laser beams should be clearly visible in the chamber, which indicates successful source activation. Only one pair of sources is used at any

one time, and the next pair is activated only after the previous pair is completely emptied. During normal MOT operation, a pair of sources is run continuously at $\sim 5-6$ A current. The operating current is adjusted to give the desired Rb pressure of $\sim 2-8\times10^{-10}$ Torr. As the dispensers get older, the operating current usually has to be increased to reach the same pressure. These activation and operating parameters were determined empirically for our setup. We decided to use pairs of sources to increase the time between source replacement. A single source typically ran out of Rb after ~ 3 months of day to day use.

3.5.4 UV LIAD

Ultraviolet light-induced atom desorption (UV LIAD) is a method to control the alkali pressure in the vacuum chamber with faster response times than those obtained from sources that are based on resistive heating. UV LIAD is based on the principle that atoms which are adsorbed onto the walls of the vacuum chamber can be desorbed efficiently by irradiation with incoherent UV light. The process does not rely on heating of a source and subsequent slow cooling. The desorption rate instantaneously increases and decreases as the desorption light is switched on and off. UV LIAD has been systematically investigated and shown to lead to efficient loading of a Cs MOT in a quartz cell [120], and a dual-species ^{87}Rb$-^{40}$K MOT in a stainless steel chamber [121].

In Ref. [121], it was demonstrated that the number of atoms in the MOT loaded with LIAD depends linearly on the wavelength of the desorption light. The highest number was obtained at the lowest wavelength $\lambda = 400$ nm. In that experiment, the maximum atom number depended linearly on the intensity of the desorption light for intensities smaller than ~ 5 mW/cm^2 and started to saturate at larger intensities.

To obtain the largest intensities and lowest wavelengths, we use two 10 Watt UV

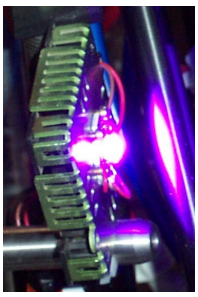

Figure 3.17: Photo of a mounted UV LED array used for UV LIAD.

LED arrays (LEDEngin LZ4-20UA10) centered at 400 nm to shine UV light at the chamber from both sides through the larger viewports. Each LED array is driven by a regulated LED driver (Buckpuck 3021-D-I-700) at 700 mA and can be switched on and off via TTL input. The LED arrays have to be actively cooled and are mounted on heat sinks with cooling fans. Fig. 3.17 shows a photo of a mounted LED array.

3.6 Magnetic field coils

3.6.1 Coil frame design

The design of the magnetic coils and coil frame had to fulfill a number of constraints. Eight magnetic field coils are needed for the operation of the experiment. The two anti-Helmholtz coils that generate the quadrupole magnetic field for the mirror MOT have to be at an angle of 45° with the atom chip surface, to ensure the correct circular polarization of the reflected beams. The quadrupole magnetic field gradient needed for the operation of the MOT is $\sim$ 10 G/cm [29] and has to be attainable with the MOT current supply (Sorensen 80-37, 80 V, 37 A). Six bias coils are needed to be able to generate homogenous offset fields of tens of Gauss in any direction while staying within the current and voltage range of the bias coil current supplies (Kepco BOP 20-20M, $\pm$20 V, $\pm$20 A). All coils have to fit around the main vacuum chamber without obstructing any of the viewports. It must be possible to move the MOT coils

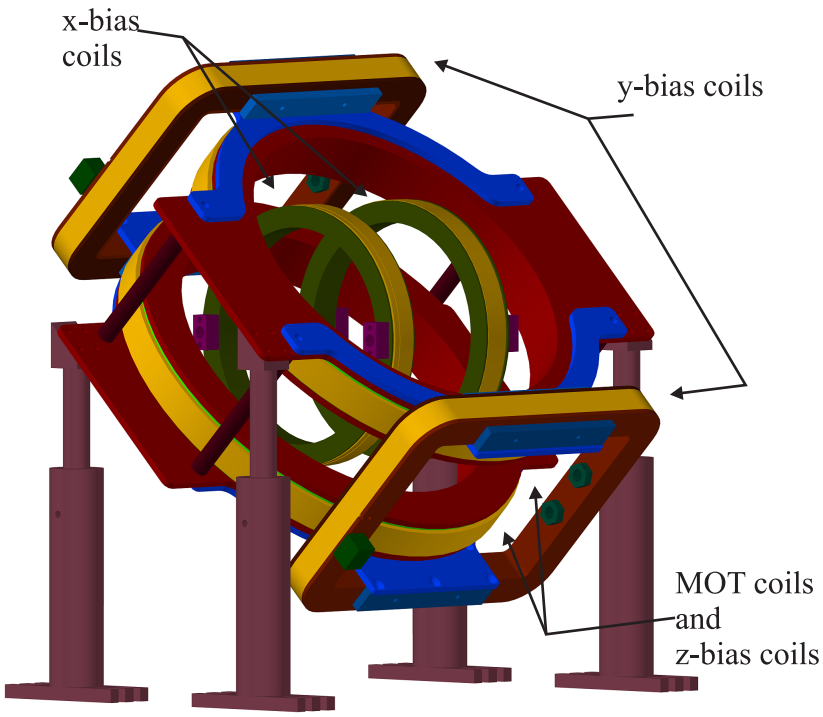

Figure 3.18: Sketch of the coil setup.

around the chamber freely within a few mm in each direction to rough-align the zero of the quadrupole field with the desired MOT location about 2 mm below the center of the atom chip surface.

Fig. 3.18 shows a sketch of the coil setup that meets the constraints. Each coil is wound on a shell machined from aluminum. A coil frame holds the MOT, y-bias and z-bias coils, while the x-bias coil shells slide onto the large viewports on each side of the vacuum chamber. The coil frame rests on the table via four feet consisting of stainless steel all thread posts in custom made aluminum post-holders and bases. Each threaded post is equipped with a leveling nut that determines the height of the post above the post-holder. The height of the coil frame can be adjusted by hand-turning the four leveling nuts to different heights. The coil frame can be positioned freely and is secured by clamping down the bases of the post-holders. The rectangular y=bias coils are mounted onto the MOT coil shells at a perpendicular angle. The

Table 3.1: Summary of coil parameters. The coil separation is measured between coil centers. ID: inner diameter.

Coil Pair	Inner Coil Size	Separation	Turns	R (Ω)	L (mH)	B-Field
MOT	10" ID	3.75"	100	0.58	10.4	n.a.
X-Bias	6" ID	3.45"	75	0.84	3.6	8.1 G/A
Y-Bias	8.9" × 6.9"	12.48"	72	1.26	3.2	1.6 G/A
Z-Bias	11.94" ID	3.75"	30	0.6	1.2	2.2 G/A

z-bias coils are wound on top of the MOT coils.

Each coil shell is water cooled. The bias coil shells are cooled by pumping water through water channels on the inside walls of the shell. The MOT coils are water cooled via rectangular cooling blocks attached to the outside of the coil shells. In order to fit within the limited space around the chamber, the radius-to-distance ratio of the MOT coil pair is 1.3, which deviates from the ideal ratio of 1.0 for anti-Helmholtz configuration. This deviation affects the slopes of the quadrupole field: the ratio of axial vs. radial slope becomes 2.1 instead of the ideal 2. However, this is easily compensated for by adjusting the power balance of the MOT beams and does not hinder operation of the MOT. The parameters of the coils are summarized in Table 3.1.

All the coils are pre-wound onto their shells. After the coils are wound, the coil setup is assembled around the chamber in the following steps:

- The two x-bias coils are slid onto the large viewports.
- The top MOT coil shell is positioned around the chamber and the two back feet of the coil frame are attached to the "ears" on the MOT coil shell.
- The bottom MOT coil is positioned around the chamber and the two front feet

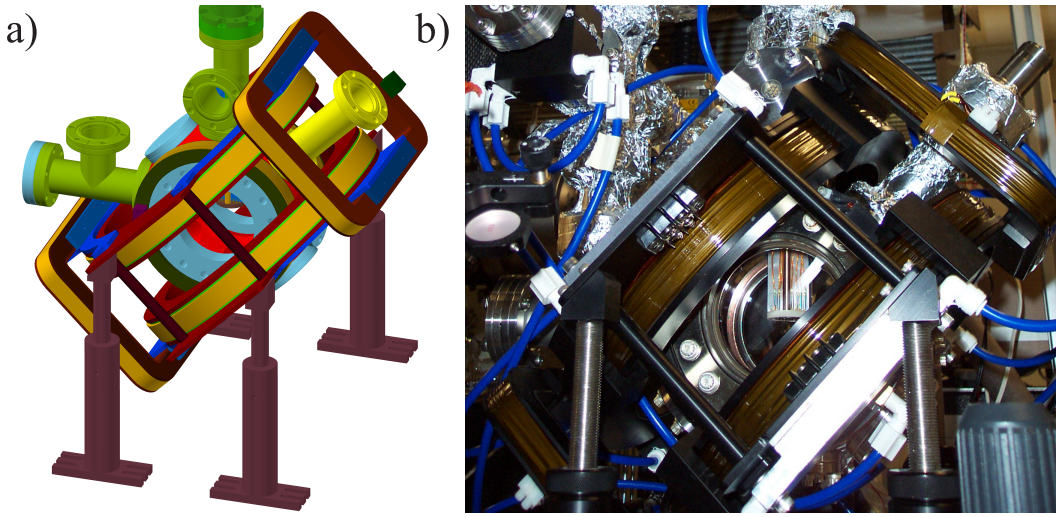

Figure 3.19: Sketch (a) and photo (b) of the coil setup assembled around the chamber.

are attached to it.

- The bottom MOT coil is connected to the top MOT coil with four aluminum cylinders that also hold the mounting brackets for the y-bias coils and the water cooling blocks.

- The rectangular y-bias coils are clamped onto the MOT coils via their mounting brackets and set screws.

- Water and electrical connections are made. Each coil shell is equipped with terminal blocks to allow for easy electrical connections.

A sketch and photo of the assembled coil setup is shown in Fig. 3.19.

3.6.2 Coil electrical setup

The MOT coils are powered by a 80 V, 37 A power supply (Sorensen DCS80-37) in current programming mode. The MOT coils are run at a current of 30 A, corresponding to an axial field gradient of 14 G/cm and a radial gradient of 7 G/cm at the center between the coils.

The bias coils are powered by a set of four ± 20 V, ± 20 A bipolar current supplies (Kepco BOP20-20), also in external current programming mode. The bias coil currents are set initially to position the MOT below the exact center of the atom chip. During loading of the magnetic traps, bias coil currents are then switched and ramped to values that maximize the atom number in each of the magnetic traps.

3.6.3 MOT coil switching circuit

In order to transfer atoms most effectively from the MOT into the macroscopic z-wire trap, the MOT has to be switched off in less than a ms. Due to the large inductance of the MOT coils, the current does not switch off fast enough without added circuitry. The measured switching times for the MOT when using the remote programming without extra switching circuitry was ~ 20 ms.

Fig. 3.20 shows the circuit employed to switch the MOT coils off fast. The circuit is based on Alan Stummler's "Mag-O-Matic" design [122]. A high power insulated gate bipolar transistor (IGBT, Semikron 200G125, 1.2 kV, 125 A) is connected in series with the coil return. It is bypassed to ground by a series of reverse transient voltage suppression diodes. The IGBT gate is driven by a commercial IGBT driver (SKHI 10/12 (R)) which is controlled via a TTL input. When the IGBT is in conducting mode, the voltage across it is a few volts and the TVS diodes are not conducting. When the IGBT is switched into non-conducting mode, the back-emf becomes equal to the breakdown voltage of the TVS array, at which point the diodes start conducting. The current in the coils decreases quickly according

$$\frac{dI}{dt} = -\frac{V_{\mathrm{Z}}}{L}, \tag{3.1}$$

where V_{Z} is the breakdown voltage of the TVS array. The switching time can be adjusted by adjusting the number of TVS diodes. The fastest switching is obtained when V_{Z} is just below the maximum IGBT voltage. A back-emf larger than the IGBT

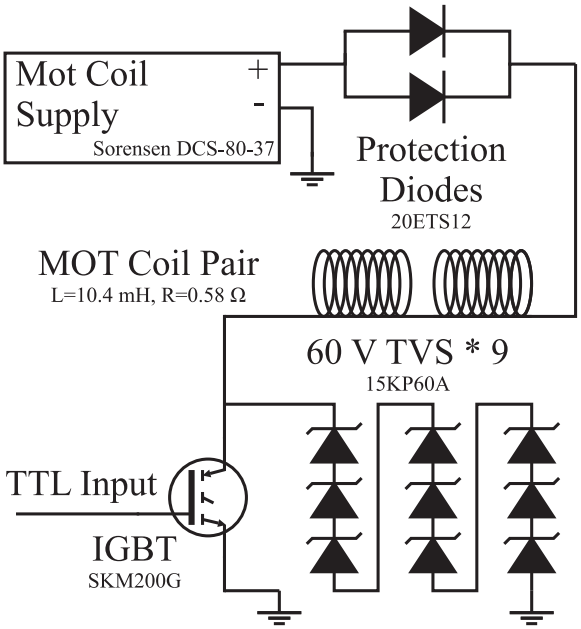

Figure 3.20: MOT coil switching circuit. The circuit switches the MOT coils off in 450 μs. It is based on a high power IGBT and a series of high power transient voltage suppressing diodes. When the IGBT opens, the coil current decreases according to $\dot{I} = -V_{\rm Z}/L$, where $V_{\rm Z}$ is the breakdown voltage of the diode array. The IGBT gate driving circuit is not shown.

voltage rating would destroy the IGBT. For the MOT coil circuit, $V_{\rm Z} \approx 9 \times 60$ V and the switching time of the MOT coils is ~ 450 μs.

3.6.4 Bias coil switching circuits

The x-bias coils have to be switched on fast to effectively load atoms from the MOT into the magnetic trap. Due to the large inductance of the bias coils, switching the bias coils with the current programming of the power supplies took $5-10$ milliseconds. The slow switching of the x-bias field was one of the main causes of low atom numbers $N < 10^6$ in initial experiments.

Fig. 3.21 shows the circuit employed to switch the x-bias coils. The circuit provides us with fast on switching and fast off switching capability in times < 500 μs. It can

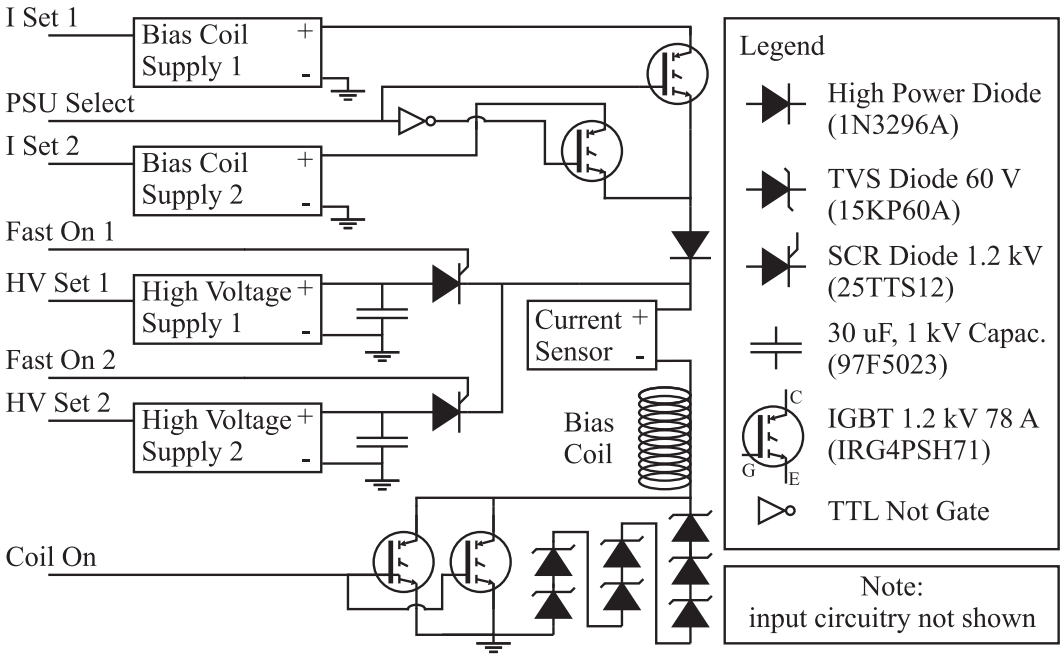

Figure 3.21: X-bias coil switching circuit. The circuit switches the bias coil pair quickly on and off. It also allows to quickly switch between current values. Fast on switching is done by discharging a high voltage capacitor into the coils. The capacitor is discharged by applying a pulse to the silicon-controlled rectifier diode (SCR). Fast off switching is done through IGBTs and TVS diodes. Switching between currents is done by switching between two capacitors and two different power supplies.

also be used to switch between two different currents at similar speeds.

High voltage capacitors are pre-charged with high voltage supplies (Pico Elec. 15VV1) to voltages depending on the desired coil currents, usually between $100 - 300$ V. The pre-charge voltage is set by the analog "HVset" inputs, where 1 V on the input results in 100 V pre-charge. In order to switch the coils on fast, a silicon controlled rectifier diode (SCR) is switched into conduction mode with a short positive voltage pulse of duration < 1 ms, the "FastOn" TTL input. This connects the pre-charged capacitor to the positive side of the coil pair. The capacitor discharges into the coil quickly as part of the newly formed LC circuit. When the coil current reaches

its maximum, the voltage is at zero and the SCR stops conducting. The regular coil power supply (Kepco BOP20-20M) is now connected to the circuit through a diode. The diode only started conducting when the voltage at the positive end of the coil decreased below the diode drop. The power supply is now supplying all the current, and the capacitor can be re-charged.

In the circuit for the x-bias coils, two capacitors can be separately charged to different voltages and separately discharged into the coils. This enables us to preset two different currents and quickly switch between them. In addition, two power supplies can be connected to the circuit. The desired supply can be selected remotely through an IGBT based high power switch. We found that the Kepco power supply output current behaved erratically when a single supply was quickly switched between different currents on timescales of 100 μs, probably due to internal filter capacitors that were not discharging fast enough. To overcome this problem, we switch to a different Kepco supply that has been idle for seconds before discharging the second capacitor. In this circuit, IGBTs and TVS arrays are present on the return side of the coils. They are used to switch the coils off quickly.

The y- and z-bias coils are equipped with similar switching circuits. However, the y- and z-bias circuits only contain one capacitor and have no PSU switching capability.

The switching circuits described here are unipolar while the Kepco power supplies are bipolar. It turned out that we had to apply negative currents to the y-bias coils to move the MOT position into best overlap with the magnetic trap. During the loading of the magnetic trap, a small positive y-bias was needed to increase the mode matching between the z-trap and the MOT and obtain the largest atom numbers. To switch the y-bias coils between positive and negative currents within hundreds of μs, while still keeping all the functionality of the capacitor-based fast switching circuit,

we built the IGBT solid state crossover relay (SSR) circuit shown in Fig. 3.22. We use the SSR to change the coil polarity in such a way that the previously described capacitor switching circuit still works. During the short switching period of the relay of a few μs, the current through the coil has to be zero to prevent back-emf in the SSR that can potentially destroy the transistors.

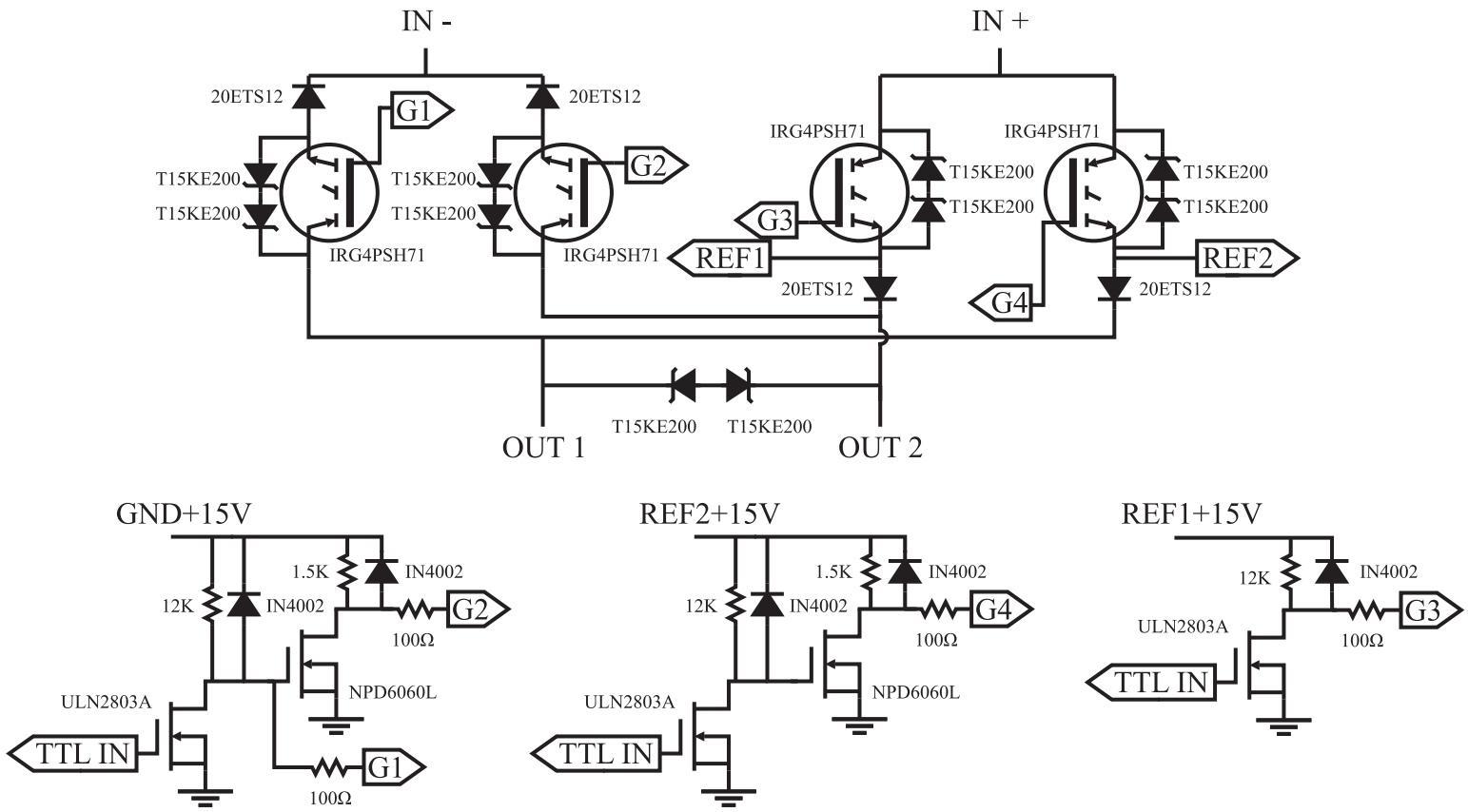

Figure 3.22: Solid state crossover relay used to switch current direction on the y-bias coil. Depending on a TTL control signal, either input "+" is connected to output 1 and input "-" to output 2, or the connections are flipped so that input "+" is connected to output 2 and input "-" to output 1. With this relay, the unipolar fast switching circuitry can be used with arbitrary coil current directions. The relay requires three 15 V DC power supplies, two of which are floating to different (small) voltages during operation. We use cheap off-the-shelf regulated brick supplies for this purpose.

3.7 Rydberg excitation laser

3.7.1 Second-harmonic generation

The Rydberg excitation laser is a homebuilt 480 nm second-harmonic generation (SHG) system locked to a Fabry-Perot reference cavity (CVI OSA300-12). Fig. 3.23 shows a schematic of our SHG setup, consisting of ECDL, tapered amplifier (TA), and 1 cm long periodically poled lithium niobate waveguide crystal (PPLN) [123, 124]. The ECDL is a homebuilt laser similar to the one shown in Ref. [125]. We use a

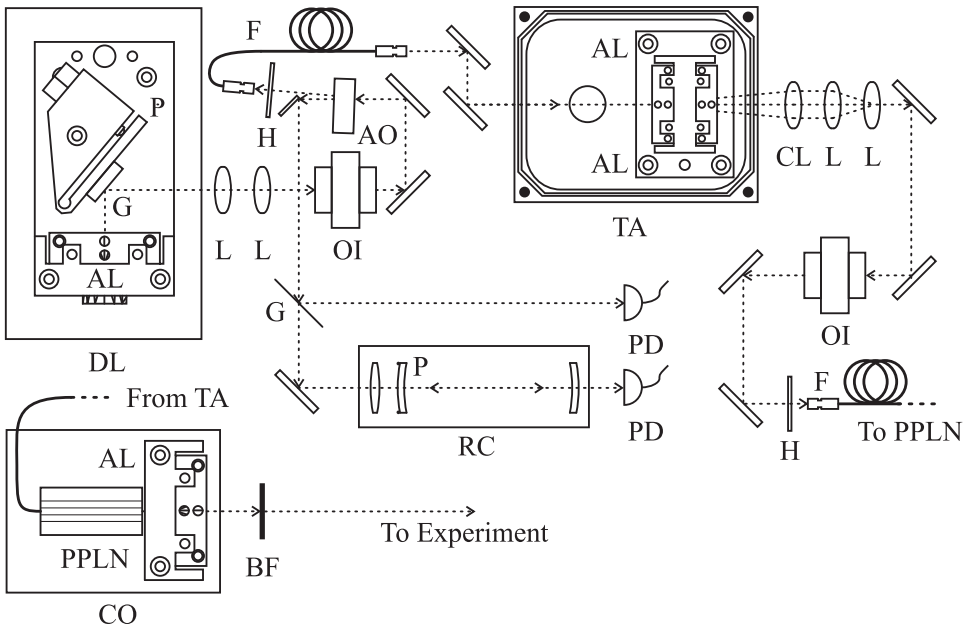

Figure 3.23: Second-Harmonic-Generation system for Rydberg excitation. Following the light path, the labels are DL: external-cavity diode laser, AL: aspheric lens, G: grating, P: piezo-electric transducer, L: spherical lens, OI: optical isolator, AO: accousto-optic modulator, H: half-wave plate, F: polarization-maintaining single-mode optical fiber, TA: tapered amplifier, CL: cylindrical lens, PPLN: periodically poled lithium-niobate waveguide crystal, CO: crystal oven, BF: bandpass filter, G: glass slide, RC: reference cavity, PD: photodiode.

100 mW, 960 nm Fabry-Perot laser diode (QPhotonics QLD-960-100S). The diode is powered by a combined low noise current supply/temperature controller (Wavelength Electronics LDTC0520) and thermally stabilized with a Peltier element. After initial collimation with an asphere (Thorlabs C230TME-B) and a pair of convex lenses ($f =$ 50 and $f = 125$ mm, B-coated), the output light from the ECDL passes through an optical isolator (OFR IO-3C-960-VLP) which keeps back-reflections from entering the laser. After the isolator, the light passes through an accousto-optic modulator (AOM, Isomet 1205C-1) to filter out any amplified spontaneous emission coming back from the input facet of the tapered amplifier. The first order from the AOM is used as the main light beam, to be amplified and frequency-doubled. After the AOM, the main light beam is coupled into a polarization-maintaining fiber to increase the transverse mode quality. A half-wave plate is used to align the polarization with the fiber input facet. After exiting the fiber, the light is coupled into a tapered amplifier (m2k TA-0950-1500-CM) with an aspheric lens (Thorlabs C330TME-B), and amplified. The amplified light, which is highly astigmatic, is re-collimated with another asphere (Thorlabs C330TME-B) and a cylindrical lens ($f = 50$ mm, B-coated). Two spherical lenses ($f = 125$ mm, B-coated and $f = 50$ mm, B-coated) down-collimate the light to couple it into another optical isolator (OFR IO-3-960-HP). This optical isolator prevents back-reflections from the crystal input facet from entering the amplifier. The light is then coupled via a fiber pigtail into the 1 cm PPLN waveguide crystal (HCPhotonics). The waveguide crystal doubles the frequency, generating light at a wavelength of 480 nm. The crystal is seated in an oven and heated to the phase-matching temperature of 92 °C. After collimation with an asphere (C330TME-A) and passing through a bandpass filter (Thorlabs FGB37) that filters out residual IR light, the light is ready to be used for experiments. The zeroth order of the first AOM serves as reference beam. It is split into two beams with a glass slide. One part

passes through the slide and is coupled into the Fabry-Perot cavity. The other part is reflected by the slide, acquired with a photodiode, and serves as amplitude reference. The intensity of the fringe pattern at the output of the cavity is also measured with a photodiode. The intensity reference signal is then subtracted from the cavity signal to give an output signal that is linear in frequency and centered around 0 volts. We tune the cavity so that the 0 volt point is located in the center of the rising edge of a cavity transmission peak (side-of-fringe locking).

3.7.2 Rydberg laser locking circuit

To lock the frequency of the Rydberg excitation laser, we implemented a digital locking circuit on a field-programmable gate array (FPGA). Our FPGA lockbox takes the cavity signal as input and outputs the necessary feedback voltages to both piezo and diode current to keep the frequency of the ECDL constant. We use a commercially available, inexpensive FPGA board (Digilent Nexys 2). The gains of the feedback loops can be controlled through a user interface running on an attached computer. Our FPGA-based lockbox is described in detail in Appendix A. From the rms value of the cavity signal, we estimate blue laser linewidths of < 1 MHz when locked to the side of the cavity fringe.

3.8 Microwaves

3.8.1 Waveguide assembly

To excite transitions between nearby Rydberg states in 4-level ladder-type EIT experiments, we use microwave radiation. Our RF source is a HP8340B synthesized sweeper that is tunable between 10 MHz and 26.5 GHz with output power up to 10 mW. We chose the K-band frequency range of 12.4-18.0 GHz to excite Rydberg to Rydberg transitions around $n = 55$ for Rb and around $n = 60$ for Cs. This range of n are

states that we can reach easily with our Rydberg excitation SHG laser system. The output of the microwave generator is connected to an isolator (Sierra Tech. I1118) via SMA to prevent back-reflections from entering the source. The isolator is connected via SMA cable to a WR-62 waveguide adapter. The adapter is followed by a 50% waveguide directional coupler (HP P752A). One output of the directional coupler is connected to a crystal detector (HP P424A) that can be used to monitor the microwave power. The other end of the directional coupler is connected to a horn antenna (Sperry AT-157/U) which is used to aim the microwaves at the atoms.

3.9 Imaging system

3.9.1 Imaging setup

The absorption image of the atom cloud is recorded with a monochrome cooled CCD camera (Apogee Alta U32). The camera has 2184×1472 square pixels of size 6.8 μm$\times$ 6.8 μm each, with an analog-to-digital conversion resolution of 16-bit per pixel. It is connected to the computer via USB.

The CCD camera has a mode called kinetics mode, in which multiple images can be acquired in rapid succession at the cost of active CCD area. In kinetics mode, a part of the CCD is blocked by an aperture and functions as storage area for the electrons accumulated during previous exposures. Due to technical limitations, the electrons can only be shifted vertically so that the blocked area has to fill the whole horizontal range of the CCD. When taking a series of n rapid images in kinetics mode the vertical size of the blocked area must be a fraction (n-1)/n of the full CCD array vertical size, so that the vertical size of the active area shrinks to 1/n of the full vertical CCD size.

On receipt of a camera trigger, in kinetics mode, the CCD is exposed for the first time but no read-out takes place afterwards. Instead of a readout, the electrons are

moved vertically into to the dark part of the CCD array. Following images move the sequence further down the array until the whole array is filled with a sequence of time-delayed images, the latest at the top and the earliest at the bottom. After the last image in such a series has been exposed, the full CCD is readout.

The imaging beam is collimated to a FWHM of 5 mm and aligned along the longitudinal axis of the z-wire center segment. The imaging polarization is controlled with a quarter-wave plate and changed to circular polarization before it enters the chamber. After exiting the chamber, the imaging beam is up-collimated by imaging optics, which consist of two positive lenses ($f = 75$ mm and $f = 125$ mm). It then passes through a 780 nm IR interference filter before hitting the bare CCD array of the camera. Due to the imaging optics, the absorption image on the CCD is 1.67 times larger than the real cloud. When analyzing images, this is taken into account by using an effective pixel size of 4.08 μm $\times$ 4.08 μm.

Two additional cameras are used to capture the fluorescence of the mirror MOT in realtime. The camera feeds are displayed on a TV screen to position and peak up the MOT. One camera (Edmund Optics NT56-580) looks at the MOT from below through a turning mirror and a home-made telescope made of two positive lenses ($f = 175$ mm and $f = 50$ mm). The lenses were chosen so that the atom chip fills up the full TV screen and the MOT is displayed large enough to discern small displacements or asymmetries in the MOT shape. The other camera (Watec WAT902H-Ultimate) looks at the MOT from the side at an angle of $\sim 80^\circ$ to the imaging beam through a commercial adjustable zoom lens (Canon $18 - 108$ mm f2.5 Zoom Lens).

All cameras are equipped with 780 nm interference filters.

3.9.2 Absorption imaging

To derive the optical density and atom number from absorption imaging, three images are needed. The first image is a dark image I_{dark}, taken without any imaging light. Because of the IR filter in front of the camera, only stray light with a wavelength of 780 ± 2 nm contributes to the dark image. The dark image is taken once in the morning and re-taken after any change to the setup or switching sequence that results in a change of stray light hitting the CCD. The second image is the absorption image itself I_{abs}, an image taken with the imaging light and the atoms present. The third image is the background image I_{bg}, an image with imaging light present but without the atoms. Using the camera's kinetics mode, we acquire I_{bg} at a delay of 100 ms from I_{abs} with a single camera trigger.

For intensities below saturation of the atomic transition, the intensity distribution after absorption is given by the Beer-Lambert law

$$I(x, y) = I_0(x, y)\, e^{-D(x,y)}, \tag{3.2}$$

here $I_0(x, y)$ is the initial intensity of the imaging beam, and D is the optical density,

$$D(x, y) = \sigma \int n(x, y, z)\, dz = \sigma\, \tilde{n}(x, y), \tag{3.3}$$

where n is the number density, $\tilde{n}$ is the column number density, and σ is the absorption cross section for the given polarization of imaging light.

The optical density is obtained directly from the camera images through Eq. 3.2.

$$D(x, y) = -\ln\left(\frac{I(x, y)}{I_0(x, y)}\right) = \ln\left(\frac{I_{\mathrm{bg}}(x, y) - I_{\mathrm{dark}}(x, y)}{I_{\mathrm{abs}}(x, y) - I_{\mathrm{dark}}(x, y)}\right), \tag{3.4}$$

as long as the intensity incident on the camera is low enough to not saturate the camera pixels and the imaging beam intensity is below the saturation intensity of the optical transition. The atom number can be obtained by summing over the pixels

and dividing by σ

$$N = \frac{1}{\sigma} \int D(x,y)\, dx\, dy = \frac{1}{\sigma} \sum_{i,j} D(x_i, y_i)\ \Delta_x\ \Delta_y, \tag{3.5}$$

where Δ_x and Δ_y are the horizontal and vertical pixel sizes. The atom cloud usually has a Gaussian distribution, and we can alternatively use a 2-dimensional Gaussian fit function to obtain the FWHM of the density distribution in the x and y directions, FWHM_x and FWHM_y, as well as the peak optical density at the center, D_{peak},

$$f(x,y) = b + D_{\mathrm{peak}}\ \exp\left(-\frac{(x-x_0)^2}{2\sigma_x^2}\right) \exp\left(-\frac{(y-y_0)^2}{2\sigma_y^2}\right), \tag{3.6}$$

where

$$\sigma_{x,y} = \frac{\mathrm{FWHM}_{x,y}}{2\sqrt{2\ln(2)}}. \tag{3.7}$$

Due to the 2D fitting procedure which takes all pixel values into account, this gives an estimate of the atom number that is less affected by imaging noise,

$$N = \frac{D_{\mathrm{peak}}}{\sigma}\, \frac{\pi}{\ln(16)}\, \mathrm{FWHM}_x\ \mathrm{FWHM}_y. \tag{3.8}$$

An automatic 2D Gaussian fit routine was implemented in Mathematica, and used to fit all the images presented in this thesis.

3.9.3 Imaging software

To acquire absorption images with the Apogee camera in kinetics mode, we programmed our own image acquisition software in C++. A screenshot of the user interface is shown in Fig. 3.24. The software uses the camera's kinetics mode to acquire images and automatically calculates the optical density from Eq. 3.2 within a specified region of interest. The calculation is done for every shot, using the full 16-bit dynamic resolution of the camera. The result is displayed in a color scheme of choice, and can be output to ASCII files at 16-bit resolution or BMP files at 8-bit resolution. The mapping of pixel values to brightness values on the screen can be

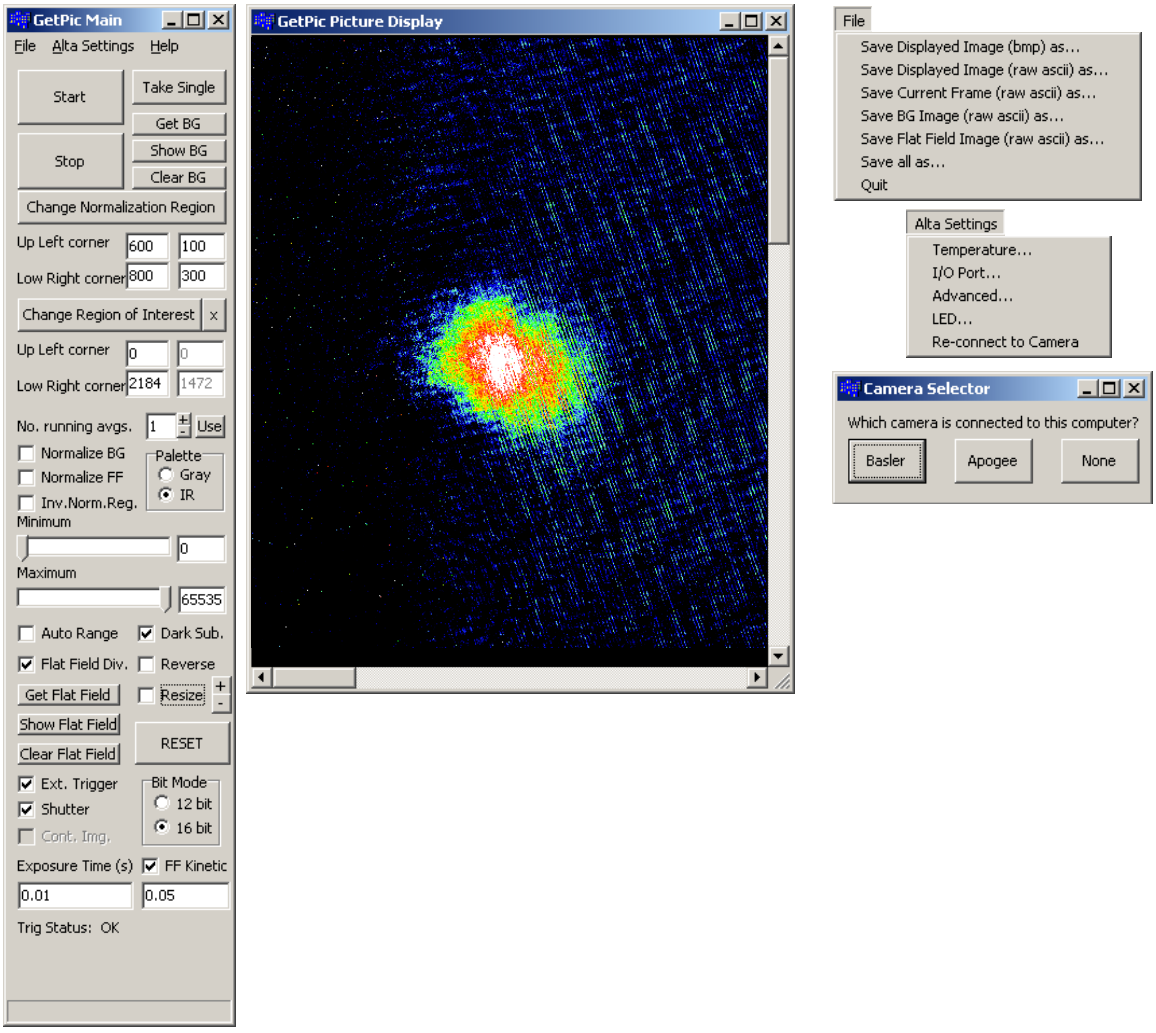

Figure 3.24: User interface of the imaging software written in C++.

adjusted to display different subsets of the full dynamic range. Automatic acquisition of running averages is also supported, as are automatic or manual normalization of background images.

3.9.4 Fluorescence imaging

We also use fluorescence imaging as a way to estimate the atom number in the MOT [126]. In this technique, the fluorescence light from the MOT is collected with a lens, and focussed on a calibrated photodetector while the MOT is on. The background

light power without any atoms in the MOT is also measured and subtracted from each measurement. The power measured with the detector is related to the total fluorescence power radiated by the MOT via

$$P_{\text{tot}} = \frac{\alpha}{\beta} P_{\text{det}}, \tag{3.9}$$

where P_{det} is the light power measured with the detector, α is a geometric factor relating the fraction of light collected by the lens to the total amount of light power emitted by the MOT in all directions, and β is a loss factor due to the losses at interfaces. α is given by

$$\alpha = \frac{4\pi a^2}{\pi r^2}, \tag{3.10}$$

where a is the distance from the MOT to the center of the lens, and r is the radius of the lens. In our measurements, the lens is a 1" optic (focal length $f = 50$ cm), $r = 12.7$ mm, positioned just outside one of the small viewports of the chamber, $a = 11.66$ cm. β is the product of the transmittance of each interface that the fluorescence light passes. In our case the Kodial glass chamber window has a transmittance of 92% at $\lambda = 780$ nm and the two glass air interfaces on the lens have a 4% loss per surface, so $\beta = 0.92 \times 0.96 \times 0.96$. The atom number is deduced from P_{tot} via

$$N = \frac{P_{\text{tot}}}{P_{\text{single}}}, \tag{3.11}$$

where P_{single} is the fluorescence power emitted by a single atom, given as the product of photon energy and emission rate

$$P_{\text{single}} = \frac{\hbar}{\omega_l} \frac{\Gamma}{2} \frac{I_{\text{tot}}/I_s}{1 + I_{\text{tot}}/I_s + (2\,\delta/\Gamma)^2}, \tag{3.12}$$

where I_s is the saturation intensity of the cooling transition, Γ is the spontaneous decay rate of the excited state, ω_l is the laser frequency, δ is the detuning of the cooling laser, and I_{tot} is the average intensity at the MOT. The average intensity can

be calculated from the beam powers and waists via

$$I_{\text{tot}} = 2\left(\frac{P_x}{\pi\,\omega_{xx}\,\omega_{xy}} + \frac{P_y}{\pi\,\omega_{yx}\,\omega_{yy}} + \frac{P_z}{\pi\,\omega_{zx}\,\omega_{zy}}\right). \tag{3.13}$$

Here, ω_{ij} is the waist of beam i along the direction j. For example, in our case, $P_x = P_y = P_z = 4$ mW and $\omega_{ij} = \text{FWHM} \times \left(\sqrt{2\ln(2)}\right)^{-1}$, where the full width at half maximum FWHM = 10 mm for each beam in each direction (the beams are Gaussian and approximately circular when they enter the chamber).

3.10 Control system

3.10.1 NI-DAQ board setup

The experiment is remotely controlled from a desktop PC running Windows XP. Two DAQ boards from National Instruments, an NI6254 with 32 digital output channels and an NI6723 with 32 analog output channels, are used to generate analog and digital control sequences with 10 μs temporal resolution at a low repetition rate of 0.1 Hz. The internal clock of the NI6254 is used as 100 kHz master sample clock for both boards.

3.10.2 DAQ control software

The DAQ boards are controlled through a pulse sequencer program written in C++. The program allows for easy configuration of digital pulses with negative or positive polarity, digital bursts of arbitrary length, an arbitrary number of voltage events per analog channel and an arbitrary number of linear ramps per analog channel. In addition, any channel can be modulated at arbitrary frequency and user-selected duty cycle, the repetition rate of the pulse sequence can be chosen, and specific configurations can be saved and later recalled. Screenshots of the user interface are shown in Fig. 3.25.

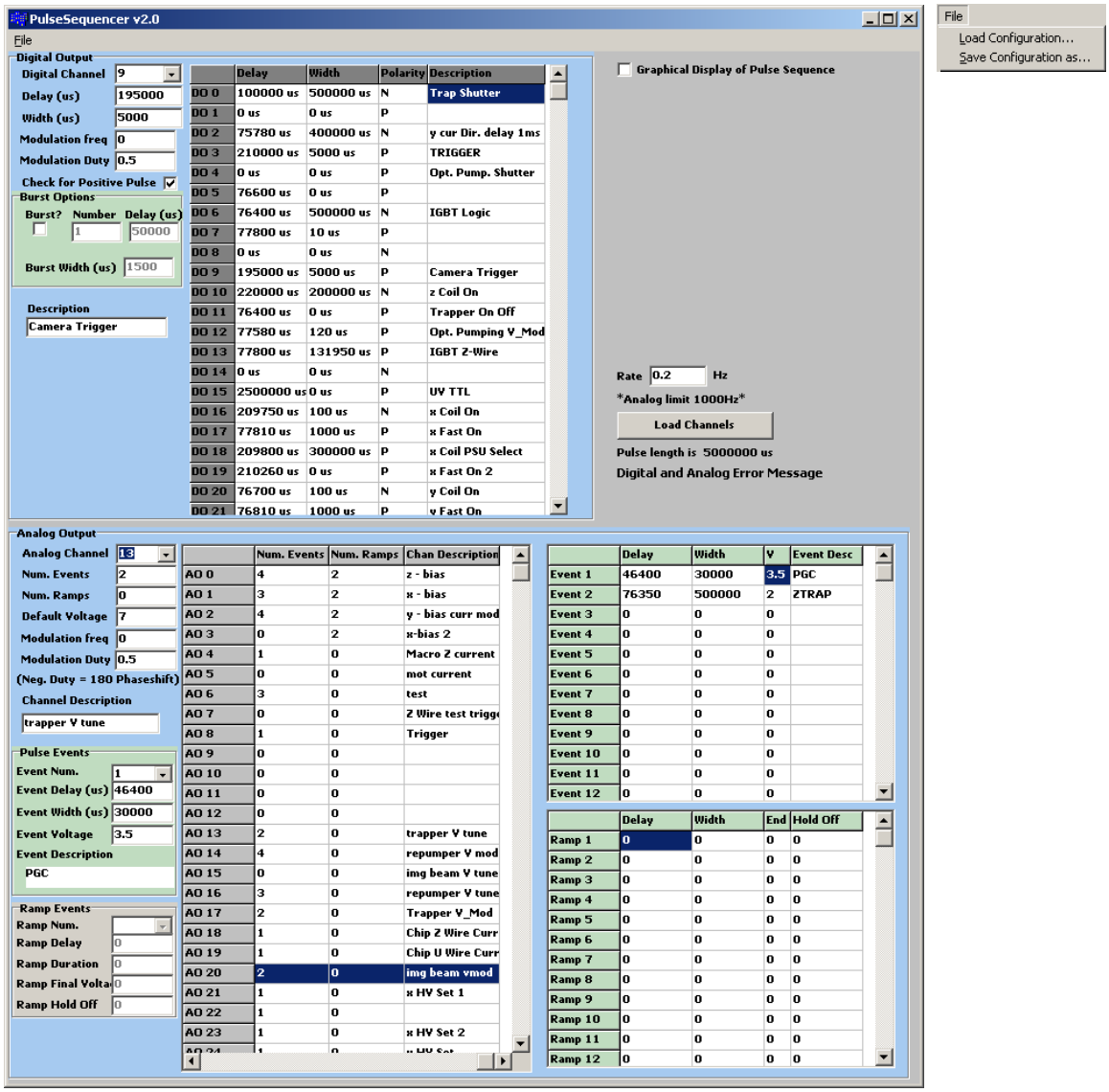

Figure 3.25: User interface of the pulse sequencing software written in C++.

3.10.3 Channel configuration

Table 3.2 and Table 3.3 summarize the channels used in the experiment. The analog channel voltage range is -10 V to 10 V. In order to gain a fine-grained control over the beam powers, the imaging and MOT beam AOM amplitude signals pass through an OP27-based amplifier with a gain of 1/7. The imaging beam AOM frequency signal passes through a 10 Hz low-pass filter to minimize intensity fluctuations.

When updating channel parameters, the re-configuration of all channels on both boards takes longer than a second. During this time, the boards hold all channels at their last voltage values, which depend on the exact time the user initiated the re-configuration and are unpredictable. To prevent these unpredictable voltages and hold times, all channels are first quickly set to zero before the full new channel buffers are re-written to the board. This is done by re-configuring the boards to a repeating sequence consisting of 1 sample of zero voltage per channel before writing the full new sequence to the boards.

Even with this precaution in place, the y-bias current direction SSR could still be switched while there is some current running through the y bias coil, which would destroy the relay. To prevent this situation, the y-bias current direction signal passes through an FPGA based digital delay circuit that delays the signal by 1 ms. This ensures that during a reconfiguration, the SSR input is switched to zero only after all other channels have already been set to zero.

Table 3.2: Digital channels used to remotely control the experiment. The operational definition column describes the effect of setting the digital channel to high. OP: optical pumping.

Usage	Channel	Operational Definition
MOT Shutter	DO0	Close MOT beam shutter
Camera Trigger	DO9	Initiate camera exposure
OP Shutter	DO4	Close OP Shutter
OP AOM Amplitude	DO12	Turn on OP beam
UV LIAD LEDs	DO15	Turn off UV LEDs
MOT IGBT	DO6	Turn on MOT coil current
Copper Z IGBT	DO13	Turn on copper z-wire current
X-Bias IGBT	DO16	Turn on x-bias coil current
X-Bias Fast On 1	DO17	Discharge capacitor 1 into x-bias coils
X-Bias Fast On 2	DO19	Discharge capacitor 2 into x-bias coils
X-Bias PSU Select	DO18	Select second x-bias coil PSU
Y-Bias IGBT	DO20	Turn on y-bias current
Y-Bias Fast On	DO21	Discharge capacitor into y-bias coils
Y-Bias Direction	DO2	Select negative current on y-bias coils
Z-Bias IGBT	DO10	Turn on z-bias coil current
Z-Bias Fast On	DO22	Discharge capacitor into z-bias coils

Table 3.3: Analog channels used to remotely control the experiment. The operational definition column describes the quantitative effect of the voltage output, V_c, of each channel.

Usage	Channel	Operational Definition
MOT Coil Current	AO5	$I = 7.4$ A/V V_c
X-Bias Current PSU 1	AO1	$I = -0.667$ A/V V_c
X-Bias HV Set 1	AO21	$V \approx 100$ V_c
X-Bias Current PSU 2	AO3	$I = -2$ A/V V_c
X-Bias HV Set for PSU 2	AO22	$V \approx 100$ V_c
Y-Bias Current	AO2	$I = -0.667$ A/V V_c
Y-Bias HV Set	AO24	$V \approx 100$ V_c
Z-Bias Current	AO0	$I = -0.667$ A/V V_c
Z-Bias HV Set	AO25	$V \approx 100$ V_c
Copper Z-Wire Current	AO4	$I = 14.68$ A/V V_c
MOT AOM Frequency	AO13	$\Delta f = 2\ (5.824/\text{V}\ V_c + 63.967)$ MHz
MOT AOM Amplitude	AO17	Maximum power at $V_c = 7$ V
Repumping AOM Frequency	AO16	$\Delta f = 2 \times (3.3792/\text{V}\ V_c + 46.741)$ MHz
Repumping AOM Amplitude	AO14	Maximum power at $V_c = 2$ V
Imaging AOM Frequency	AO15	$\Delta f = 2\ (8.736/\text{V}\ V_c + 63.967)$ MHz
Imaging AOM Amplitude	AO19	Maximum power at $V_c = 7$ V
Chip Z-Wire Current	AO18	$I = 0.3$ A/V V_c
Chip U-Wire Current	AO19	$I = 0.3$ A/V V_c

Chapter 4

Atom chip assembly

4.1 Introduction

In this chapter, the assembly of the atom chip setup is described in detail. This includes the chip and foil mirror manufacturing, the mechanical assembly of the chip mount and the heat sink, the attachment of the foil mirror to the chip surface, the electrical wire bonding to the chip pads, and the electrical connections from the chip mount to the electrical feedthroughs.

4.2 Chip manufacturing

The chip currently in use was manufactured for us at Hanscom Air Force Base. However, we have made significant progress towards manufacturing our own atom chip. This progress is detailed in the following paragraphs.

4.2.1 Manufacturing method

We use the method of electroplating shown in Fig. 4.1 to pattern $\sim$ 7 μm thick microscopic wires onto our substrates [115, 19]. First, a thin metallic seed layer is evaporated onto a substrate. Then, photoresist is applied on top of this seed layer, exposed, and developed. The substrate is then placed in an electroplating solution where the metal is grown everywhere on the seed layer except on the areas protected by the resist. This allows for the wires to be grown to nearly the entire thickness of the resist. After electroplating, the resist is removed and a wet etch is used over the entire chip. The wet etch is used to remove a layer of metal of the same thickness as the seed layer. This results in the wires now being electrically isolated from each

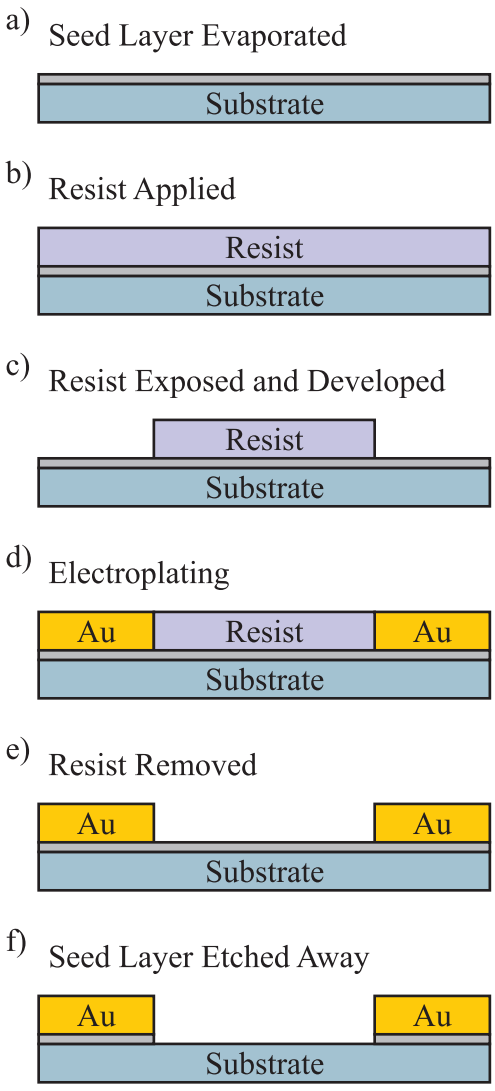

Figure 4.1: Sketch of atom chip manufacturing steps. a) a metallic seed layer is deposited on the insulating substrate, b) photoresist is spun on, c) the photoresist is exposed and developed, d) the seed layer is grown to a thickness of $\sim 7\ \mu$m in-between the resist via electroplating, e) the resist is removed, f) the remaining seed layer is etched away.

other.

4.2.2 Choice of materials

Considering the choice of substrate material, a few criteria are important. Since the wires on the atom chip need to be electrically isolated from each other, a non-conductive substrate is needed to prevent leakage currents into the substrate or shorting of the wires. Also, during operation of the atom chip, relatively large currents, on the order of several Amperes, are passing through the microscopic wires patterned on top of the substrate. These currents cause Joule heating of the wires. Since the atoms are trapped in a ultra-high vacuum chamber, thermal conductance through the substrate into an attached heat sink is the only process that allows dissipation of heat away from the chip wires. Therefore, a substrate with a good thermal conductivity is needed to dissipate the heat quickly. For these reasons, the substrates most often used are silicon (Si), sapphire (Al203), and aluminum nitride (AlN). We chose aluminum nitride because of its high thermal conductivity, $170 - 280$ W m^{-1} K^{-1}, compared to Si, $80 - 150$ W m^{-1} K^{-1}, and sapphire, $30 - 35$ W m^{-1} K^{-1}.

We purchased AlN wafers of size $4.5" \times 3.75" \times 0.025"$, polished on both sides to an average roughness of 50 nm, from Valley Design Corporation to use as our substrates. Each one of these rectangular wafers is cut into smaller pieces using a dicing saw (MicroAutomation 1100). When photoresist is spun onto a substrate, the thickness of the resist is usually thicker at the edges than everywhere else. To accommodate for this edge bead the substrates must have approximately 5 mm of clearance on all sides of the design. This extra area is sawed away after the wires are fabricated. Another restriction on the substrate is that it needs to be approximately square to provide even spinning of the resist. Our mask design has two atom chip masks on it, meaning that two atom chips can be patterned on a single piece of substrate. Keeping

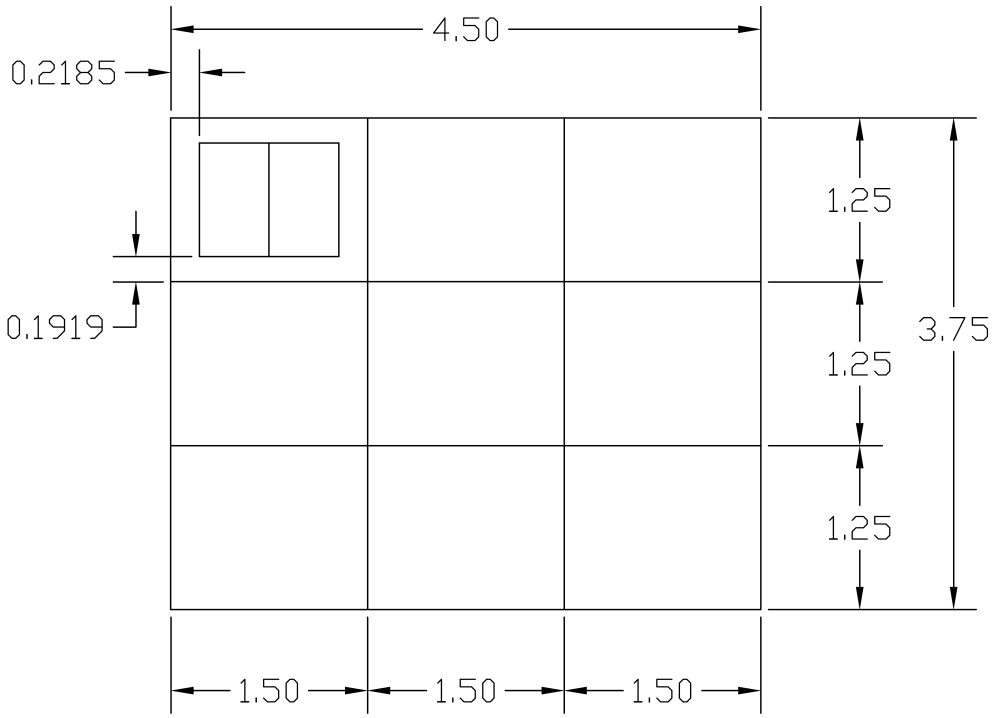

Figure 4.2: Cutting dimensions of the AlN wafer. Two atom chips can be patterned on one piece of cut substrate. Approximately 5 mm clearance is provided at the edges of each piece to account for the edge bead created during the spin-on of photoresist. Dimensions are in inches.

in mind these restrictions, the full wafer was therefore cut down to nine 1.25" $\times$ 1.5" rectangular pieces as shown in Fig. 4.2.

Concerning the choice of metal for the wires, a high electrical conductivity is necessary to prevent excessive Joule heating of the wires and to limit the possibility of burning up a chip. Due to the ease of thermal evaporation, gold and silver are the most common metals used for this application. Both the thermal conductivity (Au: 3.17 $\mathrm{Wm^{-1}K^{-1}}$, Ag: 4.29 $\mathrm{Wm^{-1}K^{-1}}$) and electrical conductivity (Au: 4.55 $\Omega^{-1}\mathrm{cm}^{-1}$, Ag: 6.21 $\Omega^{-1}\,\mathrm{cm}^{-1}$) are roughly equivalent. Since silver is prone to tarnishing, and a setup for gold evaporation and electroplating is readily available through the SPM group at the University of Oklahoma, we chose to use gold for the wires on the chip.

Concerning the choice of photoresist for the lithography, we chose AZ nLOF 2070, a strongly viscous negative resist that has proven successful for atom chip fabrication [116]. The high viscosity of the resist allows for a thickness of resist layers exceeding 7 μm.

4.2.3 Spinning of resist

Before arrival of the AlN wafers, the AZ nLOF 2070 resist was first tested on silicon substrates to determine approximate resist thickness and various parameters for the lithography process. To test the photolithography, substrates are first thoroughly cleaned. This is done by a sequence of ultrasonic baths in acetone, methanol and isopropyl alcohol (IPA) for 5 minutes each. Between baths, the cleaning solutions are blown off the substrate using dry nitrogen to prevent residue from adhering to the substrate and interfering with the resist. The substrates are then baked at 200°C on a hot plate for at least 10 minutes to remove any moisture. The resist is then spun on at a speed of 1000 rpm for 10 seconds and 2500 rpm for 45 seconds using a Laurell WS-400Bz-NPP-Lite spinner.

4.2.4 Photolithography

The photolithography mask was manufactured according to our specifications by the University of Alberta Nanofab Facility using a laser pattern generator (Heidelberg Instruments DWL200). It consists of a chrome pattern on a 5" × 5" piece of glass. The mask design is shared with the local SPM group. It is divided into four 2.5" ×2.5" quarter plates, which are cut out after receipt of the mask. One of those quarter plates contains two of our atom chip design patterns aligned side by side, as depicted in Fig. 4.3. The atom chip designs were drawn in Autocad and converted to the required gerber format using the program L-Edit. Both designs are identical apart

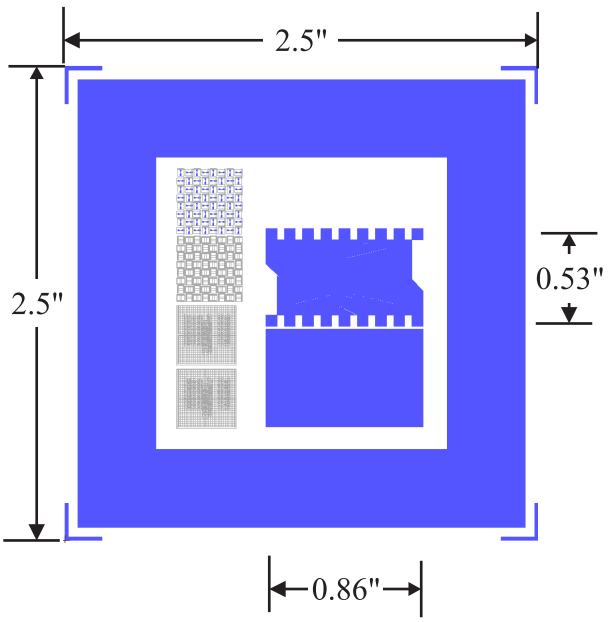

Figure 4.3: Design of the photolithography mask that contains two of our atom chip designs (lower right corner), along with other circuit designs of the local SPM group. The mask consists of a chrome layer on glass. The blue area denotes the chrome layer.

from the gap sizes used to define the chip wires. The first design uses 40 μm gap sizes to define the microscopic wires, and the second design uses 4 μm gap sizes. The remaining mask area contains lithography patterns designed by the SPM group.

Multiple exposure times of the resist were tested, and the optimum was found to be around 7 to 9 seconds. After exposing the resist to ultraviolet light in the mask aligner (Karl Suss MJB3) through a standard test mask, the substrates are baked at 110 °C for 1 to 2 minutes to activate the resist. The substrate is then suspended in a developing solution (AZ 300 MIF) for 1 to 2 minutes while being slightly agitated to remove the resist not exposed to the light. From the testing done on silicon, we determined that the resolution is mainly limited by the edge bead. The edge bead causes the mask to have poor contact with the resist, as illustrated in Fig. 4.4. This results in diffraction of the light and negatively affects the transfer of the wire pattern onto the resist. During subsequent sets of experiments performed on the AlN

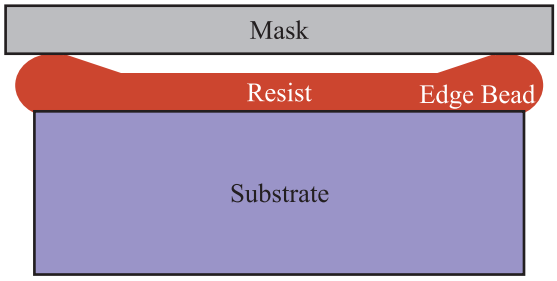

Figure 4.4: Demonstration how an edge bead can create poor contact between the mask and resist, limiting the resolution of the photolithography.

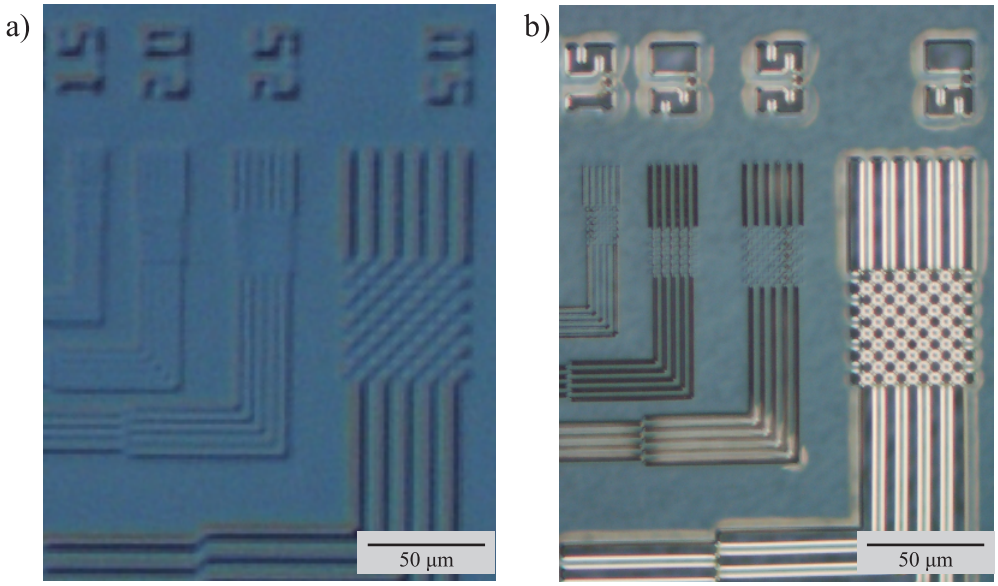

Figure 4.5: Comparison of lithography results on AlN substrate with (a) poor mask contact resulting from edge bead and (b) with edge bead removed. It is clear the lithography resolution is higher when the edge bead is removed.

substrate, we found that removing the edge bead with a swab (Ted Pella applicator 81530) and acetone greatly reduces this effect and allows for higher resolution, as exemplified in Fig. 4.5. A cotton swab such as a Q-tip should not be used to remove the edge bead, because it can leave fibers in the resist which can interfere with the lithography.

Through further testing on the AlN substrates, we found that a 8 second exposure

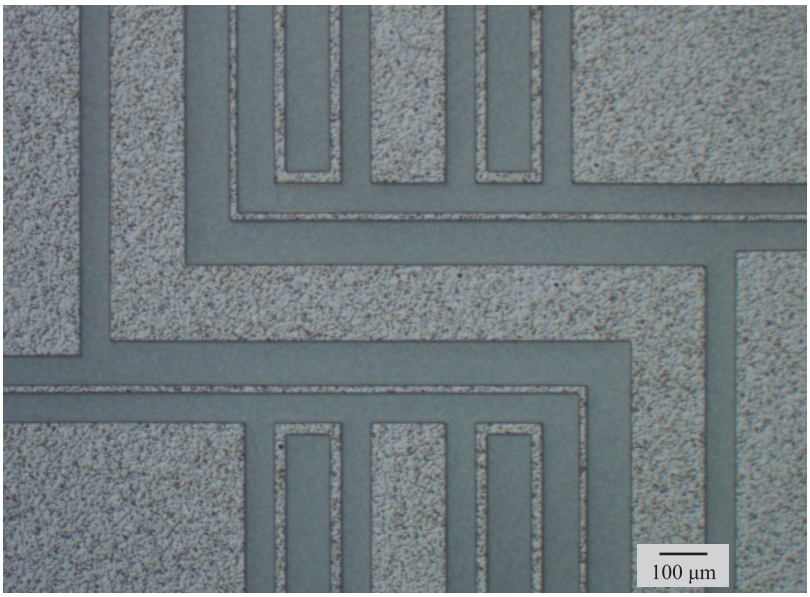

Figure 4.6: Chip design on AlN. The darker blue is the negative photoresist while the lighter blue is the AlN substrate.

time, 90 second post exposure bake time and 60 second developing time provided a satisfactory transfer of the chip design with its 40 micron gap sizes, as shown in Fig. 4.6. Using a profilometer (Ambios XP-2), we measured the thickness of the resist to be 7 μm.

When cleaning the resist off the AlN substrate the wire pattern was still visible to the eye as a difference in reflectivity of the surface. The areas where resist was removed during developing were slightly matted. Through experimentation with piranha etch and other cleaning methods it was determined that the pattern left was in fact not resist still adhered to the substrate, but rather a difference in surface topography of the AlN caused by the developer. It was shown through repeated lithography that this difference in surface roughness has negligible effect upon subsequent patterning.

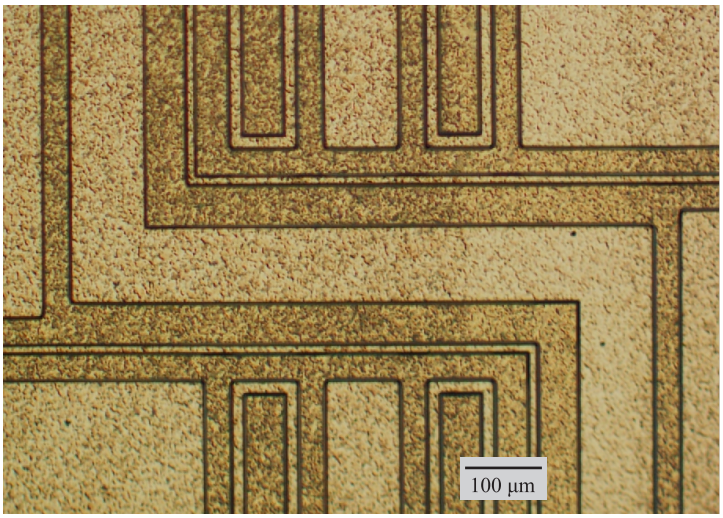

Figure 4.7: Chip design on Au seed layer. Dark gold color is resist. Lighter area is the seed layer where the wires will be electroplated in.

4.2.5 Metal evaporation

When evaporating the Au seed layer onto the AlN substrate, a thin adhesion layer must be deposited first to allow the Au to adhere to the substrate. We thermally evaporate a 5 nm chromium adhesion layer, followed by a 50 nm thick Au seed layer. With a profilometer measurement, we measured the thickness of this seed layer to be closer to 65 nm. The discrepancy can be attributed to error in the calibration of the thickness measurement during evaporation.

The same lithography parameters as on the AlN are used on the Au seed layer surface to transfer the resist pattern with similar results. The previously determined parameter set, consisting of an 8 second exposure time, 90 second post exposure bake time and 60 second developing time, provides an adequate transfer of the 40 micron gap sized chip design to the seed layer as shown in Fig. 4.7.

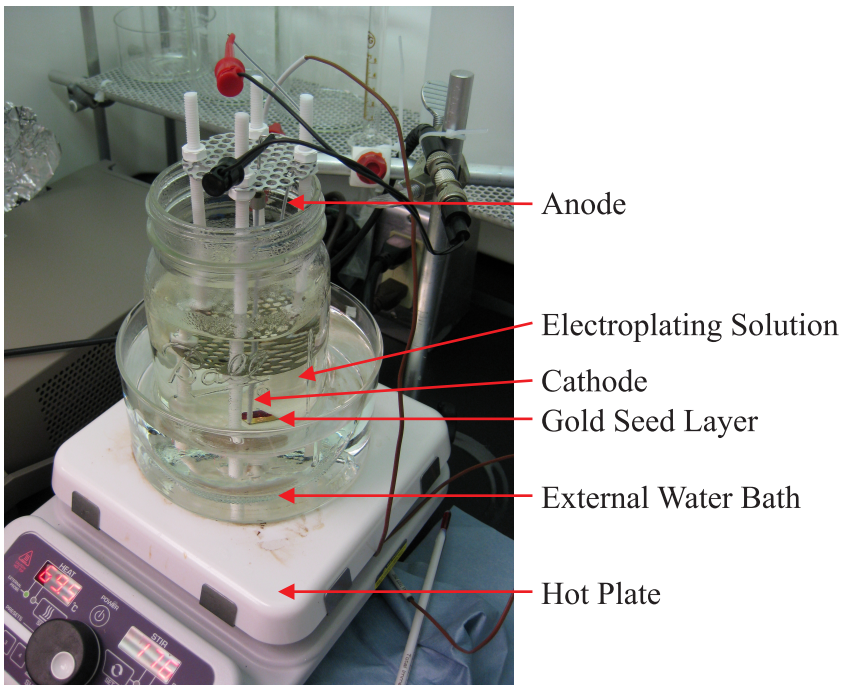

Figure 4.8: Setup used for electroplating. The anode penetrates into the electroplating solution to a distance of 4.8 cm away from the cathode. The cathode current is controlled with a power supply (Keithley Sourcemeter 2400, not shown).

4.2.6 Electroplating

To grow the microscopic wires to a thickness of $\sim 7\ \mu$m, we use electroplating. The resist pattern on the chip acts as a mold for the electroplated gold. With an applied electric potential to the metal surface, gold ions in the electroplating solution deposit on the seed layer and form the microscopic chip wires.

In initial tests, we successfully electroplated gold at a rate of 30 nm/min onto a test sample. The test sample was a 12 mm $\times$ 10.5 mm Si substrate with a chromium/gold seed layer on top. Half of the test sample was covered with photoresist, the other half was exposed. Our electroplating setup is shown in Fig. 4.8. We use 600 ml of TG-25E RTU solution by Technic Inc., a ready-to-use gold electroplating solution. The electroplating solution is held at a temperature of 62 °C, by partially submerging

the electroplating setup in an external water bath which is temperature stabilized at 70 °C with a hot plate. The anode to cathode separation is 4.8 cm and the current is set at 0.63 mA for one hour at a voltage difference of ~ 0.5 V. The plating area used during the electroplating tests was 6 mm $\times$ 10.5 mm. After one hour of electroplating, the thickness of the grown gold layer was 1.8 μm, measured with a profilometer.

More tests need to be done using the atom chip seed layers with resist patterns on them to determine the optimum plating current and temperature to grow the chip wires to thicknesses of ≥ 7 μm.

4.2.7 Etching

We use a commercial Au etching solution (Transene TFA) to remove the seed layer after electroplating. The solution etches at a rate of 2.8 nm per second. Using this etching solution and carefully measuring the etching time, we successfully etched away the chromium/gold seed layer on that half of the Si test sample that was used to perform initial electroplating tests.

The manufacturing process is set up and we are ready to etch the seed layer on a real atom chip, once the electroplating is optimized using real atom chip seed layers.

4.3 Current atom chip

The atom chip in the current system was manufactured for us by Steve Miller's research group at the Air Force Research Laboratory in Hanscom, Massachusetts. The manufacturing process involved photolithography and electroplating on top of Silicon. The Si substrate had a 200 nm SiO_2 insulation layer on top. Starting with this substrate, a 200 Å thick Ti adhesion layer was evaporated on top of the SiO_2, followed by a 500 Å thick Au seed layer. Then, using photolithography, the wire structures were patterned onto a layer of photoresist on top of the seed layer. This

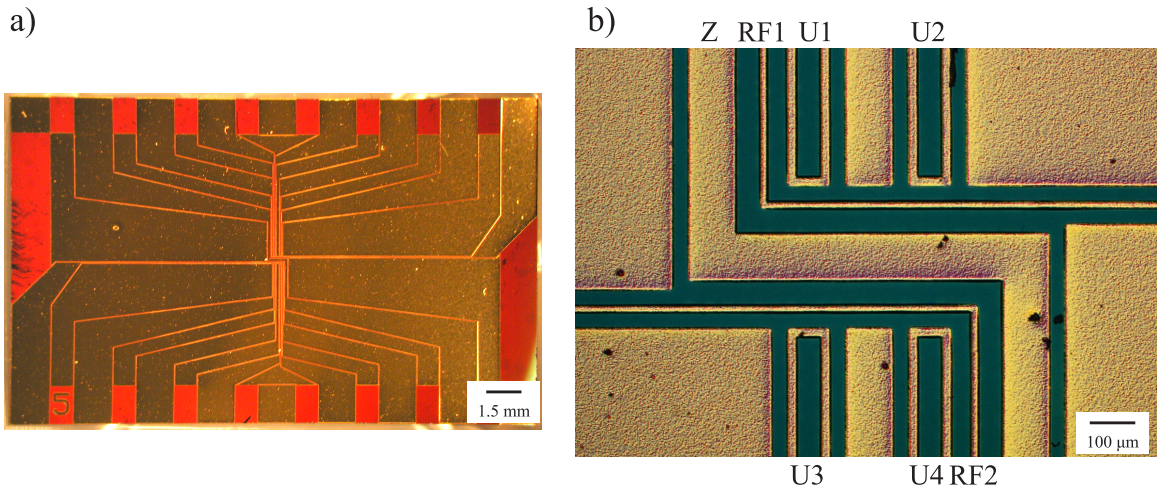

Figure 4.9: Microscope image of the atom chip. a) whole chip, b) magnified view of the center region.

was done via a lithography mask manufactured according to our mask design. Using electroplating, the seed layer of Au was then grown between the resist walls to a thickness of $\sim$ 9.5 μm. Subsequent etching removed the seed layer, resulting in a fully defined wire pattern. A microscope image of the center wire pattern of the chip is shown in Fig. 4.9. The 40 μm wide gaps in the reflective gold layer can be seen. The gold layer was originally used to reflect two of the four MOT beams and form a mirror MOT at a distance of $\sim$ 2 mm from the chip center. The gaps define the current carrying microscopic wires that are used to create magnetic trapping potentials for trapping and compressing the atoms at distances of a few hundred microns from the chip surface.

4.4 Foil mirror manufacturing

When loading the mirror MOT from the first version of the atom chip, it became obvious that the trapped atom number suffered from the diffraction pattern on the reflected MOT beams due to the gaps in the chip surface. When the MOT center

was moved to a position below the exact center of the chip, the MOT density profile would become severely distorted and holes could be seen to appear in the MOT. The holes would change shape when moving the MOT beams but could not be made to disappear. We therefore decided to add a mirror surface on top of the atom chip.

The mirror is manufactured by thermal evaporation of a thin metal gold film onto 50 μm thick Kapton foil. The evaporation is done on a 2" $\times$2" size piece of Kapton foil. As any other element destined to end up in the UHV system, the foil is thoroughly cleaned in an ultrasonic cleaner using first acetone and then methanol as cleaning solvents. Then, a 20 nm thick chromium adhesion layer is evaporated, followed by a 150 nm thick gold layer. The thickness of the gold layer has to be bigger than 100 nm to ensure a reflectivity $R > 96\%$ as calculated from the theory of thin film reflectivity [127] with the index of refraction and absorption coefficients taken from Refs. [128, 129].

After thin film evaporation, the foil mirror is cut to shape. To keep the mirror surface from being damaged during the cutting process, the mirror is placed with the gold layer facing down onto a stack of several lens papers. A stainless steel block of size 0.76" $\times$ 0.397" and height 0.4" with a finely polished lower surface is then pressed on the back of the foil mirror. The lower surface of the steel block was polished with 1000 grit sandpaper. While the steel block is pressed to the back of the foil mirror, a cut is made around the outer edges of the block with a clean razor blade. Many small foil mirrors are cut out of the larger piece in this fashion, and the best result is chosen to be glued onto the atom chip later.

The reflectivity of the foil mirrors produced in this way is measured to be 92% at 780 nm when reflecting a laser beam of waist radius $\sim$ 5 mm. The reflected beam profile looks identical to that of the incident beam. There are no discernible diffraction patterns. For comparison, the reflectivity of the atom chip surface is only 81% and

the reflected beam profile is extremely distorted due to the diffraction patterns caused by the gaps between the microscopic wires.

The foil mirror is not attached to the atom chip until after chip is glued onto the ceramic mount.

4.5 Rinsing

Before mounting the chip, it has to be rinsed and cleaned to remove any dust or other particles. This is done by holding the chip with plastic tweezers diagonally over a glass beaker and squirting first acetone, then methanol onto it from an oblique angle. After such rinsing, the atom chip is sonicated in methanol for five minutes and inspected for defects.

4.6 Assembling the ceramic mount

The assembly of the chip mount is done in the following steps:

- Pins are glued into the mount.
- Gold wires are bonded to the pins with silver epoxy.
- The gold wires are bent up to make room for the atom chip.
- The macroscopic copper z-wire is glued into the mount.
- The atom chip is glued into the mount on top of the z-wire.
- The gold wires are bent back down.
- The gold wires are bonded to the contact pads on the chip using silver epoxy.
- The foil mirror is glued on top of the chip surface.

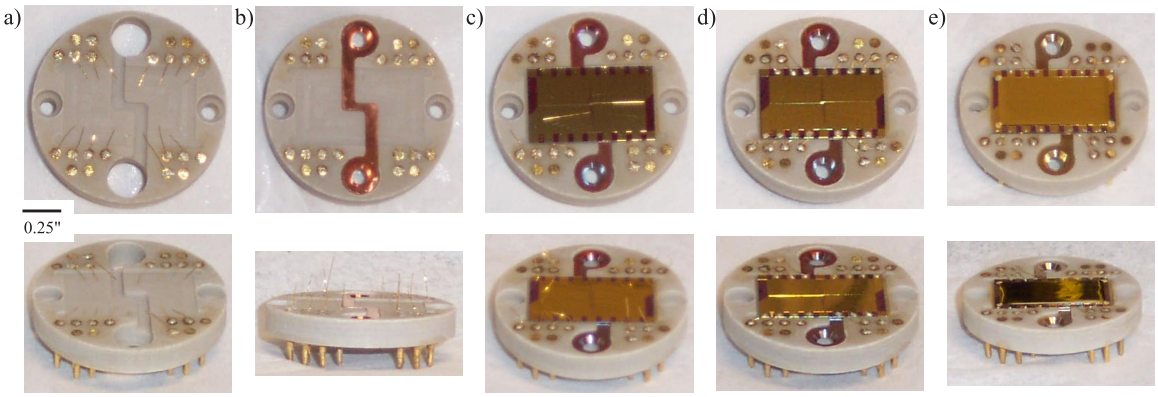

Figure 4.10: Photos of the ceramic mount after various steps of the chip mount assembly. The mount is shown after gluing the pins and wire bonding to the pins (a), after bending up the wires and gluing the z wire (b), after gluing in the atom chip (c), after wire bonding to the chip pads (d), and after attaching and grounding the foil mirror (e).

- The foil mirror is contacted to a grounded pad on the chip with silver epoxy.

A sequence of photos of the chip mount at various stages in the assembly process is shown in Fig. 4.10. In the following paragraphs, each of these steps is explained in detail.

4.7 Gluing pins

The pins (Lesker FTADPEEK-M) are first filed down using a pin vise and sandpaper so that they are flush with the ceramic mount surface when inserted into the mount.

After thorough cleaning, the pins are inserted into the mount. To force the pins into the correct positions while applying and curing the epoxy, the ceramic mount is fastened upside down to an aluminum block. The aluminum block is covered with a 1 mm thick piece of Teflon and a thin layer of Kapton and has four tapped holes. The slightly flexible Teflon layer is needed to ensure the mount can be pressed onto the block firmly without being damaged. The additional Kapton foil keeps the pins from being glued to the Teflon layer. Using four screws with large washers, the ceramic

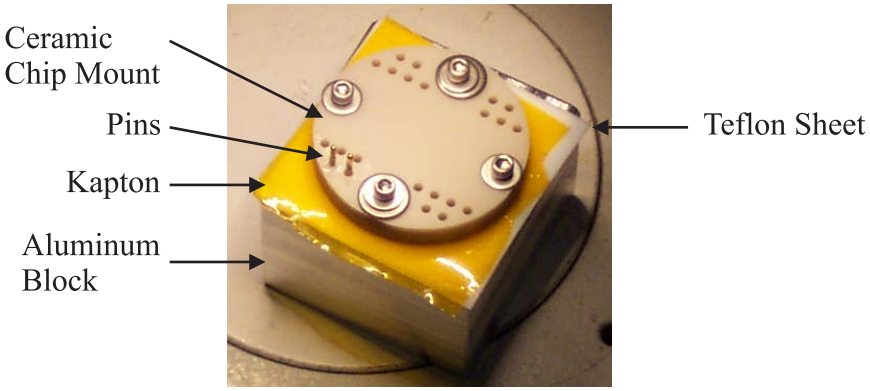

Figure 4.11: Setup used to glue the pins into the ceramic mount. The pins are inserted into the mount, and the mount is fastened upside down onto an aluminum block covered with a layer of Teflon and Kapton foil. The flexible Teflon pushes on the pin heads and forces the pins into their correct positions. Epoxy is then applied to the backside of the pins.

mount is pressed firmly upside down onto the flexible Teflon layer. This forces all the pins into their correct positions. Fig. 4.11 shows a photo of this setup used to glue the pins. The photo is of an initial test where only two of the 22 pins were glued.

The Epoxy (Epotek H77) is applied to the backside of the pins under a microscope. A piece of stainless steel wire is used as applicator. Care has to be taken to fill in as much of the pinholes as possible while staying clear of the center surface on the back of the mount. Any epoxy there would be disastrous to the thermal contact between the chip mount and the aluminum heat sink later.

After epoxy is applied to all the pins, the mount is baked in a clean oven for 1 hr at 150° C, while still being attached to the aluminum block. After baking, the ceramic mount is detached from the block, the Teflon and Kapton are removed, and the pins are checked for mechanical stability.

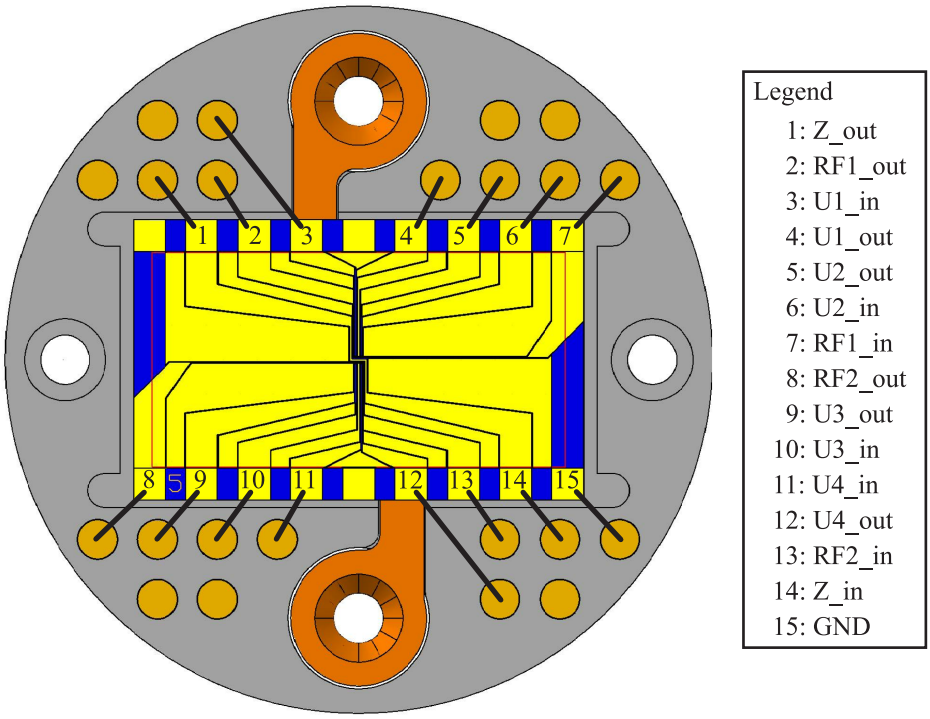

Figure 4.12: Sketch of the assembled atom chip mount showing the positions of gold wires and the designations of the contact pads.

4.8 Wire bonding to pins

The electrical connections between the heads of the pins and the atom chip are made with 5 mil gold wire and UHV compatible silver epoxy (Epotek H20E-175). For each pin that will be used, a piece of wire is cut and positioned with plastic tweezers on the pin head so that it is pointing toward the atom chip key. The length and position of each of the wires is chosen so that they reach the position where the respective pad on the atom chip will be. A sketch of the wire positions is shown in Fig. 4.12. A small drop of silver epoxy is applied to each wire to bond it to the pin head. The epoxy is applied under the microscope with a stainless steel wire. The mount is baked for 2.5 hours at 150 °C to cure the silver epoxy. Afterwards, each wire is bent up to make room for the insertion of the atom chip.

4.9 Gluing copper z-wire

The copper z-wire is glued onto the mount with H77 epoxy. A thin layer of epoxy is applied to the bottom surface of the z-wire key using a piece of a razor blade as spatula. The epoxy layer is made as thin as possible. The z-wire is positioned and centered in the key, and the mount is baked at 150° C for one hour to cure the epoxy.

4.10 Gluing atom chip

The atom chip is glued onto the mount in the same way as the copper z-wire. The bottom surface of the chip key, including the top of the copper z-wire are coated with a thin, uniform layer of epoxy. The chip is positioned in the center of the chip key under a microscope, and the mount is baked again at 150° C for an hour.

4.11 Wire bonding to chip

To bond the gold wires to the contact pads on the chip, the wires are first bent down onto the chip pads with plastic tweezers. This is done under the microscope to ensure that each wire makes contact with the respective pad on the chip. To bond the wires, a small drop of H20E silver epoxy is applied to each pad with stainless steel wire. This is also done under the microscope. Afterwards, the mount is baked for 2.5 hours at 150 °C to cure the silver epoxy.

4.12 Gluing foil mirror

To attach the foil mirror to the top of the atom chip surface, the chip mount is first positioned on top of a clean piece of Aluminum and put into the oven. Plastic tweezers are then used to position the foil mirror so that it is centered on the chip surface. A stainless steel weight with a polished lower surface is used to flatten the

mirror and hold it in place while the epoxy is applied. The dimensions of the weight are 0.688" $\times$ 0.393" and it is 2.5" high. The bottom surface of the weight was polished using 1000 grit sandpaper. The weight is centered on top of the foil mirror, leaving the corners exposed. After ensuring that the weight and mirror are centered on the chip and that they clear the existing wire bonds, a small drop of non-conductive H77 epoxy, diameter < 1 mm, is applied to each corner of the foil mirror using stainless steel wire as applicator. The epoxy is applied so that it bridges the gap between the corners of the mirror and the atom chip surface. After applying the epoxy, the oven door is shut carefully, making sure the weight and mirror are not moving. The assembly is then baked at 150 °C for one hour. After the epoxy is cured and the mount has cooled down, the weight is carefully removed from the foil mirror. The mirror should now be flat and securely attached to the atom chip.

4.13 Grounding foil mirror

The last step in the atom chip mount assembly is the grounding of the foil mirror surface. This is done by contacting the mirror surface to an unused pad on the atom chip referred to as the ground pad (GND). A drop of H20E silver epoxy is applied to the corner of the mirror above the GND pad. The drop is applied with stainless steel wire under the microscope. The drop has to be big enough to form a conductive bridge from the mirror surface to the pad on the atom chip surface, but small enough to keep it from contacting any other conductor on the atom chip. A photo of a finished, correctly applied grounding bridge is shown in Fig. 4.13.

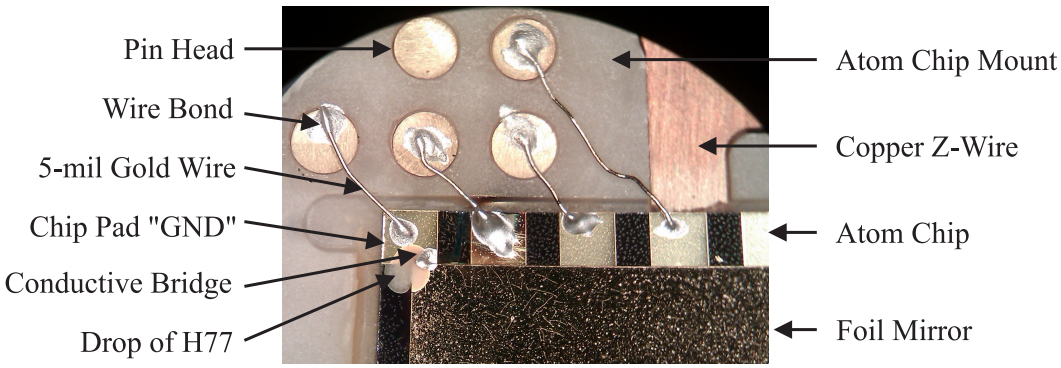

Figure 4.13: Microscope image of some of the finished silver epoxy wire bonds on the chip mount. The conductive bridge used to ground the foil mirror surface is shown. Next to the conductive bridge, one of the four drops of non-conductive epoxy can be seen, used to attach the foil mirror to the atom chip.

4.14 Assembling heat sink

Before the atom chip mount can be attached to the aluminum heat sink, the heat sink has to be assembled. The heat sink is mounted onto two copper rods of a high power electrical feedthrough (Lesker EFT0543253). The other two copper rods function as electrical conductors to supply current to the copper z-wire.

Before the aluminum heat sink is attached, the air side of the feedthrough is first secured to the cooling cup. With the cooling cup attached, the feedthrough can stand securely on the table surface with the copper rods pointing up. The cooling dewar is not attached to the assembly yet.

A sketch of the heat sink assembly sequence is shown in Fig. 4.14. The aluminum heat sink is slid onto the two of the four 0.25" copper rods that serve as cold fingers. In order to ensure that the atom chip will be centered in the chamber, the end of the heat sink should be 8.21" away from the inner surface of the feedthrough flange. This means that the rods should penetrate a distance of 4.07" into the heat sink. After the heat sink is in place, it is compressed from the long side with six stainless steel

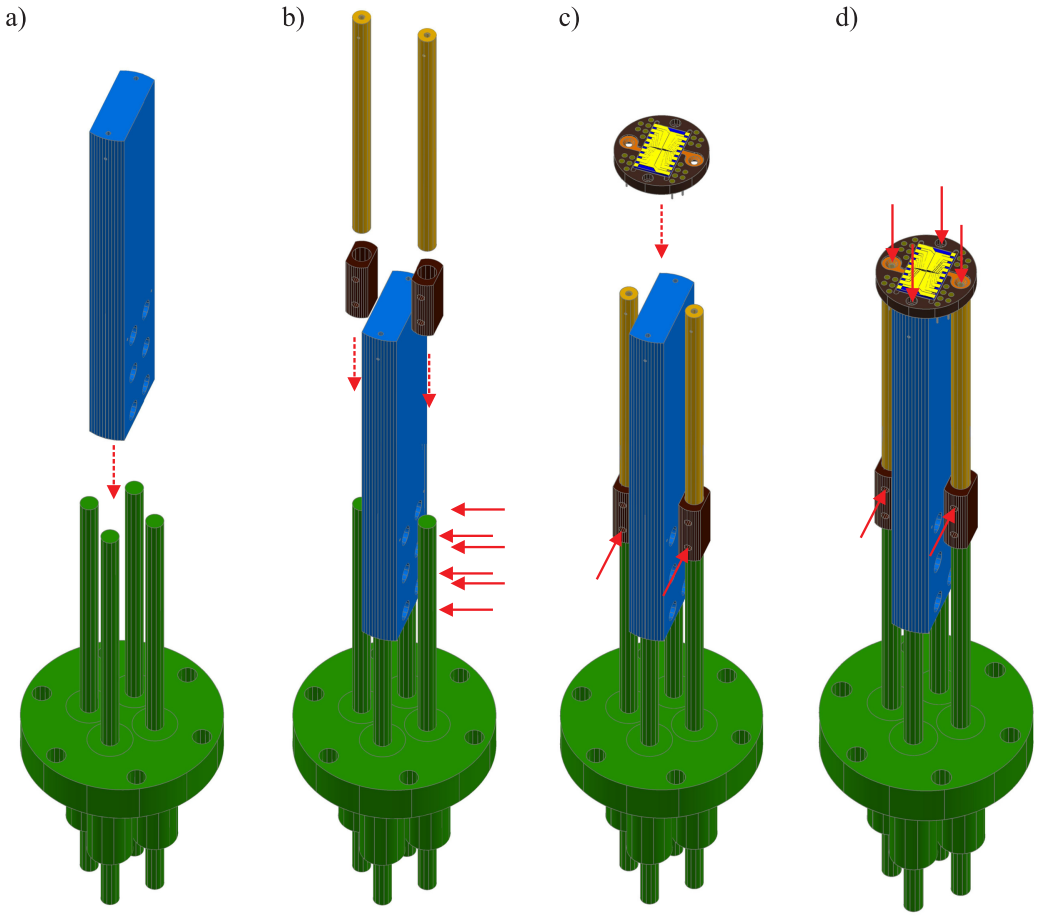

Figure 4.14: Sketch of the heat sink assembly steps. Dashed red arrows denote the joining of parts and solid red arrows denote the insertion positions of fasteners. a) The aluminum heat sink is slid onto the copper cold fingers. b) The heat sink is secured to the cold fingers by compressing the saw cut with six screws, and extension rods are attached to the current-carrying copper rods with barrel connectors. c) The lower two set screws on the barrel connectors are tightened, and the atom chip mount is lowered onto the heat sink. d) The atom chip mount is secured with four screws, and the upper two set screws on the barrel connectors are tightened.

screws. The screws compress the saw cut in the heat sink and ensure proper thermal contact between the aluminum and the cold fingers.

The two Cu rods that function as electrical connections to the copper z-wire are extended with 4.2" long 0.25" diameter Be-Cu extension rods. The extension rods are connected with homemade barrel connectors. The extension rods are threaded on one side to allow easy connection to the copper z-wire. The barrel connectors are secured to the feedthrough rods, but the extension rods are left loose in the barrel connectors and are not fastened until after the atom chip mount and the copper z-wire are attached.

The ceramic atom chip mount is now mounted to the aluminum heat sink with two stainless steel screws. At the same time, the copper z-wire is attached to the extension rods with two screws. Fastening the copper z-wire to the loose extension rods will pull them up to the correct height. With the extension rods fixed at the proper heights, the barrel connectors are then fastened. The barrel connectors now provide electrical contact from the feedthrough rods to the copper z-wire, and the heat sink assembly is finished.

4.15 Electrical connections

After the heat sink is assembled, the electrical connections from the pins to the low power electrical feedthrough (MDC 9152005 9-pin type c feedthrough on a 2.75" size flange) are made. First, a 4-way 2.75" cross is attached to the high power feedthrough in the orientation shown in Fig. 4.15. One side of the cross serves to hold the low power electrical feedthrough, the opposite side of the cross is blanked off and can be used in future expansions of the setup.

The electrical connections from the pins on the chip mount to the 9-pin electrical feedthrough are now made using Kapton coated UHV compatible copper wires (MDC

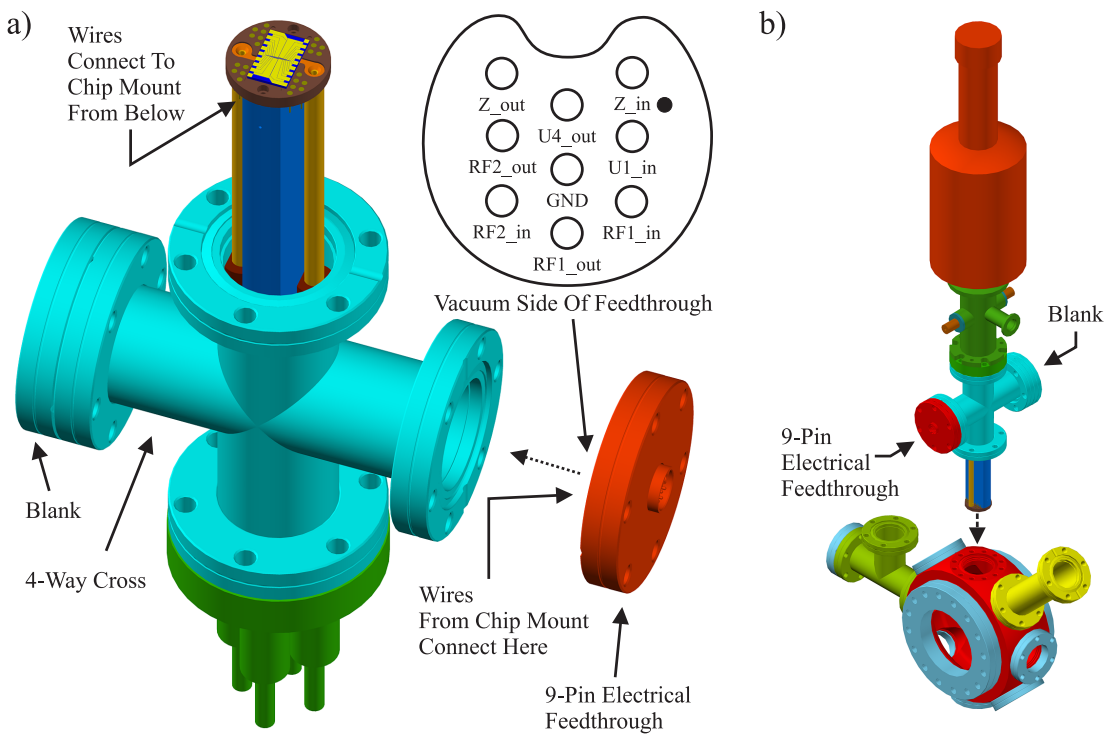

Figure 4.15: Sketch illustrating the electrical connections between the chip mount and the 9-pin low power electrical feedthrough. The pairs of pins U1_out-U2_in, U2_out-U3_in, U3_out-U4_in are connected directly using short wires to ensure correct in-series operation of the microscopic u-wires. The other pins are then connected to the 9-pin feedthrough as shown.

KAP2 22 AWG). The wires are first cut to appropriate lengths and crimped on both sides with identical female sockets (Lesker, FTADPEEK). The cylindrical sockets provide a mechanically stable, snug fit onto the chip mount pins and the feedthrough pins. The pairs of pins U1_out-U2_in, U2_out-U3_in, and U3_out-U4_in are connected directly using short wires. This guarantees correct in-series operation of the microscopic u-wires. Connections between the remaining pins on the chip mount and the feedthrough are then made according to the inset in Fig. 4.15a). To prevent accidental grounding of any connection on the electrical feedthrough, a small ceramic bead is inserted onto each vacuum-side feedthrough pin prior to connection of a socket.

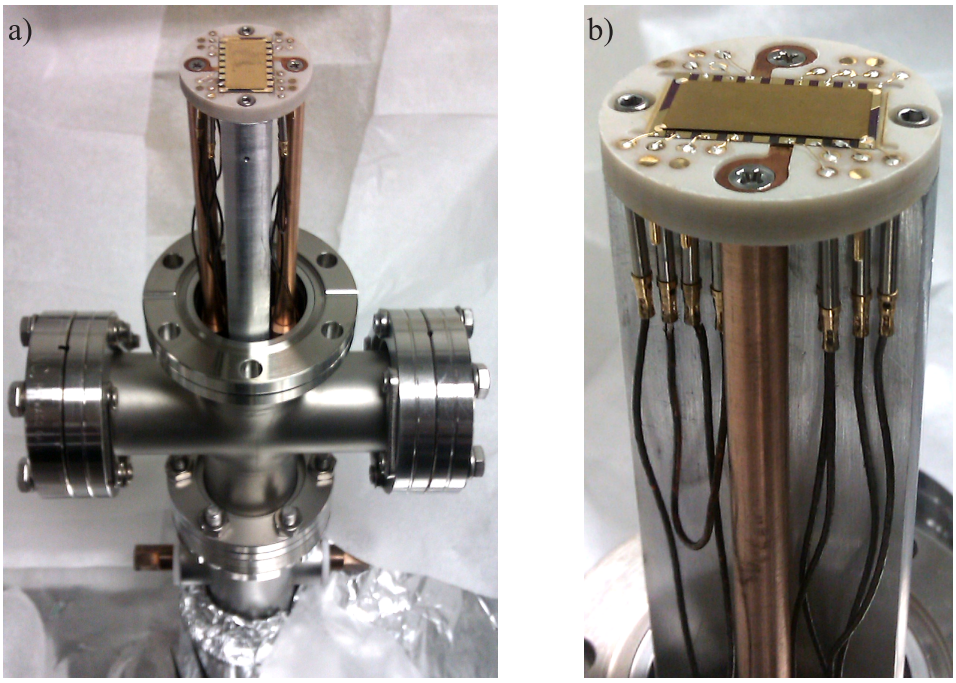

Figure 4.16: Photos of the chip setup after all electrical connections are made. a) overview, b) close-up of the chip mount.

Once all the wire connections are made, electrical consistency is tested with a multimeter. If consistency is met, the electrical feedthrough is fastened to the side of the cross. Photos of the finished assembly are shown in Fig. 4.16.

4.16 Insertion of atom chip into chamber

After the electrical connections are made, the dewar is attached to the cooling cup and the atom chip assembly is inserted into the top viewport of the vacuum chamber in the orientation shown in Fig. 4.15b. A photo of the atom chip assembly after insertion into the chamber is shown in Fig. 4.17. This completes the atom chip assembly.

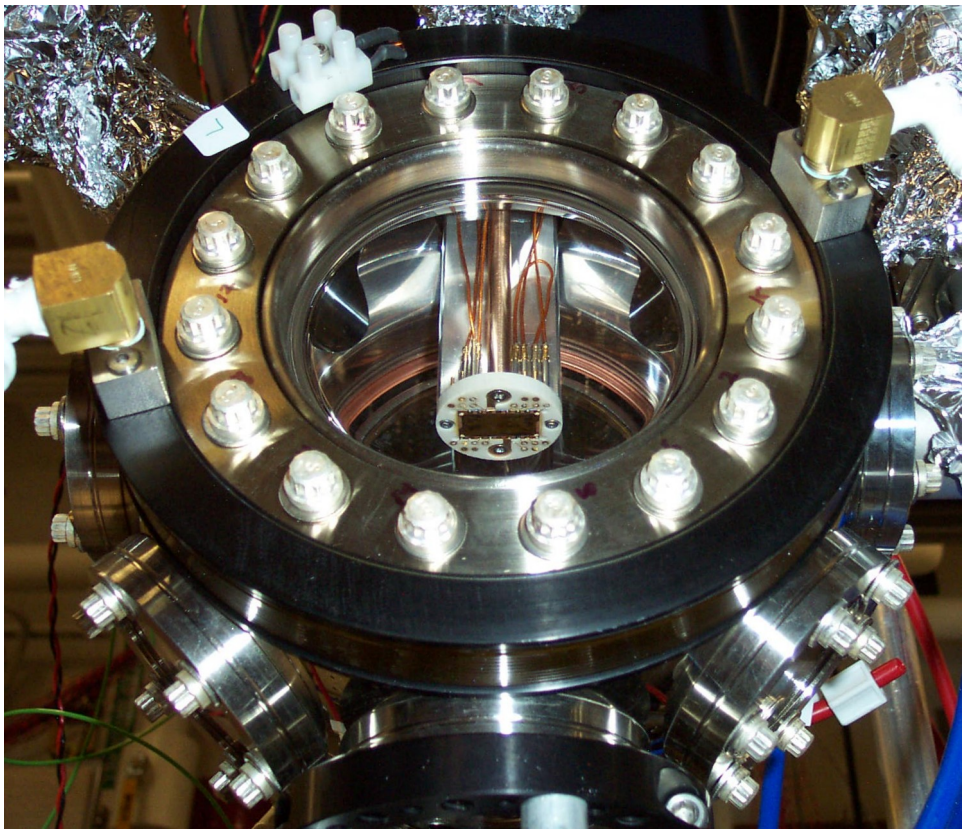

Figure 4.17: Photo of the atom chip assembly after it was inserted into the vacuum chamber.

Chapter 5

Cold atoms on the chip

5.1 Introduction

The loading sequence of the atom chip proceeds from the initial vapor-loaded mirror magneto-optical trap (MOT) to the microscopic wire trap created with the z-shaped wire on the atom chip. The sequence involves the loading of the MOT, a cold MOT phase (CMOT), the transfer of atoms into a macroscopic z-wire magnetic trap (z-trap), a compression phase in which atoms are moved closer to the chip surface (compressed z-trap), and finally the transfer of atoms into the microscopic wire trap (chip trap). In this chapter, the setup used for loading the magnetic trap is detailed, followed by a discussion of the heating of the atom chip, and a summary of the loading sequence. Then each step in the sequence is described in some detail. The chapter closes with an outlook on future atom chip experiments.

5.2 Trapping setup

The experimental setup used for cooling and trapping is shown in Fig. 5.1. The four MOT cooling beams are labeled +X, -X, Y and Z, to coincide with a right-handed cartesian coordinate system (x, y, z) with origin at the zero of the quadrupole field generated by the MOT coils. The zero is located a few mm below the center of the atom chip surface. The z-axis points diagonally upward along the MOT coil center axis, the x-axis points horizontally and perpendicular to the center segment of the atom chip z-wire, and the y-axis points diagonally downward away from the atom chip surface, as shown in Fig. 5.1. The +X- and -X-beams are left-handed circularly (LHC) polarized, and counterpropagate horizontally below the atom chip

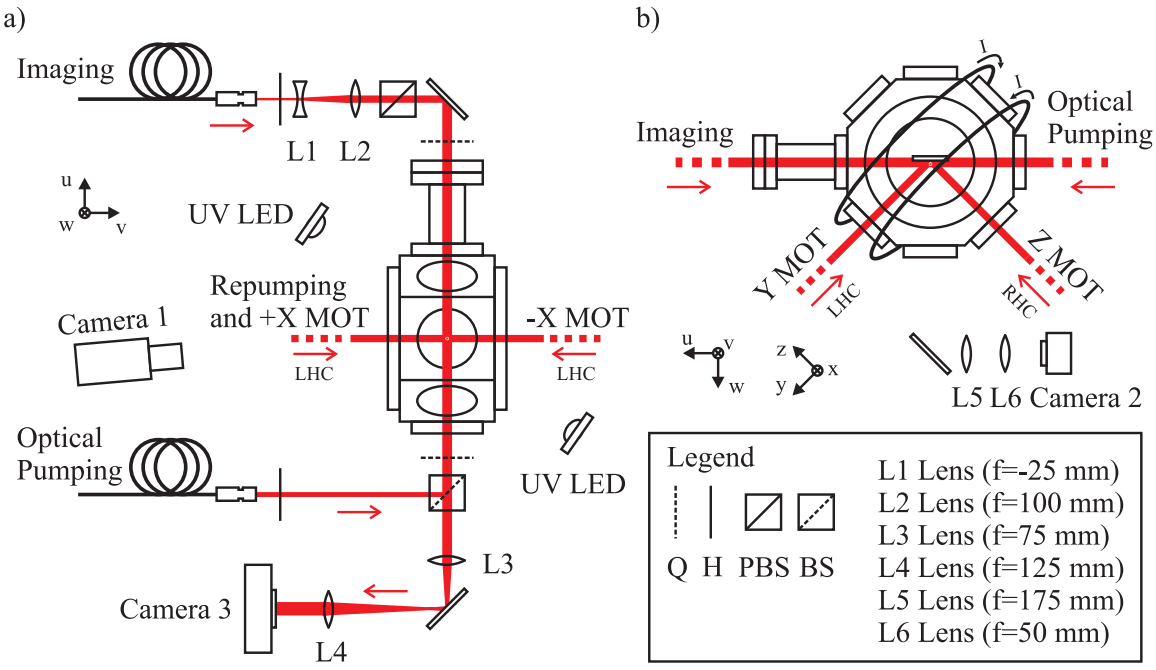

Figure 5.1: Atom trap setup. a) top view, b) side view. Note that positive currents through the x-, y-, and z-bias coil pairs (not shown) create uniform magnetic fields in the positive x-, y-, and z-directions, respectively. The x-, y- and z-directions are indicated by arrows in b). The coordinate system (u, v, w) is used when referring to absorption images. The u-, v- and w-directions are indicated by arrows in a) and b). Q: Quarter-wave plate, H: half-wave plate, PBS: polarizing beamsplitter cube, BS: non-polarizing beamsplitter cube.

along the x-axis. The repumping light copropagates with the +X-beam and is also LHC polarized. The top third of the X-beams are cut off by the atom chip mount. The Z-beam is right-handed circularly (RHC) polarized and enters the chamber from below at an angle of 45°. It propagates along the center axis of the MOT coils, and reflects off the atom chip mirror surface. The reflected beam is LHC polarized and counterpropagates with the Y-beam. The Y-beam is LHC polarized and also reflects off the atom chip mirror. The reflected beam is RHC polarized and counterpropagates with the Z-beam. In the region just below the atom chip where all beams meet, there

are six beams overlapping, one pair of counterpropagating beams parallel to each of the three cartesian axes (x, y, z). In this region, the beams perpendicular to the MOT coil center axis are LHC polarized, and the beams parallel to the MOT coil center axis are RHC polarized. This gives the correct $\sigma^+ - \sigma^-$ configuration along each axis that is necessary for the operation of a MOT.

The MOT is positioned ~ 1.5 mm away from the chip mount. This is the closest distance we can achieve in the experiment. In order to capture as many atoms as possible in the MOT, the diameter of the MOT is large, FWHM ≈ 1 mm. Moving the MOT closer to the chip surface leads to collisions of atoms with the chip and a drastic reduction of the atom number. Being able to move the MOT up to this distance proved to be crucial to load the magnetic trap. In early attempts, we tried to load the magnetic trap from a MOT that was further away from the atom chip, ~ 3 mm, but were unable to transfer more than 10^5 atoms into the magnetic trap, because of the imperfect mode-matching between the two traps.

The direction of the x-, y-, and z-axes are shown in Fig. 5.1b. When referring to absorption images and the magnetic trapping potentials, a second Cartesian coordinate system, (u, v, w), will be used, with origin at the center of the lowest atom chip mount surface. The orientation of the (u, v, w) coordinate system is illustrated in Fig. 5.1a. The u- and v-axes are parallel to the plane of the atom chip surface, and the w-axis points vertically down, away from the chip. The chip wire surface is located behind the 50 μm thick foil mirror, and is recessed in the mount by 80 μm. The exact position of the atom chip surface with respect to the chip mount is measured with a micrometer screw gauge, since it depends on the thickness of the layer of epoxy used to glue the chip to its mount.

Also shown in Fig. 5.1 are the configuration of the imaging beam and optical pumping beam. The imaging beam and optical pumping beam are counterpropagating and

enter the chamber along a horizontal axis parallel to the u-axis and perpendicular to the axis of the +X- and -X-beams. They are overlapped via a non-polarizing beamsplitter cube.

The imaging beam is up-collimated to a FWHM of 5 mm. It then passes through a half-wave plate and a polarizing beamsplitter used to adjust beam power and filter the polarization. A quarter-wave plate is used to change polarization to circular before the beam enters the vacuum chamber. After passing through the atom cloud, the imaging beam passes through the imaging optics shown in Fig. 5.1 and is detected by a CCD camera. One pixel in the absorption image on the bare CCD screen corresponds to an area of 4.08 μm $\times$ 4.08 μm in real space.

The optical pumping beam has a FWHM of 2 mm. The intensity is adjusted to ~ 2.2 mW cm^{-2} with a neutral density filter. A quarter-wave plate is used to adjust the optical pumping beam polarization to circular before it enters the chamber.

The positions of the three cameras used to image the MOT are also shown in Fig. 5.1. Camera 1 (Watec WAT902H-Ultimate) and camera 2 (Edmund Optics NT56-580) are used to look at the fluorescence of the MOT from the side and from below in realtime, which aids in the positioning of the MOT during daily alignment. Camera 3 is the astronomy CCD camera (Apogee Alta U-32) used for absorption imaging of the MOT and the magnetic traps as described in Section 3.9.

5.3 Trapping potential calculations

The trapping potentials for the magnetic traps are calculated using finite element methods (FEM) and numerical integration of the Biot-Savart law as described in Section 2.6. The FEM result for the current density of the macroscopic copper z-wire is shown in Fig. 5.2, together with a comparison of the resulting fields to those obtained with a simpler current density model. In the simple model, the current

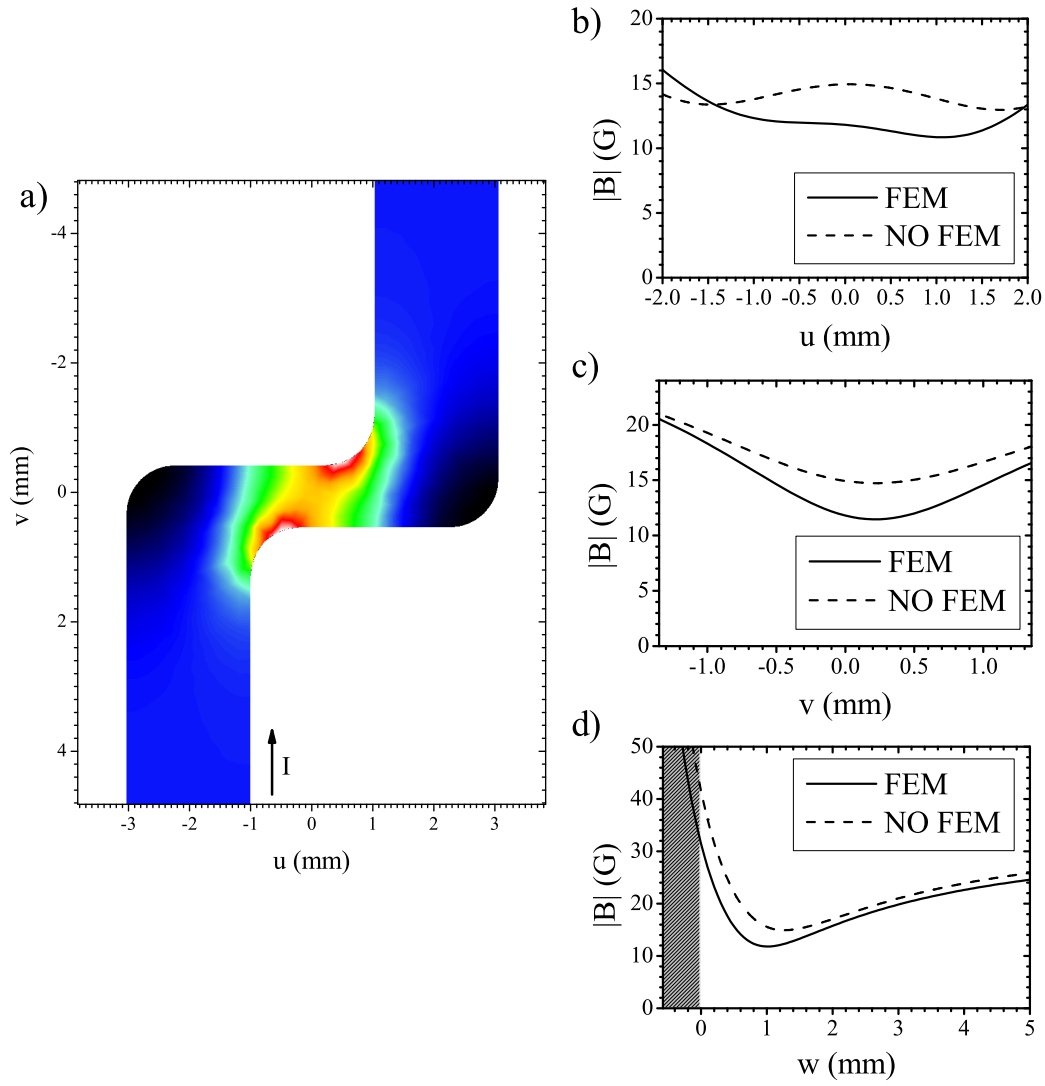

Figure 5.2: Current density distribution and magnetic fields calculated for the macroscopic copper wire. The wire is 2 mm high. a) Joule heating in the wire. Black (white) corresponds to the minimum (maximum) current density. In b), c) and d), the magnetic fields from the finite-element currents (solid) are compared to a simpler model (dashed). The current and bias fields parameters are $I = 30$ A, $B_v = 16.2$ G, $B_u = 27.64$ G, and $B_w = 2.72$ G. Note that w points into the page in a).

density is assumed to be uniform in the straight segments of the wire, and to curve around the wire corners in concentric circular arcs. The FEM-based potentials are more accurate and differ from the simple model calculations by more than 20%. The bump in the potential seen in Fig. 5.2c illustrates the effects of overcompensation of the Ioffe field. The bias field B_u is too large to create a tight trapping potential in the longitudinal direction. Note that the z-wire surface is located 500 μm behind the w = 0 plane, as denoted by the gray area in Fig. 5.2d.

In order to find the optimum bias field values for the magnetic traps, trapping potential curves are first calculated, taking into account the experimental constraints such as the maximum currents on the bias field coils and the initial position of the atom cloud. The bias field values in the calculation are optimized manually to overlap the various potentials. Fig. 5.3 shows the result of the calculations. Three different magnetic traps are used in the loading sequence. Note that, due to the different z-wire geometries of the macroscopic and microscopic traps and the large size of the MOT, only approximate matching of the potentials can be obtained at each step of the loading sequence. The approximate matching of the potentials is critical for maximizing the number of atoms in the atom chip trap.

The z-trap, loaded from the MOT atoms, is formed by running current through the mm size copper z-shaped wire behind the chip. The z-trap is chosen to be shallow to minimize the heating when atoms are loaded from the much larger MOT cloud. If the trap frequency of the z-trap is larger than the trapping frequency of the MOT, atoms loaded from the wings of the MOT into the z-trap gain energy as they move in the magnetic potential. Because the trap frequency of the MOT is on the order of one kHz, the characteristic time for this effect is on the order of milliseconds. To minimize this heating, the trap frequencies of the z-trap are chosen to be < 1 kHz. The z-trap is then compressed and moved closer to the chip to a distance of 260 μm

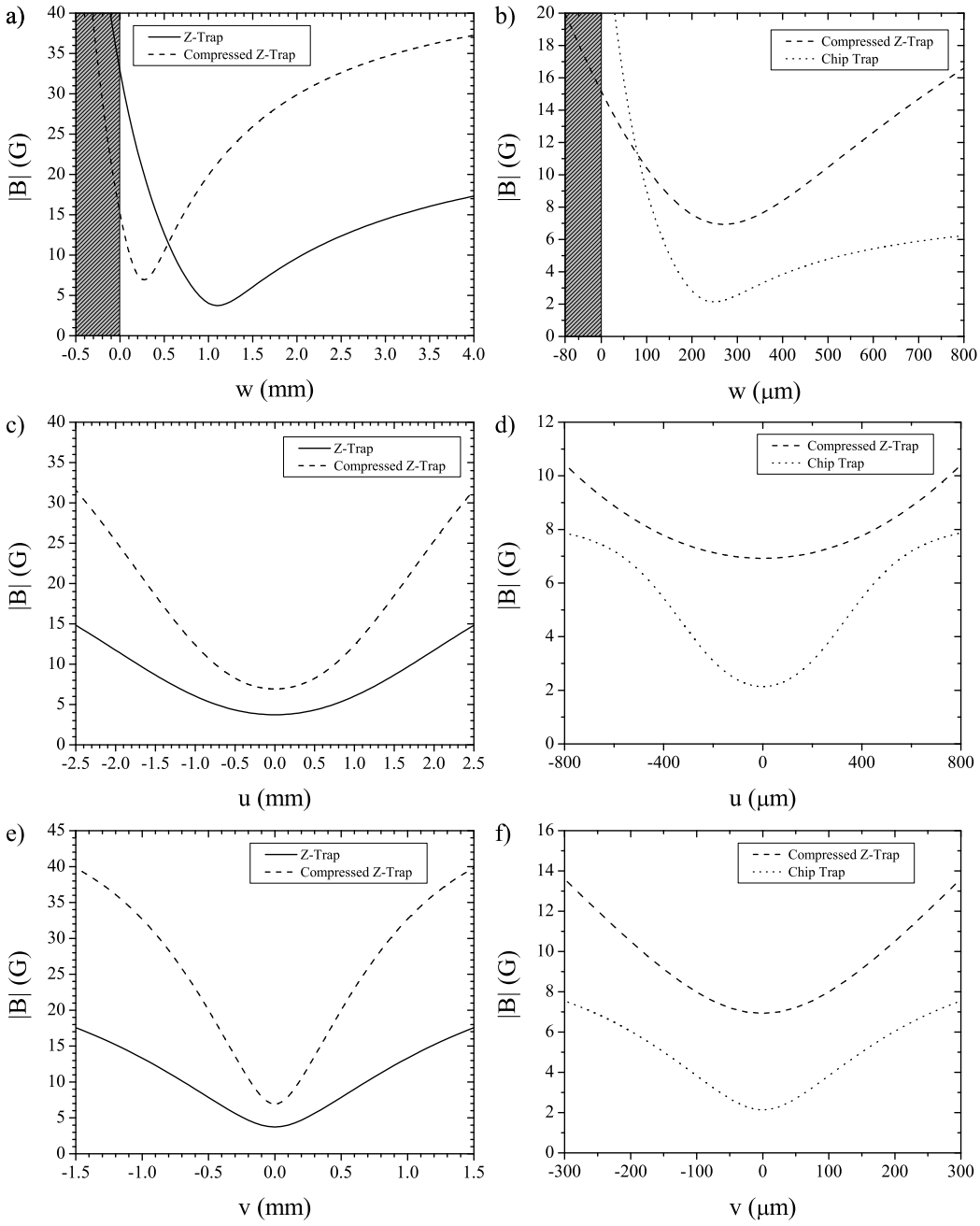

Figure 5.3: Magnetic fields calculated for the three magnetic traps employed during the loading sequence. The z-trap (solid), compressed z-trap (dashed), and chip trap (dotted) are shown. The fields along the three perpendicular axes w, u and v are shown. Each curve in c), d), e) and f) is evaluated at the w coordinate of the respective trap minimum.

away from the chip mount. From this compressed z-trap, the atoms are transferred into the chip trap. The chip trap is created using the microscopic gold wire on the chip surface. The change in the Ioffe field between the macroscopic and microscopic trap does not result in heating if the fields are switched fast enough to ensure non-adiabaticity. Here, non-adiabaticity means that the atoms are not accelerated during the switching of the fields. The trap frequencies in the two traps are ~ 1 kHz, so that non-adiabaticity is ensured as long as the magnetic fields are switched faster than ~ 1 ms [88].

In the experiment, the bias fields are initialized to the calculated values, and then varied to optimize the atom number and trap shape. Table 5.1 shows the calculated and experimentally optimized applied fields for the different magnetic traps. The difference between the calculated and empirical values is of the order of a few Gauss. The difference is most probably due to stray magnetic fields in the vacuum chamber. Such stray fields of a few Gauss might be caused by residual magnetization of some of the parts used in the atom chip assembly. Stray fields could also be due to residual magnetic fields from nearby magnets from ion pumps and optical isolators. Background fields of a few Gauss are indeed present in the vicinity of the chamber, as verified with a Gaussmeter. However, it is difficult to measure the exact magnetic field inside the chamber, close to the atom chip surface. Manual optimization of the bias coil currents for each trap, albeit tedious, is therefore necessary.

Table 5.1: Parameters of the magnetic traps. Applied bias fields for the magnetic traps are given in the (x, y, z) coordinate system. The calculated and experimentally optimized bias field values are shown. The discrepancy is most probably due to stray magnetic fields in the chamber.

Parameter	Z-Trap	Compressed Z-Trap	Chip Trap
Current (A)	34.4	34.4	1.82
Trap Freq. (Hz)			
ω_u	170	258	556
ω_v	591	1213	1824
ω_w	590	1219	1759
Calc. Bias Field (G)			
B_x	21.48	41.89	7.73
B_y	10.59	10.59	2.12
B_z	10.59	10.59	2.12
Exp. Bias Field (G)			
B_x	21.48	41.89	6.44
B_y	10.59	10.59	2.12
B_z	14.35	14.35	5.17

5.4 Heating of the atom chip

To generate the chip trap potential, relatively large currents of several Ampere have to be pushed through a wire that is only 100 μm wide and 9 μm high.[1] At these currents, Joule heating becomes a concern. A semi-empirical theory of the Joule heating of atom chips has been developed in Ref. [115]. A resistive measurement of the heating of the atom chip in vacuo is shown in Fig. 5.4, and compared to the theory of Ref. [115] with no adjustable parameters. In this measurement, the current through the chip wire is pulsed for 10 ms, and the voltage is monitored using the monitor output on the chip wire power supply. The voltage is converted into a temperature using the known temperature coefficient of the resistance of gold. We found that filling the cooling dewar with ice water is enough to keep the atom chip from heating up more than 20 °C as long as currents of < 3 A are used. Filling the dewar with liquid nitrogen or dry ice turned out to be detrimental to the initial atom number in the MOT, most probably because the chip assembly starts to act like a cryogenic pump and depletes the Rb gas density in the MOT region.

[1] The atom chip is manufactured using photolithography and electroplating. In this method, the thickness of the wire is limited to be on the order of the smallest features present on the atom chip, which are the 10 μm wide RF-wires.

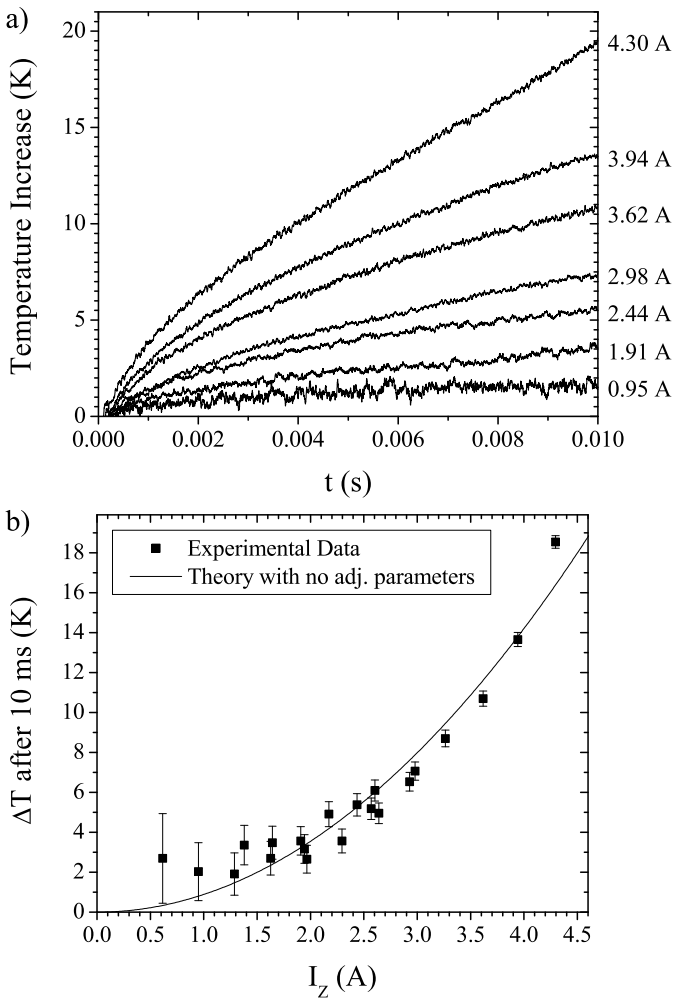

Figure 5.4: Measured heating of the atom chip z-wire. a) Time dependence of the heating for applied currents up to 4 A, b) Temperature increase within 10 ms as a function of applied current.

5.5 Loading sequence

A summary of the chip trap loading sequence is shown in Table 5.2. In the following sections, the different phases of the loading sequence are described in detail.

Table 5.2: Loading sequence of the atom chip trap. w_0 is the distance to the lowest chip mount surface, 80 μm away from the chip wire surface. Errors are standard deviations obtained by taking multiple absorption images.

Phase	Duration (ms)	N (10^6)	T (μK)	w_0 (μm)	FWHM$_v$ (μm)	FWHM$_w$ (μm)
MOT	9500	6.0 ± 0.96	245 ± 16	~ 1500	775 ± 33	909 ± 58
CMOT	30	2.64 ± 0.15	9.25 ± 0.26	1588 ± 20	526 ± 6	560 ± 11
Optical Pumping	1					
Z-Trap	134	1.32 ± 0.12	53 ± 4	1394 ± 5	542 ± 28	559 ± 26
Compressed Z-Trap	5	1.0 ± 0.13	86 ± 3	291 ± 5	403 ± 23	529 ± 30
Chip Trap	10+	0.58 ± 0.05	385 ± 45	147 ± 25	322 ± 22	400 ± 20

5.6 Mirror MOT

5.6.1 Mirror MOT parameters

The MOT is loaded with a cooling laser detuning of $\delta = -17$ MHz. The repumping laser is held on resonance. The Rb sources are usually run continuously at a current of 4 A per source. They can also be pulsed in short bursts or replaced with UV LIAD if necessary. The pressure in the chamber is typically 5×10^{-10} torr during operation of the MOT. The MOT coils are operated at a current of 30 A, corresponding to an axial (radial) field gradient of 14 $\mathrm{G\,cm^{-1}}$ (7 $\mathrm{G\,cm^{-1}}$) at the MOT position. To find the MOT initially, the wave plates that control the beam balancing and the polarization of the various beams are rough-adjusted using a power meter to check beam powers and a polaroid strip to check polarizations. The power is 4 mW per beam. The cooling beam profiles are Gaussian with a FWHM of 10 mm. The beams are rough-aligned to hit the center of each viewport and the center of the atom chip. This is done by attaching a pair of rubber bands to the bolt heads on each viewport such that the they mark the viewport centers. The +X- and -X-beams are then lowered from the center position so that roughly the top third of each beam is clipped by the atom chip mount. The fluorescence image of the MOT is monitored on a CRT TV via the live feed from cameras 1 and 2. The MOT cloud is found by changing the beam polarizations by small amounts until a weak fluorescence of the MOT atoms becomes visible. The polarizations, beam balancing, and beam pointing are adjusted to optimize the atom number in the MOT to give the brightest fluorescence image. The positioning of the MOT is then optimized. The centering of the MOT on the atom chip is checked via camera 2. The vertical distance from the MOT center to the chip mount is verified via camera 1. The ideal MOT position is perfectly centered with respect to the chip, about 1.5 mm below the chip mount surface. Large changes in the MOT position are made by physically adjusting the magnetic coil frame height

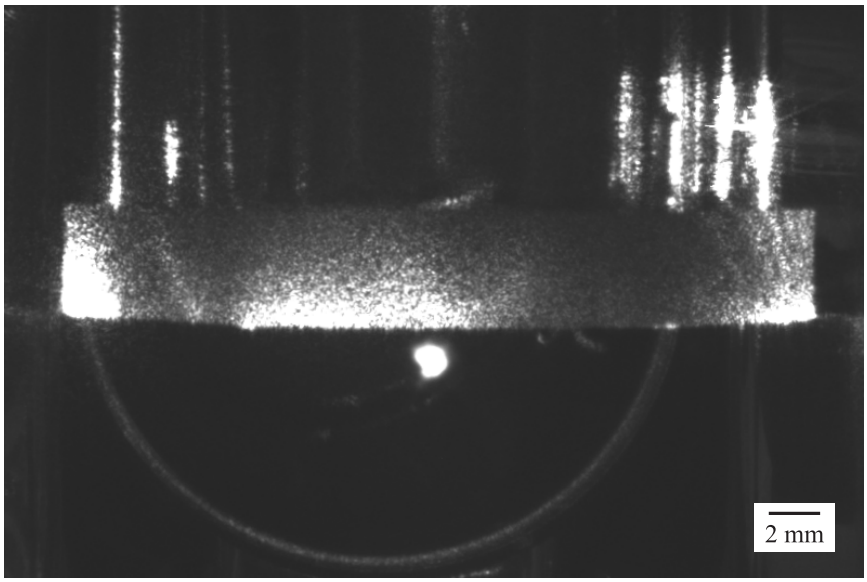

Figure 5.5: Fluorescence image of the cold atoms in the mirror MOT, hovering 1.5 mm below the chip.

and position. Small changes in the MOT position are made by adjusting the x-, y- and z-bias coil currents to move the zero of the magnetic field. After a change in MOT position, the beam pointing and polarization are re-adjusted for largest atom number. A photo of the MOT fluorescence after the MOT has been peaked up in this manner is shown in Fig. 5.5. A re-tweak of the MOT is performed every morning, in order to keep the atom number and position of the MOT stable over several months. Using the (x, y, z) coordinate system shown in Fig. 5.1b, the optimized bias field to position the MOT 1.5 mm below the atom chip surface was found to be $B_x = 0.71$ G, $B_y = -1.6$ G, and $B_z = 3.2$ G. The y-bias coil current had to be negative to optimize the MOT position. To achieve a negative y-bias coil current, the solid-state crossover relay input is held high during the MOT loading phase (see Section 3.6.4).

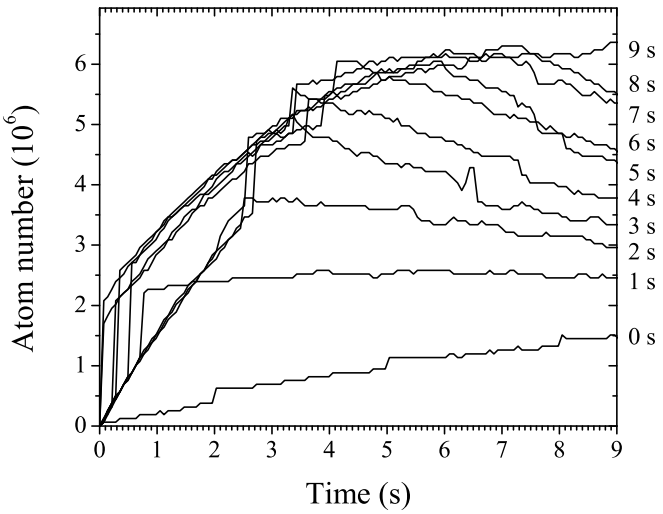

Figure 5.6: Loading curves of the MOT for various durations of LIAD pulses. The UV LEDs are pulsed on together with the MOT magnetic field at time zero. The LEDs are turned off after various delays. Each curve is labeled on the right by the delay used.

5.6.2 UV LIAD

The effect of turning on the UV LED arrays during the loading of the MOT is shown in Fig. 5.6. The LIAD loading curves are measured with a calibrated photodiode by imaging the MOT fluorescence onto the detector area. The Rb sources are off during these measurements. The increased loading rate due to LIAD is evident. The LIAD measurements were done with an early version of the atom chip that did not have a foil mirror on the surface. This is the reason for the comparatively low atom number. The gaps between the gold wires on the atom chip surface caused diffraction of the reflected MOT beams. This created holes in the MOT which prevented us from moving the MOT closer to the chip than 3 mm without losing all of the atoms.

5.6.3 Loading curve

After attachment of the foil mirror to the atom chip, the loading rate of the MOT was measured again. The measurement was done by imaging the MOT fluorescence onto

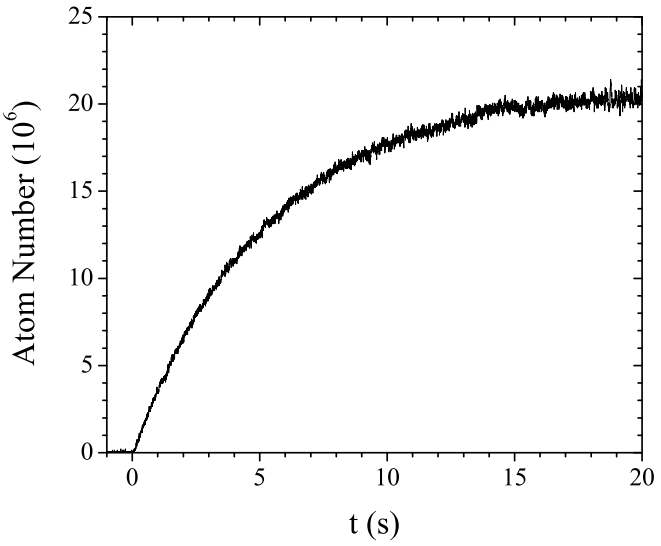

Figure 5.7: Loading curve of the MOT after installation of the foil mirror. During this measurement, the MOT was 3 mm away from the chip surface, just as during the LIAD measurements. The foil mirror increased the atom number by a factor of 3.5.

the entrance aperture of a photomultiplier tube. The atom number was calibrated separately using absorption imaging. The resulting curve is shown in Fig. 5.7. A maximum atom number of $N = 21 \times 10^6$ was measured with the foil mirror in place. In these measurements, the MOT was still ~ 3.0 mm below the atom chip surface, a distance that proved too far away to load the magnetic trap. The foil mirror enables us to move the MOT closer to the atom chip surface without losing all of the atoms. At the closer distance of 1.5 mm, the peaked up MOT contains $(6.4 \pm 1.5) \times 10^6$ atoms. The quoted shot-to-shot noise in the atom number, $\Delta N/N = 23\%$, was measured by analyzing 50 separate absorption images that were taken under the same conditions. It is approximately the same during all phases of the loading sequence.

5.6.4 Absorption images

In order to take an absorption image of the cold cloud, all lasers are switched off with the AOMs at a time t_0, typically after a 9.5 s long loading time of the MOT. The quadrupole and bias coil IGBTs are switched at the same time to turn off the magnetic fields. The camera is then triggered to take a pair of images in kinetics mode. The camera trigger goes high 21 ms before the first imaging beam pulse. The time of 21 ms was determined empirically, and is necessary to allow the camera shutter to open fully. The camera exposure time is set to 10 ms, which is the minimum exposure time that can be set on this camera model. The delay between kinetics mode exposures is set to 100 ms. During each of the two camera exposures, the imaging beam is pulsed once, with a pulse duration of 100 μs. The pulse duration is chosen so that the full dynamic range of the camera is utilized and the CCD array is not saturating. The pulse duration depends on the imaging beam power, which is typically 80 μW. The first imaging beam pulse is triggered after a delay τ measured from t_0. The second imaging pulse happens 100 ms later and is used as the background image. The imaging beam polarization and detuning are fine-tuned to maximize the contrast in the absorption image. A typical absorption image of the MOT is shown in Fig. 5.8. The atom number is obtained from an absorption image by fitting all pixels of the image to Eq. 3.6 and calculating N via Eq. 3.8. The MOT atom number deduced from the absorption image in Fig. 5.8 is 6.0×10^6.

5.6.5 Temperature

The temperature of the cold cloud is measured using time-of-flight absorption imaging (TOF). Several absorption images are taken at variable delays τ. Each image is fit to the Gaussian fit function, Eq. 3.6, using all the pixels in the image to find the full width at half maximum in the horizontal, $\mathrm{FWHM_v}$, and vertical, $\mathrm{FWHM_w}$, directions.

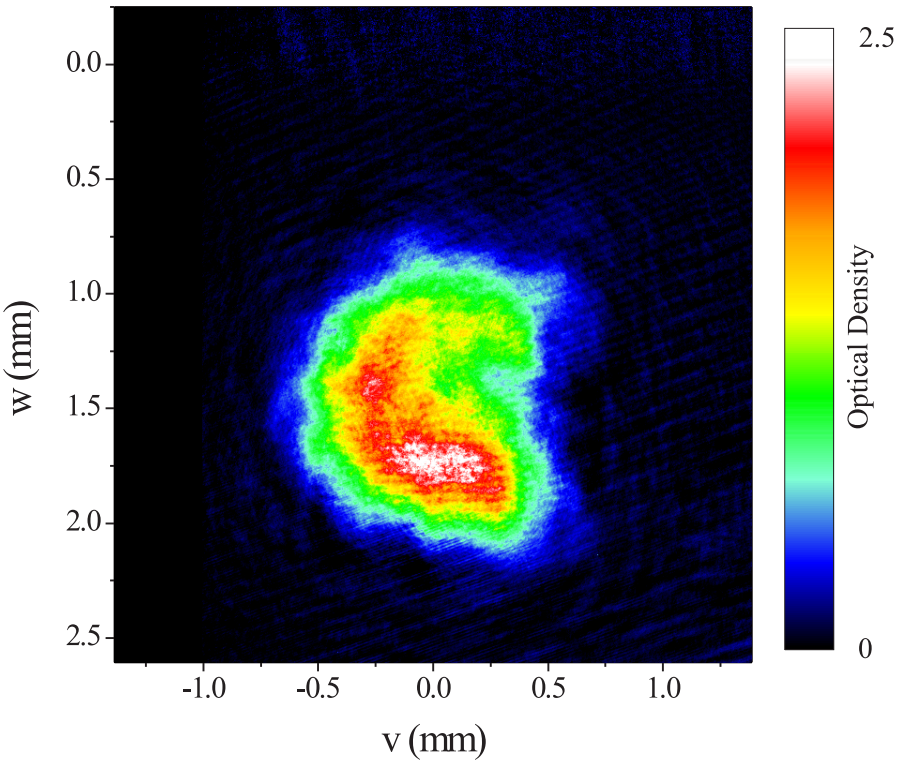

Figure 5.8: Absorption image of the MOT, taken while the MOT was on.

The temperature is obtained by fitting FWHM_v to the expression [130]

$$\mathrm{FWHM}(\tau) = \sqrt{\mathrm{FWHM}_0^2 + \frac{8\ln(2)k_B T}{m}\tau^2}, \tag{5.1}$$

where k_B is the Boltzmann constant, T is the temperature of the sample, m is the atomic mass, and FWHM_0 is the cloud size at zero delay time. A measured TOF curve for the MOT is shown in Fig. 5.9. The temperature of the MOT obtained from the fit is (245 ± 16) μK. The quoted error is the standard error from the fit. The MOT is slightly hotter than the Doppler temperature $T_D = 145$ μK. To reduce the temperature of the MOT, we employ a polarization gradient cooling phase.

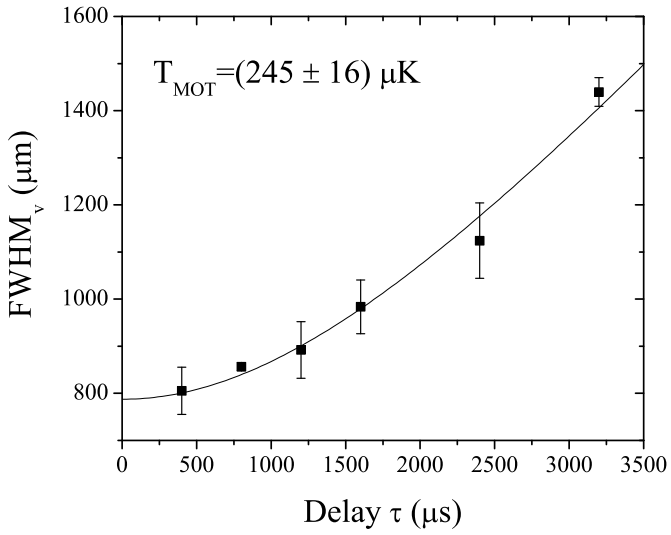

Figure 5.9: Time-of-flight temperature measurement of the MOT.

5.7 Cold MOT (CMOT)

Before loading the magnetic trap from the MOT, the atoms are cooled down in a cold MOT (CMOT) phase. The CMOT relies on polarization gradient cooling to lower the temperature below the Doppler limit. Due to polarization gradient cooling effects, the temperature in a MOT is proportional to the light shift parameter $\Lambda = \Omega^2/(|\delta|\Gamma)$ according to Eq. 2.90 [101]. By increasing the red-detuning of the cooling beams and decreasing the beam intensity, the temperature in the MOT can be lowered significantly. In our case, the coldest temperature in the CMOT is achieved by applying a 30 ms long CMOT phase at the end of the MOT phase. During the CMOT phase, the cooling laser is detuned from -17 MHz to -55.3 MHz and the power in each cooling beam is reduced from ~ 4 mW to ~ 2 mW. The repumping laser power is reduced from 1 mW to 30 μW. The parameters of the CMOT are determined empirically, optimizing for the lowest temperature and highest atom number.

An absorption image of the CMOT is shown in Fig. 5.10. The atom number deduced from the absorption image is $N = 2.64\times10^6$. The results of TOF temperature

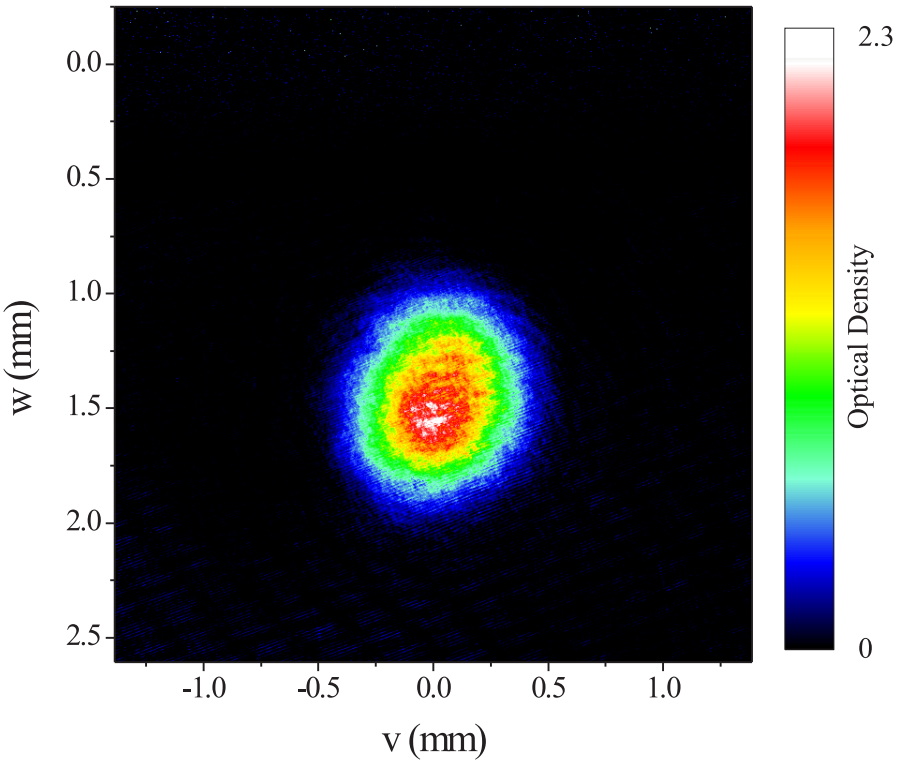

Figure 5.10: Absorption image of the cold MOT, taken at delay $\tau = 200\ \mu$s. The atom number deduced from this image is $N = 2.64 \times 10^6$.

measurements for the CMOT are shown in Fig. 5.11a). Each data point in Fig. 5.11 is the average of fits to nine separate absorption images. The error bars are the standard deviations across the nine fits. The error on the temperature is the standard error obtained from the two-parametric fit in T and FWHM_0. Also shown in Fig. 5.11 is the measured free fall of the cloud center, fit to

$$w(\tau) = w_0 + \frac{1}{2}\, g\, \tau^2, \tag{5.2}$$

with $g = 9.81\ \mathrm{m/s^2}$, to obtain the initial vertical position of the cloud $w_0 = 1.588 \pm 0.020$ mm. The temperature of the CMOT is $(9.25 \pm 0.25)\,\mu$K. Using Eq. 2.90 with the parameters of the CMOT stated above and the coefficient $C_\sigma = 0.52 \pm 0.03$

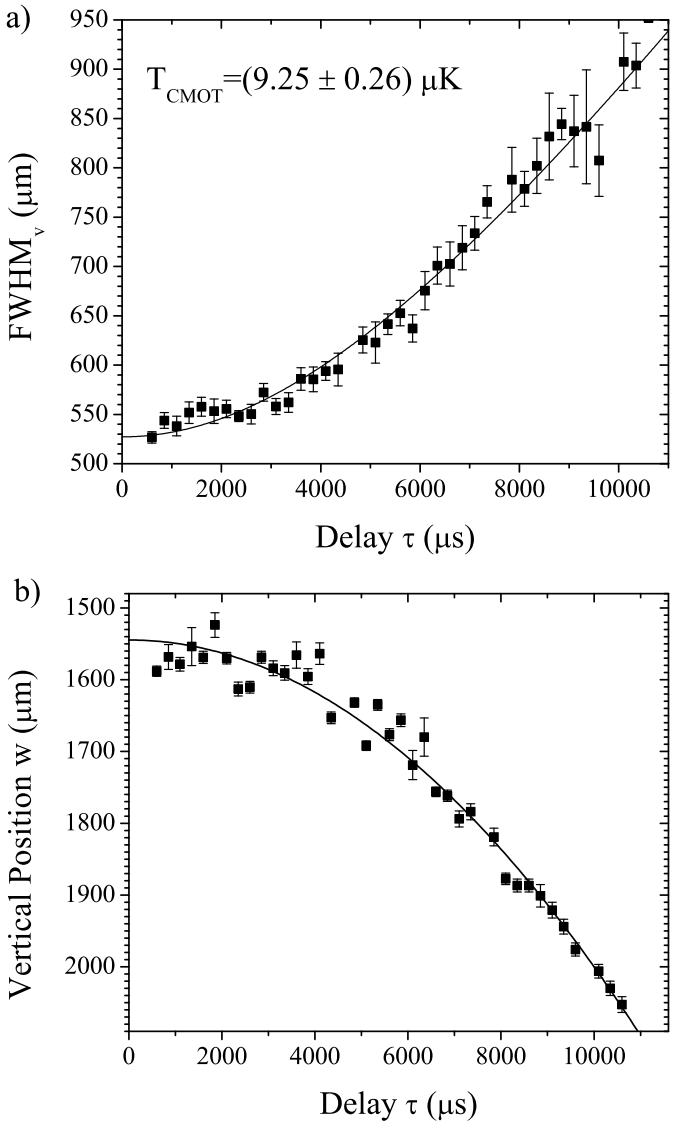

Figure 5.11: Time-of-flight temperature measurement of the cold MOT (a), and vertical center-of-mass position of the cloud (b).

for ^{87}Rb taken from Ref. [101], the predicted temperature is (9.38 ± 0.3) μK, in agreement with the measured temperature.

5.8 Optical pumping

Before the magnetic trap is loaded, an optical pumping pulse transfers the majority of the atomic population into the magnetically trapped $(F = 2, m_F = 2)$ weak-field seeking magnetic sublevel of the ground state. To prepare for the optical pumping pulse after the 30 ms long CMOT phase, the cooling light and the repumping light are first switched off. At the same time, the MOT coils and all bias fields are switched off in < 500 μs. The magnetic fields are then switched into the optical pumping configuration. 380 μs after the light has been shut off, the y-bias current has decayed sufficiently, and the solid-state crossover relay is switched from high to low to reverse the current direction on the y-bias coils. After reversal of the current direction, a positive current setting on the y-bias coils will now create a field pointing in the positive y-direction. 400 μs after the light has been shut off, the bias coils are then switched to their new values. The x-bias field is kept at 0 G, while the y-bias and z-bias fields are switched to 2 G each. This creates a field of $B_u = 2.8$ G that points in the direction of the optical pumping beam and defines the quantization axis during optical pumping. After a delay of 1 ms, long enough for the fields and any residual eddy currents to settle, a 120 μs long optical pumping pulse is applied. The polarization and duration of the optical pumping pulse are fine adjusted by maximizing the atom number in the magnetic trap. Applying the optical pumping pulse increases the atom number loaded into the magnetic trap by a factor of four. The magnetic trap is the subject of the next section.

5.9 Macroscopic magnetic trap (z-trap)

The Ioffe-Pritchard type trapping potential of the macroscopic magnetic wire trap (z-trap) is generated by running current through the copper z-shaped wire and simultaneously applying a bias field. To achieve the best loading from the CMOT into the z-trap, we apply a current of 34.4 A to the copper z-wire. The current runs through the central segment of the wire in the positive u-direction. The external bias field points mostly in the positive x-direction, but a small component in the y- and z-directions is also applied to fine tune the Ioffe field. In order to switch the x-bias field rapidly within 500 μs the high voltage capacitor circuitry, detailed in Section 3.6.4, is employed. The x-bias field is switched on 110 μs after the end of the optical pumping pulse. At the same time, the copper z-wire current is switched on. The switching time of the copper z-wire is slowed down to match that of the x-bias coils using a dummy coil, as described in Section 3.4.7. The y- and z-bias fields are used to adjust the Ioffe field. They do not have to be switched as fast as the x-bias. The y- and z-bias fields are therefore switched to their new values within 1-2 ms, using the current programming inputs on the power supplies. Starting from the calculated values, the bias fields are then adjusted empirically to optimize the atom number, position, and shape of the z-trap. The empirically determined optimum values for the z-trap bias fields are $B_x = 21.5$ G, $B_y = 10.6$ G and $B_z = 14.4$ G. The y- and z-components result in a Ioffe compensation field of $B_u = 17.6$ G in the longitudinal u-direction and a small component of $B_w = -2.66$ G pointing vertically upwards. The empirically optimized bias fields differ by a few Gauss from the calculated values. The difference is probably caused by stray magnetic fields in the chamber. The optimum pre-charge voltage on the x-bias capacitor is 230 V. This voltage gives the fastest switching without any overshoot of the current.

An absorption image of the z-trap is shown in Fig. 5.12, taken after a 133 ms long

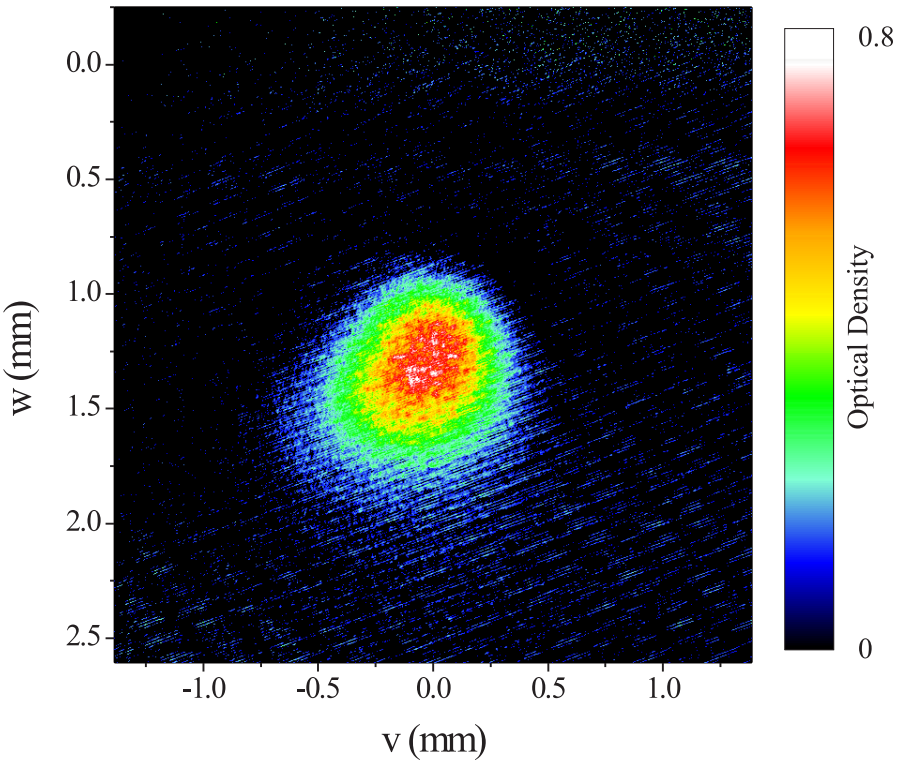

Figure 5.12: Absorption image of the z-trap, taken at delay $\tau = 500$ μs. The z-trap was loaded for 133 ms. The atom number deduced from this image is $N = 1.02 \times 10^6$.

z-trap phase during which the MOT was off. The image was taken at a delay $\tau = 500$ μs. In this image, the atom number is $N = 1.02 \times 10^6$. Some heating is observed when loading the magnetic trap from the CMOT. The heating can be attributed to the mode mismatch between the z-trap potential and the MOT which results from the anharmonic nature of the wire trap potential compared to the harmonic MOT potential (see Fig. 5.3). Results of temperature measurements for the z-trap are shown in Fig. 5.13, also taken after a 133 ms long z-trap phase. The measurement and analysis is done in the same way as for the CMOT TOF measurements. The resulting z-trap temperature is $T = (53 \pm 4)$ μK. The estimated initial center position deduced

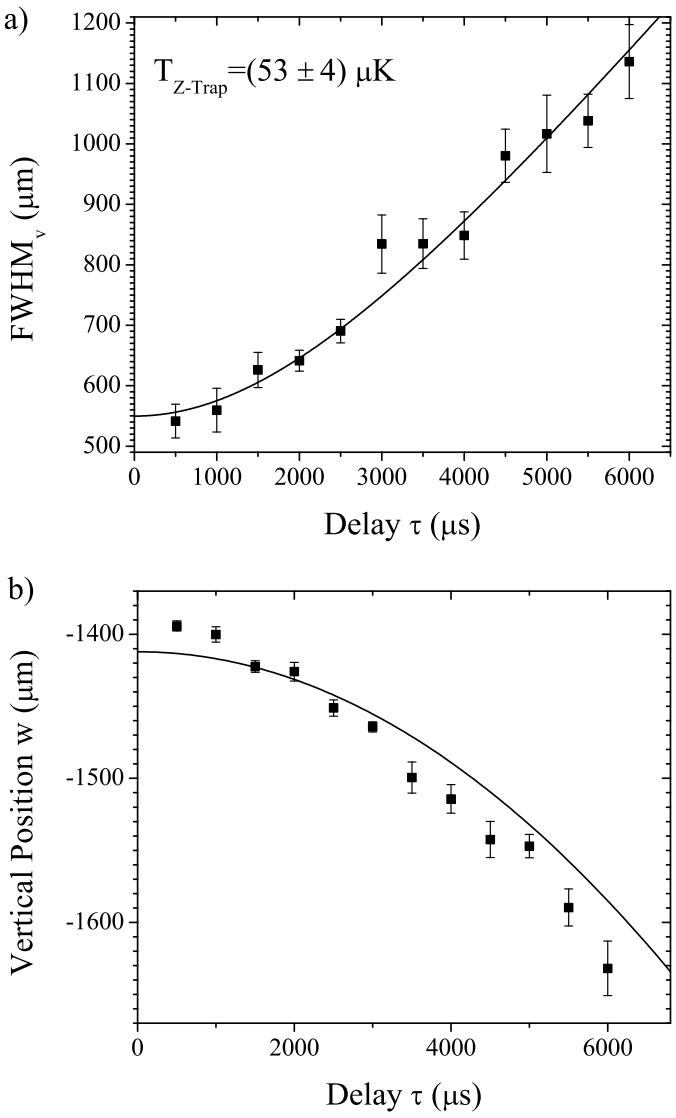

Figure 5.13: Time-of-flight temperature measurement of the z-trap (a), and vertical center-of-mass position of the cloud (b).

from the fit to the free fall equation is $w_0 = 1.394 \pm 0.005$ mm.

Before loading the microscopic atom chip trap, the z-trap is compressed to move the atoms closer to the chip surface.

5.10 Compressed z-trap

Compression of the z-trap is done by slowly ramping up the x-bias coil current from 2.7 A to 5.2 A. This increases the bias field in the u-direction from $B_u = 21.5$ G to $B_u = 41.9$ G. A ramp duration of 125 ms was found to give the largest atom numbers in the compressed z-trap and cause the least amount of heating. The compression ramp moves the trap minimum closer to the chip surface, from a distance of 1.4 mm to a distance of 300 μm. The bias field ramp is applied 1.2 ms after the z-trap is turned on. After the ramp, the fields are held constant for 5 ms before any TOF measurements are done.

An absorption image of the compressed z-trap, taken at delay $\tau = 500$ μs, is shown in Fig. 5.14. The atom number deduced from the image is $N = 1.04 \times 10^6$. The atom number in the compressed z-trap is the same as in the uncompressed z-trap. This indicates that we do not lose any atoms during the compression time. Results of TOF measurements for the compressed z-trap are shown in Fig. 5.15, taken in the same manner as the TOF measurements for the CMOT and the z-trap. The temperature of the compressed z-trap from the fit to the TOF curve is $T = (86 \pm 3)$ μK, and the vertical position of the cloud is $w_0 = 300$ μm. The compression is slow enough to only cause a small amount of heating of the sample. The center of the atom cloud is now close enough to the atom chip surface so that the microscopic trap can be loaded.

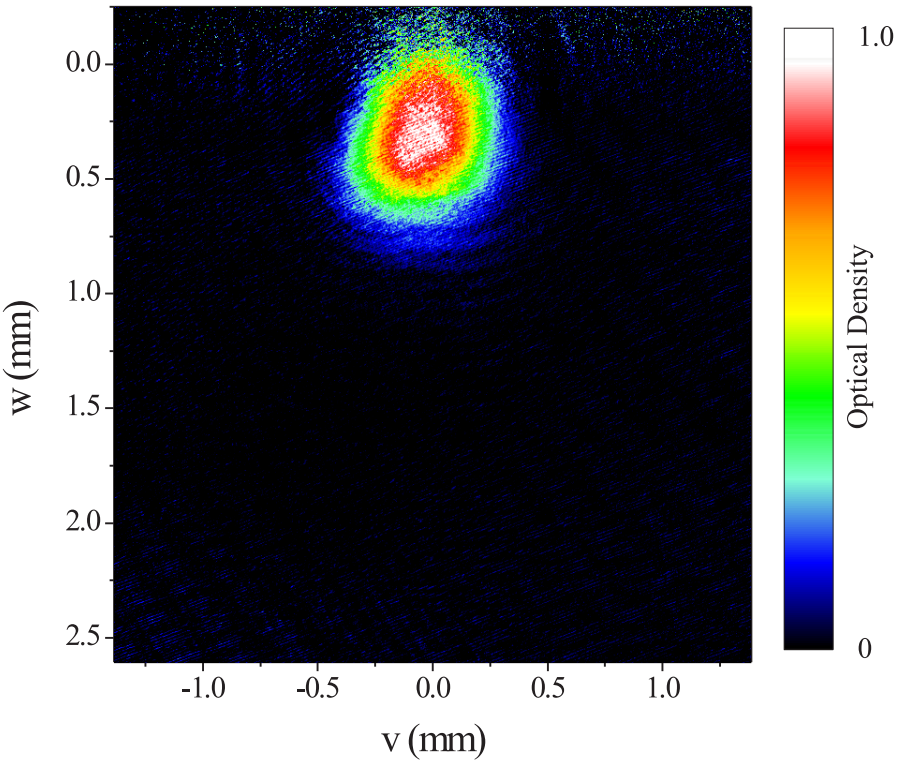

Figure 5.14: Absorption image of the compressed z-trap, taken at delay $\tau = 500$ μs. The atom number deduced from this image is $N = 1.04 \times 10^6$.

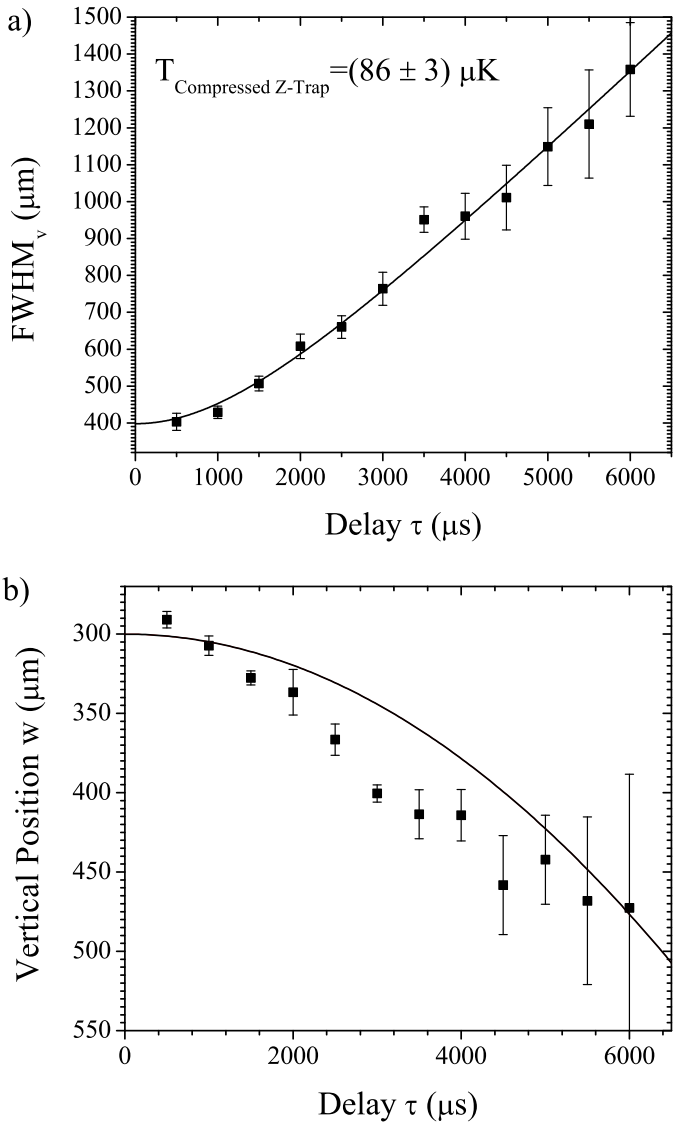

Figure 5.15: Time-of-flight temperature measurement of the compressed z-trap (a), and vertical center-of-mass position of the cloud (b).

5.11 Microscopic magnetic trap (chip trap)

The microscopic magnetic wire trap (chip trap) potential is created by running current through the microscopic z-shaped gold wire on the atom chip surface. We use a chip wire current of 1.82 A to overlap the chip trap to the compressed z-trap. Before the chip current is switched on, the y- and z-bias coils are ramped to their chip trap values, using 250 μs long ramps. Each ramp begins 250 μs before the end of the compressed z-trap phase. At the same time, the x-bias coils are switched off using the IGBTs. A delay of 50 μs after they have been switched off, the x-bias coils are switched over to the second Kepco power supply unit depicted in Fig. 3.21. The second unit has been idle for seconds, and is preset to the x-bias current needed for the operation of the chip trap. The switching is done using the "PSU select" circuit described in Section 3.6.4. This is done to circumvent problems we found with the Kepco supply changing currents erratically on time scales of ms during the atom chip loading sequence. 50 μs after switching the x-bias coils to the second supply, they are switched on using the IGBTs. After a short delay of 10 μs, the second high voltage capacitor is discharged into the x-bias coils to quickly switch on the current to its final value. After all bias fields are switched on, the chip wire current shown in Fig. 2.20 is turned on in < 100 μs using the analog programming voltage on the High Finesse power supply. The optimum bias fields for the chip trap are found to be $B_x = 6.44$ G, $B_y = 2.12$ G, and $B_z = 5.17$ G.

An absorption image of the chip trap is shown in Fig. 5.16. The result of a TOF measurement of the chip trap is shown in Fig. 5.17. At close distances to the chip mount surface, the imaging beam shows more interference noise due to diffraction. In addition, The density distribution in the chip trap is highly asymmetric and does not fit well to the two-dimensional Gaussian fit function. To obtain the data shown in Fig. 5.17, 15 absorption images were taken at each delay and averaged to reduce the

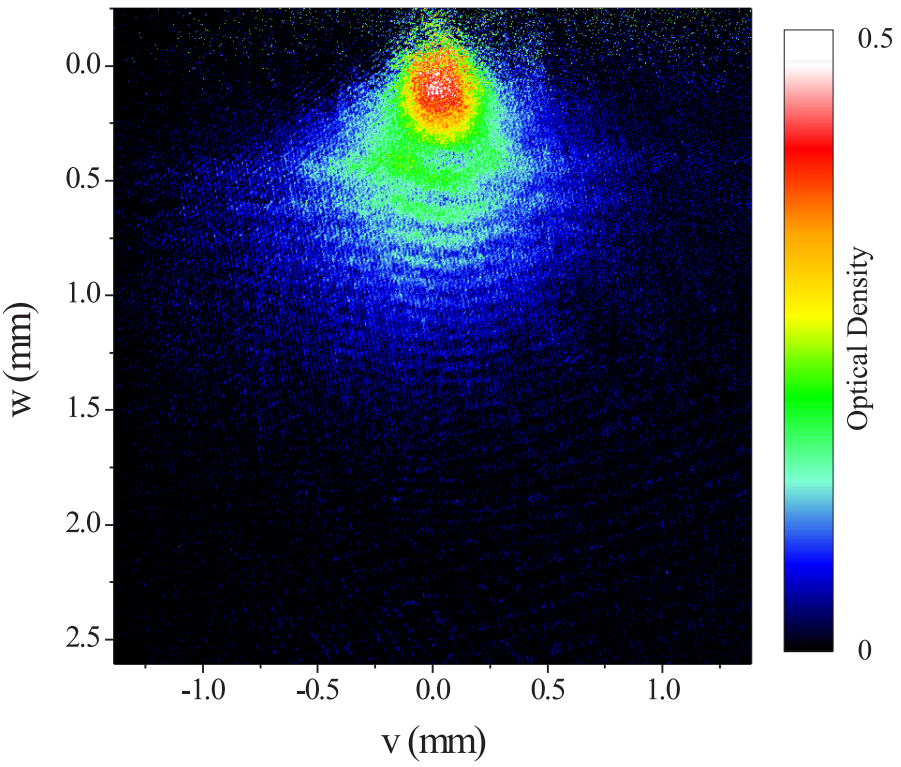

Figure 5.16: Absorption image of the chip trap while it is on. The atom number deduced from this image is $N = 5.8 \times 10^5$.

noise in the images. The resulting average image was then fit to a one-dimensional Gaussian distribution along a line in the v-direction. For each image, the position of the line was chosen manually to go through the point of peak optical density. The error bars of each data point in Fig. 5.17 represent the standard error from the 1D Gaussian fits. The approximate temperature obtained this way is $T \approx (384 \pm 44)\ \mu$K. The initial position of the cloud is $w_0 = (147 \pm 25)\ \mu$m. The atoms in the chip trap are significantly hotter than in the compressed z-trap, and about 40% of the atoms are lost during the transfer. The heating and atom loss is most probably due to imperfect mode-matching between the compressed z-trap and the chip trap. The

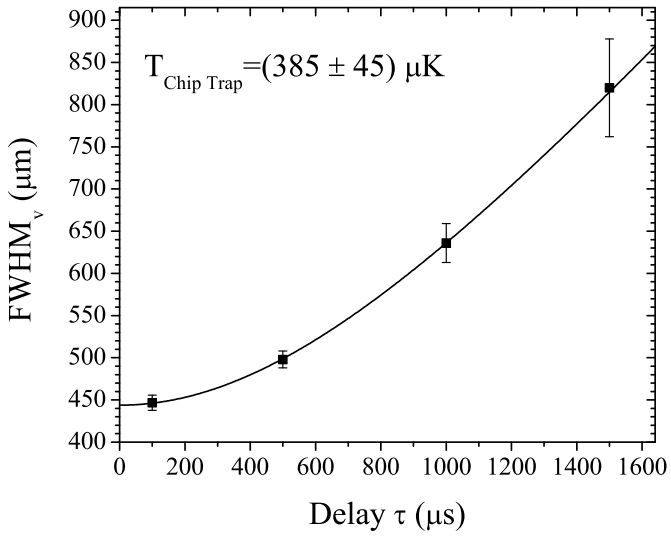

Figure 5.17: Time-of-flight temperature measurement of the chip trap.

trap frequencies of the chip trap are higher than those of the compressed z-trap, due to the shorter central segment of the wire, and the chip trap is more anharmonic than the compressed z-trap. This can cause heating when atoms are captured in the side regions or anharmonic regions of the trap where the potential energy is higher than in the compressed z-trap. The atoms gain extra kinetic energy as they are accelerated by the new trapping potential. This effect causes heating of the atoms. If necessary, the atoms in the chip trap could be cooled further by evaporative cooling.

5.12 Outlook

Once in the chip trap, the atoms are close enough to the chip surface to enable future experiments to investigate the interactions of Rydberg atoms with the nearby conducting surface through surface plasmons and polaritons. Alternatively, adiabatic RF potentials can be employed on the chip to split the atom cloud into two. The interactions of Rydberg excitations in one of the clouds with Rydberg excitations in the other cloud through long-range dipole-dipole interactions could then be investigated.

The proposed probing scheme for Rydberg atoms on the chip is electromagnetically induced transparency (Rydberg EIT). In an effort to better understand the use of EIT as a sensitive probe for Rydberg atoms, we decided to first perform measurements in a vapor cell. In the vapor cell, experiments can be done continuously without having to wait ~ 10 seconds for the magnetic traps to reload between two measurements. To investigate the sensitivity of Rydberg EIT to external perturbations, we couple the three-level system to a resonant microwave field. In addition to an extraordinary high sensitivity to the microwave amplitude, the resulting coupled 4-level system exhibits polarization effects that depend on the effectively degenerate hyperfine structure of the involved Rydberg states. These Rydberg EIT experiments are the subject of the next chapter.

Chapter 6

Ladder-type EIT with Rydberg atoms

6.1 Introduction

In this chapter, measurements on the room temperature 4-level ladder-type Rydberg EIT system are presented, in which two Rydberg levels are coupled via an applied microwave field. The dependence of the probe transmission spectrum on the microwave power and polarization is investigated. The polarization dependence is explained theoretically by taking all the magnetic sublevels of the system into account. The measurements were done to better understand the sensitivity of Rydberg EIT to external perturbations. These experiments serve as a model for future measurements on the atom chip, where we intend to use Rydberg EIT to probe the coupling of cold Rydberg atoms to surface plasmons and polaritons, and to probe interactions between cold Rydberg atoms. Due to the high sensitivity of Rydberg atoms to electric fields, the setup presented here also has potential applications as an ultra-sensitive traceable narrow-band microwave detector.

Polarization effects in the 3-level ladder-type EIT system were first observed over ten years ago by Fulton et al. [131]. The authors of Ref. [131] were able to model their system by multiplying and adding single-photon transition probabilities to arrive at effective two-photon transition probabilities between initial and final magnetic sublevels. The authors pointed out that the simplified model is only valid as long as all hyperfine splittings are larger than the largest natural linewidth in the system. Just recently, polarization effects in EIT were investigated by Moon and Noh [132] in the 3-level ladder-type system, and the authors specifically stressed the importance of taking into account all magnetic sublevels in a numerical simulation of the full density matrix evolution to explain their observations. In both experiments, the

upper state was not a Rydberg state, the hyperfine structure was resolvable, and the observed polarization effects manifested themselves in changing EIT peak heights for the different resolved hyperfine transitions. The systems studied were not coupled to a fourth level. A 4-level ladder-type Rydberg EIT system more similar to the one studied here was recently investigated in a MOT by C. S. Adams et al. [91]. The authors had to take into account all magnetic sublevels coupled by the laser fields to explain the observed transmission lineshapes. However, a specific optical pumping scheme and combination of polarizations was used, and the polarization dependence of the EIT lineshape was not further investigated. To our knowledge, the results presented here are the first observation of polarization effects in the 4-level ladder-type Rydberg EIT system.

6.2 Cs measurements

6.2.1 Methods

Initial EIT measurements were done on a Cs 4-level ladder-type system. The excitation scheme is shown in Fig. 6.1a, and a sketch of the experimental setup is shown in Fig. 6.1b. The Cs is contained in a 10 cm long vapor cell at room temperature. A probe beam, a coupling beam and microwave radiation are overlapped in the cell. The absorption of the probe light is detected as the coupling laser is scanned. The probe laser is a homebuilt external cavity diode laser, locked via saturated absorption spectroscopy, and shifted to the Cs $6S_{1/2}, F = 4 \rightarrow 6P_{3/2}, F = 5$ resonance at 852 nm. The probe light has a power of 120 μW and is collimated to a FWHM of ~ 2.5 mm. The coupling laser is a Coherent-699 dye laser tuned to the $6P_{3/2}, F = 5 \rightarrow 59D_{5/2}$ transition at 509.1695 nm. The coupling light has a power of 4.8 mW, and is collimated to a FWHM of 2.5 mm. It is chopped with a chopper wheel at 800 Hz for lock-in detection. The microwaves, tuned to the $59D_{5/2} \rightarrow 57F_{7/2}$ transition at

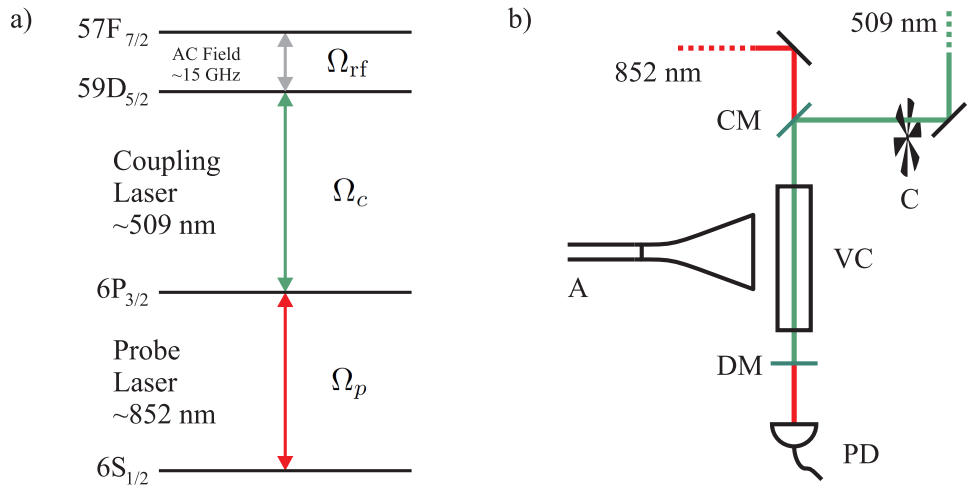

Figure 6.1: Cs Rydberg EIT setup. a) Excitation scheme, b) experimental setup. CM: cold mirror, C: chopper wheel, VC: Cs vapor cell, DM: dichroic mirror, PD: photodiode, A: microwave horn antenna.

$\sim$ 15 GHz, are aimed at the vapor cell from the side using the assembly described in Section 3.8.1. The distance from the antenna exit aperture to the center of the cell is 2.5 cm. Due to the horn antenna, the microwave beam is divergent and has a FWHM of $\sim$ 5.6 cm at the center of the vapor cell. The microwave power is varied in the experiment between 0 and 141 μW. The microwaves are linearly polarized in the vertical direction. Both laser beams are linearly polarized in the horizontal direction. Before entering the vapor cell, the coupling beam is overlapped with the probe beam using a cold mirror. After exiting the cell, the probe light passes through a dichroic mirror and is detected with a photodiode.[1] The coupling light is back reflected by the dichroic mirror so that it is also counterpropagating with the probe light. Lock-in detection is used to increase the signal-to-noise ratio.

[1]All photodiodes used are equipped with the respective narrow bandwidth (FWHM = 10 nm) interference filters, in this case it is a 852 nm filter (Thorlabs FL850-10).

6.2.2 Results

When measuring the probe absorption spectrum, we tune the microwave frequency to obtain the largest effect on the probe absorption. We see the largest effect at a microwave frequency of 15.581943344 GHZ. This agrees remarkably well with the predicted resonance frequency for the $59D_{5/2} \rightarrow 57F_{7/2}$ transition of 15.581920081 GHz, calculated using the known quantum defects as described in Section 2.3.2.

In the Cs system, we observe an effect from the microwaves at microwave powers of $\sim$ 500 nW, corresponding to AC electric field amplitudes of $\sim$ 1 mV/cm. This sensitivity is comparable to the best commercially available antenna-based microwave detectors. The high sensitivity of the system is due to the large transition dipole moments associated with the Rydberg-to-Rydberg transitions. A large transition dipole moment translates into a large Rabi frequency on these transitions, which is observed in the experiment as a splitting of the EIT peak. The sensitivity is therefore only limited by the EIT linewidth. In the Rydberg EIT system, the EIT linewidth can in principle be decreased as low as the natural linewidth of the Rydberg states of $\sim 2\pi \times 2$ kHz [133]. A reduction of the EIT linewidth could be achieved by using ultra-narrow linewidth lasers and reducing the probe intensity, or by using noise correlation spectroscopy [74] as detection method. A splitting of the EIT lineshape due to the microwaves can in principle be detected when it is a factor of 10^2 smaller than the FWHM of the main feature, which is routinely achieved when locking diode lasers to the side of a Lamb dip in saturation absorption spectroscopy. Employment of such methods, and a reduction of the linewidth from 10 MHz to $<$ 2 kHz, would make this system sensitive to AC electric field amplitudes of $<$ 10 nV/cm. For comparison, current state-of-the-art traceable RF electric field sensors based on the electro-optic effect in nonlinear crystals such as LiNbO3 have sensitivities on the order of 10 μV/cm [134, 135]. Since the microwave Rabi frequency is proportional to the transition dipole

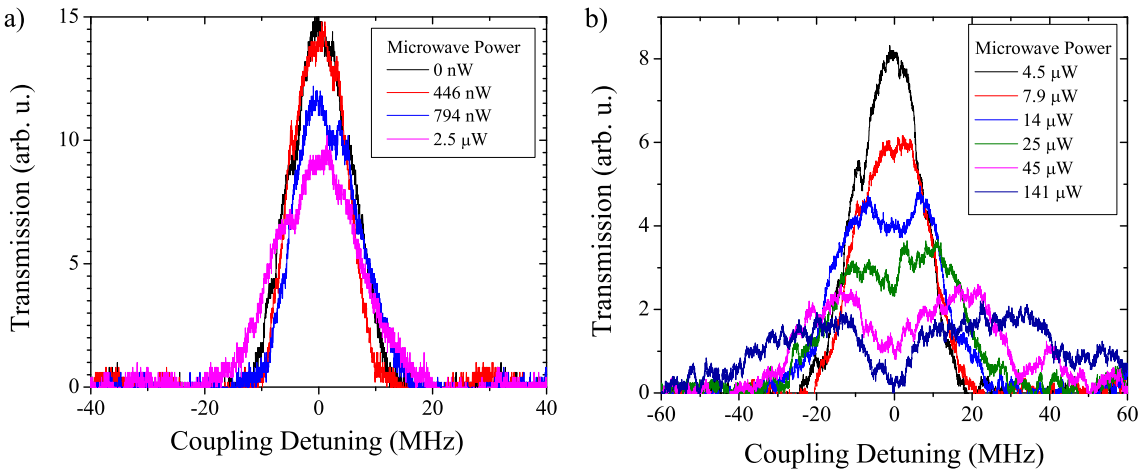

Figure 6.2: Measured EIT in Cs. Shown is the probe transmission vs. detuning of the coupling beam. a) low microwave powers, b) high microwave powers. The microwaves cause a broadening and splitting of the EIT peak.

moment between nearby Rydberg states, which scales as n^2, the sensitivity can be further increased by using higher Rydberg states. Using $n > 100$ instead of $n \approx 50$, the sensitivity can in principle be brought into the range of a few nV/cm, which would be more sensitive than any currently available microwave detector. In addition, a microwave detector based on this system is inherently traceable, since it depends only on the atomic properties and does not require calibration.

In Fig. 6.2, measured probe transmission spectra are shown for different microwave powers. As the microwave power is increased, the EIT peak first decreases in amplitude and broadens. At intermediate microwave powers, the expected absorption dip appears in the center of the EIT peak. At the largest microwave powers, the EIT peak is split into two separate peaks. The appearance of the absorption dip and the splitting of the EIT peak are both predicted by the theory described in Section 2.4.3 and plotted in Fig. 2.10. An unknown dephasing mechanism leads to the additional broadening and reduction of the peak heights with increasing microwave power. Common sources of dephasing are collisional broadening and transit time broadening.

Collisional broadening is due to collisions between ground state atoms and Rydberg atoms. It is estimated to be < 3 MHz/Torr [136]. The pressure in the cell is given by the vapor pressure of Cs at room temperature, $P \approx 2$ μTorr, and collisional broadening should therefore be negligible. Transit-time broadening is due to the limited interaction time as atoms move through the laser beam at thermal velocities. The transit-time limited linewidth is given by [137]

$$\delta_\nu = \frac{4 \ln 2}{2\pi} \frac{|\boldsymbol{v}|}{\mathrm{FWHM}}, \tag{6.1}$$

where $|\boldsymbol{v}|$ is the mean thermal velocity and FWHM is the laser spot size. This gives ~ 1.3 MHz for a laser spot size of FWHM $= 100$ μm and a mean thermal velocity $v = 300$ m s^{-1}. The spot size in the experiments is 2.5 mm, and therefore transit time broadening is also negligible. Another source of dephasing is the coupling of the system to other Rydberg levels through black-body radiation. The black-body decay rates of the Rydberg states around $n = 50$ are on the order of 1 kHz, which is negligible. The observed dephasing is most probably due to diffuse reflection of microwaves from the optical table surface, which we identified as a source of dephasing in later experiments with Rb.

In Fig. 6.3, the effect of detuning the microwaves from resonance is shown. The frequency of the absorption dip changes with the three-photon detuning. This is similar to 3-level EIT systems, where the frequency of the EIT signal was shown to depend only the two-photon detuning [49].

Further measurements were done on the ^{87}Rb system, and are described in the next section.

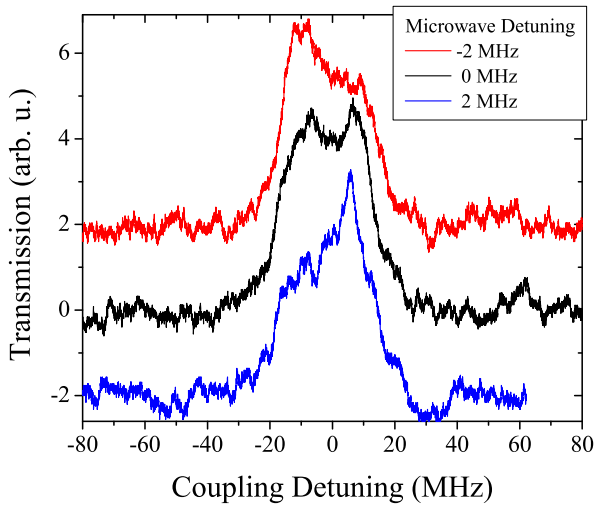

Figure 6.3: Effect of detuning the microwaves in the Cs system, measured at a microwave-power of 14 μW.

6.3 Rb measurements

6.3.1 Methods

The excitation scheme used for EIT measurements in the ^{87}Rb 4-level ladder-type system is shown in Fig. 6.4a, and a sketch of the experimental setup is shown in Fig. 6.4b. The Rubidium is contained in a 1 cm long vapor cell, heated to 85°C. In order to prevent the rubidium from condensing on the cell windows, the cell is situated in an oven. The oven has dimensions of $\sim$ 4" $\times$ 4" $\times$ 4" and is made out of five AR coated square windows (Edmund Optics NT46-103) that were glued with high-temperature epoxy. The oven is heated by heating an aluminum block, dimensions $\sim$ 1" $\times$ 1" $\times$ 1", with a cartridge heater. The probe beam is derived from the imaging beam in the atom chip setup. It is on resonance with the $5S_{1/2}, F = 2 \rightarrow 5P_{3/2}, F = 3$ transition, and has a FWHM of 1.9 mm after it exits the fiber. The probe power is $\sim$ 89 μW. A homebuilt noise-eater feedback loop is used to stabilize the power of the probe beam. Before it enters the vapor cell, a piece of the probe beam is

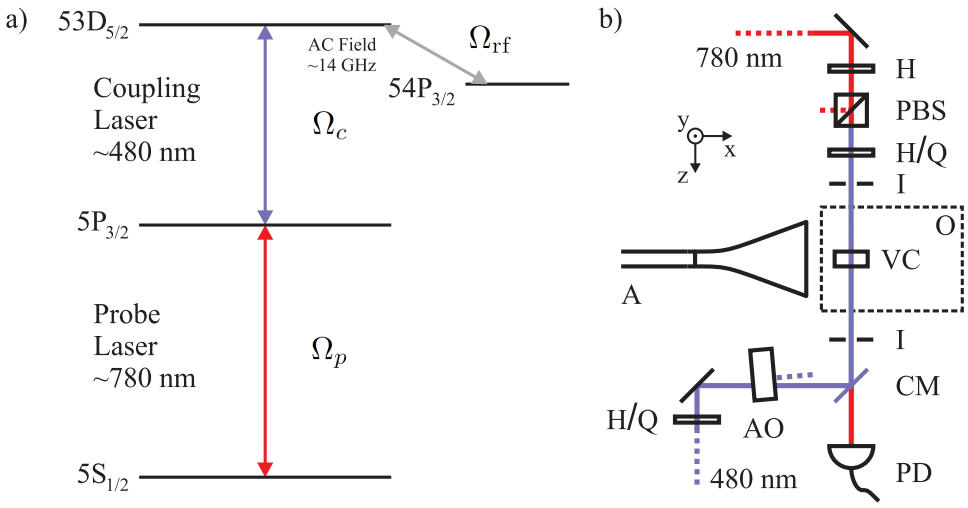

Figure 6.4: Rb EIT setup. a) Excitation scheme, b) experimental setup. H: half-wave plate, PBS: polarizing beamsplitter cube, H/Q: half-wave plate or quarter-wave plate, I: iris, O: oven, VC: Rb vapor cell, CM: cold mirror, AO: accousto-optic modulator, PD: photodiode.

split off with a non-polarizing beamsplitter cube and directed onto a photodiode to measure the probe power. The photodiode signal is used as the error signal and fed into a FPGA-based PID controller identical to the one described in Appendix A. The output signal of the PID is connected to the power modulation input on the imaging AOM (AOM nr. 3 in Fig. 3.4) to close the loop. The coupling beam is generated by the Rydberg excitation laser described in Section 3.7 and is tuned to the transition $5P_{3/2}, F = 3 \rightarrow 53D_{5/2}$ at 480.0049 nm. It has a FWHM of ~ 1.5 mm and a power of ~ 4 mW. Before the coupling beam enters the cell, it is passed through an AOM and modulated at ~ 100 kHz for lock-in detection. The coupling beam is scanned slowly over the EIT peak at a rate of ~ 1 MHz s^{-1} by changing the length of the Fabry-Perot reference cavity with a piezoelectric transducer (see Fig. 3.23). The microwaves are tuned to the $53D_{5/2} \rightarrow 54P_{3/2}$ transition at ~ 14 GHz and are coupled in from above. The microwave beam exiting the horn antenna has an

angular divergence of 30°. From the distance between antenna and cell, $d = 2.54$ cm, we calculate the FWHM of the microwave beam to be 5.7 cm. The power of the microwaves is reduced from the set value at the generator by 3.5 dB due to the losses in the isolator and the directional coupler (see Section 3.8.1). The polarization of the microwaves is varied by rotating the antenna. The polarizations of both laser beams are filtered with polarizing beamsplitter cubes and adjusted with half- or quarter-wave plates. A cold mirror is used to overlap the coupling beam with the probe beam in a counterpropagating geometry. The probe absorption is detected on a photodiode.

The Cartesian coordinate system shown in Fig. 6.4b) is used when discussing beam polarizations. The z-axis is parallel to the probe beam propagation direction, and is chosen as the quantization axis.

6.3.2 Results

In ^{87}Rb, we observe the largest effect on the probe absorption spectrum at a microwave frequency of 14.2368 GHz, in reasonable agreement with the calculated value of 14.2318 GHz from the known quantum defects.

The measured probe transmission spectra for different microwave powers are shown Fig. 6.5a. Here, the probe and coupling beams are circularly polarized and the microwaves are linearly polarized in the x-direction. The results are similar to those obtained with Cs. At low powers, the microwaves cause a broadening and a reduction of the amplitude of the EIT transmission peak. At intermediate powers, the expected absorption dip appears inside the EIT transmission peak. At larger powers, the EIT peak is split into two peaks by the microwaves. Results of the corresponding calculation with no adjustable parameters are shown in Fig. 6.5b. The calculation is done by solving the density matrix equations in the 4-level system in steady state. The results are integrated over the thermal velocity distribution of atoms in the vapor cell

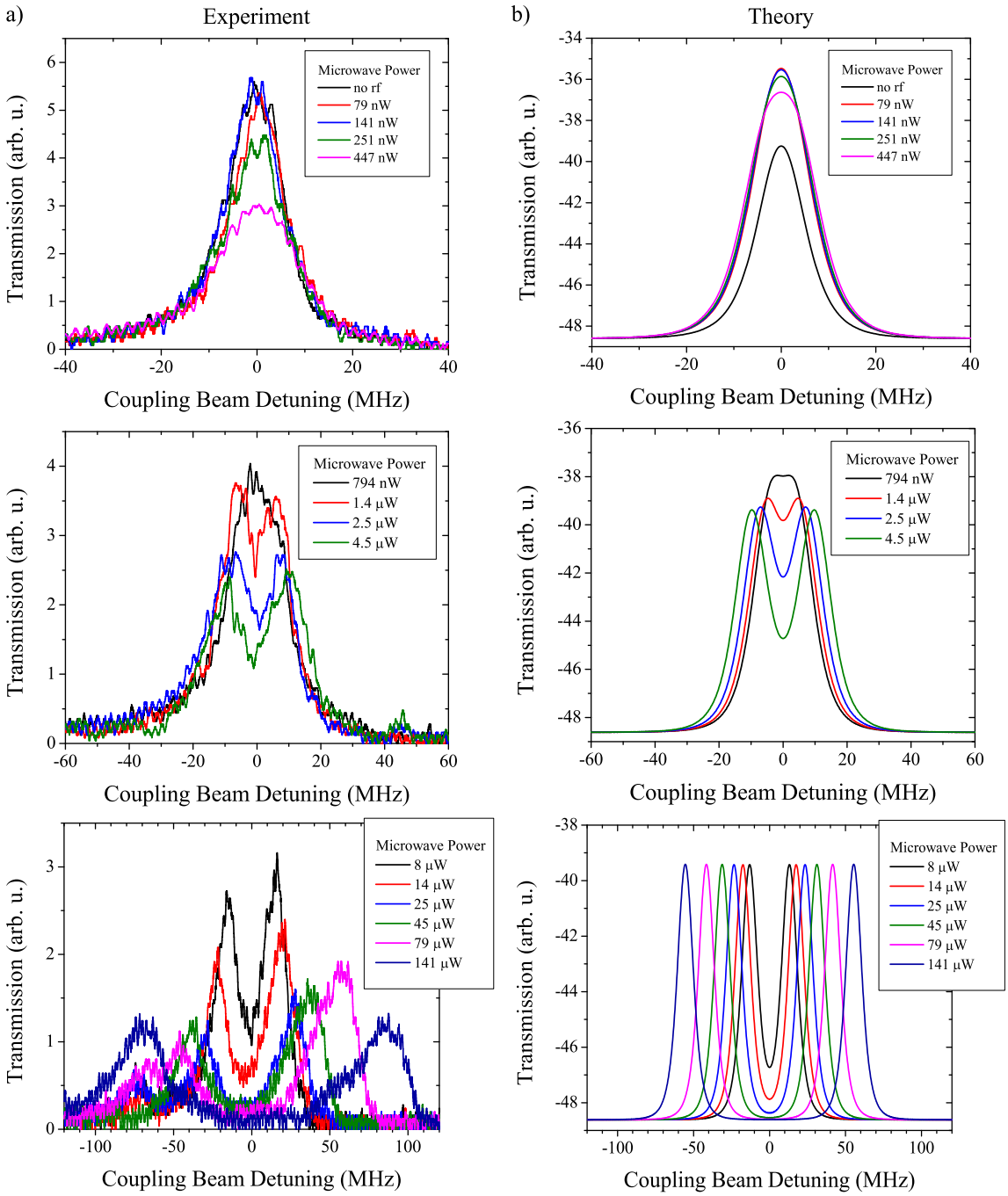

Figure 6.5: Rb EIT measurements. Probe transmission vs. coupling beam detuning. The effect of increasing the microwave power is to split and broaden the EIT peak. a) Experiment, b) 4-level theory with no adjustable parameters.

as explained in Sections 2.4.3 and 2.4.5. Assuming perfect σ^+ polarization of both beams and perfect optical pumping, the four relevant levels in the system are taken to be the $5S_{1/2}, F = 2, m_F = 2$ ground state, the $5P_{3/2}, F = 3, m_F = 3$ excited state, the $53D_{5/2}, F = 4, m_F = 4$ Rydberg state and the $54P_{3/2}, F = 3, m_F = 3$ Rydberg state. The Rabi frequencies are then determined with Eq. 2.54 to be $\Omega_p = \sqrt{1/3} \times \Omega^0_{(5S,5P)}$, $\Omega_c = \sqrt{2/5} \times \Omega^0_{(5P,53D)}$, $\Omega_{\mathrm{rf}} = \sqrt{1/5} \times \Omega^0_{(53D,54P)}$. The numerical factors are due to the angular part of the transition dipole moment, and the Ω^0 depend on the electric field amplitude and the radial matrix element $\zeta_{(nL,n'L')}$ as defined in Eq. 2.55. The radial matrix elements ζ involving Rydberg atoms are calculated by numerical integration. Using the wavefunctions described in Section 2.3.3, we get $\zeta_{(5S,5P)} = 5.17763\, a_0$, $\zeta_{(53D,54P)} = 3611\, a_0$, and $\zeta_{(5P,53D)} = 0.024\, a_0$. From the measured powers and spot sizes, we determine the electric field amplitudes to determine the Rabi frequencies $\Omega_p = 2\pi \times 10.4$ MHz and $\Omega_c = 2\pi \times 0.150$ kHz. Ω_{rf} is varied between 0 and $2\pi \times 111$ MHz. Decay rates involving Rydberg states are calculated as described in Section 2.3.4. The decay rate between Rydberg states is approximated to be equal to the black body decay rate $\Gamma_{34} = 2\pi \times 1$ kHz [59], and the decay of the upper Rydberg state is approximated by the radiative rate $\Gamma_{32} = 2\pi \times 1.2$ kHz [59]. The decay rate of the excited state is set to the known value of $\Gamma_{21} = 2\pi \times 6.0666$ MHz [1]. The spontaneous decays give rise to dephasing terms with rates $\Gamma/2$. No additional dephasing terms are used. The probe laser and the microwaves are assumed to be perfectly on resonance, $\Delta_1 = \Delta_3 = 0$, while the coupling detuning Δ_2 is varied. For the integration over the thermal distribution of velocities, the detunings are replaced by $\Delta_1 \to -k_p\, v$, $\Delta_2 \to \Delta_2 + k_c\, v$, where k_p and k_c are the wavenumbers of the probe and coupling beams, respectively. The Doppler shift of the microwaves is ignored, because it is less than 15 kHz due to the long wavelength of the microwaves, $\lambda_{\mathrm{rf}} = 2.1$ cm. As can be seen in Fig. 6.5b, the theory predicts the initial width of the

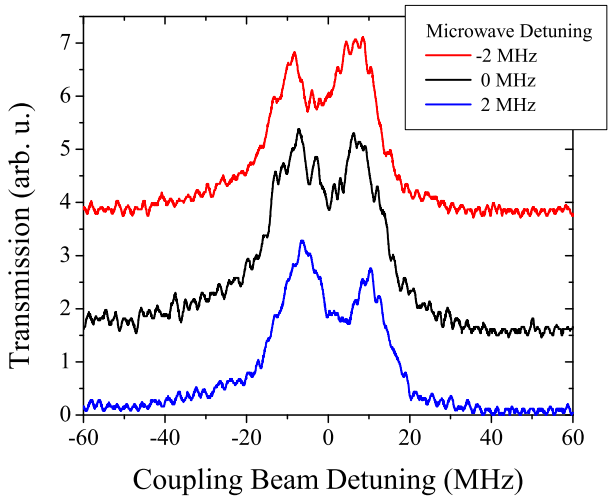

Figure 6.6: Effect of detuning the microwaves in Rb, measured at a microwave power of 1.4 μW.

EIT peak and the measured splitting at intermediate microwave powers correctly, but does not account for the additional broadening, and peak height reduction at larger microwave powers. For the same reasons as in the Cs system, transit-time broadening and collisional broadening are negligible. We found that a source of some additional broadening of the peaks is dephasing caused by back-reflections of microwaves from the optical table surface.

The effect of changing the detuning of the microwaves is shown in Fig. 6.6. Compared to the Cs system, the shift of the absorption dip has the opposite sign, because the energetic order of the Rydberg levels is inverted.

To further investigate the EIT lineshape in the four level system, we studied the polarization effects.

6.3.3 Polarization effects

When we rotate the microwave antenna to change the polarization of the microwaves from transverse linear (x) to longitudinally linear (z), the measured absorption spec-

trum changes dramatically. Depending on the laser beam polarizations, the double peak structure, depicted in Fig. 6.7c, changes to either a single transmission peak, as depicted in Fig. 6.8c, or a three-peak structure, as depicted in Fig. 6.9c. This unexpected effect can not be explained in the 4-level approximation, and is due to the hyperfine structure of the Rydberg levels. The effect can be understood qualitatively by considering the magnetic sublevels of the system. Depending on the polarization of the light fields, there can be significant population in Rydberg hyperfine levels that are not coupled by the microwaves. The case of circular beam polarization and transverse microwave polarization is sketched in Fig. 6.7. The laser beams optically pump into the highest m_F Rydberg sublevel. Since the microwave polarization is transverse linear, it is a superposition of σ^+ and σ^- and has the selection rule $\Delta m_F = \pm 1$. The microwaves therefore couple the atoms to the second Rydberg state, resulting in the observed splitting of the EIT peak into two peaks shown in Fig. 6.7c. The case of circular beam polarization and longitudinal microwave polarization is sketched in Fig. 6.8. Since the microwaves are now π-polarized, the selection rule is $\Delta m_F = 0$ and the populated Rydberg sublevel is not coupled by the microwaves anymore. The effect of the microwaves is diminished and a single unperturbed EIT peak obtains, as shown in Fig. 6.8c. The case of linear beam polarization and longitudinal microwave polarization is sketched in Fig. 6.9. In this case, both coupled and uncoupled Rydberg sublevels are populated. This results in a spectrum consisting of an unperturbed EIT peak due to the uncoupled sublevel populations and a split peak due to the coupled sublevel populations, as shown in Fig. 6.9c. This qualitative discussion demonstrates that all magnetic sublevels should be taken into account, including the hyperfine structure of the Rydberg levels, to predict the polarization effects in the transmission spectrum. The details of such a 52-level calculation are described in Section 2.4.4. As an example, calculated transmission spectra for $T = 0$ K and

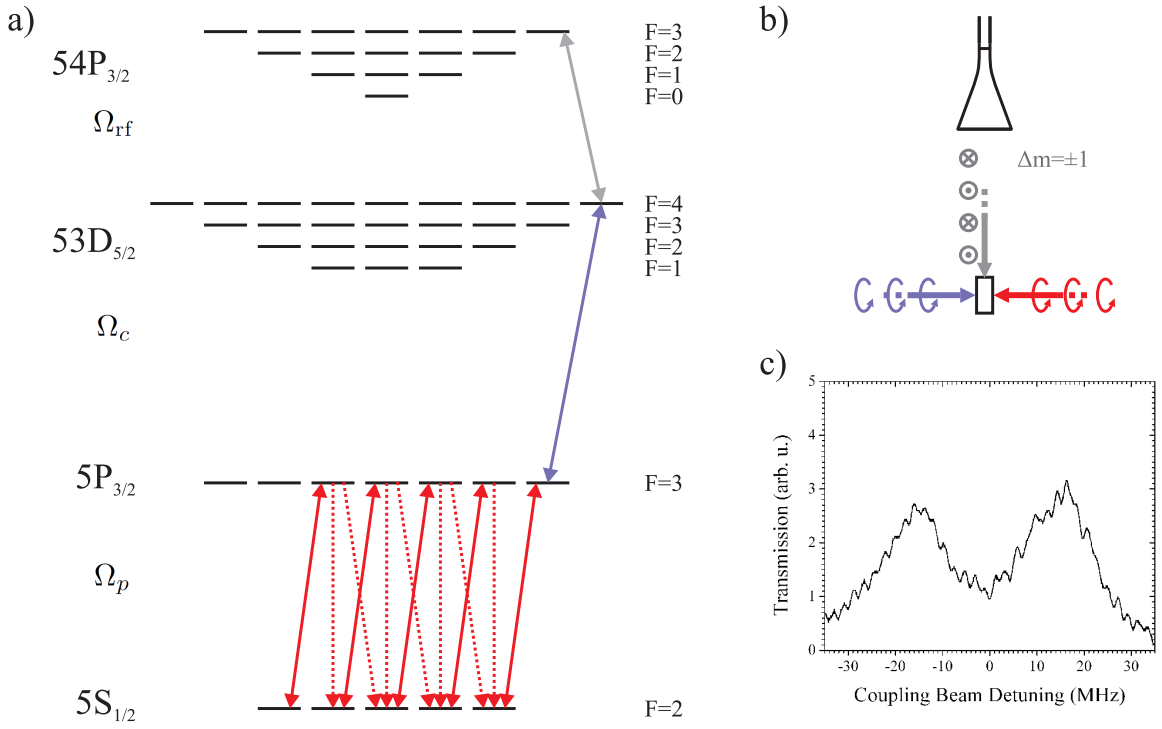

Figure 6.7: Sketch of polarization effects for σ^+ beam polarization and transverse linear microwaves. a) Schematic of all magnetic sublevels in the system. For clarity, the 54P level is drawn energetically above the 53D level instead of below. Transitions deemed most important are highlighted by solid arrows (absorption/stimulated emission) and dashed arrows (spontaneous decay). b) Geometric configuration of the fields and antenna. c) Resulting EIT lineshape. Optical pumping preferentially populates a 53D sublevel that is coupled to the 54P state by the microwaves.

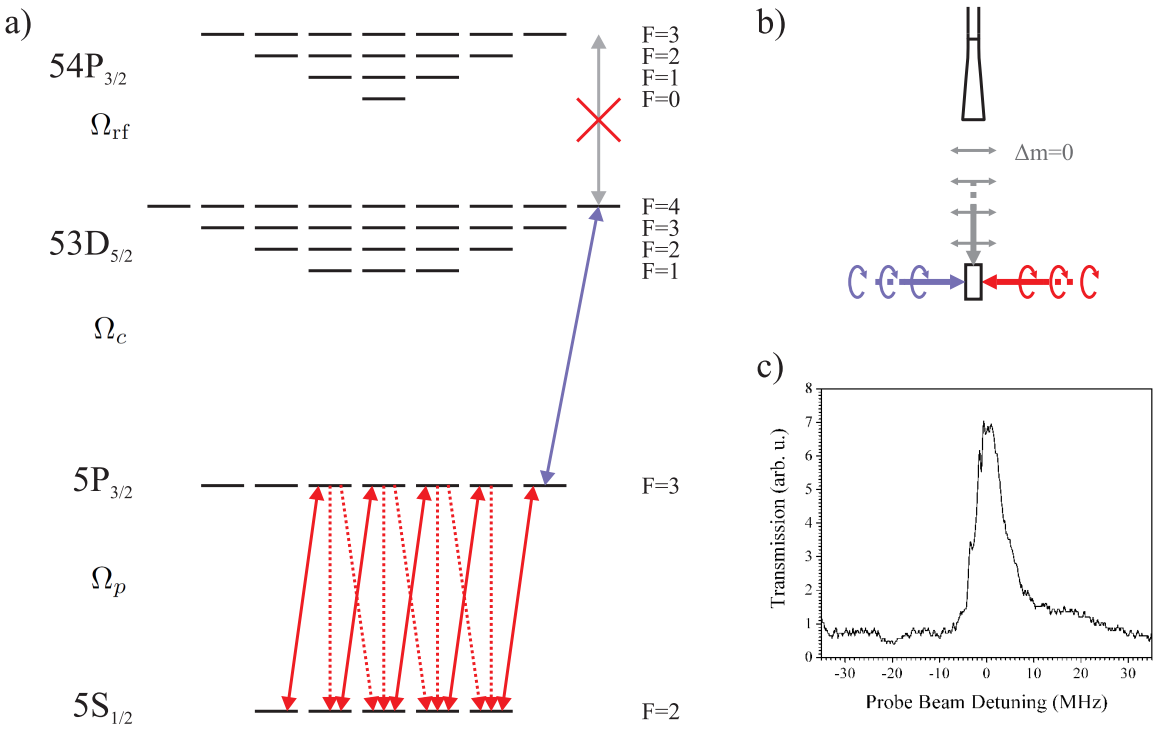

Figure 6.8: Sketch of polarization effects for σ^+ beam polarization and longitudinal linear microwaves. a) Schematic of all magnetic sublevels in the system. For clarity, the 54P level is drawn energetically above the 53D level instead of below. Transitions deemed most important are highlighted by solid arrows (absorption/stimulated emission) and dashed arrows (spontaneous decay). b) Geometric configuration of the fields and antenna. c) Resulting EIT lineshape. Optical pumping preferentially populates a 53D sublevel that is not coupled to by the microwaves, denoted by the red X. The effect of the microwaves is reduced.

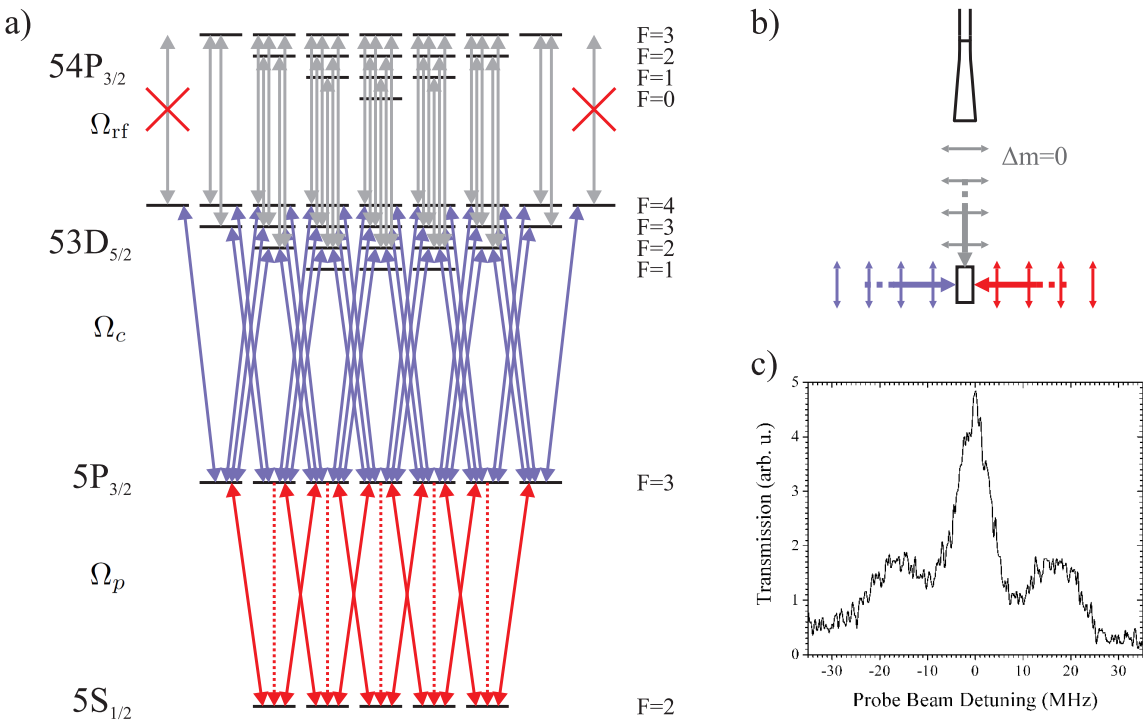

Figure 6.9: Polarization effects for linear beam polarization and longitudinal linear microwaves. a) Schematic of all magnetic sublevels in the system. For clarity, the 54P level is drawn energetically above the 53D level instead of below. Transitions deemed most important are highlighted by solid arrows (absorption/stimulated emission) and dashed arrows (spontaneous decay). b) Geometric configuration of the fields and antenna. c) Resulting EIT lineshape. Both coupled and uncoupled (denoted by red crosses) Rydberg sublevels are populated. The uncoupled sublevels are denoted by red crosses.

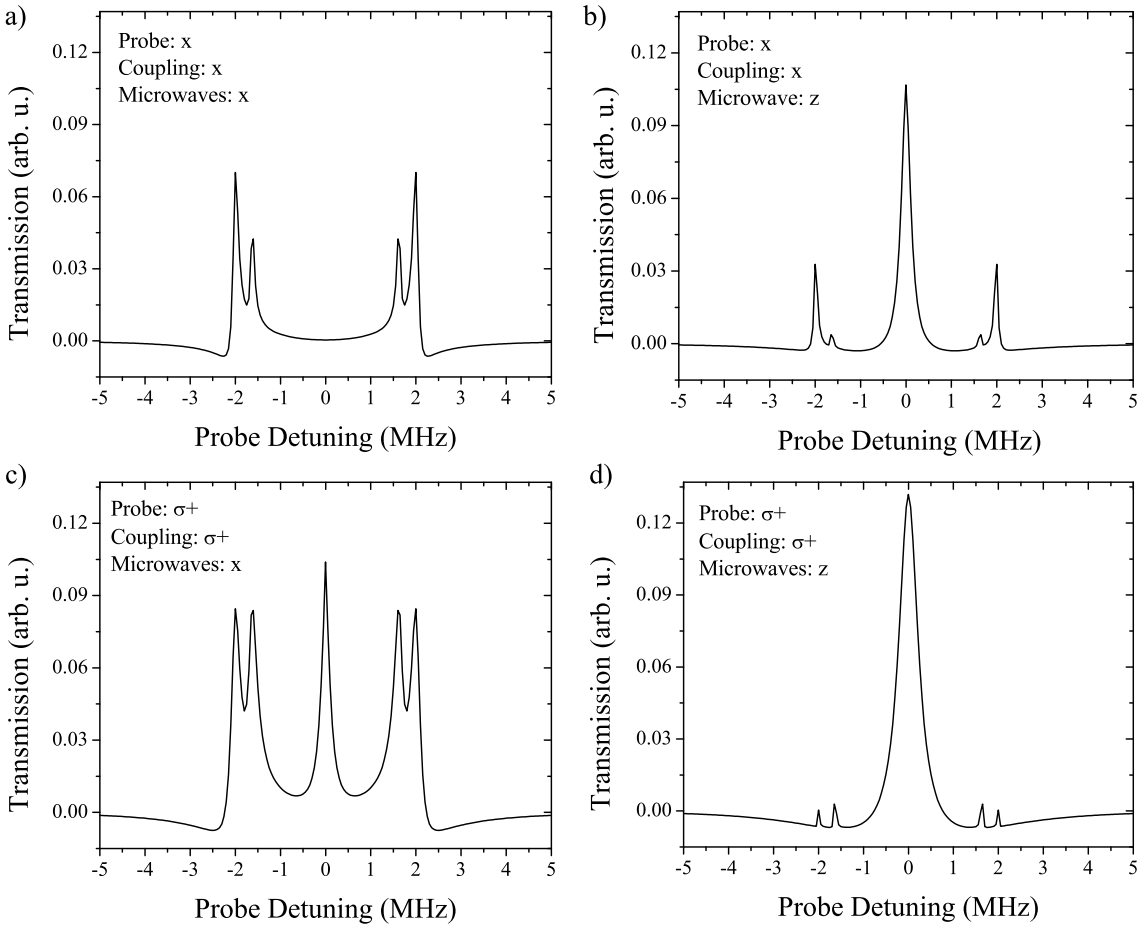

Figure 6.10: Polarization effects in calculated probe transmission spectra at $T = 0$ K. The density matrix evolution in the 52-level system was solved numerically for different polarizations. a) All fields linearly polarized along x, b) beams along x and microwaves along z (π-polarization), c) beams circular (σ^+-polarization) and microwaves along x, d) beams circular and microwaves along z.

$\Omega^0_{(5S,5P)} = 2\pi \times 1.73$ MHz, $\Omega^0_{(5P,53D)} = 2\pi \times 2.25$ MHz and $\Omega^0_{(54P,53D)} = 2\pi \times 8.17$ MHz are shown in Fig. 6.10, for four different sets of polarizations. Here, the probe detuning is varied. Due to the lock-in detection, the experimentally measured quantity is $A - A'$ where A is the transmission in the presence of the coupling light and A' is the transmission in the absence of the coupling light. To simulate this effect in the calculation, both A and A' are calculated separately and subtracted from each

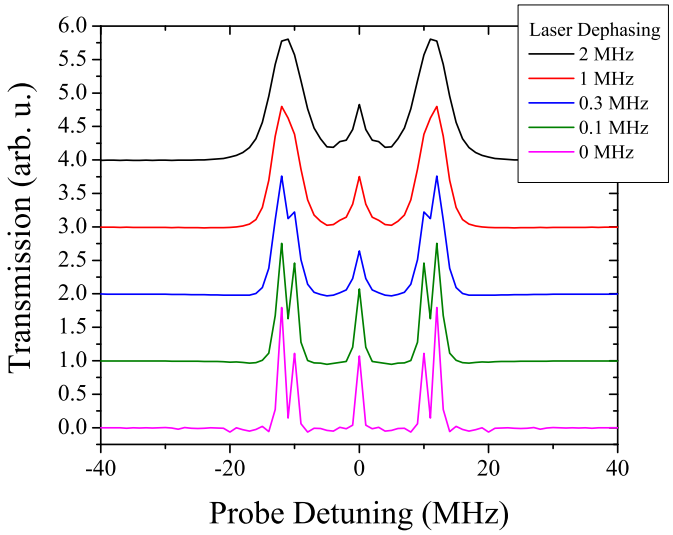

Figure 6.11: Effect of dephasing terms due to finite laser linewidths on the calculated probe transmission spectra. The calculation was done for $T = 85$ °C, including all 52-levels and the average over thermal velocities. The laser beams are σ^+ polarized and the microwaves linearly along x.

other. The calculation reveals different numbers of transmission peaks, depending on the microwave and beam polarizations. As can be seen in Fig. 6.10, some of the predicted peaks have an unexpected double-peak substructure.

To compare the 52-level theory to the experiments, which are done at $T = 363.2$ K, we integrate the probe transmission over the thermal velocity distribution of the atoms. Additional dephasing rates γ_c, γ_p due to the finite laser linewidths of the coupling and probe beams are also included. The dephasing due to the laser light is incorporated through the dephasing operator L_d as described in Section 2.4.4. The effect of the dephasing terms is to wash out the substructure in the split EIT peaks, as shown in Fig. 6.11. From the manufacturer's specifications of the Toptica diode lasers and the linewidth measurements we performed on our homebuilt SHG system (see Fig. A.4), we estimate our current laser linewidths to be approximately $\gamma_c = \gamma_p = 2\pi \times 1$ MHz, dominated by low frequency technical noise such as vibrational

and thermal noise during the slow scans that typically take tens of seconds. The substructure in the split EIT peaks is therefore not observed in our experiment.

In the experiment to measure the polarization effects, the probe is scanned slowly (~ 1 MHz s^{-1}) over the EIT peak using the imaging AOM, while the coupling laser is held at constant frequency. To increase the EIT signal, the coupling beam is weakly focussed through the vapor cell with a positive lens ($f = 400$ mm). This results in a reduced coupling beam FWHM of ~ 250 μm, and increased bare Rabi frequency $\Omega^0_{(5P,53D)} = 2\pi \times 1.4$ MHz. For the probe, $\Omega^0_{(5S,5P)} = 2\pi \times 8.64$ MHz. The microwave power is kept fixed at 14 μW, resulting in $\Omega^0_{(54P,53D)} = 2\pi \times 78.3$ MHz. To reduce the dephasing caused by diffuse microwave reflections from the optical table surface, the Rb cell is seated on a rectangular sheet of microwave absorber. A comparison of the measured spectra to the full 52-level calculations with no adjustable parameters is shown in Fig. 6.12. The theory is in good agreement with the experimental results. Small remaining discrepancies in the lineshapes are most probably due to imperfect polarizations. Polarizations impurities are most probably due the birefringence of the oven and vapor cell windows, the imperfect extinction ratios of the beamsplitter cubes and the AOM in the coupling beam.

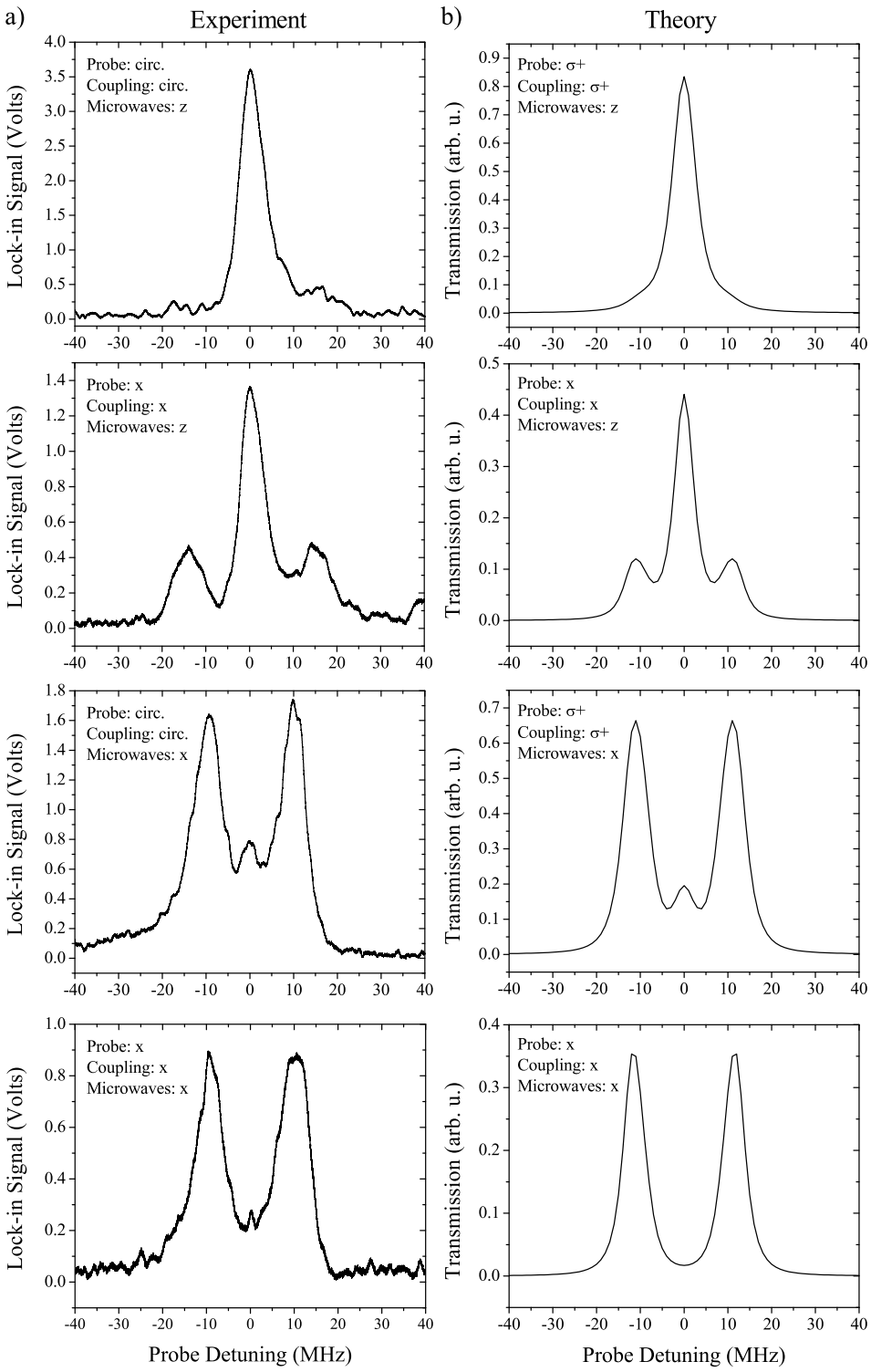

Figure 6.12: Polarization effects on the probe transmission in Rb EIT. a) Experimental results, b) 52-level theory with no adjustable parameters.

6.4 Conclusion

In conclusion, we presented measurements of electromagnetically induced transparency (EIT) in the 4-level ladder system. The system includes two Rydberg states that are resonantly coupled by microwave radiation. We looked in detail at the perturbed EIT lineshape and found that it depends in a non-trivial way on the power and polarization of the microwaves. We found that the lineshape can only be calculated by taking into account the hyperfine structure of the Rydberg states and all magnetic sublevels of the system. We calculated the lineshape using a 52-level theory with no adjustable parameters and the theory agreed qualitatively with the experiment. We identified the diffuse reflection of microwaves from the optical table surface as an important dephasing mechanism. In the future, the Rydberg EIT probe scheme will be implemented in the atom chip setup and used there to probe the coupling of cold Rydberg atoms to surface excitations and other Rydberg atoms. Our current room temperature setup is sensitive to microwave amplitudes of ~ 1 mV cm^{-1}, which is slightly better than commercially available microwave antennas. We argued that it should be possible to increase the sensitivity into the regime of a few nV cm^{-1} by employing narrow bandwidth lasers and by using Rydberg states with higher principal quantum numbers. This is the first time a double dark resonance has been used for electrometry with Rydberg atoms.

Chapter 7

Cold Rydberg gas calculations

7.1 Introduction

We intend to use our atom chip for future experiments on the dynamics of cold Rydberg atoms in a microscopic double well potential. In order to understand the behavior of cold Rybderg atoms in a double well, we first need to understand the long-range interactions between Rydberg atoms.

In this chapter, the results of calculations of Rydberg atom pair interaction potentials are presented. The calculations were done for the cold Cs Rydberg gas, and show that ultralong-range molecules can be formed between two Rydberg atoms. At high principal quantum numbers $n \sim 89$, a pair of Rydberg atoms can be weakly bound at internuclear distances of several micrometers. The binding forces are the electric multipolar interactions. This was the first ever large-scale calculation of Rydberg interaction potentials by direct matrix diagonalization. The results complement calculations done previously using perturbation theory, but also reveal new features not observed in the perturbation approach, such as many avoided crossings in the potential curves. The avoided crossing change the potential shapes and lead to long-range bound states. These long-range dimers were subsequently observed in our lab [55]. These are the largest dimers ever observed. The first part of this chapter was published as Ref. [138], and the second part of this chapter was published as Ref. [139]. The content of both publications was adapted to the context of this thesis.

In the first part, calculations of potential curves for very high n (89D) Cs Rydberg atom pairs, including a background electric field are presented. From these potentials, it is shown that energy transfer occurs at rates of $\sim 30-70$ MHz, background electric fields play an important role and dipole-dipole and quadrupole-quadrupole induced

avoided curve-crossings should lead to conversion of electronic to kinetic energy, n-changing collisions, and to observable ultracold long-range Rydberg molecules.

In the second part, bound states at long-range ($R \sim 5$ μm) are analyzed for pairs of Cs atoms in the 89D and neighboring states. These wells are due solely to avoided crossings between the Van der Waals pair interaction potentials. The depth of the wells is ~ 40 MHz, and vibrational spectra consist of hundreds of bound states. The properties of two of these wells are calculated at different electric fields ($\sim$ mV cm^{-1}), since the electric field changes the well depth and shape. Estimated properties are the lifetimes (~ 400 μs), the lineshapes, and the two-photon excitation and detection rates ($\sim$ Hz) from the 6P state at a temperature of $T = 40$ μK for these molecules.

The calculations presented in this chapter were confirmed by multiple experiments done in our group and in collaboration with the group of Luis Marcassa at the University of Sao Paolo, Brazil. We observed photo-initiated collisions in the cold Cs Rydberg gas that agreed with our Rydberg potential calculations [60], and we detected ultralong-range Rydberg-atom Rydberg-atom molecules that also agreed with the potential calculations [55]. We were able to explain electric field effects observed in the excitation of cold Rydberg-atom pairs [140, 141]. Recently, we were able to explain the observed manipulation of the decay of nD+nD quasi-molecules with an applied electric field by evaluating Landau-Zener dynamics on our calculated potential curves [142].

7.2 Calculation of interaction potentials in a cold Rydberg gas

7.2.1 Introduction

Ultracold Rydberg gases are intriguing quantum systems. Current interest is focussed on applications in quantum computing [6], the physics of ultracold plasmas [143, 44, 144], and the nature of dipolar interactions. Phenomena such as resonant energy transfer [145, 45, 44], Rydberg excitation blockade [41], quantum computing [6, 7], Rydberg atom collisions [41, 146], and long-range Rydberg molecules [47, 147] all require accurate calculation of Rydberg atom pair potentials for a quantitative comparison of theory to experiment and identification of spectral features. Though the Rydberg gas is a system where many-body interactions can dominate [146, 148, 149], accurate knowledge of two body potentials is still important.

Cold Rydberg atom physics is dominated by near zone (μm) Coulombic interactions. These long-range interactions are tunable by electric fields (E-fields) and principal quantum number selection. Here, we focus on Cs Rydberg atom pair interactions in the near zone for energies around the 89D89D states. These states were chosen in light of the work done in our research group. We quantitatively show that for these states 1) near-resonances dominate the interactions and cause many avoided crossings between the potential curves that lead to observable molecular and/or collisional resonances, 2) many states mix making matrix diagonalization the only accurate calculation method [149], and 3) small E-fields on the order of tens of mV cm^{-1} and the fine-structure significantly perturb the energies on a scale easily resolvable by high-resolution spectroscopy. We calculate energy transfer rates, and note that the time-scale is on the order of hundreds of nanoseconds.

A perturbative calculation of the potential for a pair of atoms in 1/R yields the

Van der Waals coefficients [4]. However, non-degenerate perturbation theory smoothly goes over into degenerate perturbation theory as the potentials approach each other and eventually cross. The nondegenerate case gives a $1/R^6$ leading dipole-dipole contribution, the degenerate case a $1/R^3$ dipole-dipole contribution. For the dense high n Rydberg states considered here and used in the majority of experiments, the near-resonant terms become non-negligible and lead to avoided crossings at large R on the order of μm. Recent experimental and theoretical results suggest that diagonalization of the Hamiltonian in a reasonably truncated basis is more appropriate for a cold Rydberg gas than the perturbative calculation of Van der Waals coefficients [44]. This is true especially when background E-fields are varied and changes of the potentials are studied. Matrix diagonalization directly accounts for the off-resonant, near-resonant, and resonant interactions.

We find that small applied E-fields can be used to tune the Rydberg interactions. The main effect of E-fields is to mix the zero-field eigenstates and shift the asymptotic potential energies. Depending on the magnitude of the applied E-field, attractive potentials can be changed into repulsive potentials, and avoided crossings between potential curves can be made to appear and disappear at different internuclear distances.

7.2.2 Hamiltonian

When two Rydberg atoms are separated by distances of several μm, as in typical cold trapped Rydberg gases, dipole and quadrupole interactions dominate. The Hamiltonian used for the calculation includes the dipole-dipole, dipole-quadrupole and quadrupole-quadrupole interactions between atom pairs in their respective Stark-

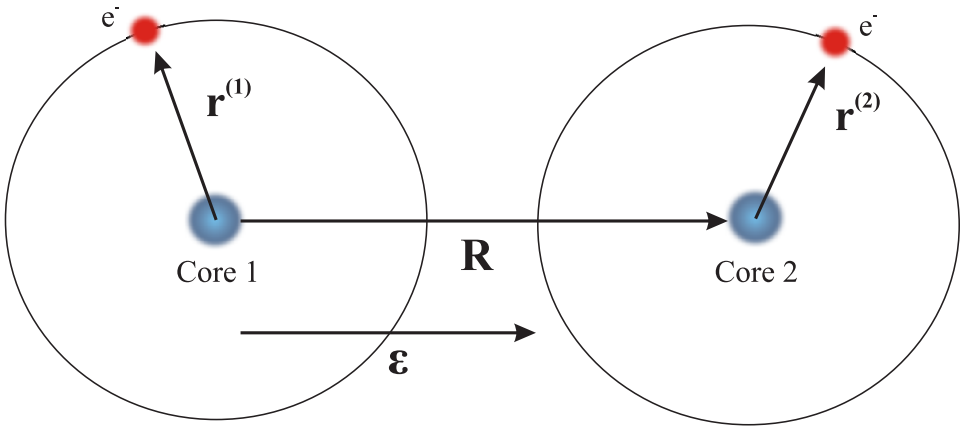

Figure 7.1: Two Rydberg atoms interact via electric multipole interactions over a long internuclear distance R of several μm. A small applied electric field $\sim$ mV cm^{-1} along the internuclear axis is denoted by $\boldsymbol{\epsilon}$.

shifted atomic states. The Hamiltonian is [147]

$$\widetilde{\langle\alpha|}\widetilde{\langle\beta|}H(R)\widetilde{|\alpha'\rangle}\widetilde{|\beta'\rangle} = \delta_{\alpha\alpha'}\delta_{\beta\beta'}E_{\alpha\beta} + \widetilde{\langle\alpha|}\widetilde{\langle\beta|}\left(\sum_{L_1,L_2=1}^{2}\sum_{m=-L_<}^{L_<} C_{L_1L_2m}\frac{{r^{(1)}}^{L_1}{r^{(2)}}^{L_2}}{R^{L_1+L_2+1}}Y^{(1)}_{L_1\,m}\,Y^{(2)}_{L_2\,-m}\right)\widetilde{|\alpha'\rangle}\widetilde{|\beta'\rangle}, \tag{7.1}$$

with

$$C_{L_1L_2m} = (-1)^{L_2}\frac{4\pi}{\left[(2L_1+1)\,(2L_2+1)\right]^{1/2}}\frac{(L_1+L_2)!}{\left[(L_1+m)!\,(L_1-m)!\,(L_2+m)!\,(L_2-m)!\right]^{1/2}}. \tag{7.2}$$

where Greek letters denote sets of atomic quantum numbers $\{n, l, j, m_j\}$, including the fine-structure, $L_<$ denotes the smaller value of L_1 and $L_2 2$, and direct products are abbreviated as $|\alpha\rangle|\beta\rangle = |\alpha\rangle \otimes |\beta\rangle$. See Fig. 7.1 for a diagram of the system. Superscripts denote atom 1 vs. atom 2 spherical coordinates from the respective atom's nucleus. The internuclear distance, R, is taken to be oriented along the quantization axis z, which is also the E-field axis. The tilde denotes an eigenfunction

of the Stark Hamiltonian, and $E_{\alpha\beta} = E_\alpha + E_\beta$ denotes the asymptotic ($R \to \infty$) Stark-shifted pair energies. Incorporating the fine-structure this way corresponds to a j-j coupling scheme [150]. The pair states are labeled by the full set of zero-field quantum numbers for each atom $|n_1, l_1, j_1, m_{j_1}\rangle|n_2, l_2, j_2, m_{j_2}\rangle$. This basis is closest to the physical situation because the electron clouds of the atoms do not overlap. The only interactions are long-range multipole interactions. The coupling of L to S in the separated atoms is strong compared to the coupling of each L and S to the molecular axis. In this model, $M = m_{j_1} + m_{j_2}$ remains a good quantum number. The interactions are treated as perturbations of the single atoms. Since the field is held fixed along the internuclear axis, the quantization axis used for diagonalizing the Stark Hamiltonian coincides with the quantization axis used for the multipolar interaction Hamiltonian. Thus, the Stark Hamiltonian and the multipolar interaction Hamiltonian do not mix different M.

The range of valid R is estimated to be 2.5 μm $< R <$ 1 mm for 89D and adjacent pairs. The range of validity is set by the conditions that retardation effects are negligible, the dipole and quadrupole interactions dominate higher multipole interactions, and exchange can be ignored. Neglect of retardation effects gives an upper bound set by the reduced wavelength $R_{\max} = \bar{\lambda}$ [151]. Between dipole coupled states in the region around 89D, $\bar{\lambda} > 1$ mm. Neglect of higher multipoles than the quadrupoles is justified using the scaled Van der Waals coefficients [4]. Even at the lowest R considered in this paper, $R = 3$ μm, the energy shifts due to octopole interactions (C_7) are on the order of 10^{-4} cm^{-1}, which is 1% of the combined dipole and quadrupole contributions. They quickly drop to below 10^{-6} cm^{-1} at $R = 6$ μm. The lower bound for R is the LeRoy radius [152], $R_{\rm LR} = 2(\sqrt{\langle\alpha|r^2|\alpha\rangle} + \sqrt{\langle\beta|r^2|\beta\rangle})$. Below the LeRoy radius, exchange interactions become non-negligible. For 89D pairs $R_{\rm LR} \sim 2.5$ μm. The average distance between atoms in a cold Rydberg gas at typical experimental

number densities of $\sim 10^6$ cm$^{-3} - 10^{10}$ cm^{-3} is ~ 3 μm $- 25$ μm, well within the range of valid R.

7.2.3 Numerical method

We calculate the interaction potentials in three steps: 1) calculation of Stark-shifted single atom energies and basis states, 2) selection of an appropriate truncated pair basis, and 3) diagonalization of the Hamiltonian in the Stark-shifted pair basis.

In a typical experiment, a background E-field will be present. The E-field will lift the angular momentum degeneracy and the correct single atom states $|\widetilde{\alpha}\rangle$ are the Stark eigenstates. The permanent dipole moments of the $|\widetilde{\alpha}\rangle$ lead to interaction terms in the diagonal of H in addition to the off-diagonal transition terms. The Stark shifted atom states are calculated by finding the eigenvectors of the Stark Hamiltonian [57]. Zero E-field asymptotic energies E_α for the atomic states are obtained from empirical quantum defects up to order 8 [64] supplemented by the empirical fine-structure splittings [65]. We found convergence of the Stark energies for $j_{\max} = 27/2$. An example of the calculated single atom Stark energies for Cs 89D and surrounding states is shown in Fig. 7.2.

Radial matrix elements are obtained by numerical integration. For states with a large quantum defect ($l \leq 3$) the radial wavefunctions are calculated numerically using RADIAL [67] with the l-dependent model potential from [66]. Accuracy of the numerical wavefunctions is ensured by comparing the energies with the ones obtained from quantum defects. For the Stark fan states ($l > 3$), hydrogenic wavefunctions are used.

Due to the close spacing of the energy levels at $n \sim 89$, a large number of states mix at distances of several μm, and the two-state approximation cannot be made if spectroscopic accuracy (error $< 10^{-3}$ cm^{-1}) is desired. However, the basis has to be

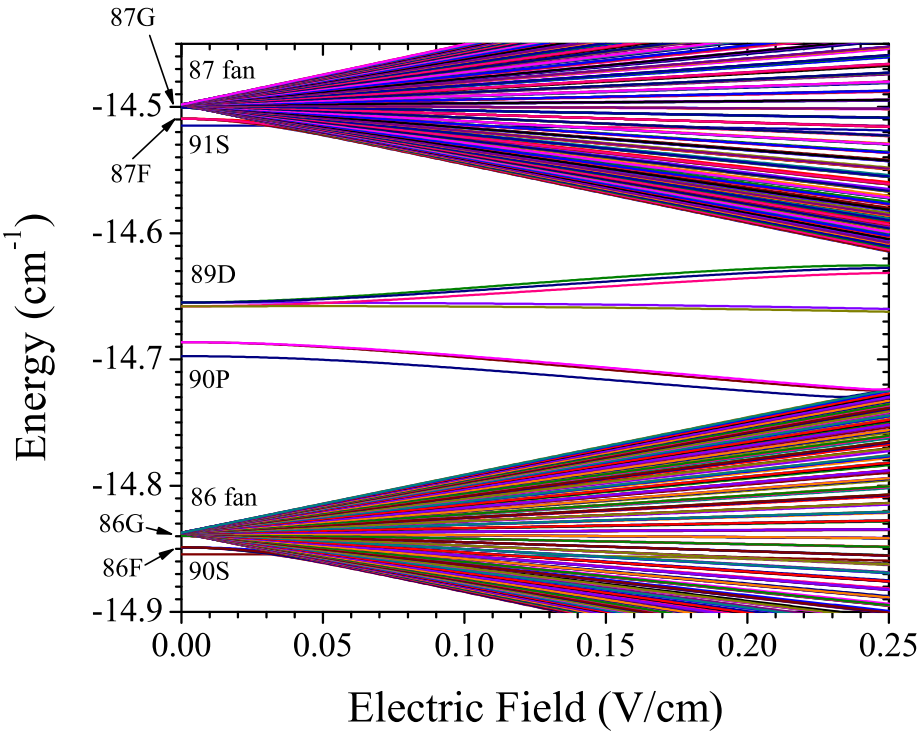

Figure 7.2: Calculated single atom Stark energies for Cs 89D and adjacent states.

truncated to make numerical calculation feasible. Each calculation is done including all m_j pairs in the truncated basis that give the same $M = m_{j1} + m_{j2} = 0$. Truncation is done by including only those atom pair Stark states that are close in energy and most coupled to the states of interest. This works because transition matrix elements decrease quickly with Δn [57]. Convergence on the level of 10^{-4} cm^{-1} is acquired only by large pair basis sizes of ~ 6000 close-lying states at each M. For higher M, slightly smaller basis sizes can be used (~ 4000 basis states at $M = 5$). The process is computationally intensive but was easily parallelized for a cluster architecture.

7.2.4 Rotation of Hamiltonian

For the potentials presented here, the electric field is chosen to be parallel to the internuclear axis. This choice makes the calculation simpler, because H is block

diagonal with respect to M. As long as the electric field is small enough to not polarize the atoms, the angular dependence of the interaction energies is small, and this choice is justified. Using our program, we can also calculate the interaction potentials for the case where the electric field is at an arbitrary angle with respect to R. The method is briefly summarized in this section.

The multipolar interaction Hamiltonian (ignoring monopoles) can be written as a series of powers of 1/R:

$$H(r_1,\theta_1,\phi_1;r_2,\theta_2,\phi_2;R) \propto \sum_{l_1=1}^{\infty}\sum_{l_2=1}^{\infty}\sum_{m=-l_<}^{+l_<} C_{l_1,l_2,m}\frac{r_1^{l_1}r_2^{l_2}}{R^{l_1+l_2+1}}Y_{l_1}^{m}(\theta_1,\phi_1)Y_{l_2}^{-m}(\theta_2,\phi_2), \tag{7.3}$$

where (r,θ,ϕ) are the electronic coordinates for each atom, and R is the internuclear distance. Terms with $l=1$ are dipolar in nature, terms with $l=2$ are quadrupolar in nature. So the term with $l_1=1$, $l_2=2$ would be a part of the dipole-quadrupole interaction. In the case where the electric field is parallel to the internuclear axis, atomic wavefunctions are written in terms of the same coordinates (r,θ,ϕ) as the Hamiltonian. This is because in the Hamiltonian, θ is measured with respect to the internuclear axis which defines the z-axis. In this case, calculation of the Hamiltonian matrix elements involves calculation of the radial matrix elements and calculation of integrals of products of three spherical harmonics. Those integrals simplify to products of Clebsch-Gordan coefficients as follows:

$$\int_0^{\pi}\int_0^{2\pi}\sin(\vartheta)Y_{n_1}^{m_1}(\vartheta,\varphi)Y_{n_2}^{m_2}(\vartheta,\varphi)Y_{n_3}^{m_3}(\vartheta,\varphi)^* d\varphi d\vartheta =$$
$$\sqrt{\tfrac{(2n_1+1)(2n_2+1)}{4\pi(2n_3+1)}}\,\langle n_1\ n_2\ 0\ 0 \mid n_1\ n_2\ n_3\ 0\rangle\,\langle n_1\ n_2\ m_1\ m_2 \mid n_1\ n_2\ n_3\ m_3\rangle \quad .$$

In the case where the electric field is at angle Θ to the internuclear distance, atomic wavefunctions are written in terms of coordinates (r,θ',ϕ'). These coordinates are measured in a coordinate system with z-axis along the electric field. The primed coordinate system is thus rotated with respect to the one used in the Hamiltonian,

which has its z-axis along the internuclear axis. The rotation that has to be applied to the Hamiltonian to make easy integration possible is the one that assures that the Hamiltonian is also written in terms of primed coordinates. Unprimed angles appear in the Hamiltonian only as arguments of spherical harmonics. The rotation of spherical harmonics from the unprimed to the primed system is given simply by the identity

$$Y_l^m(\theta,\phi) = \sum_{m'} D^l_{m'm}(\Theta,\Phi,\Xi) Y_l^{m'}(\theta',\phi'), \tag{7.4}$$

where D are the Wigner rotation matrix elements, expressed in the basis of spherical harmonics [53]. The D depend on the Euler angles, here Θ should be $\sphericalangle(\mathbf{E},\mathbf{R})$. A direct expression of the D in terms of sums over the half Euler-angles was found by Wigner. The above expression is used to replace the spherical harmonics in the Hamiltonian by sums over other spherical Harmonics that now depend on the primed coordinates. Note that the above rotation conserves l, but mixes m. Thus dipolar interactions stay dipolar, and quadrupolar interactions stay quadrupolar. However, the resulting rotated Hamiltonian is not block diagonal with respect to M anymore in the Stark-shifted atomic pair basis as it was if the field was directed along the internuclear axis. This makes the calculation more difficult because it requires a dramatic increase in the number of basis states. Even on a cluster supercomputer, the Hamiltonian matrix has to be spread out on several compute nodes using the SCALAPACK library.

In calculations of the angular dependence of potentials for Cs 90D pairs and surrounding states, we found that varying the angle between the internuclear axis and the electric field changed the potential energies by less than 3 MHz at $R = 5$ μm at an applied field of 100 mV cm^{-1}. Inside the range of 5 μm, the interaction due to the induced dipole terms in the diagonal of H can dominate or at least be the same size as the interaction due to the transition dipole moments in the off-diagonal

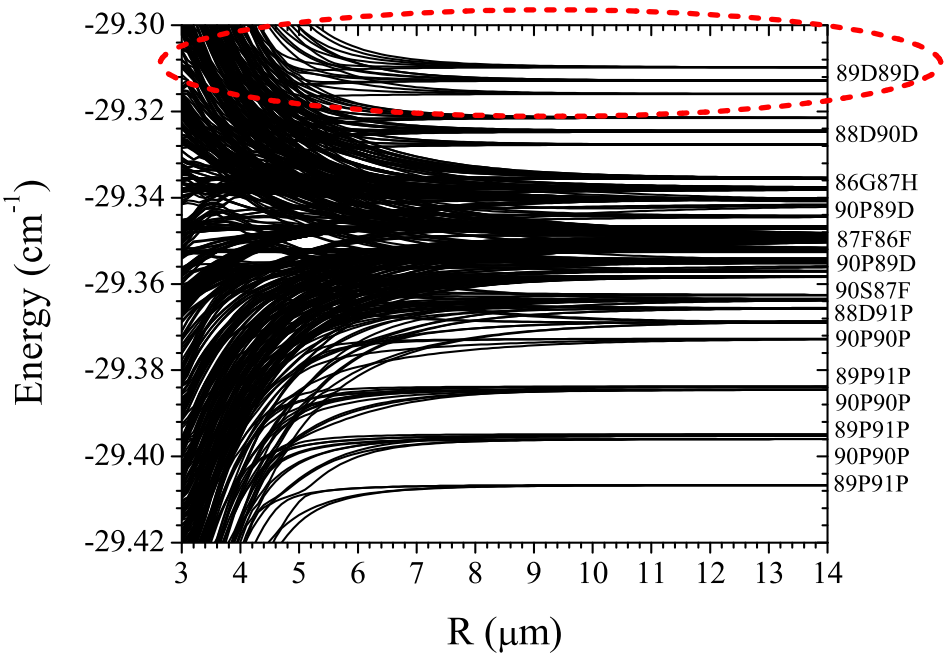

Figure 7.3: Overview of the pair potentials of the 89D89D and surrounding states for zero background E-field. Labels are zero-field labels. The 89D89D potentials are circled.

elements of H. Compared to the energy scales and fields considered here, this angular dependence should be negligible for the cases considered in this thesis.

7.2.5 Results

An overview of the pair potentials around the 89D89D pair states is shown in Fig. 7.3 for $M = 0$ and zero E-field. The energy changes shown in the figures are entirely due to near resonant interactions. While the curves at zero E-field basically reproduce those found in [4] by perturbation theory, there are differences on the scale of $\sim 10^{-3}$ cm^{-1}, as shown in Fig. 7.4. Major differences are that we obtain the avoided crossings between potentials and stronger attractive curves. We attribute these to the fact we use matrix diagonalization instead of perturbation theory, and that we

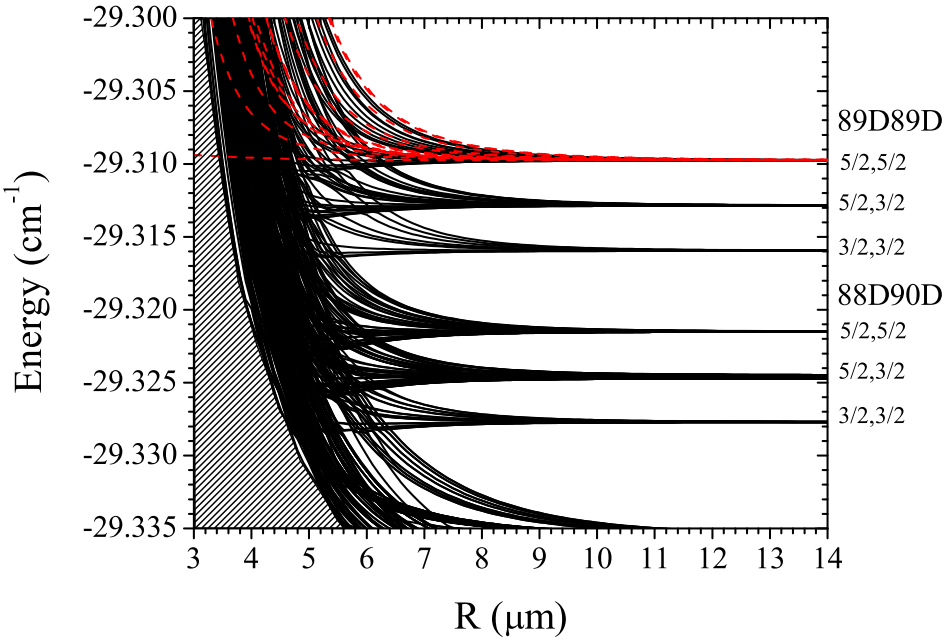

Figure 7.4: Comparison of pair potentials calculated via matrix diagonalization (solid black) to those from Ref. [4] calculated via perturbation theory (dashed red). Potentials for all M are plotted. The background field is zero. Note that the perturbative calculations did not include the fine-structure and therefore converge asymptotically to a single energy. For ease of comparison, the asymptotic energy of the perturbative potentials is chosen to be the $89D_{5/2}89D_{5/2}$ pair.

include the fine-structure.

Results for $M = 2$ on a smaller energy scale are shown in Fig. 7.5, for a background E-field of 28 mVcm^{-1}. The electric field introduces additional weak long-range attractive interactions as it induces permanent dipole moments aligned with the internuclear axis on each atom. The field also mixes the pair states and shifts the energy levels. There are two effects that lead to the splitting of degenerate asymptotic pair states and avoided crossings between states that are not dipole coupled at zero E-field. The E-field causes a $1/R^3$ resonant coupling between the asymptotically degenerate

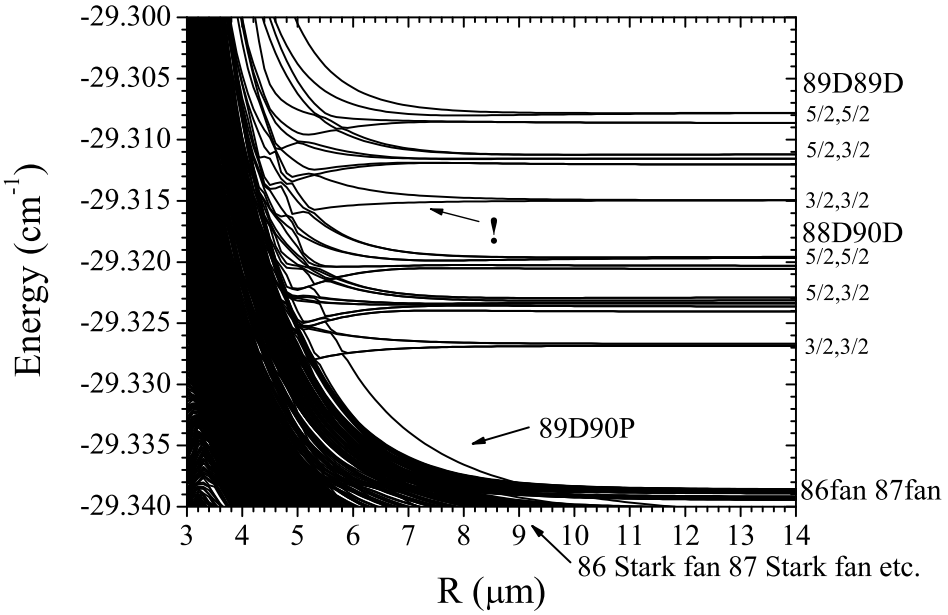

Figure 7.5: Pair potentials of the 89D89D and surrounding states for $M = 2$ for a background E-field of 28 mV cm^{-1}. Pairs of numbers below a given label are the respective j_1, j_2 combinations. The exclamation mark denotes the splitting of degenerate states caused by the E-field and the quadrupole-quadrupole interaction. For small R, the manifold of Stark fan pairs appears that can lead to large energy transfer and eventual ionization.

states and the quadrupole-quadrupole interaction creates a $1/R^5$ resonant coupling between such states. The former effect is due to the mixing by the Stark effect, the latter effect is due to the non-vanishing quadrupole moments of the 89D states.

For small $R \lesssim 4$ μm, atoms moving on the attractive potentials will enter the dense manifold of n=86, n=87 Stark fan pairs. This dense manifold exists even at zero background E-field, as states are split due to the mutual fields of the atoms. Motion along the potentials through the many avoided crossings in this manifold of states can then lead to population transfer to higher n states, and eventual Penning ionization. A Landau-Zener (LZ) analysis of our data indicates that atoms will enter

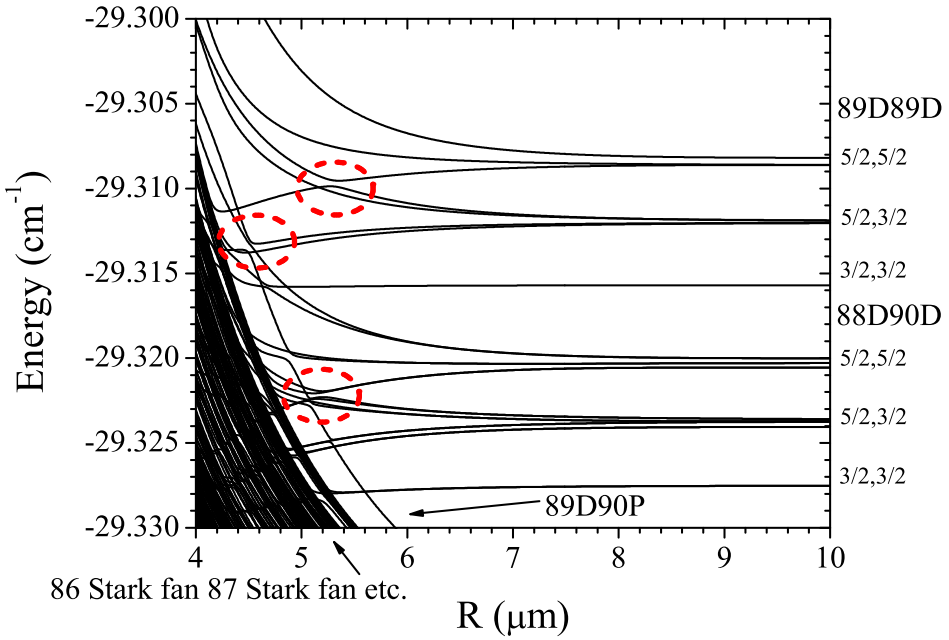

Figure 7.6: Pair potentials of the 89D89D and surrounding states for $M = 3$ for a background E-field of 28 mV cm^{-1}. Some avoided crossings are circled.

the manifold with $\sim 90\%$ probability. Inside the manifold, $R \sim 3 - 4$ μm, atoms pass through several different avoided crossings (LZ probability each $\sim 10\% - 90\%$) to other n, l states. This picture is similar to the field ionization of single atoms viewed as motion along the Stark fan [153], and can play an important role in the first steps toward evolution to ultracold plasma. These features are consistent with experiments that have measured n-changing collisions as a Rydberg gas evolves into a plasma [154, 155]. Relevant to this point is that almost all asymptotes have some attractive curves because this is a complicated function of the energies and m_j-values of closely coupled states.

In Fig. 7.7, potentials for $M = 3$ at a slightly smaller energy scale are shown, and some avoided crossings can be seen. Similar avoided crossings are also found for other low M values. These features lead to the formation of potential wells with depths of

$\sim 10^{-3}$ cm^{-1} at distances $R \sim 4 - 8$ μm. The wells we find support $\sim 300 - 500$ bound states, with a spacing $\sim 10^{-5}$ cm^{-1} [156]. A LZ estimate shows that the energy gaps at the crossings are large enough to make these vibrational states stable over a time far in excess of the radiative lifetime of the single atoms ($\sim$ seconds). The wells will lead to observable spectral features of width ~ 30 MHz in the high density regime [46]. The possibility of deep wells caused by avoided crossings was mentioned in Ref. [47] for Rb. We note that the wells we find from avoided crossings for Cs are at least 2 orders of magnitude deeper than those found by considering the dispersion coefficients alone for Rb [47], and that they are tunable by changing the E-field. The effect of increasing the E-field on the $M = 3$ states is shown explicitly in Fig. 7.6. It can be seen that the potential curves are highly tunable with small E-fields - the formation of long-range molecules is controllable from an external parameter. The wells are analyzed in more detail in Section 7.3.

The dipole and quadrupole interactions induce a mixing of Stark shifted pair states in addition to the mixing of single atom states by the Stark effect from the background E-field. At $R = 6$ μm, $M = 3$, the various 89D89D pairs contain total admixtures of other Stark pairs of $1.5 - 3.4\%$. Using zero-field labels, for 89D89D, the largest admixtures are from the various fine structure components of the 90P90P, 87F90P, 90P89D, 87F86F and 86F91P, 87F90S, 90P91S pairs, in order of decreasing magnitude. The combined effect of the E-field together with the quadrupole interactions results in coupling of otherwise dipole forbidden states, most prominently the 90P89D state. These states contribute to the energy shifts. The opening of these new collision channels presents additional modes of internal energy conversion for the attractive potential curves.

For comparison, we also calculated potentials for Cs 23P pairs and surrounding states, shown in Fig. 7.8. For these, the admixture of other states at $R = 6$ μm is less

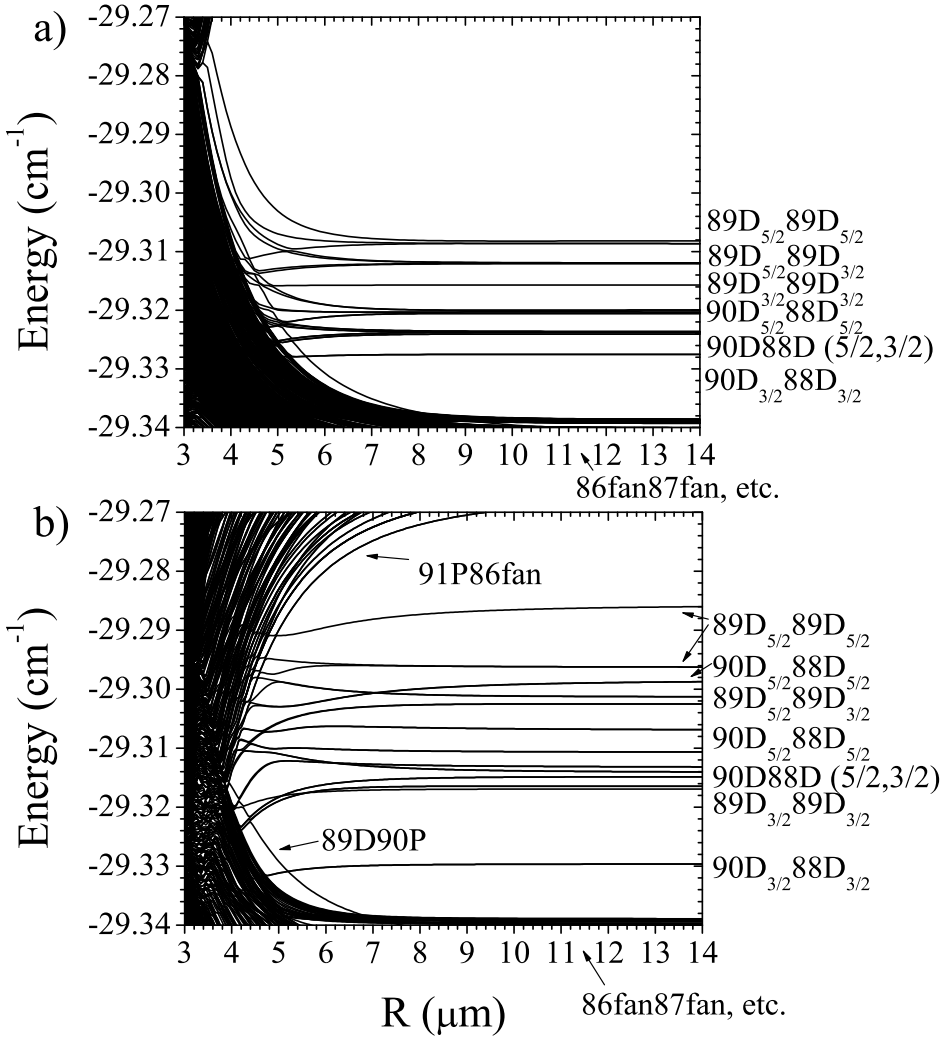

Figure 7.7: Pair potentials of the 89D89D and surrounding states for $M = 3$ obtained by matrix diagonalization for different background E-field magnitudes: a) 28 mV cm^{-1} and b) 120 mV cm^{-1}.

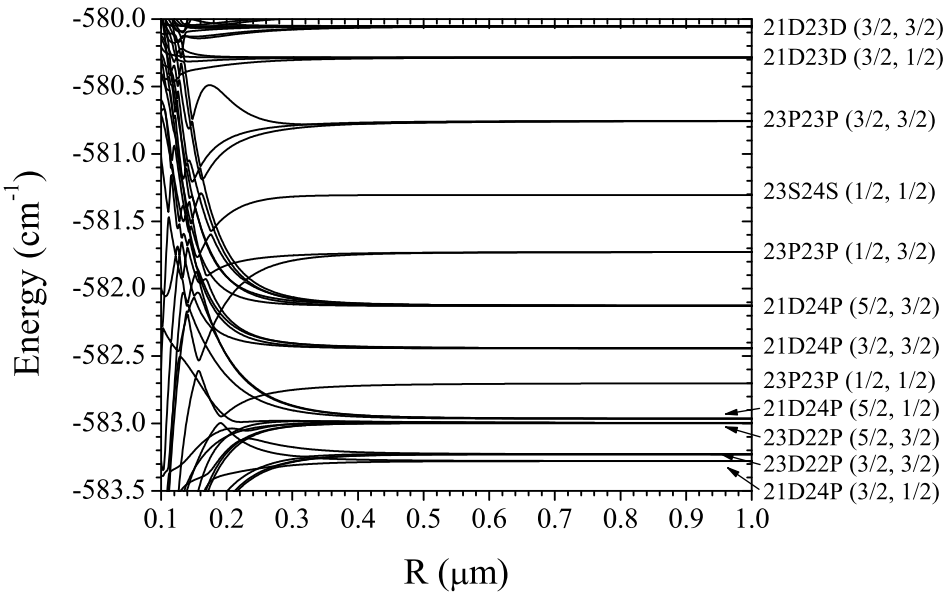

Figure 7.8: Pair potentials of the 23P23P and surrounding states for $0 \leq M \leq 5$, obtained by matrix diagonalization for a background E-field magnitude of 60 mV cm^{-1}. Note the change of scales compared to the $n \sim 89$ potentials. Labels in parentheses denote the (j_1, j_2) quantum numbers of the respective pair.

than 10^{-9}%. The admixtures for 23P become non-negligible only in the range $R <$ 0.5 μm, corresponding to densities of $> 10^{12}$ cm^{-3}. Experimentally, these densities would be difficult to attain in anything but a dipole trap or magnetic trap. Conversion of internal energy is dramatically reduced for states around $n \sim 23$. Compared to the $n \sim 89$ potentials on the energy scale of Fig. 7.3, the $n \sim 23$ potentials are flat for all internuclear distances $R > 1$ μm.

To gain further insight into the time scales for the interactions to develop, we define the total transition rate Γ associated with the off-diagonal matrix elements at a specific R,

$$\Gamma = \sum_{\alpha,\beta} \frac{1}{h} \frac{\left|\widetilde{\langle\alpha|}\widetilde{\langle\beta|}H|89\widetilde{D,j,m_j}\rangle|89\widetilde{D,j',m_j'}\rangle\right|^2}{E_{\alpha\beta} - E_{\mathrm{89D89D}}}, \tag{7.5}$$

where the sum is over all states that are not 89D89D pairs. For $R = 6$ μm, $M = 3$,

$\Gamma = 35 - 69$ MHz. Individual channels with largest rates are to the zero-field labeled 90P90P ($\sim$ 11 MHz), 87F90P ($\sim$ 7 MHz), 90P89D, 86F87F (both $\sim$ 3 MHz), 86F91P, 91P86F, 91S86F (all $\sim$ 0.4 MHz). The rates vary depending on the specific fine-structure states. Thus, for experiments taking place in time intervals shorter than $\sim$ 100 ns, the atoms will behave as an 89D pair wave packet that dynamically evolves on the potentials. Conversely, for experiments taking place over longer time intervals, the excited atom pairs will behave as stationary eigenstates. The fact that there are many states with similar rates means that excitation transfer in the gas, a highly disordered system, will generally be complicated.

7.3 Analysis of long-range molecular Rydberg atom - Rydberg atom potentials

7.3.1 Introduction

Long-range ($\sim$ 5 μm) Rydberg diatoms have been the subject of several recent theoretical studies [47, 157, 158] because of the unique nature of these peculiar molecules. The two-photon excitation of these kinds of molecules gives rise to new features that can be observed in the energy spectrum of a cold Rydberg gas. These resonances are important because the (nonlinear) optical properties of and interactions taking place in a cold Rydberg gas are sensitive to the positions of all the energy states, including those of the Rydberg molecules. The use of the interactions and nonlinear optical properties of a cold Rydberg gas are essential for quantum computation schemes based on cold Rydberg atoms [6].

In this section, we analyze long-range Cs Rydberg molecules that consist of electronic doubly excited configurations. We concentrate on molecular resonances that are energetically close to singly excited Rydberg absorption lines in the region of $n \sim 89$. The vibrational energy spacing, electric field dependence and spectral lineshape are calculated. We also present estimates of the Rydberg molecule lifetime and excitation rate.

7.3.2 Bound states

As described in the last section, the matrix diagonalization of the multipole interaction Hamiltonian for pairs of highly excited Cs Rydberg atoms in the presence of a small electric field along the internuclear axis reveals potential wells at very large internuclear distances of $R \sim 5$ μm. These wells are due to avoided crossings between the potentials. They appear at small electric field, $\epsilon = 30$ mV cm^{-1}, and shift

and change shape with increasing electric field. Molecular resonances resulting from such wells have been proposed as a possible explanation of unexpected spectral features that have been observed [46]. Here, we will focus on investigating some of the properties of these potential wells.

Fig. 7.9 shows the $M = 3$ pair interaction potentials of 89D89D, 88D90D and surrounding pair states for four different applied fields. We will consider the two avoided crossings that are labeled C1 and C2 at $\epsilon = 30$ mV cm^{-1}, and C1' and C2' at $\epsilon = 60$ mV cm^{-1}. At $\epsilon = 120$ mV cm^{-1}, the Stark shift is significant and causes many states to cross and change energy in such a way that the avoided crossings disappear. The atomic energy levels at high n are so closely spaced in energy that many similar wells can be found, for example in the $M = 2$ potentials, for different combinations of principal quantum numbers.

Fig. 7.10 shows the potential wells at the crossings C1 and C2 in detail, including the bound state wavefunctions and eigenvalues for ν=0, 99, and 199. There are hundreds of bound vibrational states in each well. There are 398, 372, 291, and 348 states in C1, C2, C1', and C2' respectively. The bound state wavefunctions and the vibrational energies were calculated using the program LEVEL [156].

Fig. 7.11 shows the spacings between successive vibrational levels for the same four wells. Apart from the lowest lying states, which have energy spacings of hundreds of kHz, the higher vibrational states are effectively a continuum, with spacings on the order of kHz. The spacings change with the electric field.

Since we are modeling the creation of these molecules at ultracold temperatures ($T \approx 40$ μK), we neglect the rotation of the molecules. This is done on the grounds that the centrifugal distortion at such temperatures for large R for the heavy Cs atoms is negligible. This can be seen from a classical estimate. In a MOT at $T = 40$ μK, the most probable relative velocity in the center of mass frame will be, $v \approx$ 4.9 cm/s.

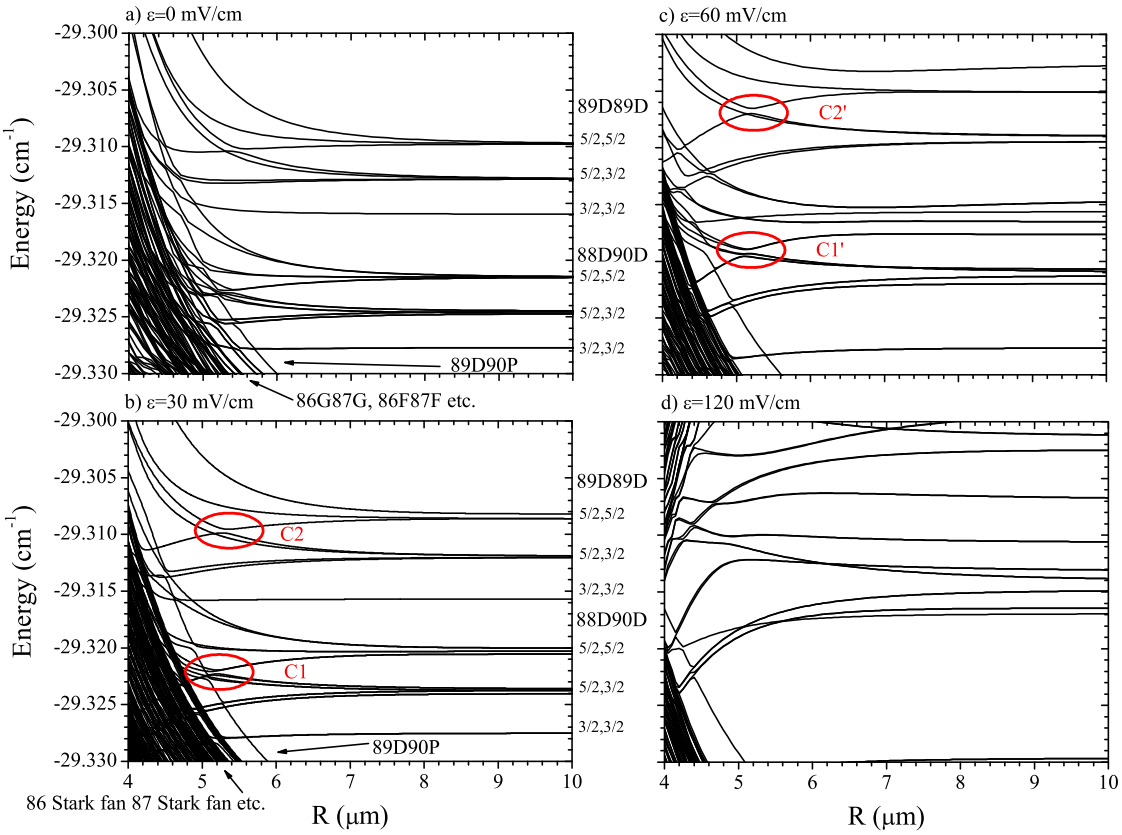

Figure 7.9: Long-range wells in the pair potentials of the Cs 89D89D and surrounding states for $M = 3$ for a background E-field of a) 0 mV cm^{-1}, b) 30 mV cm^{-1}, c) 60 mV cm^{-1}, and d) 120 mV cm^{-1}. Potential wells C1 and C2 in b) and C1' and C2' in c) are circled. Pairs of numbers below a given label are the respective j_1, j_2 combinations. Labels for small fields are asymptotic zero-field quantum numbers. At larger fields, c) and d), even the asymptotic ($R \to \infty$) states begin to mix. The zero field quantum numbers become meaningless, apart from M.

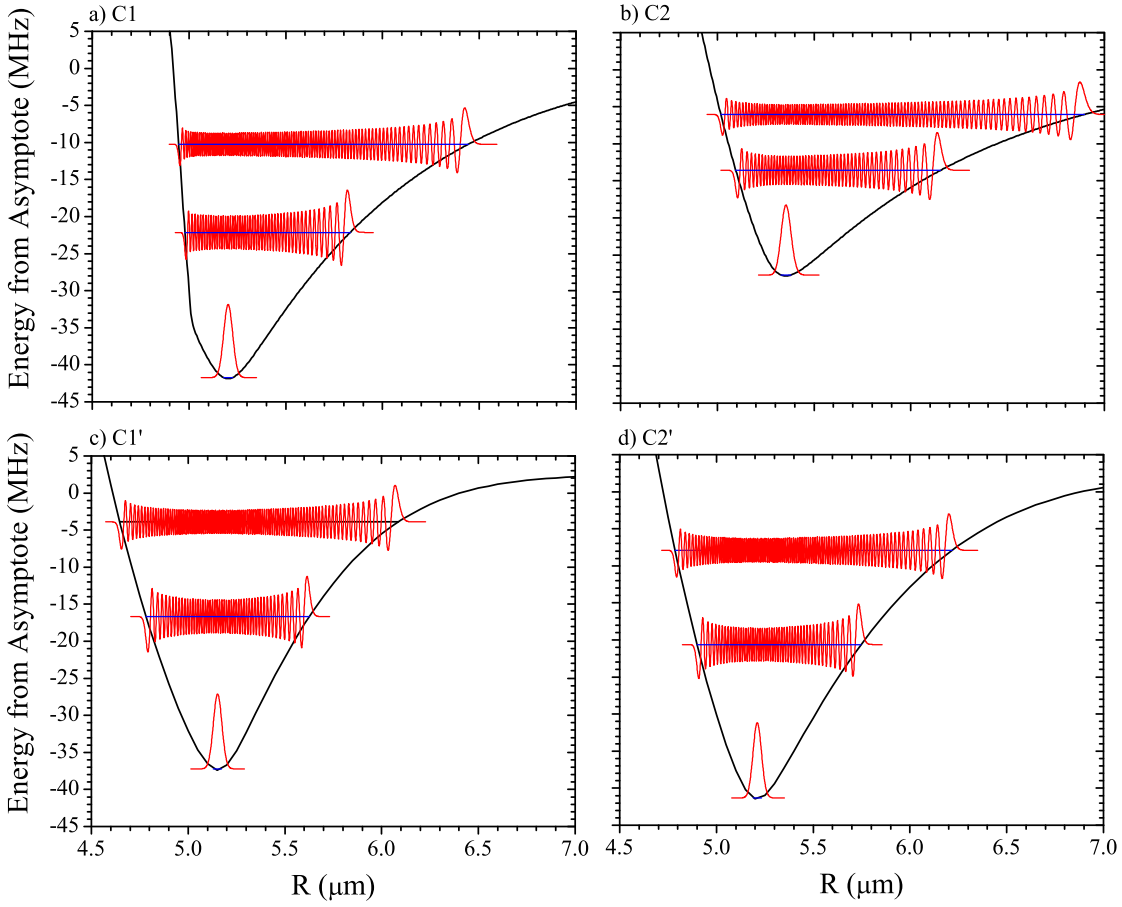

Figure 7.10: Detail of the potential wells that are circled in Fig. 7.9: a) C1, b) C2, c) C1', and d) C2'. The bound vibrational ($J = 0$) wavefunctions for ν=0, 99, and 199 and corresponding eigenvalues are indicated. The energy axis is the atom-pair energy. The energetic zero is chosen as the asymptotic ($R \to \infty$) pair energy of the state correlating at zero field to $89D_{5/2}89D_{5/2}$ ($M = 3$) for C1, C1' and $88D_{5/2}90D_{5/2}$ ($M = 3$) for C2, C2'. The kink in the potential curve at $R = 5$ μm in a) is due to an additional avoided crossing with a very small gap size of 2 MHz. It is further discussed in the text.

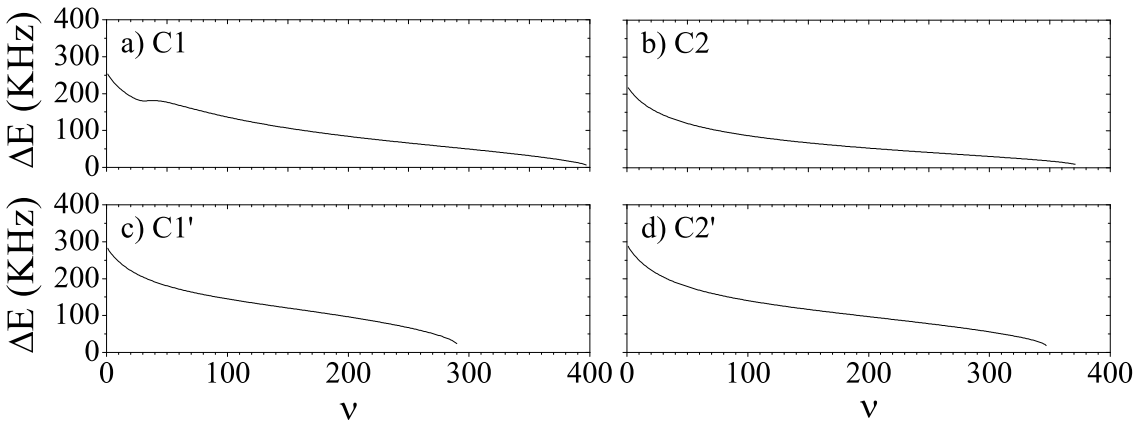

Figure 7.11: Vibrational ($J = 0$) energy spacings vs. vibrational quantum number ν for the potential wells circled in Fig. 7.9. Upper vibrational states in these wells form an effective continuum, with spacings on the order of kHz. The kink in a) results from the kink in Fig. 7.10a) at $R = 5$ μm.

If the molecule rotates at this velocity, the time to trace one complete revolution of the nuclei at $R = 5$ μm is $\tau_{\rm rev} = 630$ μs, which is larger than our estimated radiative lifetime of the bound states. With the same parameters, the maximum classical nuclear angular momentum is $l_{\rm max} = \mu v R \approx 261$ in units of $\hbar$, μ being the reduced mass. The rotational constant of the long-range Rydberg molecule is $B \approx 3$ Hz. The maximum rotational energy will then be 154 kHz, much less than the typical narrow-band cw laser line width. The rotational energy will, however, be on the order of the vibrational energy spacings shown in Fig. 7.11. This means that if one considers the full set of all rovibrational states in the potential wells, the energy spectrum will be observed to be even closer to a true continuum, with spacings between rovibrational states on the order of hundreds of Hz, or less.

One subtle point arises here due to the background field. If the molecule rotates, the orientation of the body-fixed internuclear axis with respect to the lab-fixed field axis will change in time, resulting in a slowly varying AC field component both per-

pendicular and parallel to the internuclear axis. This is an effect similar in principle to magnetic spin resonance. In order to account for this small effect, the more complicated Hamiltonian for arbitrary field direction described in Section 7.2.4 needs to be solved, and a dynamic consideration of the AC field component by introducing an approximation similar to the rotating wave approximation would be needed. We are currently working to develop this theory in detail.

7.3.3 Lifetimes

The wells found in our calculations arise from avoided crossings between pair states that are close in energy. An estimate of the lifetime of the bound states must include the predissociation channels and ionization channels, through Auger processes, in addition to the radiative decay channel. For the two wells shown, we make a simple Landau-Zener estimate to get an estimate of the lifetime due to predissociation [159]. Assuming one dominant predissociation channel, the Landau-Zener probability of making a nonadiabatic jump to the lower potential in one traversal is

$$P_{\mathrm{LZ}} = \exp\left(-2\pi \frac{(1/2\ \Delta E)^2}{\hbar\,(dE_1/dR - dE_2/dR)\,v}\right), \tag{7.6}$$

where E_1 and E_2 are the two potentials, $v = dR/dt$ is the nuclear velocity in the center of mass frame on the upper potential, and ΔE is the potential gap. With exception of the well C1, the gaps are on the order of 10 MHz for the crossings considered here. Assuming the worst case, we let $v \approx \sqrt{2\,\delta E/\mu}$, where the depth of the well, $\delta E \approx 50$ MHz, and the reduced mass, $\mu = 1/2\ m_{\mathrm{Cs}}$. The slopes of the potentials are estimated from the potential curves of Fig. 7.9, to be $dE_1/dR \approx -dE_2/dR \approx 61\ \mathrm{MHz}\,\mu\mathrm{m}^{-1}$. The probability of dissociation in half a vibrational period is then on the order of $P_{\mathrm{LZ}} \approx 5 \times 10^{-7}$. This is negligible at the slow velocity of the atoms in the wells of $v \approx 60\ \mathrm{cm\,s}^{-1}$. The calculated probability, P_{LZ}, leads to a lower limit for the predissociation half-life for all vibrational states of $\tau_{\mathrm{LZ}} > 100$ ms.

The well C1 has to be considered separately, since it displays an additional avoided crossing with a very small gap. This feature is seen in Fig. 7.10a as a kink on the inner wall of the potential, and as a kink in the vibrational spacings in Fig. 7.11a.

The gap is so small, 2 MHz, that any bound state close in energy to or above this kink will predissociate with $\tau_{\mathrm{LZ}} < 1$ μs. This will affect all but the lowest few bound states. Due to the Stark shift, this feature disappears at higher fields. It is already negligible for C1' at $\epsilon = 60$ mV cm^{-1}. This is particularly interesting, because the electric field has the effect of stabilizing the molecule. The externally imposed field controls the molecule formation to some extent.

The contribution to the lifetime due to Auger autoionization processes is negligible due to the large internuclear separation at $R = 5$ μm. It can be seen from Fig. 7.9 that ionization will take place as the system follows potentials through the manifold formed by the high l states at $R < 4$ μm because of the many avoided crossings. In effect, one atom field ionizes the other in this region. The newly created ion can then in turn field ionize the remaining Rydberg atom. For the bound molecular states, this process does not take place, since the molecular potentials are repulsive at short range.

The radiative lifetime due to spontaneous emission is estimated to be close to the atomic lifetime. Black-body radiation will affect the lifetime since it affects the lifetime of the Rydberg states. Using the semiempirical polynomial scaling law from Ref. [95], the radiative lifetime of the d-states around n=89 is $\approx$ 466 μs. Thus $\tau_{\mathrm{rad}} < \tau_{\mathrm{LZ}}$ by several orders of magnitude, making radiative decay the dominant decay channel. This lifetime is long enough to allow for the observation of the long-range Rydberg molecules.

7.3.4 Lineshapes

The lineshape associated with excitation into the potential wells C1, C2, C1', and C2' from the 6P excited MOT state can be estimated from the Franck-Condon factors for the excitation. We first assume that the electronic contribution to the transition matrix element from two 6P atoms to the vibrational states in the well is constant over the extent of the wells. The dominant electronic pair states along the wells have only small admixtures of other states, ∼several percent. The value of the dipole moments will then be approximately the same as the asymptotic ($R \to \infty$) atomic transition dipole moments. We expect the change in dipole moments with R to be less than 10 percent of the asymptotic value. The primary contribution to the lineshape then comes from the overlap of the initial scattering wavefunction ($\psi_i(R)$) with the vibrational wavefunction ($\psi_\nu(R)$) in the well, FC = $|\langle\psi_i|\psi_\nu\rangle|^2$. Due to the two photon nature of the excitation process, ψ_i is the scattering wavefunction of a 6P88D or 6P90D pair for C1, C1', and of a 6P89D pair for C2, C2'.

We define a thermally (phase-)averaged effective Franck-Condon overlap factor as

$$\overline{\mathrm{FC}}(\nu) = \int_0^\infty \int_{R_0}^{R_1} f(E)|\langle\psi_i(k(E),R)|\psi_\nu(R)\rangle|^2\, dR\, dE \tag{7.7}$$

where R_0 and R_1 are the boundaries of a sufficiently large grid that encompasses all of the vibrational states, and f(E) is the Maxwell-Boltzmann distribution of energies. If E is the thermal kinetic energy of the nuclei, it is distributed according to a Maxwell-Boltzmann probability density $f(E)$. The FWHM thermal spread in energy at $T \sim 40\ \mu$K used here is 1.5 MHz. The integration over energy reflects the weighted averaging over the thermal wavelengths and phases for ψ_i. The asymptotic nuclear wavefunction is $\psi_i(k,R) = C\sin(k\,R+\delta(k))$ [160] where C is a normalization constant, k is the wavevector magnitude $k(E) = \sqrt{2\mu E/\hbar^2}$, $\mu = 1/2\, m_{\mathrm{Cs}}$ is the reduced mass, and δ is the phase shift. Although the wavefunctions are highly oscillatory, the integral over R is evaluated rather easily numerically by the method of Fast-Fourier-Transform.

We used $C = \sqrt{2/(2\,\mu\mathrm{m})}$ to normalize ψ_g, estimated from the radial extent of the wells. The phase shift δ depends on the scattering length [160]. It is expected to change by $\sim 2\pi$ over the thermal energy range at $T = 40\ \mu$K. While FC will depend on δ, and therefore on the scattering length of the initial state, the thermal energy distribution will be responsible for averaging over all of the phases. The dependence on δ should therefore be negligible for the averaged quantity $\overline{FC}$. We calculated $\overline{FC}$ for eight different values of δ, $\delta = 0, 1/4\,\pi, \ldots, 7/4\,\pi$. The maximum relative change of $\overline{FC}$ with δ was on the order of a few percent. On the scale of the plots shown in Fig. 7.12, there is no discernable dependence of the final averaged $\overline{FC}$ on the specific value of δ chosen, and the scattering length used. To simulate the effect of exciting the bound states with a typical dye laser linewidth of 1 MHz, we convolute $\overline{FC}$ with a Lorentzian of FWHM = 1 MHz and arrive at an estimated spectral lineshape for the excitation of the molecules.

Fig. 7.12 shows the convoluted and unconvoluted thermally averaged Franck-Condon overlap factors $\overline{FC}$ for the two potential wells at $\epsilon = 30$ mV cm^{-1} (C1 and C2) and at $\epsilon = 60$ mV cm^{-1} (C1' and C2'). The lineshape is qualitatively similar to Fig. 7.12 for other crossings found in the $M = 2$ potentials. The width of the overall shape changes from well to well, and is in the range of several tens of MHz. These wells, if observed, should appear in the spectra as features to the red or between the split atomic fine-structure lines. The maximum values of the averaged Franck-Condon factors are on the order of 1% for all the crossings found. Such a molecular resonance has to be created with a 2-photon transition to conserve angular momentum, since it involves a two electron excitation from P-states into D-states. The 88D90D line is favorable for possible observation using a single laser frequency ω, since no resonant power-broadened single photon transition will be near. In contrast, the 89D89D resonance would be hard to observe, since it is close to the 89D atomic

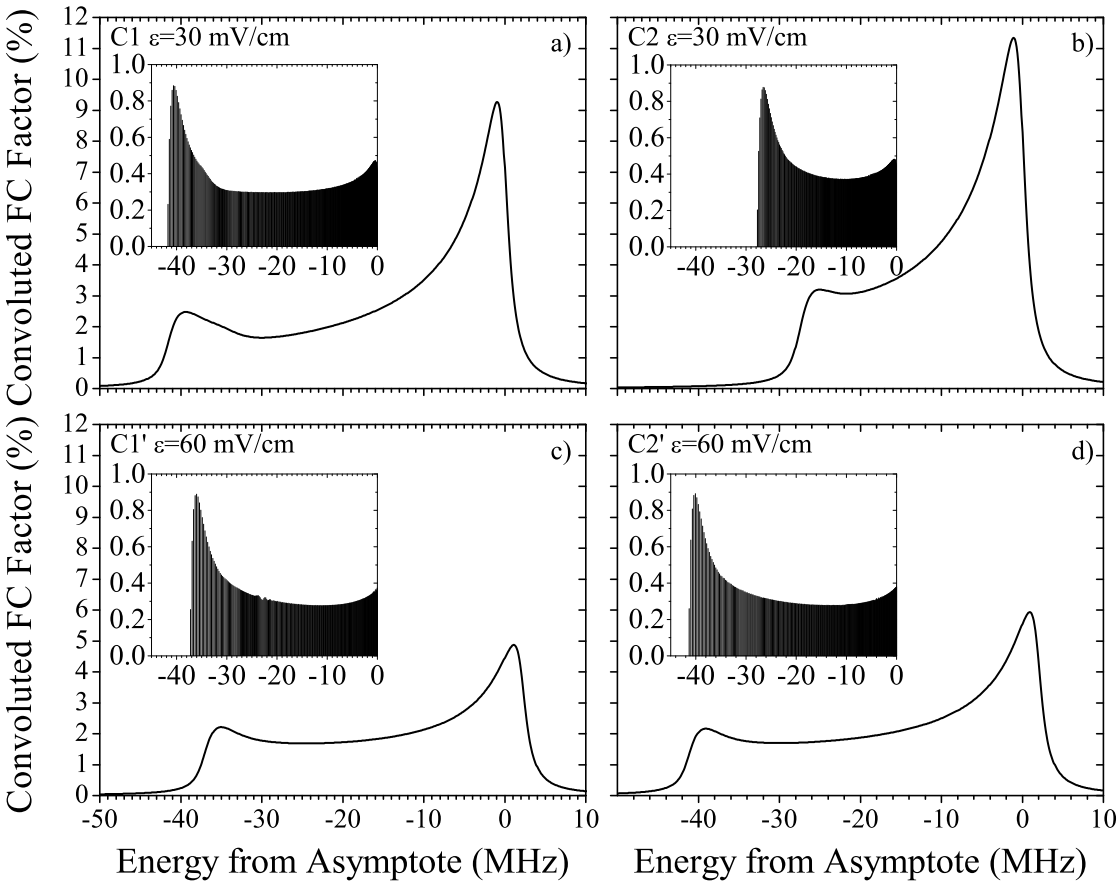

Figure 7.12: Effective thermally averaged Franck-Condon overlap factors $\overline{FC}$ vs. binding energy for the transition of a pair of 6P atoms into the crossings circled in Fig. 7.9. The main plots of a), b), c), and d) show the values of $\overline{FC}$ convoluted with a 1 MHz laser linewidth for the wells C1, C2, C1' and C2', respectively. The insets show the unconvoluted values of $\overline{FC}$ for the same wells. The energetic zero is chosen as the asymptotic ($R \to \infty$) pair energy of the state correlating at zero field to $89D_{5/2}89D_{5/2}$ ($M = 3$) for C1, C1' and $88D_{5/2}90D_{5/2}$ ($M = 3$) for C2, C2'.

single photon resonances.

7.3.5 Two-photon excitation rate

Assuming one contributing intermediate state to the two-photon excitation process and neglecting fine-structure, the two-photon excitation cross-section [161] on resonance with the 88D90D molecular state can be written in SI units as

$$\sigma_{fi}^{(2)}(\omega) = \frac{\pi}{2}\overline{FC}\left(\frac{\mu_0}{\epsilon_0}\right)\left(\frac{\mu_{fm}\mu_{mi}}{\hbar^2(\omega_m-\omega)}+\frac{\mu_{fm'}\mu_{m'i}}{\hbar^2(\omega_{m'}-\omega)}\right)^2\rho_f(\omega_f=2\omega). \tag{7.8}$$

Here, index i denotes the initial, indices m and m' the intermediate, and index f the final state. μ are the electronic transition dipole moments of the atomic transitions for each of the pair of atoms, $(\omega_m-\omega)$ are the detunings of the photons from the intermediate state, ρ_f is the density of states for the final state. We consider the excitation from the 6P state into the well C1 formed by 88D90D to estimate the observable signal. The closest lying allowed intermediate states, are the 6P88D and 6P90D pair states. Assuming these are the dominant intermediate states, we consider the two-photon excitation process as depicted in Fig. 7.13. To approximate $\sigma_{fi}^{(2)}(\omega)$, we use $\overline{FC}=0.01$. The dipole moments are estimated to be the atomic transition moments averaged over all m for unpolarized light, $\mu_{mi}\approx\langle 6\mathrm{P}|\langle 6\mathrm{P}|er_1|88\mathrm{D}\rangle|6\mathrm{P}\rangle = -1.424\times10^{-2}\,ea_0$, $\mu_{fm}\approx\langle 88\mathrm{D}|\langle 6\mathrm{P}|er_2|88\mathrm{D}\rangle|90\mathrm{D}\rangle = -1.375\times10^{-2}\,ea_0$. From symmetry $\mu_{m'i}=\mu_{fm}$, and $\mu_{fm'}=\mu_{mi}$. r_1 and r_2 are the electron distances measured from the respective atom core. The detuning from the 6P88D state is 10.3 GHz and the detuning from the 6P90D state is 10.0 GHz. Since we are interested in the resolution limited cross-section, the density of states is limited by the width $\Gamma_i = 5.22$ MHz of the initial atomic states $(6P_{3/2})$ to be $\rho_f=(2\pi\,\Gamma_i)^{-1}$.

Using this cross-section, we can estimate the expected ion detection rates in an experiment. Our experimental setup involves excitation from the $6P_{3/2}(F=5)$ state to high n ($n\sim89$) Rydberg states in a Cs MOT. The excited Rydberg atoms are pulse-

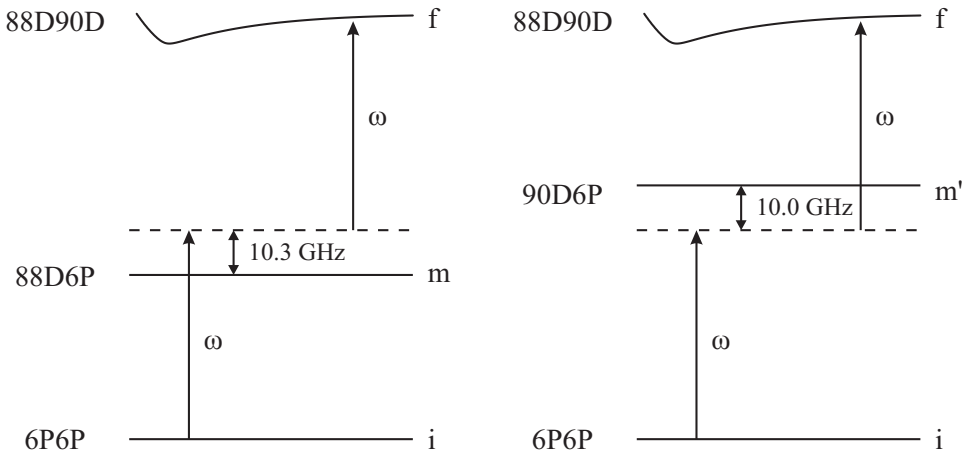

Figure 7.13: Schematic of the two-photon excitation into the well C1. The two possible choices for the intermediate state are shown. Due to the large R between the atoms in the final state, each of the two atoms will interact mostly with one of the two photons, and the pair transition dipole moments reduce to the atomic ones. Thus the left arrow is a transition taking place mostly on atom 1, the right arrow is a transition taking place mostly on atom 2.

field ionized and the ions are detected with an MCP detector [130]. The transition rate into the final state, W, is obtained from

$$W = \sigma_{fi}^{(2)}(\omega)\, I^2, \tag{7.9}$$

where I is the incident laser intensity. With W, the number of excited molecules, N, in one experiment in steady state can be estimated from the rate equations [137] as

$$N = \frac{N_t}{1 + \frac{W+\gamma}{W}}, \tag{7.10}$$

where N_t is the total number of atoms illuminated, and γ is a dephasing rate that limits the coherent two-photon process. N_t is equal to the number density of atoms n times V. Since the limited lifetime of the 6P state will dominate the dephasing processes, we estimate $\gamma = 5.22$ MHz. In our experiment, the excitation laser is focussed into the Cs MOT to create a cylindrical excitation volume of length $L \sim$

500 μm, with a radius at the focus of $r = 50$ μm. The excitation volume is then $V = \pi r^2 L$. Further parameters are $I = 255$ Wcm^{-2}, and assuming an average spacing of 5 μm between the cold Rydberg atoms, $n \approx 10^{10}$ cm^{-3}. If the repetition rate of the experiment is 1 kHz, using these parameters, we predict an ion creation rate of ≈ 6 Hz. This is low, but above the typical noise in a PFI detection scheme and thus should be detectable.

7.3.6 Conclusion

In conclusion, we calculated accurate pair potentials of the high n Cs 89D Rydberg atom pairs and surrounding states, including quantum-defect energies, near-resonant interactions, fine structure, and effects of a small background E-field parallel to the internuclear separation. This is the first calculation of Rydberg potentials that includes all the above essential features. Our results have confirmed former estimates based on scaling [149], but also revealed new features. We found many avoided crossings at R of several μm. These crossings cause potential wells that are at least two orders of magnitude deeper than the ones found before from perturbation theory for Rb [47]. We calculated energy transfer rates, and noted that energy transfer involves many states and that the time scale for state-to-state couplings at n=89, $R = 6$ μm, is hundreds of nanoseconds. We also showed that the Stark fan states should play an important role in initial ionization of ultracold plasmas.

We investigated some of the potential wells that appear in the calculated pair potentials at large internuclear distances around 5 μm, when a small background electric field of tens of mV cm^{-1} is applied along the internuclear axis. The wells are unique in that they feature a quasi-continuum of bound states, are found at extremely long range, and are solely due to the interplay between Van der Waals interactions and the additional Stark effect from the background field. The background E-field

actually stabilizes the molecule. We estimated an upper bound on the lifetimes of these states of > 400 μs, by considering a Landau-Zener model of predissociation, radiative decay, and ionization. Radiative decay was calculated to be the dominant decay mechanism. The Rydberg molecules are observable as two-photon resonances in Rydberg spectra. These resonances appear as small features to the red or between the atomic lines with linewidths on the order of tens of MHz, and a unique lineshape. We estimated the ion-detection count rates for one of the molecular states that is removed from any resonant atomic line. A two-photon excitation into this long-range bound state from a Cs MOT at $T = 40$ μK at a initial Cs $6P_{3/2}(F = 5)$ density of $\sim 10^{10}$ cm^{-3}, followed by pulse-field ionization and subsequent single ion detection gives count rates of ~ 6 Hz.

This work was verified by experiments done in our group using pulsed-field ionization time-of-flight spectroscopy in a Cs MOT. We measured the kinetic energy gain of two Cs Rydberg atoms excited onto a repulsive 88D90D pair potential. The measured kinetic energy agreed with the one deduced from the calculated pair potential curve [60]. We excited long-range Cs Rydberg atom-Rydberg atom molecules close to the 89D89D pair state and the excitation energies agreed with the positions of wells in the calculations [139]. We used the Coulomb repulsion to deduce the equilibrium separation of long-range $(n-1)$D$(n+1)$D Cs Rydberg atom molecules, $64 \leq n \leq 67$, and found good agreement with the pair potential calculations [55]. In collaboration with the group of Luis Marcassa, we were able to explain the observed population transfer from $32S_{1/2}$ to $32P_{3/2}$ states in a cold Rb Rydberg gas using the calculated mixing fractions of other Rydberg states, obtained from the eigenvectors in our pair potential calculations [140]. Recently, we explained the manipulation of the decay rate of nDnD quasi-molecules, $29 \leq n \leq 41$, with a DC electric field using a Landau-Zener type analysis of the dynamics on our calculated potential curves [142].

Future directions are to investigate the collision dynamics at small R to gain more understanding of energy transfer and plasma formation.

Chapter 8

Conclusion and outlook

In conclusion, we constructed and characterized an atom chip setup for experiments with cold ^{87}Rb Rydberg atoms. We demonstrated that we can load the chip with $\sim 6 \times 10^5$ cold ^{87}Rb atoms at distances of ~ 150 μm away from the chip surface.

Our method of choice to probe Rydberg energy levels is electromagnetically induced transparency with Rydberg atoms (Rydberg EIT). To better understand the method, we performed Rydberg EIT measurements with room-temperature Cs and ^{87}Rb. In the EIT experiments, we used microwaves to couple the 3-level ladder-type Rydberg EIT system to a second Rydberg level. The role of the microwaves was to simulate the effects of atom-surface interactions in future experiments on the atom chip. The coupled levels in Cs were $6S_{1/2}, F = 4$, $6P_{3/2}, F = 5$, $59D_{5/2}$ and $57F_{7/2}$. The coupled levels in ^{87}Rb were $5S_{1/2}, F = 2$, $5P_{3/2}, F = 3$, $53D_{5/2}$ and $54P_{3/2}$. We observed polarization effects in the Rb system that changed the EIT lineshape dramatically. We were able to explain the observed polarization effects on the transmission lineshapes only by taking into account all magnetic sublevels, including the hyperfine structure of both Rydberg levels. To our knowledge, this is the first observation of polarization effects in Rydberg EIT. In addition, we found that the Rydberg EIT system has potential application as a highly sensitive traceable narrow-band microwave detector.

In order to better understand the long-range interactions between Rydberg atoms, we calculated the pair interaction potentials of cold Cs Rydberg atoms, including the fine-structure and a small applied electric field. We found that avoided crossings between potential curves lead to long-range wells that support hundreds of bound states for atom pairs at internuclear distances of several μm.

In the near future, we plan to use the current atom chip for two experiments. First, we want to investigate the decoherence rates and energy level shifts due to interactions between Rydberg atoms and nearby surfaces. To observe small shifts < 1MHz and perturbations of the transmission lineshape using Rydberg EIT, we would like to achieve the smallest EIT linewidth. Our measurements on Rydberg EIT suggest that the currently observed EIT linewidths can be reduced by reducing the laser linewidths. Since the laser linewidths are limited by low frequency technical noise, we should be able to decrease the effective laser linewidths by scanning the probe laser quickly within a few hundred μs over the EIT peak. Since lock-in detection does not work when scanning the laser that fast, we will need to average many separate scans to increase the signal-to-noise ratio. In order to be able to average many scans, we need to reduce the drift of the Rydberg excitation laser. We plan to implement a better frequency stabilization by locking the Rydberg excitation laser to a second, separate EIT setup that will be used solely as frequency reference.

Second, we want to study the dynamics of Rydberg atoms in a microscopic double well potential. Our atom chip contains several wires for future experiments on Rydberg atoms in double wells. u-wires on the chip can be used to change the aspect ratio of the trapped cloud, and RF-wires that run alongside the central z-wire segment can be used to generate RF adiabatic potentials. Using a combination of RF and DC current-carrying wires, our microscopic trapping potentials can be designed to trap atoms in a microscopic double well, where two clouds of cold atoms are separated by a small distance < 10 μm [12]. At these separations, the long-range dipole-dipole interactions between high-lying Rydberg excitations in each of the two clouds will become observable through shifts of the Rydberg energy levels. We plan to test and optimize the transfer of atoms into the double well potential and probe the two separate clouds using Rydberg EIT.

In the long-term future, we intend to use the setup presented in this thesis with other atom chip designs as well. At the moment, we are working on an atom chip design that includes a waveguide for surface polaritons [162, 163]. The idea behind the design is to couple Rydberg excitations in a cold cloud of atoms to surface polaritons on the waveguide. The polaritons might travel several mm in the waveguide and could then be coupled to a second cloud of cold atoms at the waveguide exit. Such polariton waveguides might be used in the future to construct coherent polariton circuits for the transfer of Rydberg excitations and, ultimately, quantum computing.

References

[1] D. A. Steck, "Rubidium 87 D Line Data," available online at http://steck.us/alkalidata, (revision 2.1.4, December 23, 2010).

[2] J. Ye, S. Swartz, P. Jungner, and J. L. Hall, "Hyperfine structure and absolute frequency of the 87Rb 5P3/2 state," Opt. Lett. **21**, 1280 (1996).

[3] S. Bize, Y. Sortais, M. S. Santos, C. Mandache, A. Clairon, and C. Salomon, "High-accuracy measurement of the 87Rb ground-state hyperfine splitting in an atomic fountain," Europhys. Lett. **45**, 558 (1999).

[4] K. Singer, J. Stanojevic, M. Weidemüller, and R. Côté, "Long-range interactions between alkali Rydberg atom pairs correlated to the n s n s, n p n p and n d n d asymptotes," J. Phys. B: At. Mol. Opt. Phys. **38**, S295 (2005).

[5] M. Saffman, T. G. Walker, and K. Mølmer, "Quantum information with Rydberg atoms," Rev. Mod. Phys. **82**, 2313 (2010).

[6] D. Jaksch, J. I. Cirac, P. Zoller, S. L. Rolston, R. Côté, and M. D. Lukin, "Fast Quantum Gates for Neutral Atoms," Phys. Rev. Lett. **85**, 2208 (2000).

[7] M. D. Lukin, M. Fleischhauer, R. Cˆté, L. M. Duan, D. Jaksch, J. I. Cirac, and P. Zoller, "Dipole Blockade and Quantum Information Processing in Mesoscopic Atomic Ensembles," Phys. Rev. Lett. **87**, 037901 (2001).

[8] K. Mølmer, L. Isenhower, and M. Saffman, "Efficient Grover search with Rydberg blockade," J. Phys. B: At. Mol. Opt. Phys. **44**, 184016 (2011).

[9] H. Kübler, J. P. Shaffer, T. Baluktsian, R. Löw, and T. Pfau, "Coherent excitation of Rydberg atoms in micrometre-sized atomic vapour cells," Nature Photon. **4**, 112 (2010).

[10] A. Tauschinsky, R. M. T. Thijssen, S. Whitlock, H. B. van Linden van den Heuvell, and R. J. C. Spreeuw, "Spatially resolved excitation of Rydberg atoms and surface effects on an atom chip," Phys. Rev. A **81**, 063411 (2010).

[11] E. Urban, T. A. Johnson, T. Henage, L. Isenhower, D. D. Yavuz, T. G. Walker, and M. Saffman, "Observation of Rydberg blockade between two atoms," Nature Photon. **5**, 110 (2009).

[12] I. Lesanovsky, T. Schumm, S. Hofferberth, L. M. Andersson, P. Krüger, and J. Schmiedmayer, "Adiabatic radio-frequency potentials for the coherent manipulation of matter waves," Phys. Rev. A **73**, 033619 (2006).

[13] A. K. Mohapatra, T. R. Jackson, and C. S. Adams, "Coherent Optical Detection of Highly Excited Rydberg States Using Electromagnetically Induced Transparency," Phys. Rev. Lett. **98**, 113003 (2007).

[14] *Atom Chips*, edited by J. Reichel and V. Vuletić (Wiley, San Francisco, 2011).

[15] J. Fortágh and C. Zimmermann, "Magnetic microtraps for ultracold atoms," Rev. Mod. Phys. **79**, 235 (2007).

[16] W. Hänsel, P. Hommelhoff, T. W. Hänsch, and J. Reichel, "Bose-Einstein condensation on a microelectronic chip," Nature **413**, 498 (2001).

[17] H. Ott, J. Fortagh, G. Schlotterbeck, A. Grossmann, and C. Zimmermann, "Bose-Einstein Condensation in a Surface Microtrap," Phys. Rev. Lett. **87**, 230401 (2001).

[18] T. van Zoest, N. Gaaloul, Y. Singh, H. Ahlers, W. Herr, S. T. Seidel, W. Ertmer, E. Rasel, M. Eckart, E. Kajari, S. Arnold, G. Nandi, W. P. Schleich, R. Walser, A. Vogel, K. Sengstock, K. Bongs, W. Lewoczko-Adamczyk, M. Schiemangk, T. Schuldt, A. Peters, T. Könemann, H. Müntinga, C. Lämmerzahl, H. Dittus, T. Steinmetz, T. W. Hänsch, and J. Reichel, "Bose-Einstein Condensation in Microgravity," Science **328**, 1540 (2010).

[19] R. Folman, P. Treutlein, and J. Schmiedmayer, in *Atom Chips*, edited by J. Reichel and V. Vuletić (Wiley, San Francisco, 2011), Chap. 3, pp. 61–117.

[20] W. Hänsel, J. Reichel, P. Hommelhoff, and T. W. Hänsch, "Magnetic Conveyor Belt for Transporting and Merging Trapped Atom Clouds," Phys. Rev. Lett. **86**, 608 (2001).

[21] T. Schumm, S. Hofferberth, L. M. Andersson, S. Wildermuth, S. Groth, I. Bar-Joseph, J. Schmiedmayer, and P. Krüger, "Matter-wave interferometry in a double well on an atom chip," Nature Phys. **1**, 57 (2005).

[22] Y.-J. Wang, D. Z. Anderson, V. M. Bright, E. A. Cornell, Q. Diot, T. Kishimoto, M. Prentiss, R. A. Saravanan, S. R. Segal, and S. Wu, "Atom Michelson Interferometer on a Chip Using a Bose-Einstein Condensate," Phys. Rev. Lett. **94**, 090405 (2005).

[23] D. Heine, W. Rohringer, D. Fischer, M. Wilzbach, T. Raub, S. Loziczky, X. Liu, S. Groth, B. Hessmo, and J. Schmiedmayer, "A single-atom detector integrated on an atom chip: fabrication, characterization and application," New Journal of Physics **12**, 095005 (2010).

[24] F. Ramírez-Martínez, C. Lacroûte, P. Rosenbusch, F. Reinhard, C. Deutsch, T. Schneider, and J. Reichel, "Compact frequency standard using atoms trapped on a chip," Advances in Space Research **47**, 247 (2011).

[25] P. Treutlein, P. Hommelhoff, T. Steinmetz, T. W. Hänsch, and J. Reichel, "Coherence in Microchip Traps," Phys. Rev. Lett. **92**, 203005 (2004).

[26] M. P. A. Jones, C. J. Vale, D. Sahagun, B. V. Hall, and E. A. Hinds, "Spin Coupling between Cold Atoms and the Thermal Fluctuations of a Metal Surface," Phys. Rev. Lett. **91**, 080401 (2003).

[27] M. Antezza, L. P. Pitaevskii, and S. Stringari, "Effect of the Casimir-Polder force on the collective oscillations of a trapped Bose-Einstein condensate," Phys. Rev. A **70**, 053619 (2004).

[28] J. Fortágh, H. Ott, S. Kraft, A. Günther, and C. Zimmermann, "Surface effects in magnetic microtraps," Phys. Rev. A **66**, 041604 (2002).

[29] H. J. Metcalf and P. v. d. Straten, *Laser Cooling and Trapping* (Springer, New York, 1999).

[30] E. L. Raab, M. Prentiss, A. Cable, S. Chu, and D. E. Pritchard, "Trapping of Neutral Sodium Atoms with Radiation Pressure," Phys. Rev. Lett. **59**, 2631 (1987).

[31] J. Reichel, W. Hänsel, and T. W. Hänsch, "Atomic Micromanipulation with Magnetic Surface Traps," Phys. Rev. Lett. **83**, 3398 (1999).

[32] M. A. Clifford, G. P. T. Lancaster, R. H. Mitchell, F. Akerboom, and K. Dholakia, "Realization of a mirror magneto-optical trap," J. Mod. Opt. **48**, 1123 (2001).

[33] T. F. Gallagher, *Rydberg Atoms* (Cambridge University Press, New York, 1994).

[34] H. Maeda, J. H. Gurian, and T. F. Gallagher, "Nondispersing Bohr Wave Packets," Phys. Rev. Lett. **102**, 103001 (2009).

[35] J. R. Rydberg, "On the Structure of the Line-Spectra of the Chemical Elements," Philosophical Magazine, 5th series **29**, 331 (1890).

[36] E. Amaldi and E. Segr, "Effetto della Pressione Sui Termini Elevati Degli Alcalini," Il Nuovo Cimento (1924-1942) **11**, 145 (1934), 10.1007/BF02959828.

[37] E. Fermi, "Sopra lo Spostamento per Pressione delle Righe Elevate delle Serie Spettrali," Il Nuovo Cimento (1924-1942) **11**, 157 (1934), 10.1007/BF02959829.

[38] T. W. Hänsch, "Repetitively Pulsed Tunable Dye Laser for High Resolution Spectroscopy," Appl. Opt. **11**, 895 (1972).

[39] J. M. Raimond, G. Vitrant, and S. Haroche, "Spectral line broadening due to the interaction between very excited atoms: 'the dense Rydberg gas'," Journal of Physics B: Atomic and Molecular Physics **14**, L655 (1981).

[40] D. Comparat and P. Pillet, "Dipole blockade in a cold Rydberg atomic sample," J. Opt. Soc. Am. B **27**, A208 (2010).

[41] D. Tong, S. M. Farooqi, J. Stanojevic, S. Krishnan, Y. P. Zhang, R. Côté, E. E. Eyler, and P. L. Gould, "Local Blockade of Rydberg Excitation in an Ultracold Gas," Phys. Rev. Lett. **93**, 063001 (2004).

[42] J. Honer, R. Löw, H. Weimer, T. Pfau, and H. P. Büchler, "Artificial Atoms Can Do More Than Atoms: Deterministic Single Photon Subtraction from Arbitrary Light Fields," Phys. Rev. Lett. **107**, 093601 (2011).

[43] R. Heidemann, U. Raitzsch, V. Bendkowsky, B. Butscher, R. Löw, and T. Pfau, "Rydberg Excitation of Bose-Einstein Condensates," Phys. Rev. Lett. **100**, 033601 (2008).

[44] W. Li, P. J. Tanner, and T. F. Gallagher, "Dipole-Dipole Excitation and Ionization in an Ultracold Gas of Rydberg Atoms," Phys. Rev. Lett. **94**, 173001 (2005).

[45] M. Mudrich, N. Zahzam, T. Vogt, D. Comparat, and P. Pillet, "Back and Forth Transfer and Coherent Coupling in a Cold Rydberg Dipole Gas," Phys. Rev. Lett. **95**, 233002 (2005).

[46] S. M. Farooqi, D. Tong, S. Krishnan, J. Stanojevic, Y. P. Zhang, J. R. Ensher, A. S. Estrin, C. Boisseau, R. Côté, E. E. Eyler, and P. L. Gould, "Long-Range Molecular Resonances in a Cold Rydberg Gas," Phys. Rev. Lett. **91**, 183002 (2003).

[47] C. Boisseau, I. Simbotin, and R. Côté, "Macrodimers: Ultralong Range Rydberg Molecules," Phys. Rev. Lett. **88**, 133004 (2002).

[48] K.-J. Boller, A. Imamolu, and S. E. Harris, "Observation of electromagnetically induced transparency," Phys. Rev. Lett. **66**, 2593 (1991).

[49] M. Fleischhauer, A. Imamoglu, and J. P. Marangos, "Electromagnetically induced transparency: Optics in Coherent Media," Rev. Mod. Phys. **77**, 633 (2005).

[50] R. P. Abel, C. Carr, U. Krohn, and C. S. Adams, "Electrometry near a dielectric surface using Rydberg electromagnetically induced transparency," Phys. Rev. A **84**, 023408 (2011).

[51] K. J. Weatherill, J. D. Pritchard, R. P. Abel, M. G. Bason, A. K. Mohapatra, and C. S. Adams, "Electromagnetically induced transparency of an interacting cold Rydberg ensemble," J. Phys. B: At. Mol. Opt. Phys. **41**, 201002 (2008).

[52] J. D. Pritchard, D. Maxwell, A. Gauguet, K. J. Weatherill, M. P. A. Jones, and C. S. Adams, "Cooperative Atom-Light Interaction in a Blockaded Rydberg Ensemble," Phys. Rev. Lett. **105**, 193603 (2010).

[53] R. N. Zare, *Angular Momentum* (Wiley, San Francisco, 1988), pp. 194–196.

[54] I. I. Sobel'man, *Introduction to the Theory of Atomic Spectra* (Pergamon Press, Oxford, 1972).

[55] K. R. Overstreet, A. Schwettmann, J. Tallant, D. Booth, and J. P. Shaffer, "Observation of electric-field-induced Cs Rydberg atom macrodimers," Nature Phys. **5**, 581 (2009).

[56] V. Bendkowsky, B. Butscher, J. Nipper, J. P. Shaffer, R. Löw, and T. Pfau, "Observation of ultralong-range Rydberg molecules," Nature **458**, 1005 (2009).

[57] M. L. Zimmerman, M. G. Littman, M. M. Kash, and D. Kleppner, "Stark structure of the Rydberg states of alkali-metal atoms," Phys. Rev. A **20**, 2251 (1979).

[58] M. S. O'Sullivan and B. P. Stoicheff, "Scalar polarizabilities and avoided crossings of high Rydberg states in Rb," Phys. Rev. A **31**, 2718 (1985).

[59] I. I. Beterov, I. I. Ryabtsev, D. B. Tretyakov, and V. M. Entin, "Quasiclassical calculations of blackbody-radiation-induced depopulation rates and effective lifetimes of Rydberg nS, nP, and nD alkali-metal atoms with $n \leq 80$," Phys. Rev. A **79**, 052504 (2009).

[60] K. R. Overstreet, A. Schwettmann, J. Tallant, and J. P. Shaffer, "Photoinitiated collisions between cold Cs Rydberg atoms," Phys. Rev. A **76**, 011403 (2007).

[61] M. Mack, F. Karlewski, H. Hattermann, S. Höckh, F. Jessen, D. Cano, and J. Fortágh, "Measurement of absolute transition frequencies of ^{87}Rb to nS and nD Rydberg states by means of electromagnetically induced transparency," Phys. Rev. A **83**, 052515 (2011).

[62] J. Han, Y. Jamil, D. V. L. Norum, P. J. Tanner, and T. F. Gallagher, "Rb nf quantum defects from millimeter-wave spectroscopy of cold ^{85}Rb Rydberg atoms," Phys. Rev. A **74**, 054502 (2006).

[63] W. Li, I. Mourachko, M. W. Noel, and T. F. Gallagher, "Millimeter-wave spectroscopy of cold Rb Rydberg atoms in a magneto-optical trap: Quantum defects of the ns , np , and nd series," Phys. Rev. A **67**, 052502 (2003).

[64] K.-H. Weber and C. J. Sansonetti, "Accurate energies of nS, nP, nD, nF,and nG levels of neutral cesium," Phys. Rev. A **35**, 4650 (1987).

[65] P. Goy, J. M. Raimond, G. Vitrant, and S. Haroche, "Millimeter-wave spectroscopy in cesium Rydberg states. Quantum defects, fine- and hyperfine-structure measurements," Phys. Rev. A **26**, 2733 (1982).

[66] M. Marinescu, H. R. Sadeghpour, and A. Dalgarno, "Dispersion coefficients for alkali-metal dimers," Phys. Rev. A **49**, 982 (1994).

[67] F. Salvata, J. M. Fernández-Vareaa, and J. W. Williamson, "Accurate numerical solution of the radial Schrödinger and Dirac wave equations," Comp. Phys. Comm. **90**, 151 (1995).

[68] A. L. d. Oliveira, M. W. Mancini, V. S. Bagnato, and L. G. Marcassa, "Measurement of Rydberg-state lifetimes using cold trapped atoms," Phys. Rev. A **65**, 031401 (2002).

[69] V. A. Nascimento, L. L. Caliri, A. L. de Oliveira, V. S. Bagnato, and L. G. Marcassa, "Measurement of the lifetimes of S and D states below $n = 31$ using cold Rydberg gas," Phys. Rev. A **74**, 054501 (2006).

[70] J. Tallant, D. Booth, and J. P. Shaffer, "Photoionization rates of Cs Rydberg atoms in a 1064-nm far-off-resonance trap," Phys. Rev. A **82**, 063406 (2010).

[71] S. E. Harris, "Electromagnetically Induced Transparency," Phys. Today **50:7**, 36 (1997).

[72] J. P. Marangos, "Electromagnetically induced transparency," J. Mod. Opt. **45**, 471 (1998).

[73] E. Arimondo, in *Coherent Population Trapping in Laser Spectroscopy*, Vol. 35 of *Progress in Optics*, edited by E. Wolf (Elsevier, New York, 1996), pp. 257 – 354.

[74] Y. Xiao, T. Wang, M. Baryakhtar, M. Van Camp, M. Crescimanno, M. Hohensee, L. Jiang, D. F. Phillips, M. D. Lukin, S. F. Yelin, and R. L. Walsworth, "Electromagnetically induced transparency with noisy lasers," Phys. Rev. A **80**, 041805 (2009).

[75] R. P. Abel, A. K. Mohapatra, M. G. Bason, J. D. Pritchard, K. J. Weatherill, U. Raitzsch, and C. S. Adams, "Laser frequency stabilization to excited state transitions using electromagnetically induced transparency in a cascade system," Appl. Phys. Lett. **94**, 071107 (2009).

[76] M. M. Kash, V. A. Sautenkov, A. S. Zibrov, L. Hollberg, G. R. Welch, M. D. Lukin, Y. Rostovtsev, E. S. Fry, and M. O. Scully, "Ultraslow Group Velocity and Enhanced Nonlinear Optical Effects in a Coherently Driven Hot Atomic Gas," Phys. Rev. Lett. **82**, 5229 (1999).

[77] D. Budker, D. F. Kimball, S. M. Rochester, and V. V. Yashchuk, "Nonlinear Magneto-optics and Reduced Group Velocity of Light in Atomic Vapor with Slow Ground State Relaxation," Phys. Rev. Lett. **83**, 1767 (1999).

[78] H. Wu, M. Xiao, and J. Gea-Banacloche, "Evidence of lasing without inversion in a hot rubidium vapor under electromagnetically-induced-transparency conditions," Phys. Rev. A **78**, 041802 (2008).

[79] M. Mücke, E. Figueroa, J. Bochmann, C. Hahn, K. Murr, S. Ritter, C. J. Villas-Boas, and G. Rempe, "Electromagnetically induced transparency with single atoms in a cavity," Nature **465**, 755 (2010).

[80] A. K. Mohapatra, M. G. Bason, B. Butscher, K. J. Weatherill, and C. S. Adams, "A giant electro-optic effect using polarizable dark states," Nature Phys. **4**, 890 (2008).

[81] S. F. Yelin, V. A. Sautenkov, M. M. Kash, G. R. Welch, and M. D. Lukin, "Nonlinear optics via double dark resonances," Phys. Rev. A **68**, 063801 (2003).

[82] C. Cohen-Tannoudji and S. Reynaud, "Simultaneous saturation of two atomic transitions sharing a common level," J. Phys. B **10**, 2311 (1977).

[83] R. M. Whitley and C. R. Stroud, "Double optical resonance," Phys. Rev. A **14**, 1498 (1976).

[84] S. N. Sandhya and K. K. Sharma, "Atomic coherence effects in four-level systems: Doppler-free absorption within an electromagnetically-induced-transparency window," Phys. Rev. A **55**, 2155 (1997).

[85] C. Wei, D. Suter, A. S. M. Windsor, and N. B. Manson, "ac Stark effect in a doubly driven three-level atom," Phys. Rev. A **58**, 2310 (1998).

[86] L. Mandel and E. Wolf, *Optical Coherence and Quantum Optics* (Cambridge University Press, New York, 1995).

[87] B. Young, M. Kasevich, and S. Chu, in *Atom Interferometry*, edited by P. R. Berman (Academic Press, San Diego, 1997), pp. 363–405.

[88] R. Shankar, *Principles of quantum mechanics* (Springer, New York, 1994).

[89] C. Cohen-Tannoudji, J. Dupont-Roc, and G. Grynberg, *Atom-Photon Interactions* (Wiley, San Francisco, 1998).

[90] S. H. Autler and C. H. Townes, "Stark Effect in Rapidly Varying Fields," Phys. Rev. **100**, 703 (1955).

[91] M. Tanasittikosol, J. D. Pritchard, D. Maxwell, A. Gauguet, K. J. Weatherill, R. M. Potvliege, and C. S. Adams, "Microwave dressing of Rydberg dark states," J. Phys. B **44**, 184020 (2011).

[92] J. Gea-Banacloche, Y.-q. Li, S.-z. Jin, and M. Xiao, "Electromagnetically induced transparency in ladder-type inhomogeneously broadened media: Theory and experiment," Phys. Rev. A **51**, 576 (1995).

[93] H. S. Moon, W.-K. Lee, and H. S. Suh, "Hyperfine-structure-constant determination and absolute-frequency measurement of the Rb $4D_{3/2}$ state," Phys. Rev. A **79**, 062503 (2009).

[94] A. R. Edmonds, *Angular Momentum in Quantum Mechanics* (Princeton University Press, Princeton, 1974).

[95] X. He, B. Li, A. Chen, and C. Zhang, "Model-potential calculation of lifetimes of Rydberg states of alkali atoms," J. Phys. B: At. Mol. Opt. Phys. **23**, 661 (1990).

[96] J. W. Farley and W. H. Wing, "Accurate calculation of dynamic Stark shifts and depopulation rates of Rydberg energy levels induced by blackbody radiation. Hydrogen, helium, and alkali-metal atoms," Phys. Rev. A **23**, 2397 (1981).

[97] P. D. Lett, R. N. Watts, C. I. Westbrook, W. D. Phillips, P. L. Gould, and H. J. Metcalf, "Observation of Atoms Laser Cooled below the Doppler Limit," Phys. Rev. Lett. **61**, 169 (1988).

[98] J. Dalibard and C. Cohen-Tannoudji, "Laser cooling below the Doppler limit by polarization gradients: simple theoretical models," J. Opt. Soc. Am. B **6**, 2023 (1989).

[99] C. N. Cohen-Tannoudji and W. D. Phillips, "New Mechanisms for Laser Cooling," Phys. Today **43**, 33 (1990).

[100] C. Salomon, J. Dalibard, W. D. Phillips, A. Clairon, and S. Guellati, "Laser Cooling of Cesium Atoms Below 3 μK," Europhys/ Lett. **12**, 683 (1990).

[101] C. D. Wallace, T. P. Dinneen, K. Y. N. Tan, A. Kumarakrishnan, P. L. Gould, and J. Javanainen, "Measurements of temperature and spring constant in a magneto-optical trap," J. Opt. Soc. Am. B **11**, 703 (1994).

[102] G. Breit and I. I. Rabi, "Measurement of Nuclear Spin," Phys. Rev. **38**, 2082 (1931).

[103] M. Born and R. Oppenheimer, "Zur Quantentheorie der Molekeln," Annalen der Physik **389**, 457 (1927).

[104] L. D. Landau and E. M. Lifshitz, *Quantum Mechanics: Nonrelativistic Theory* (Pergamon Press, Oxford, 1965).

[105] A. Schwettmann, J. Franklin, K. R. Overstreet, and J. P. Shaffer, "Stark slowing asymmetric rotors: Weak-field-seeking states and nonadiabatic transitions," J. Chem. Phys. **123**, 194305 (2005).

[106] J. R. Rubbmark, M. M. Kash, M. G. Littman, and D. Kleppner, "Dynamical effects at avoided level crossings: A study of the Landau-Zener effect using Rydberg atoms," Phys. Rev. A **23**, 31073117 (1981).

[107] E. Majorana, "Atomi orentati in campo magnetico variabile," Nuovo Cimento **9**, 43 (1932).

[108] E. Majorana, in *Ettore Majorana Scientific Papers*, edited by G. F. Bassani (Springer, New York, 2006), pp. 125–133, (translated from Italian into English).

[109] D. E. Pritchard, "Cooling Neutral Atoms in a Magnetic Trap for Precision Spectroscopy," Phys. Rev. Lett. **51**, 1336 (1983).

[110] A. Haase, D. Cassettar, B. Hessmo, and J. Schmiedmayer, "Trapping Neutral Atoms with a Wire," Phys. Rev. A **64**, 043405 (2001).

[111] J. Denschlag, D. Cassettari, and J. Schmiedmayer, "Guiding Neutral Atoms with a Wire," Phys. Rev. Lett. **82**, 2014 (1998).

[112] M. Lyly, J. Ruokolainen, and E. Jarvinen, in *CSC report on scientific computing 1999-2000*, edited by S. Kotila and J. Haataja (CSC Scientific Computing Ltd., Espoo, Finland, 2001), pp. 156–159.

[113] J. Estève, C. Aussibal, T. Schumm, C. Figl, D. Mailly, I. Bouchoule, C. I. Westbrook, and A. Aspect, "Role of wire imperfections in micromagnetic traps for atoms," Phys. Rev. A **70**, 043629 (2004).

[114] S. Du, M. B. Squires, Y. Imai, L. Czaia, R. A. Saravanan, V. Bright, J. Reichel, T. W. Hänsch, and D. Z. Anderson, "Atom-chip Bose-Einstein condensation in a portable vacuum cell," Phys. Rev. A **70**, 053606 (2004).

[115] S. Groth, P. Krüger, S. Wildermuth, R. Folman, T. Fernholz, J. Schmiedmayer, D. Mahalu, and I. Bar-Joseph, "Atom chips: Fabrication and thermal properties," Appl. Phys. Lett. **85**, 2980 (2004).

[116] D. Jervis, "Fabrication of an atom chip," Master's thesis, University of Toronto, Toronta, Canada, 2007.

[117] R. Folman, P. Krúger, J. Schmiedmayer, J. Denschlag, and C. Henkel, "Microscopic Atom Optics: From Wires to an Atom Chip," Adv. At. Mol. Opt. Phy. **48**, 263 (2002).

[118] F. Baumgärtner, R. J. Sewell, S. Eriksson, I. Llorente-Garcia, J. Dingjan, J. P. Cotter, and E. A. Hinds, "Measuring Energy Differences by BEC Interferometry on a Chip," Phys. Rev. Lett. **105**, 243003 (2010).

[119] S. Hofferberth, I. Lesanovsky, B. Fischer, J. Verdu, and J. Schmiedmayer, "Radiofrequency-dressed-state potentials for neutral atoms," Nature Phys. **2**, 710 (2006).

[120] P. Zhang, G. Li, Y.-c. Zhang, Y. Guo, J. Wang, and T. Zhang, "Light-induced atom desorption for cesium loading of a magneto-optical trap: Analysis and experimental investigations," Phys. Rev. A **80**, 053420 (2009).

[121] C. Klempt, T. van Zoest, T. Henninger, O. Topic, E. Rasel, W. Ertmer, and J. Arlt, "Ultraviolet light-induced atom desorption for large rubidium and potassium magneto-optical traps," Phys. Rev. A **73**, 013410 (2006).

[122] S. Aubin, M. H. T. Extavour, S. Myrskog, L. J. LeBlanc, J. Estve, S. Singh, P. Scrutton, D. McKay, R. McKenzie, I. D. Leroux, A. Stummer, and J. H. Thywissen, "Trapping Fermionic ^{40}K and Bosonic ^{87}Rb on a Chip," J. Low Temp. Phys. **140**, 377 (2005), 10.1007/s10909-005-7322-5.

[123] A. Jechow and R. Menzel, "Efficient blue light generation by frequency doubling of a broad-area diode laser in a compact external cavity," Appl. Phys. B **89**, 507511 (2007).

[124] M. Maiwald, S. Schwertfeger, R. Güther, B. Sumpf, K. Paschke, C. Dzionk, G. Erbert, and G. Tränkle, "600 mW optical output power at 488 nm by use of a high-power hybrid laser diode system and a periodically poled MgO:LiNbO3 bulk crystal," Opt. Lett. **31**, 802 (2006).

[125] K. B. MacAdam, A. Steinbach, and C. Wieman, "A narrow-band tunable diode laser system with grating feedback, and a saturated absorption spectrometer for Cs and Rb," Amer. J. Phys. **60**, 1098 (1992).

[126] C. G. Townsend, N. H. Edwards, C. J. Cooper, K. P. Zetie, C. J. Foot, A. M. Steane, P. Szriftgiser, H. Perrin, and J. Dalibard, "Phase-space density in the magneto-optical trap," Phys. Rev. A **52**, 1423 (1995).

[127] M. Born and E. Wolf, *Principles of Optics*, 6 ed. (Cambridge University Press, Cambridge, 1997).

[128] L. G. Schulz, "The Optical Constants of Silver, Gold, Copper, and Aluminum. I. The Absorption Coefficient k," J. Opt. Soc. Am. **44**, 357 (1954).

[129] L. G. Schulz and F. R. Tangherlini, "Optical Constants of Silver, Gold, Copper, and Aluminum. II. The Index of Refraction n," J. Opt. Soc. Am. **44**, 362 (1954).

[130] J. Tallant, K. R. Overstreet, A. Schwettmann, and J. P. Shaffer, "Sub-Doppler magneto-optical trap temperatures measured using Rydberg tagging," Phys. Rev. A **74**, 023410 (2006).

[131] D. McGloin, M. H. Dunn, and D. J. Fulton, "Polarization effects in electromagnetically induced transparency," Phys. Rev. A **62**, 053802 (2000).

[132] H. S. Moon and H.-R. Noh, "Polarization dependence of double-resonance optical pumping and electromagnetically induced transparency in the $5S_{1/2}-5P_{3/2}-5D_{5/2}$ transition of ^{87}Rb atoms," Phys. Rev. A **84**, 033821 (2011).

[133] A. Javan, O. Kocharovskaya, H. Lee, and M. O. Scully, "Narrowing of electromagnetically induced transparency resonance in a Doppler-broadened medium," Phys. Rev. A **66**, 013805 (2002).

[134] J. Berger, K. Petermann, H. Fähling, and P. Wust, "Calibrated electro-optic E-field sensors for hyperthermia applications," Physics in Medicine and Biology **46**, 399 (2001).

[135] T. Meier, C. Kostrzewa, K. Petermann, and B. Schüppert, "Integrated Optical E-Field Probes with Segmented Modulator Electrodes," Journal of Lightwave Technology **12**, 1497 (1994).

[136] Y. Rabin and F. Rebentrost, "On the self-shift and broadening of Doppler-free Rydberg 2s spectral lines in alkali atoms," Opt. Comm. **40**, 257 (1982).

[137] W. Demtröder, *Laser Spectroscopy*, 3 ed. (Springer, New York, 2003).

[138] A. Schwettmann, J. Crawford, K. R. Overstreet, and J. P. Shaffer, "Cold Cs Rydberg-gas interactions," Phys. Rev. A **74**, 020701 (2006).

[139] A. Schwettmann, K. R. Overstreet, J. Tallant, and J. P. Shaffer, "Analysis of long-range Cs Rydberg potential wells," J. Mod. Opt. **54**, 2551 (2007).

[140] V. A. Nascimento, L. L. Caliri, A. Schwettmann, J. P. Shaffer, and L. G. Marcassa, "Electric Field Effects in the Excitation of Cold Rydberg-Atom Pairs," Phys. Rev. Lett. **102**, 213201 (2009).

[141] J. S. Cabral, J. M. Kondo, L. F. Gonçalves, V. A. Nascimento, L. G. Marcassa, D. Booth, J. Tallant, A. Schwettmann, K. R. Overstreet, J. Sedlacek, and J. P. Shaffer, "Effects of electric fields on ultracold Rydberg atom interactions," J. Phys. B: At. Mol. Opt. Phys. **44**, 184007 (2011).

[142] J. S. Cabral, J. M. Kondo, L. F. Gonçalves, L. G. Marcassa, D. Booth, J. Tallant, and J. P. Shaffer, "Manipulation of quantum state transfer in cold Rydberg atom collisions," New J. Phys. **12**, 093023 (2010).

[143] N. Vanhaecke, D. Comparat, D. A. Tate, and P. Pillet, "Ionization of Rydberg atoms embedded in an ultracold plasma," Phys. Rev. A **71**, 013416 (2005).

[144] F. Robicheaux and J. D. Hanson, "Simulation of the Expansion of an Ultracold Neutral Plasma," Phys. Rev. Lett. **88**, 055002 (2002).

[145] A. Fioretti, D. Comparat, C. Drag, T. F. Gallagher, and P. Pillet, "Long-Range Forces between Cold Atoms," Phys. Rev. Lett. **82**, 1839 (1999).

[146] I. Mourachko, D. Comparat, F. de Tomasi, A. Fioretti, P. Nosbaum, V. M. Akulin, and P. Pillet, "Many-Body Effects in a Frozen Rydberg Gas," Phys. Rev. Lett. **80**, 253 (1998).

[147] M. R. Flannery, D. Vrinceanu, and V. N. Ostrovsky, "Long-range interaction between polar Rydberg atoms," J. Phys. B: At. Mol. Opt. Phys. **38**, S279 (2005).

[148] I. Mourachko, W. Li, and T. F. Gallagher, "Controlled many-body interactions in a frozen Rydberg gas," Phys. Rev. A **70**, 031401 (2004).

[149] F. Robicheaux, J. V. Hernández, T. Topçu, and L. D. Noordam, "Simulation of coherent interactions between Rydberg atoms," Phys. Rev. A **70**, 042703 (2004).

[150] G. Herzberg, *Molecular Spectra and Molecular Structure I* (Krieger, Florida, 1989).

[151] D. L. Andrews and G. Juzeliūnas, "Intermolecular energy transfer: Retardation effects," J. Chem. Phys. **96**, 6606 (1992).

[152] R. J. Le Roy, "Long-Range Potential Coefficients From RKR Turning Points: C_6 and C_8 for B($3\Pi^+_{0u}$)-State Cl_2, Br_2, and I_2," Canadian Journal of Physics **52**, 246 (1974).

[153] L. Perotti, "Ionization of Rydberg alkali-metal atoms in quasistatic electric fields: A classical view of the n^{-5} scaling of the threshold field," Phys. Rev. A **73**, 053405 (2006).

[154] A. Walz-Flannigan, J. R. Guest, J.-H. Choi, and G. Raithel, "Cold-Rydberg-gas dynamics," Phys. Rev. A **69**, 063405 (2004).

[155] W. Li, M. W. Noel, M. P. Robinson, P. J. Tanner, T. F. Gallagher, D. Comparat, B. Laburthe Tolra, N. Vanhaecke, T. Vogt, N. Zahzam, P. Pillet, and D. A. Tate, "Evolution dynamics of a dense frozen Rydberg gas to plasma," Phys. Rev. A **70**, 042713 (2004).

[156] R. J. LeRoy, "LEVEL 8.0 A Computer Program for Solving the Radial Schrödinger Equation for Bound and Quasibound Levels," Chemical Physics Research Report CP-661, University of Waterloo, Waterloo (unpublished).

[157] C. H. Greene, A. S. Dickinson, and H. R. Sadeghpour, "Creation of Polar and Nonpolar Ultra-Long-Range Rydberg Molecules," Phys. Rev. Lett. **85**, 2458 (2000).

[158] C. Ates, T. Pohl, T. Pattard, and J. M. Rost, "Antiblockade in Rydberg Excitation of an Ultracold Lattice Gas," Phys. Rev. Lett. **98**, 023002 (2007).

[159] M.-L. Almazor, O. Dulieu, M. Elbs, E. Tiemann, and F. Masnou-Seeuws, "How to get access to long range states of highly excited molecules," Eur. Phys. J. D **5**, 237 (1999), 10.1007/s100530050251.

[160] A. S. Davidov, *Quantum Mechanics*, 2 ed. (Pergamon Press, Oxford, 1966).

[161] R. W. Boyd, *Nonlinear Optics* (Academic Press, San Diego, 2003).

[162] D. L. Mills and E. Burstein, "Polaritons: the electromagnetic modes of media," Reports on Progress in Physics **37**, 817 (1974).

[163] R. Zia and M. L. Brongersma, "Surface plasmon polariton analogue to Young's double-slit experiment," Nature Nanotech. **2**, 426 (2007).

[164] A. Schwettmann, J. Sedlacek, and J. P. Shaffer, "Field-programmable gate array based locking circuit for external cavity diode laser frequency stabilization," Review of Scientific Instruments **82**, 103103 (2011).

[165] C. E. Wieman and L. Hollberg, "Using diode lasers for atomic physics," Rev. Sci. Inst. **62**, 1 (1991).

[166] A. Mooradian, "Laser Linewidth," Phys. Today **38:5**, 42 (1985).

[167] S. D. Saliba and R. E. Scholten, "Linewidths below 100 kHz with external cavity diode lasers," Appl. Opt. **48**, 6961 (2009).

[168] K. R. Overstreet, J. Franklin, and J. P. Shaffer, "Zeeman effect spectroscopically locked Cs diode laser system for atomic physics," Rev. Sci. Inst. **75**, 4749 (2004).

[169] K. H. Ang, G. Chong, and Y. Li, "PID Control System Analysis, Design, and Technology," IEEE Trans. on Control Systems Technology **13**, 559 (2005).

[170] K. J. Åström and R. M. Murray, *Feedback Systems: An Introduction for Scientists and Engineers* (Princeton University Press, New Jersey, 2008).

[171] R. E. Haskell and D. M. Hanna, *Digital Design Using Digilent FPGA Boards VHDL/Active-HDL Edition* (LBE Books, Rochester Hills, 2009).

[172] R. F. Gutterres, C. Amiot, A. Fioretti, C. Gabbanini, M. Mazzoni, and O. Dulieu, "Determination of the 87Rb 5p state dipole matrix element and radiative lifetime from the photoassociation spectroscopy of the Rb2 0-g (P3/2) long-range state," Phys. Rev. A **66**, 024502 (2002).

[173] P. Anisimov and O. Kocharovskaya, "Decaying-dressed-state analysis of a coherently driven three-level Λ system," J. Mod Opt. **55**, 3159 (2008).

[174] R. W. P. Drever, J. L. Hall, F. V. Kowalski, J. Hough, G. M. Ford, A. J. Munley, and H. Ward, "Laser phase and frequency stabilization using an optical resonator," Appl. Phys. B **31**, 97 (1983).

[175] E. Anderson, Z. Bai, C. Bischof, S. Blackford, J. Demmel, J. Dongarra, J. Du Croz, A. Greenbaum, S. Hammarling, A. McKenney, and D. Sorensen, *LAPACK Users' Guide*, 3rd ed. (Society for Industrial and Applied Mathematics, Philadelphia, PA, 1999).

[176] L. S. Blackford, J. Choi, A. Cleary, E. D'Azevedo, J. Demmel, I. Dhillon, J. Dongarra, S. Hammarling, G. Henry, A. Petitet, K. Stanley, D. Walker, and R. C. Whaley, *ScaLAPACK Users' Guide* (Society for Industrial and Applied Mathematics, Philadelphia, PA, 1997).

Appendix A

Field-programmable gate array based locking circuit for external cavity diode laser frequency stabilization

A.1 Introduction

In this Appendix, the homebuilt locking circuit, used to lock our Rydberg excitation laser to a Fabry-Perot cavity, is described in detail. The same feedback circuit is also used in a homebuilt noise-eater setup to stabilize the probe laser power in our EIT experiments. Part of this Appendix was published as Ref. [164], together with the full source code of the project.

The external cavity diode laser (ECDL) [165] has become a widely used source of tunable narrow-linewidth laser light in atomic physics experiments. For example, it is used to generate light for laser cooling and trapping of alkali atoms. The ECDL is also an excellent source for second harmonic generation (SHG) and difference frequency generation (DFG) laser systems. With such systems, the near-infrared narrow bandwidth wavelengths of laser diodes can be converted into visible light, which is useful for the excitation of higher atomic and molecular energy states such as high-lying Rydberg states of Rb and Cs atoms and molecules [55, 56, 60].

The fundamental linewidth of an ECDL limited by spontaneous emission is $\sim$ 100 kHz or less [166, 165, 167]. However, technical noise such as vibrational and thermal noise causes a broadening of the effective laser linewidth to $\sim 5-25$ MHz on the timescale of seconds, and a drift of the laser center frequency of ~ 5 MHz min^{-1}, which is not acceptable for typical experiments in atomic physics. To keep the laser frequency from fluctuating so excessively and reduce the linewidth towards its funda-

mental limit, active stabilization is required.

Traditionally, active laser frequency stabilization is accomplished via one or more analog closed feedback loops [125]. Each loop compares the frequency of the laser light to an external reference. It then provides appropriate feedback to mechanical or electrical components of the laser to keep the frequency of the light constant.

For an ECDL, there are usually two components that receive feedback. The first component is the position of the grating that acts as the output coupler of the laser. Modifying the grating position changes the cavity length of the laser, which in turn changes the frequency of output light. The grating position is typically modified with a piezoelectric transducer. The second component that receives feedback is the injection current of the laser diode. Changing the injection current changes the refractive index n of the gain medium through the carrier density, which changes the frequency. The current also causes Joule heating which changes the frequency due to a change of the internal cavity length. The two components "piezo" and "current" have different bandwidths, and each requires a separate feedback loop. The grating position, being mechanical in nature, is usually limited in practice to loop frequencies well below 1 kHz due to the mass load on the transducer and the corresponding inertia. The diode current, being electrical in nature, has no such limitation and can provide stable frequency adjustments within the MHz regime of loop frequencies.

Here, we describe the implementation of a digital ECDL locking feedback circuit on a field-programmable gate array (FPGA). The main advantages over traditional (non FPGA-based) locking circuits are reconfigurability and a friendly user interface. The FPGA can easily and quickly be reprogrammed to add extra filters, additional loops, and other features to the circuit, without any soldering required. We also implement a graphical user interface (GUI) to control the locking circuit by a computer running Windows. The computer is connected to the FPGA through a USB connec-

tion. Locking parameters such as proportional, integral and differential gains and filter cutoff frequencies can easily be changed using the mouse or keyboard. The loop responds immediately to any changes of parameters made via the GUI, but runs autonomously on the FPGA hardware. Specifically, the execution speed of the locking circuit is independent of the speed of the attached computer that runs the GUI. We use the circuit to lock our homebuilt second harmonic generation system, operating at 480 nm for Rydberg atom experiments. We perform a measurement of the width of the electromagnetically induced transparency peak in Rb vapor, which provides an upper limit on the locked linewidth of our laser.

A.2 Signal path

The FPGA board we use is a commercial Digilent Nexys 2 1200k board that houses a Spartan3E-1200 FPGA chip as well as several other input and output headers. A grounded aluminum box (Bud Industries AC-1418) functions as an enclosure and electrical shield for the board. The enclosure was fitted with a rear panel power connection and switch, a front panel USB adapter, and front panel BNC connectors for the analog inputs and outputs. Twisted pair wires were used to connect the board headers and the BNC connectors. We use two Digilent peripheral modules (Pmod) to equip the board with two 12-bit digital-to-analog (DAC, Digilent PmodDA2) and two 12-bit analog-to-digital converters (ADC, Digilent PmodAD1). The PmodAD1 (PmodDA2) is connected to the first (second) of the four two-row 6-pin peripheral connectors on the board.

The FPGA program is stored as a bitfile on flash rom on the board. On power up, the bitfile is transferred automatically from the flash rom to the FPGA. This way, the FPGA becomes fully programmed and functional, even if no external computer is connected.

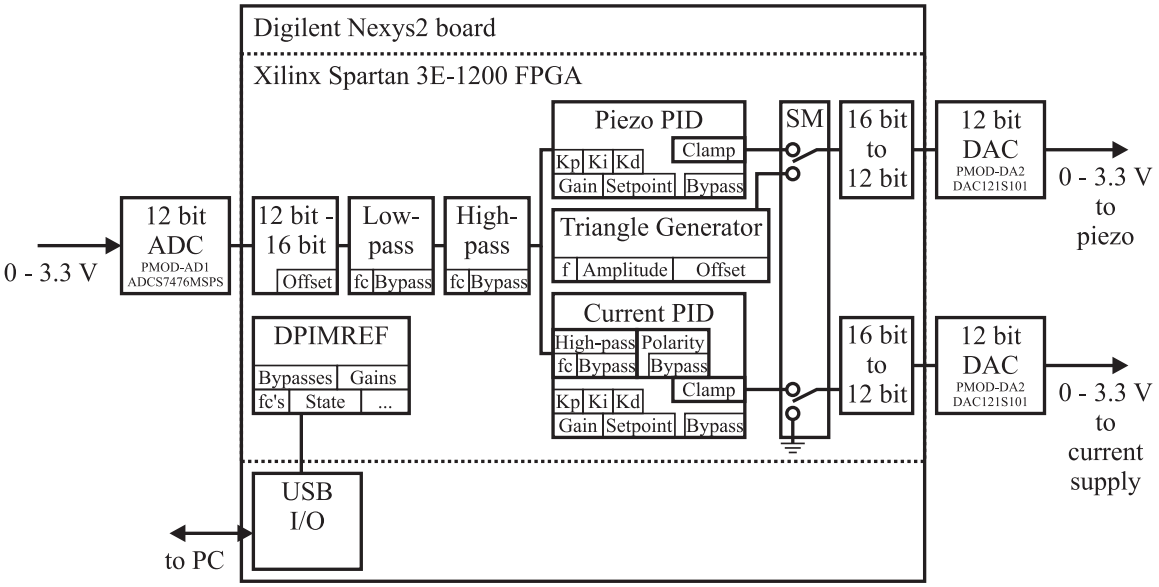

Figure A.1: Schematic of the internal signal path on the FPGA. Insets denote parameters controlled by the user interface. SM: pictorial representation of the state machine that switches between lock and scan states (debug state not shown).

Fig.A.1 shows a simplified block diagram of the signal path of the programmed locking circuit. The ADC module requires that the input signal is between 0 V and 3.3 V. This voltage should be proportional to the frequency of the laser light for small deviations from the desired lock point. A common technique to provide such a signal is saturated absorption spectroscopy [125], but one can also use a dichroic atomic vapor laser lock setup [168], a stabilized reference cavity, a fast wavemeter, or any other frequency selective device. This input signal is acquired by one of the two 12-bit ADC chips (National Semiconductor ADCS7476MSPS) on the PmodAD1 extension module and enters the FPGA as 12-bit wide positive number.

Once inside the FPGA, the 12-bit unsigned signal is first converted to a 16-bit signed number and then offset so that it is centered around zero. This is done by padding with a pair of high and a pair of low bits and then subtracting the number 8192. The conversion to 16-bit is done to prevent accumulation of rounding errors

from successive signal processing stages in the FPGA. The offset to zero is done once here to simplify programming of the high-pass filters and feedback loops. Without the offset, each high-pass filter would need separate output offset modules to keep the internal signal centered within the voltage swing of the feedback loops. The signal then passes through both a low-pass and a high-pass filter of order one which allows further shaping and noise reduction. Both filters have user adjustable cutoff frequencies and bypass options which can be set from the GUI. More elaborate filters can be programmed into the FPGA without opening the box. This flexibility is one of the advantages of the FPGA-based design.

After the initial filtering, the signal serves as simultaneous input to two proportional, integral, differential locked loops (PID). The first PID gives feedback to the piezoelectric transducer that controls the grating position (piezo PID). It is a straightforward digital implementation of a type C PID [169]. The second PID provides feedback to the driving current of the laser diode (current PID). The current PID is also a type C implementation, but contains user adjustable high-pass filters as well as an optional 180° phase-shift for the input signal. The high-pass filters are necessary to keep the two PIDs from working against each other. With the high-pass filters activated, the current PID provides feedback only at high frequencies, while the piezo PID provides feedback down to 0 Hz. The phase-shift on the current PID allows for the adjustment of the polarity of the laser diode, which affects the sign of the slope of the frequency vs. current curve. Both PIDs include the necessary clamping so that the PID output never exceeds the maximum control signal the laser components can respond to. This is necessary to prevent nonlinear breakdown of the loop due to wind-up [170].

The outputs of each PID loop are then converted back to 12-bit unsigned values. The 16-bit signed numbers are first clamped between -8192 and 8191, then shifted up

to lie between zero and 16383. The numbers are then rounded by dropping the lowest two bits to finally get an output value that lies between 0 and 4095. The digital signal then leaves the FPGA. After exiting the FPGA, the digital output signals are converted to analog voltages between 0 and 3.3 V by the two 12-bit DAC chips (National Semiconductor DAC121S101) on the PmodDA2 extension module.

The communication with the PC is done through the Digilent reference implementation of a parallel interface module (DPIMREF) that serves as the interface between the on-board USB controller and the FPGA. The DPIMREF module has access to the registers on the FPGA that are storing the PID gains and other parameters which can be changed by the user.

A.3 Timing

The FPGA master clock runs at 50 MHz. The FPGA program is synchronous with this clock whenever possible, to prevent any glitches caused by asynchronous logic [171]. The ADC and DAC run at divided clock rates of 12.5 MHz and 25 MHz, respectively. They employ a serial digital interface, and take 16 clock cycles for one conversion each. This corresponds to an input conversion time of 1.28 μs and an output conversion time of 0.64 μs. The DPIMREF module runs at a transfer rate that is automatically throttled by the speed of the USB connection to the host computer. The PID modules and filter modules on the FPGA are clocked at the master clock of 50 MHz. The low input sample rate of 780 kHz allows for the digital signal processing to take up to 64 clock cycles without ever losing a sample. The signal latencies are as follows: The input low and high-pass filters take 8 and 13 clock-cycles per sample each, and the PID loop takes 13 clock cycles to complete. The maximum total internal signal processing then takes 34 clock cycles per sample for the piezo PID, and 60 cycles per sample for the current PID. The current PID

is slower because of its additional high pass filters. The main cause of latency in our design is an increase of precision by an additional 20 bits in the filters and PID loops, which allows for very fine tuning of the PID and filter parameters. The internal latency can be reduced at the cost of this tuning precision. However, since the total latency is below the sampling period, this is necessary only if faster conversion chips are used, or if more internal data processing is added to the circuit. The circuit has an effective bandwidth of ~ 80 kHz, limited by the speed and slew rates of the ADC and DAC chips. The bandwidth could be increased further by using faster conversion chips that employ parallel digital interfaces. The faster chips could be connected to the high speed 100-pin expansion connector of the board. Examples of such chips are the Texas Instruments ADS807 ADC and the Texas Instruments DAC902 DAC. On a side note, we found that it is possible to double the bandwidth of the circuit by overclocking our ADC to 25 MHz. Even though we found no errors in daily operation at this rate, it is above the manufacturer's specified maximum value of 20 MHz and therefore not recommended.

A.4 States

Depending on user input from the GUI, a rudimentary state machine selects between three different states of the FPGA:

- "Locked" - Used to lock the ECDL. The FPGA behaves as described in the previous sections.
- "Scan" - Used to scan the laser frequency. In this mode, a triangle waveform is present on the piezo analog output. The frequency, amplitude and offset of the waveform are user selectable. The current output is set to 1.75 V. The scan offset serves as the piezo PID initial output value, to force the laser to lock to

the closest lock point as seen on the scan signal.

- "Bypass All" - Used to test the speed and accuracy of the analog-to-digital and digital-to-analog conversions. The value of the two output ports equals the value acquired at the two input ports. The signal is still converted to 16-bit signed values internally but bypasses all other components.

A.5 User interface

To establish communication between the user interface on the PC and the registers on the FPGA, two components are required. On the PC side, the DPCUTIL library by Digilent enables us to send and read bytes to and from registers on the FPGA through simple C++ function calls. The DPCUTIL library uses the same USB port that is also used to send bitfiles to the FPGA to exchanges data between the PC and the running FPGA program. The FPGA side of this communication layer is provided by DPIMREF, an EPP-style parallel interface reference implementation. DPIMREF is available as VHDL source from the Digilent website. We modified the DPIMREF source to extend the number of single-byte data exchange registers from the original eight to fifty. DPIMREF functions as the interface between the FPGA and the on-board USB controller. Once communication is established, the user can change many parameters of the locking circuit in real-time. Fig. A.2 shows screen captures of the GUI, implemented using Borland C++ Builder. Each edit field has increment and decrement buttons on its side. After positioning the cursor on the nth digit of a number, a mouse click on the $\pm$ buttons, or a press of the up or down arrow keys will change the selected parameter by $\pm 10^n$ and immediately send the new parameter to the FPGA. This ensures that the parameters can be changed quickly and smoothly, by mouse or by keyboard, over many orders of magnitude. To aid the PID tuning process, a configuration file that holds all parameter values is automatically loaded

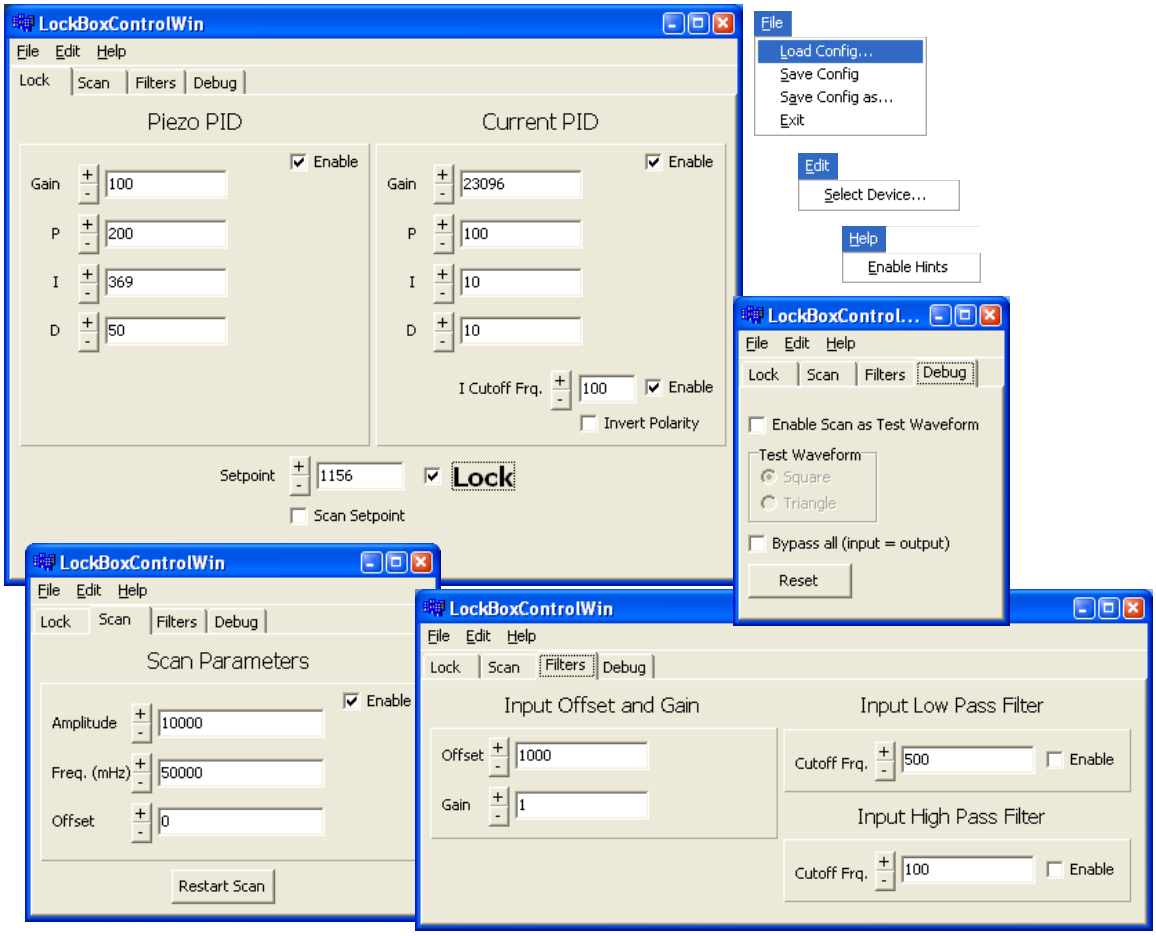

Figure A.2: Screenshots of the user interface that controls the FPGA loop, scan, filter, and debugging parameters. Shown are the main lock panel (top left), the menu options (top right), the scan control panel (bottom left), the filter settings panel (bottom right), and the debugging panel (center right). Mouse clicks on the ±-buttons or key presses of the up arrow or down arrow keys smoothly change the currently active parameter. The order of magnitude of change depends on the digit that the cursor is positioned over.

on startup and saved on exit. There is also a menu option to save and load separate configuration files.

A.6 Compiling and using the program

The VHDL source code for our locking circuit and the C++ source code for the user interface are provided online as part of Ref. [164].[1] The compilers we used are Xilinx Webpack ISE 10.1 and Borland C++ Builder 2006. The compiled Windows executable and FPGA bitfile are also provided.

The downloadable archive contains the source codes and binary files of our FPGA-based diode laser locking circuit (LockBox) and the corresponding Windows user interface (LockBoxControlWin). LockBox is written in VHDL and is intended to be uploaded to a Digilent Nexys 2 FPGA board. The compiler used was Xilinx Webpack ISE 10.1. LockBoxControlWin is written in C++ and is intended to be run on Windows computers. It makes use of Borland VCL and Digilent DPCUtil libraries. The compiler used was Borland Developer Studio 2006. Two pre-compiled LockBox FPGA bitfiles, ready to be uploaded to the FPGA, and a pre-compiled LockBoxControlWin Windows executable are also included. The project consists of 30 files. The files for the LockBox and LockBoxControlWin program are listed in Tables A.1 and A.2. The filetypes used in the project are listed in Table A.3.

The free program "Digilent Adept Suite" version 1.1.0 needs to be installed for the LockBoxControlWin user interface to function. Adept is the program used to upload bitfiles to Digilent FPGA boards, and it includes the dpcutil.dll communication library as well as the required USB drivers. These files are needed by LockBoxControlWin to communicate with the FPGA board through the USB bus.

On first startup of LockBoxControlWin, the FPGA board should be selected.

[1] See supplementary material at http://dx.doi.org/10.1063/1.3646477 for the complete VHDL and C++ source codes of our locking circuit and the user interface.

Table A.1: Files needed to compile the LockBox FPGA program.

File Name	Description
lockbox.vhdl	top level source code, main LockBox FPGA program
lowPass16bit.vhd	source code for low pass filter module
highpass16bit.vhd	source code for high pass filter module
pidPiezo.vhd	source code for Piezo PID module
pidCurrent.vhd	source code for Current PID module
triangleGenerator16bit.vhd	source code for triangle wave generator module
display.vhd	source code for on-board seven segment display utilization
dpimref_mod.vhd	modified Digilent implementation for USB data exchange
AD1RefComp_mod.vhd	modified Digilent reference implementation for PmodAD1 input board
DA2RefComp_mod.vhd	modified Digilent reference implementation for PmodDA2 output board
Nexys2-1200kLockbox.ucf	universal constraints file, port to pin mapping for Nexys2 board
LockBox.ise	Webpack ISE 10.1 project file for LockBox project
lockbox_CCLKClock.bit	compiled LockBox circuit bitfile, ready to be uploaded to FPGA
lockbox_JTAGClock.bit	compiled LockBox circuit bitfile, ready to be uploaded to onboard PROM

Table A.2: Files needed to compile the LockBoxControlWin Windows program.

File Name	Description
LockBoxControlWinMain.cpp	top level source code, main LockBoxControlWin C++ program
LockBoxControlWinMain.dfm	form definition, contains VCL user interface layout such as button positions
LockBoxControlWinMain.h	declarations for main program source
LockBoxControlWin.cpp	IDE managed program entry point
LockBoxControlWin.res	IDE managed program resources
dpcutilOMF.lib	interface to DPCUTIL.DLL, converted to OMF format
gendefs.h	global definitions for DPCDEMO Program
dpcutil.h	interface declarations for DPCUTIL.DLL
dpcdefs.h	type and constant definitions for DPCUTIL.DLL
dpcutil.lib	interface to DPCUTIL.DLL
dpcutil.dll	Digilent PC utility library for USB communication with FPGA board
LockBoxControlWin.bdsproj	Borland Developer Studio project file for LockBoxControlWin project
LockBoxControlWin.exe	compiled LockBoxControlWin executable

Table A.3: Filetypes used in the LockBoxControlWin and LockBox projects.

File Type	Description
*.bdsproj	Borland Developer Studio project, use to re-construct the project tree
*.bit	binary bitfile, compiled FPGA circuit design ready to be uploaded into the FPGA
*.cpp	C++ source code, C++ function definitions
*.dfm	Borland VCL form definitions, user interface layout
*.dll	Windows dynamic link library, pre-compiled functions to be linked into a Windows program
*.exe:	Windows executable file
*.h	C++ header, declarations of C++ functions
*.ise	Webpack ISE compiler project, use to re-construct project tree
*.lib	C++ import library, used to link a program to a dynamic link library
*.txt	ASCII text
*.ucf	Universal constraints file, mapping from ports in the program to pins on the FPGA
*.vhd, *.vhdl	VHDL source code, can be synthesized into bitfiles with a VHDL compiler

This is done by clicking on the "Select Device..." option in the "Edit" menu. The "DPCOMM Device Manager" window should now open. After a click on "Enumerate," the FPGA board name should appear in the "Connnected Devices" list. A click on the board name should make its serial number appear. Now, type an alias into the alias field and click "Add Dvc," and then "Save." This procedure has to be done only once per board.

Two pre-compiled FPGA bitfiles are provided. Both contain the same LockBox circuit implementation, but each uses a different startup clock signal. The file "lockbox_JTAGClock.bit" is generated using the JTAG clock as startup clock. This file is intended to be uploaded to the FPGA directly and will be erased from memory as soon as the FPGA board is switched off. The file "lockbox_CCLKClock.bit" is generated using the CCLK clock as startup clock. This file is intended to be uploaded to the onboard Flash ROM (PROM). Once on the PROM, the program will be uploaded to the FPGA automatically each time the FPGA board is switched on. After the initial upload of "lockbox_CCLKClock.bit" into the PROM, it is necessary to power-cycle the FPGA board once to transfer the program from the PROM onto the FPGA.

After uploading the program to the FPGA, it is recommended to perform a reset to refresh all the parameters of the locking circuit. This is accomplished by either clicking on the "Reset" button in the user interface "debug" panel, or by pushing the push-button on the board labeled "BTN2."

To check that LockBoxControlWin communicates with the FPGA board, click "Reset" on the debug panel, uncheck "Lock" on the lock panel, check "Scan enable" on the Scan panel and look for a triangle scanning waveform coming out of analog output 1.

Mouse-over hints can be enabled from the "Help" menu. If enabled, a help box is

displayed when hovering the mouse over a GUI element.

The easiest and fastest way to change parameters is to use the cursor keys: activate an edit field with the mouse, and then use cursor-left/right to select the digit and cursor-up/down to change the parameter by that order of magnitude. Parameters can also be changed by the mouse, by first positioning the cursor over the digit one wants to change, and then clicking the plus/minus buttons to the left of the respective edit field.

A.7 Performance

To test the performance of our FPGA locking circuit, we used it to lock our homebuilt 480 nm second-harmonic generation (SHG) system to a Fabry-Perot reference cavity (CVI OSA300-12), described in Section 3.7.

An intensity reference signal is subtracted from the cavity signal to give an output signal that is linear in frequency and centered around 0 volts. We tune the cavity so that the 0 volt point is located in the center of the rising edge of a cavity transmission peak (side-of-fringe locking). We add an offset of 1.75 volts to this signal and feed it into the FPGA locking circuit as the process value. While the feedback loop is engaged, the rms value of this error signal indicates the quality of the lock. When properly calibrated, it can give a rough estimate of the frequency width of the locked laser line. We find that the noise around the lock-point is Gaussian in nature with a full width at half maximum (FWHM) of 50 mV, which corresponds to a FWHM in frequency of 164 kHz. This measurement is insensitive to high-frequency noise ($\sim$ GHz) on the laser frequency which can also broaden the laser linewidth.

To measure an upper bound of the locked linewidth of our ECDL, and to show that our locking circuit is useful in an experiment, we observed electromagnetically induced transparency (EIT) [49, 71] in a rubidium vapor. EIT is advantageous for

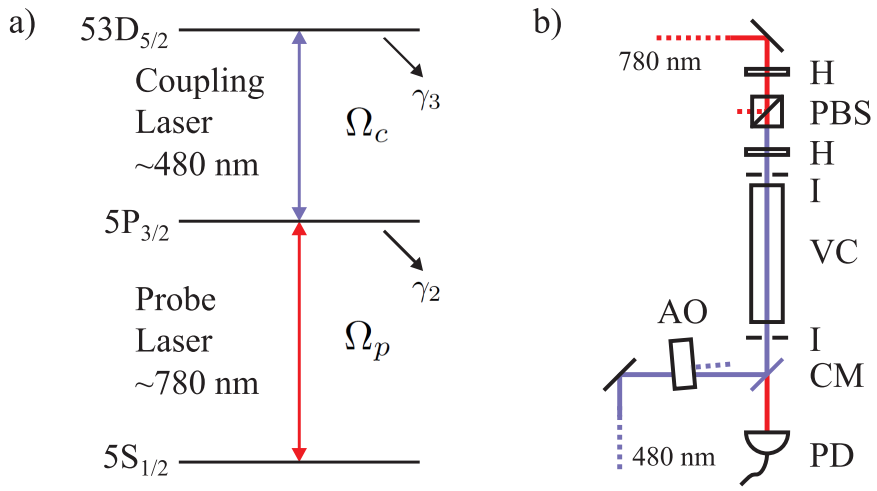

Figure A.3: Electromagnetically induced transparency to measure the linewidth of the locked laser. a) Ladder-type excitation scheme (Rydberg EIT). b) Rydberg EIT setup with counter-propagating probe and coupling beams. Labels are H: half-wave plate, PBS: polarizing beamsplitter cube, I: iris, VC: rubidium vapor cell, CM: cold mirror, PD: photodiode, AO: accousto-optic modulator.

laser linewidth measurements, since the transparency peak is much narrower than the natural linewidth of the probe transition. We observe EIT using the ladder-type excitation scheme shown in Fig. A.3(a) in a counterpropagating geometry as depicted in Fig. A.3(b).

The probe light, Rabi frequency $\Omega_p = 2\pi \times 562$ kHz,[2] is generated by a Toptica DL100 diode laser at $\lambda = 780$ nm. The probe laser is locked to the red side of the crossover peak between the $F = 2 \rightarrow F' = 1$ and $F = 2 \rightarrow F' = 3$, $5S_{1/2} \rightarrow 5P_{3/2}$ hyperfine transitions in ^{87}Rb via saturated absorption spectroscopy. The probe frequency is shifted 224 MHz to the blue by double-passing an AOM (Crystal Technologies, 3110-140), to the center of the $F = 2 \rightarrow F' = 3$ transition. It is then coupled into a polarization maintaining fiber to increase transverse beam quality. After the

[2]Apart from the Rabi frequencies, which are stated as angular frequencies in units of radians s^{-1}, all other frequencies stated in this Appendix are in units of cycles s^{-1}.

fiber, the probe light polarization is filtered with a polarizing beamsplitter cube, and adjusted with a half-wave plate to be perpendicular to the coupling laser beam polarization. After passing through a rubidium vapor cell, the probe light passes a cold mirror (Thorlabs FM02) used to overlap the blue light, and is collected with a photodiode (Thorlabs Det10A) for detection of the transparency peak. From the error signal on the saturated absorption locking circuit (Toptica Digilock 100), we estimate the FWHM linewidth of the probe laser to be ~ 100 kHz.

The coupling light, Rabi frequency $\Omega_c = 2\pi \times 150$ kHz, is generated by our SHG system. The coupling light is tuned to the $5P_{3/2}, F = 3 \rightarrow 53D_{5/2}$ transition at around 480.0052 nm. We verified the wavelength with a wavemeter (Burleigh WA-1500). The blue light is passed through an AOM (Crystal Technologies 3110-140) for lock-in modulation before being overlapped with the counterpropagating probe beam via a cold mirror.

We use lock-in detection to increase the signal-to-noise ratio of the EIT signal. The coupling light is modulated at a frequency of 24 kHz with the AOM, and scanned over the EIT peak at a rate of 3.0 MHz s^{-1}. We scan the coupling light by sweeping the piezo voltage on one of the reference cavity mirrors while the ECDL is locked to the red side of the cavity fringe using our FPGA locking circuit. Fig. A.4 shows typical EIT data. The measured linewidth on the EIT peak, averaged over several successive measurements, is 3.56 ± 0.77 MHz.[3] For many measurements, the measured linewidth is smaller than half of the natural linewidth of the probe transition, which is 6.0666 MHz [172]. This is proof that we are indeed seeing the coherent EIT effect as opposed to Autler-Townes splitting [173]. From the measured width of the EIT peak, we deduce an upper bound for the ECDL linewidth of 1.78 ± 0.39 MHz. The factor of 2 reduction is due to the frequency doubling. This width is much larger

[3]We note that if we scan the grating position on the free-running ECDL, we observe a much broader EIT peak with a FWHM of 17 MHz.

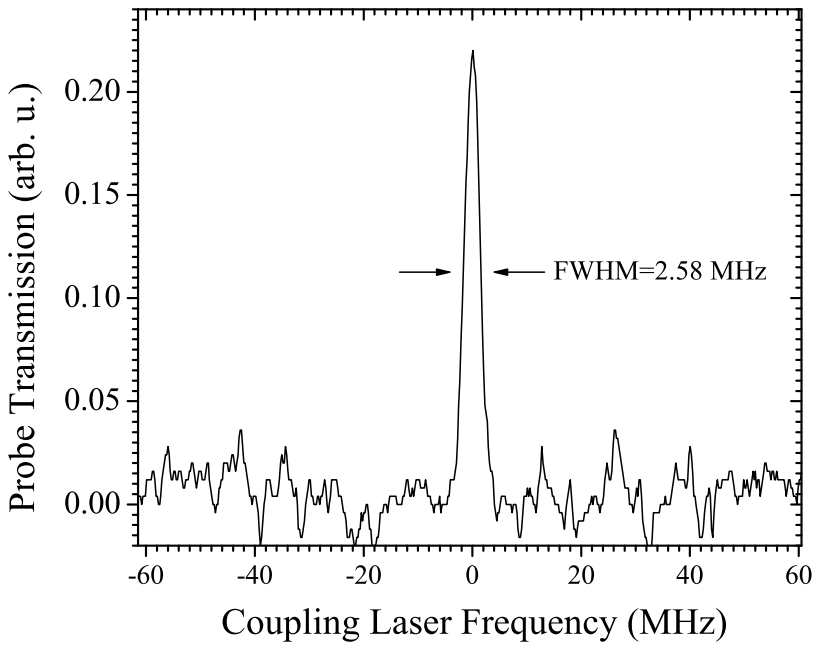

Figure A.4: EIT measurement. The probe transmission photodiode signal is plotted vs. the coupling laser detuning. The coupling laser frequency is swept by slowly ramping the reference cavity piezo voltage while the ECDL is locked to the red side of the cavity peak. The EIT peak has a width of 2.58 MHz. This corresponds to a frequency range of 1.29 MHz for the ECDL light, and gives an upper limit on the locked ECDL linewidth.

than the convolution of the linewidth of both lasers that we estimate from the error signals. We attribute this discrepancy to the thermal and vibrational noise affecting our Fabry-Perot reference cavity length, amplitude noise on the ECDL output light and broadening of the EIT peak due to residual magnetic fields. Cavity and amplitude noise can lead to a broadening of the laser linewidth without increasing the noise on the error signal. In addition, the vapor cell was not shielded from residual magnetic fields, which can also broaden the EIT peak due to the Zeeman shifts of the magnetic sublevels of all involved states. A linewidth of ≤ 1.8 MHz is good for most spectroscopic applications in atomic physics. If necessary, the linewidth could be further reduced by using a more stable frequency reference, or by using a better

locking scheme such as the Pound-Drever-Hall scheme [174].

A.8 Conclusion

In conclusion, we described a locking circuit for external cavity diode lasers implemented on a field-programmable gate array (FPGA). The software features a piezo feedback loop for the grating and a current feedback loop for the laser diode current, user-adjustable input filters, and adjustable sweep scanning and debugging options. It can be easily customized for diverse experimental requirements by changing the software and reloading it onto the FPGA, without any soldering required. The VHDL source code for the FPGA circuit is available in the supplemental materials. We described a graphical user interface that communicates with the FPGA board and offers user friendly mouse and keyboard controls to change all the feedback loop, filter, and scan parameters of the FPGA in realtime. The Borland C++ source code for the user interface is also available in the supplemental materials. We characterized the quality of the lock obtained with this circuit by locking our homebuilt second-harmonic generation laser system to a reference cavity and monitoring the error signal. The linewidth as estimated from the error signal is 164 kHz. We used electromagnetically-induced transparency to measure an upper limit on the linewidth of the locked laser and found that it is 1.78 ± 0.39 MHz. We attribute the broadening to reference cavity noise, residual amplitude noise and Zeeman shifts from stray magnetic fields, but note that the measured linewidth is small enough for most spectroscopic applications in atomic physics. Employing a more stable frequency reference could decrease the linewidth significantly, as could using the more involved Pound-Drever-Hall technique.

Appendix B

Rydberg atom pair potential program usage

B.1 Introduction

This chapter contains an explanation of the Rydberg atom-Rydberg atom long-range pair interaction computer code that was used to generate the potentials presented in Chapter 7. The calculation of Rydberg atom pair potentials in the presence of a small applied DC electric field is done in two major parts. First, Stark-shifted single atom states and energies are calculated by diagonalizing the Stark matrix. Second, the Hamiltonian for a pair of interacting Rydberg atoms is diagonalized for a range of internuclear distances R.[1] The resulting eigenvalues are the adiabatic potential energy curves. The first part of the calculation is done in Mathematica on a single computer. The second part is done in Fortran on a cluster computer. In addition to calculating the single atom Stark energies and eigenvectors, the first part of the program takes advantage of readily available special functions in Mathematica to precalculate tables of numbers which are then imported into the Fortran code. An overview of the calculation is shown in Fig. B.1. In this chapter, both parts of the calculation are described in some detail.

[1]For Cs 89D89D pairs, R ranges between 3 μm and 10 μm, and the atoms interact via long-range dipole-dipole, dipole-quadrupole and quadrupole-quadrupole interactions. The calculation could be expanded to higher order multipoles. The theory and justification for the truncation at the quadrupole level is given in Chapter 7.

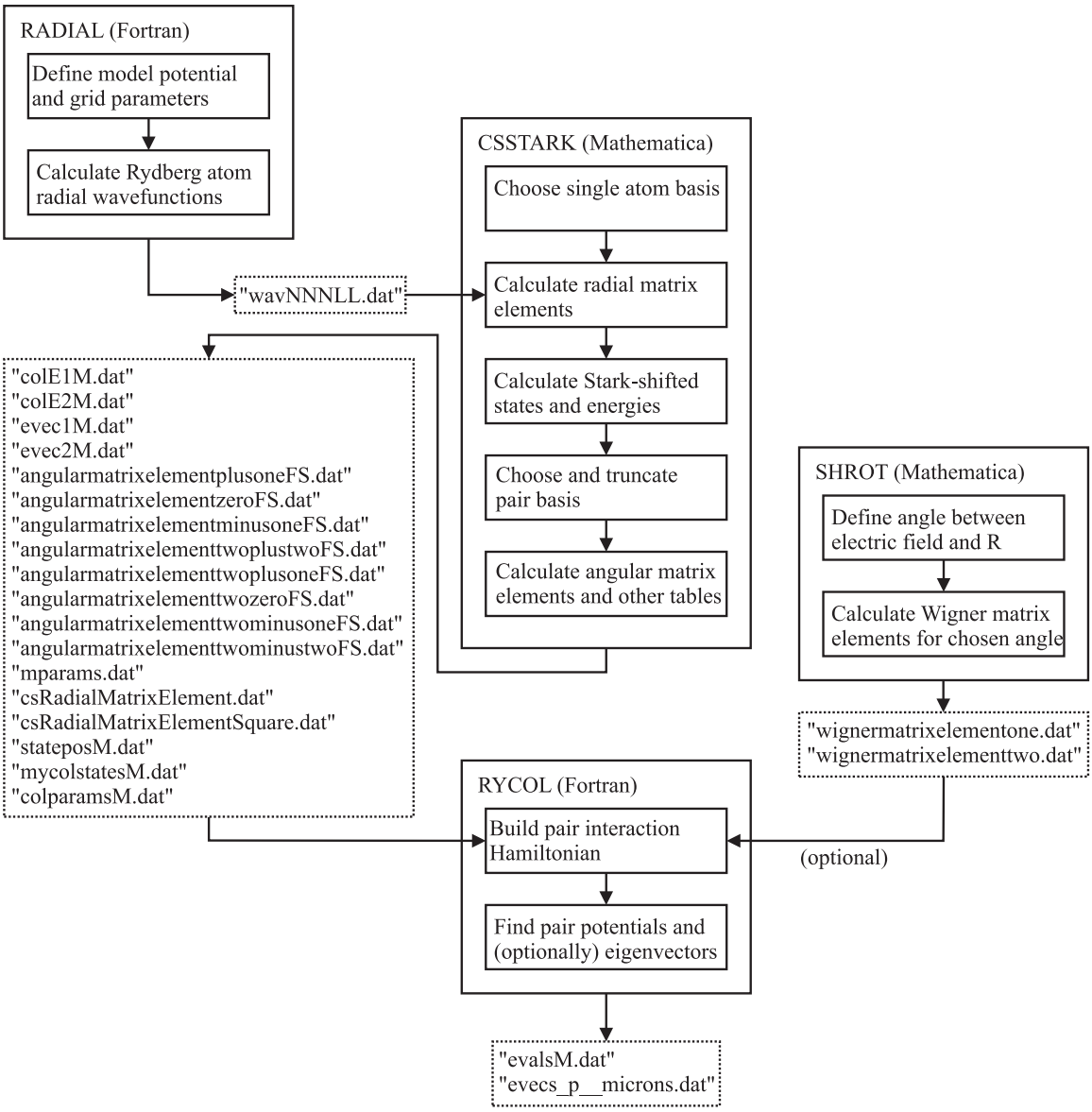

Figure B.1: Flow chart of the Rydberg pair potential calculation. Dashed boxes enclose lists of data filenames.

B.2 Mathematica program CSSTARK

In the Mathematica notebook CSSTARK (Fig. B.2), the Stark-shifted pair basis is generated and saved to disk. In addition, several tables of reusable numbers such as radial and angular matrix elements are saved to disk for use later in the Fortran code. The calculation of Stark shifts and Stark-shifted eigenstates proceeds as follows:

- Constants such as the Rydberg constant and the mass of Cs are defined.

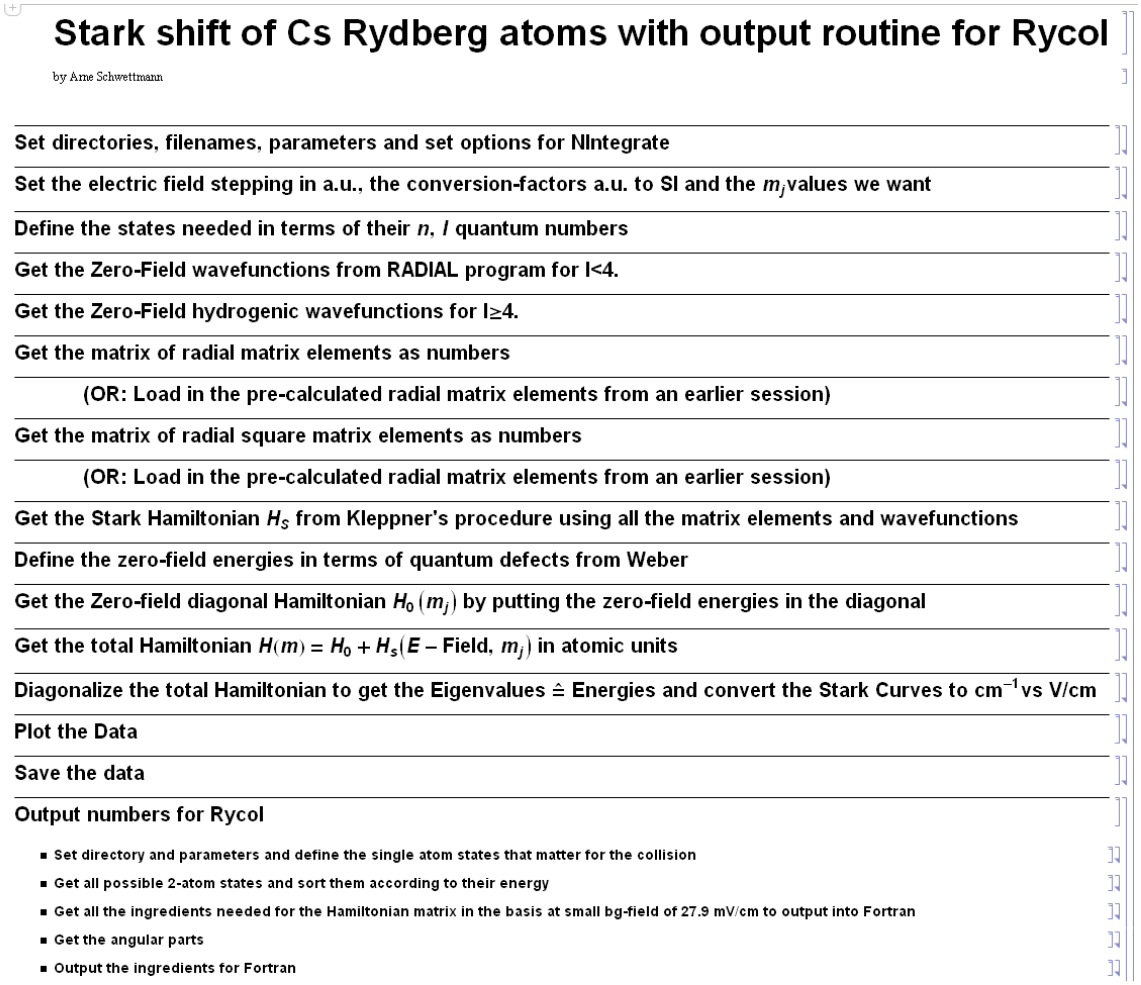

Figure B.2: Screenshot of the folded view of CSSTARK as it appears after opening the notebook in Mathematica. The headlines of the major sections of the program are shown.

- The magnitude of the background electric field, ϵ, is defined.

- A list of single atom basis states is chosen and defined in terms of n and l quantum numbers. The basis size has to be large enough to guarantee convergence of the Stark-shifted energies and eigenvectors at the desired level. Enough single atom states that are coupled by the dipole operator have to be included in the basis. A convergence check should be performed by calculating pair potentials for increasing basis sizes until the results do not change anymore at the desired level. For example, for the Cs 89D calculations, the final basis states chosen included the states 89D, 90S, 90P, 91S, 87F, 86F, 90D, 91P, 88D, 88G, 88F, 89P, as well as higher angular momentum states ($l \leq 14$) of the n=86 and n=87 states.

- The radial wavefunctions are calculated for all single atom states. For $l < 4$, the software package RADIAL [67] is used to calculate the wavefunctions as described in Section 2.3.3, and the numerical results are imported into Mathematica. For $l \geq 4$ the hydrogenic wavefunctions are defined analytically in Mathematica.

- The radial matrix elements $\langle n, l|r|n', l'\rangle$ and $\langle n, l|r^2|n', l'\rangle$ between all single atom basis states are precalculated using numerical integration. This takes the longest time of all the calculations done in the Mathematica notebook. The matrix elements $\langle n, l|r|n', l'\rangle$ are needed both for the Stark shift calculation and later to evaluate dipole-dipole interactions in the Fortran code. The matrix elements $\langle n, l|r^2|n', l'\rangle$ are needed to evaluate the dipole-quadrupole and quadrupole-quadrupole interactions in the Fortran code.

- The set of all possible (n, l, j) state labels is constructed from the set of (n, l) state labels. The state labels are numbered such that $|i, m_j\rangle_s = |n_i, l_i, j_i, m_j\rangle$,

where i is the internal ID number of the single atom state for the given m_j. This constitutes the single atom basis.

- The atomic energies at zero field, $E_{0i}^{(m_j)}$, of each state $|i, m_j\rangle_s$ are calculated using the known quantum defects as explained in Section 2.3.2.

- The Hamiltonian $H = H_0 + H_{\text{Stark}}(\epsilon)$ is built in the single atom basis $|i, m_j\rangle_s$, Since H is block diagonal in m_j, the matrix is built separately for each m_j. Here, H_0 is diagonal and contains the zero-field energies. $H_{\text{Stark}}(\epsilon)$ is the Stark Hamiltonian for the applied field magnitude ϵ. It contains only off-diagonal elements. H_{Stark} is calculated following the procedure of Ref. [57], using the precalculated radial matrix elements $\langle n, l|r|n', l'\rangle$.

- H is diagonalized separately for each value of m_j. The resulting eigenvectors are the Stark-shifted single atom states, defined by the coefficients c in the expansion

$$\widetilde{|i, m_j\rangle} = |n_i, \widetilde{l_i, j_i}, m_j\rangle = \sum_k c_{ik}|n_k, l_k, j_k, m_j\rangle, \tag{B.1}$$

  The eigenvalues are the stark-shifted energies $E_i^{(m_j)}$. Care is taken to sort the eigenvalues and eigenvectors so that each eigenvalue is assigned to the correct zero field quantum numbers.

At this point, the calculation of the Stark-shifted single atom states is done. The purpose of the remaining part of the Mathematica notebook is to prepare tables of values that will be reused many times during the building of the pair interaction Hamiltonian in the Fortran program RYCOL. First, the pair basis set is generated and truncated. The pair basis set includes all interacting atomic pairs that are close in energy to the state of interest. In the case of the Cs 89D89D calculation, this basis consisted of several thousand pair states. After the pair basis is defined, various angular matrix elements between single atom states are calculated. The need

for angular matrix elements arises due to the presence of spherical harmonics in the pair interaction Hamiltonian. Finally, all calculated values are exported from Mathematica to be used in RYCOL. The exported numbers include the zero-field quantum numbers of all pair states, the Stark-shifted energies of single atom states, the Stark-shifted eigenvectors of single atom states, the radial matrix elements between single atom states, and the angular matrix elements between single atom states. All results are saved from Mathematica as ASCII files. They are prepared in such a way that they can be imported most easily into RYCOL. Precalculating as many numbers as possible from within Mathematica makes the process of writing the Fortran code less painful. In this way, Fortran is only used for the computationally intensive parts of the problem.

Following is a more detailed account of the steps that are done in the second half of the Mathematica notebook:

- The single atom states that make up pairs to be used in the interaction potential calculation are defined in terms of their quantum numbers (n, l). These usually coincide with the original set of quantum numbers used in the Stark calculation.

- A list of full quantum numbers

$$|n^{(1)}, l^{(1)}, \widetilde{j^{(1)}}, (m_j)^{(1)}\rangle \otimes |n^{(2)}, l^{(2)}, \widetilde{j^{(2)}}, (m_j)^{(2)}\rangle \tag{B.2}$$

  of all possible pair states is generated for each $M = (m_j)^{(1)} + (m_j)^{(2)}$. The separation in M is done because the pair interaction Hamiltonian is block diagonal in M.

- The total Stark-shifted asymptotic energy at $R \to \infty$, $E = E^{(1)} + E^{(2)}$, of each pair state is calculated, and the pair states are sorted according to their energy from lowest to highest.

- The pair basis is truncated in an energy region around the pair state of interest. A convergence check revealed that, for convergence to ~ 1 MHz for Cs 89D89D and surrounding states, around 6000 pair states had to be included for M=5 (~ 4000 for M=1).

- For each M, each pair state is given a unique number that increases with increasing energy, so that

$$\widetilde{|k, M\rangle}_p = |n_k^{(1)}, l_k^{(1)}, \widetilde{j_k^{(1)}}, (m_j)_k^{(1)}\rangle \otimes |n_k^{(2)}, l_k^{(2)}, \widetilde{j_k^{(2)}}, (m_j)_k^{(2)}\rangle, \tag{B.3}$$

  where $(m_j)_k^{(1)} + (m_j)_k^{(2)} = M$. This constitutes the pair basis, and k is the pair basis state ID number.

- The zero field quantum numbers $(n^{(1)}, l^{(1)}, j^{(1)}, (m_j)^{(1)}, n^{(2)}, l^{(2)}, j^{(2)}, (m_j)^{(2)})$ of each pair state are saved as lists to the files "mycolstatesM.dat". A separate list is saved for each M.

- The Stark-shifted energies of each single atom state that comprises each pair state are written as lists. The file "colE1M.dat" contains the Stark-shifted energies of the first atom, and the file "colE2M.dat" contains the Stark-shifted energies of the second atom. Separate files are written for each value of M.

- The Stark eigenvectors of the two states making up each pair state are saved as tables. Separate files are written for each value of M. The file "evec1M.dat" ("evec2M.dat") contains the values α_{ik} (β_{ik}) in the expansion

$$\widetilde{|i, M\rangle}_p = \sum_k \alpha_{ik} |k, (m_j)_i^{(1)}\rangle \otimes \sum_p \beta_{ip} |p, (m_j)_i^{(2)}\rangle \tag{B.4}$$

  in row i and column k.

- The radial matrix elements of r between the zero-field single atom states are saved as "csRadialMatrixElement.dat." The file contains the radial matrix ele-

ment $\langle n_i l_i | r | n_k l_k \rangle$ in row i and column k. This matrix contains a lot of duplicate numbers, but makes the Fortran program easier to write.

- Similarly, the radial matrix elements of r^2 between the zero-field single atom states are saved as "csRadialMatrixElementSquare.dat." The file contains the radial matrix element $\langle n_i l_i | r^2 | n_k l_k \rangle$ in row i and column k. Again, this matrix contains a lot of duplicate numbers.

- The angular matrix elements between the single atom states are also calculated and written to a file. Matrix elements of the spherical harmonics up to order two are evaluated. For example, the file "angularmatrixelementplusoneFS.dat" contains the angular matrix elements

$$\langle l_i, j_i, m_j | Y_1^1 | l_k, j_k, m_j' \rangle \tag{B.5}$$

in row

$$i \times \left((m_j)_{\max} - (m_j)_{\min} + 1 \right) + m_j - 1/2,$$

and column

$$k \times \left((m_j)_{\max} - (m_j)_{\min} + 1 \right) + m_j' - 1/2.$$

Here $(m_j)_{\max}$ and $(m_j)_{\min}$ are the largest and smallest values of m_j that occur in the pair basis. The file "angularmatrixelementminuoneFS.dat" contains the matrix elements of Y_1^{-1}. The file "angularmatrixelementtwoplustwoFS.dat" contains matrix elements of Y_2^{+2}, and so on.

- The table and list sizes of the described files are saved to files "colParamsM.dat," to make importing into RYCOL easier. The files contain, for each M, the number of states in the single atom basis, the number of states in the pair basis, the number of rows in the angular matrix element files, the maximum l quantum number in the basis, as well as the minimum m_j value, and the maximum m_j value.

- The minimum and maximum values of M are also saved to a file. The file is called "Mparams.dat." For the 89D89D calculations, M ranges from 0 to 5 to include all combinations of 89D sublevels (the results depend only on $|M|$).

B.3 Fortran program RYCOL

The Fortran program RYCOL is written to perform the more computationally intensive tasks of the Rydberg pair potential calculations. It uses the Message Passing Interface communication layer (MPI) to parallelize computations, and is run on a cluster computer. RYCOL builds the Hamiltonian, Eq. 7.1, in the atomic pair basis and diagonalizes it for a range of values of the internuclear distance, R. The results are the adiabatic Born-Oppenheimer pair interaction potentials and, optionally, some of the corresponding eigenstates. The Hamiltonian is built using the precalculated values from Mathematica. Even after precalculating all of the numbers that are reused frequently, constructing the full Hamiltonian is still computation heavy. This is due to the large number of matrix elements ($\sim 25 \times 10^6$) and due to the many sums that arise from the mixing of single atom states by the electric field. The diagonalization of the matrix at many values of R is also computationally intensive because of the large size of the matrix. To make the computation feasible, the construction of the matrix and the loop over R are both parallelized. To save computation time, all terms of the interaction matrix that are independent of R are constructed once in the beginning, before the loop over R is started. The full interaction matrix can be written as a sum of three independent matrices, each with a different R dependence,

$$H = \frac{H_{dd}}{R^3} + \frac{H_{dq}}{R^4} + \frac{H_{qq}}{R^5} \tag{B.6}$$

The three matrices H_{dd}, H_{dq}, and H_{qq} correspond to the spherical dipole-dipole, dipole-quadrupole, and quadrupole-quadrupole interactions, respectively. In the matrix construction phase of RYCOL, the three matrices H_{dd}, H_{dq}, and H_{qq} are built and stored

in memory or saved to disk for later reuse. For the Cs 89D89D calculations, the construction of the three matrices takes up about half of the total run-time of the program. During the diagonalization phase of RYCOL, the full Hamiltonian matrix at a specific R-value is then quickly calculated by multiplying each of the three precalculated matrices with the corresponding R dependence and adding them according to Eq. B.6. This saves a large amount of computation time. The diagonalization of the matrix is implemented using a call to the function DSPEV of the LAPACK library [175].

If the basis contains a lot of states, the precalculated matrices H_{dd}, H_{dq} and H_{qq} can be too large to fit into the memory of a single compute node. If this is the case, the matrices can be spread over several nodes. The distributed matrix storage is implemented using SCALAPACK [176]. Using a custom process grid definition, the matrix can be spread out over multiple nodes, and the loop over R can still be parallelized. To accomplish this, the functions BLACS_GET and BLACS_GRIDMAP are used to create a hierarchy of process grids. An overarching (super-)grid is used to parallelize the loop over R. Each process in the super-grid diagonalizes the Hamiltonian matrix for only a few values of R, using a (sub-)grid of several nodes to store its own copy of the matrix in a distributed fashion. When distributed matrix storage is used, the diagonalization of the matrix is implemented using a call to the function PDSYEV of the SCALAPACK library.

At the end of the RYCOL program, eigenvalues (and optional eigenvectors) are output as ASCII files called "evalsM.dat". A separate file is written for each M. The output file automatically contains human-readable header lines, constructed from the pair state zero-field quantum numbers originally saved as "mycolstatesM.dat". The first column in the file contains the R value in μm, and the remaining columns contain the R dependent energies of the different pair states. The header lines contain for

each column the ID and the zero field quantum numbers of each pair state. This makes identification of the potential curves and subsequent data analysis easier.

For a specified M, a selected subset of eigenvectors can optionally be saved to files. In this case, eigenvectors are written to files called "evecs_p__microns.dat." The blank parts of the file name are filled in with the R value chosen, and p is used to denote a decimal point. A separate file is written for each R value. The eigenvectors are found in the columns of the file. Again, human-readable headers and labels are automatically written to the file. The first three rows in the file contain the R value, the pair basis state ID, and the zero-field quantum numbers of the state. The first column of the file contains the zero-field labels of the asymptotic $R \to \infty$ Stark-shifted pair state basis in which the eigenvectors are given.

B.4 Rotated Hamiltonian

A separate version of RYCOL was written to find the pair potentials for the case when the electric field is not parallel to the internuclear distance, R. The program uses Eq. 7.4 to rotate the spherical harmonics in the Hamiltonian with the help of Wigner rotation matrices. The angular matrix elements are replaced by sums over other angular matrix elements. The Wigner matrices are precalculated with an accompanying Mathematica program SHROT. For a given angle Θ between the electric field and R, SHROT calculates Wigner matrix elements according to Eq. 3.57 of Ref. [53]. It outputs two files, called "wignermatrixelementone.dat" and "wignermatrixelementtwo.dat." The file "wignermatrixelementone.dat" contains the Wigner matrix element $D^1_{m'm}(\Theta, 0, 0)$ in row m and column m'. The file "wignermatrixelementtwo.dat" contains the Wigner matrix element $D^2_{m'm}(\Theta, 0, 0)$ in row m and column m'. The Mathematica notebook also contains a set of tests, where spherical harmonics rotated with the Wigner matrices are compared against explicit evaluations in

the rotated basis, to ensure the rotated functions are correct. In the rotated case, where $\epsilon \nparallel R$, the Hamiltonian is not block diagonal with respect to M. The number of matrix elements is therefore many times larger than in the case where $\epsilon \parallel R$. For example, in the 89D89D calculation, the basis size becomes ~ 40000, and the matrix size is ~ 50 times larger than in the non-rotated case. Due to the large matrix sizes, SCALAPACK is used to find the eigenvalues of the Hamiltonian, as described in Section B.3 above.

B.5 Programs and files

In this section, the various files used for pair potential calculations are listed. Table B.1 lists the filenames of the programs. Table B.2 lists the output filenames of the CSSTARK notebook, and Table B.3 lists the output filenames of the RADIAL, RYCOL and SHROT programs.

Table B.1: Program filenames for Rydberg pair potential calculations.

Filename	Description
rycol*.f90	Full RYCOL program
rycol*_save_matrices.f90	As above, but only builds and saves H_{dd}, H_{dq}, H_{qq}
rycol*_load_matrices.f90	As above, but loads H_{dd}, H_{dq}, H_{qq} and diagonalizes $H(R)$
rycol*_rotation_scalapack_multigridding.f90	Full RYCOL for the case that ϵ is not parallel to R
rycol*_rotation_scalapack_multigridding_save_matrices.f90	As above, but only builds and saves H_{dd}, H_{dq}, H_{qq}
rycol*_rotation_scalapack_multigridding_load_matrices.f90	As above, but loads H_{dd}, H_{dq}, H_{qq} and diagonalizes $H(R)$
rycol_mpi_ib.bsub	LSF batch file to submit a RYCOL job
makefile	Used to compile RYCOL with the Intel Fortran compiler
csstark.nb	CSSTARK program
radial.for	RADIAL program
atomiclib.for	Uses RADIAL to generate a library of wavefunctions
sphericalharmonicrotation.nb	SHROT program

† The * stands for the string "_mpi_fs_spread_degeneracy_quadrupole_mcons_nostatepos".

Table B.2: Output filenames of CSSTARK program. All files are space-delimited ASCII files.

Filename	Description
colE1M.dat (colE2M.dat)	Stark-shifted energies of first (second) atom
evec1M.dat (evec2M.dat)	Stark-shifted eigenvectors of first (second) atom
angularmatrixelementplusoneFS.dat	Matrix elements of Y_1^1
angularmatrixelementzeroFS.dat	Matrix elements of Y_1^0
angularmatrixelementminusoneFS.dat	Matrix elements of Y_1^{-1}
angularmatrixelementtwoplustwoFS.dat	Matrix elements of Y_2^{+2}
angularmatrixelementtwoplusoneFS.dat	Matrix elements of Y_2^{+1}
angularmatrixelementtwozeroFS.dat	Matrix elements of Y_2^0
angularmatrixelementtwominusoneFS.dat	Matrix elements of Y_2^{-1}
angularmatrixelementtwominustwoFS.dat	Matrix elements of Y_2^{-2}
mparams.dat	Minimum and maximum value of M
csRadialMatrixElement.dat	Radial matrix elements of r
csRadialMatrixElementSquare.dat	Radial matrix elements of r^2
mycolstatesM.dat	Zero-field quantum numbers of pair states
colparamsM.dat	Contains sizes of data files for easy importing
stateposM.dat	Minimum and maximum pair state ID number

Table B.3: Output filenames of RADIAL, RYCOL and SHROT programs. All files are space-delimited ASCII files.

Filename	Description
wavNNNLL.dat†	Radial wave function data output from RADIAL
wignermatrixelementone.dat	l=1 Wigner matrix element output from SHROT
wignermatrixelementtwo.dat	l=2 Wigner matrix element output from SHROT
evalsM.dat	Pair potential output from RYCOL
evecs_p__.dat‡	Eigenvector output from RYCOL

† NNNLL denotes principal quantum number and angular momentum.

‡ _p__ stands for R (8p00 means $R = 8$ μm).

Appendix C

Rydberg EIT programs

C.1 Introduction

In this chapter, the Mathematica notebooks used to calculate the probe transmission spectra of the 4- and 52-level Rydberg EIT systems are reproduced.

C.2 4-level Rydberg EIT notebook

The 4-level Rydberg EIT spectra shown in Section 2.4.3 and Section 6.3.2 were calculated on a desktop computer. The Mathematica code that was used is reproduced on the following pages.

4-level Rydberg atom EIT

written by Arne Schwettmann for James P. Shaffer Lab

This notebook computes the probe transmission spectrum of the 4-level ladder-type Rydberg EIT system subject to 2 laser light fields and microwave radiation. Solutions are obtained by numerically solving the density matrix equations in steady state. Several example spectra are calculated at T=0 K. To simulate Rubidium measurements in a warm vapor cell, an average over the thermal velocities of the atoms is performed, and spectra are computed for a range of different microwave powers.

Init

Load in physical constants and units

```
<< PhysicalConstants`
<< Units`
```

Set the output directory

```
SetDirectory[NotebookDirectory[]];
```

Format parameters for use in header lines when exporting data

```
formatParamsForOutput[params_] := params /.
  (a_ → b_) :> "#" <> StringReplace[ToString[a], {"Δ" → "Delta", "Ω" → "Omega",
      "Γ" → "Gamma", "ħ" → "hbar"}] <> " = " <> ToString[InputForm[N[b]]]
```

Set plot options to visualize the data

```
plotOptions =
  {Joined → True, PlotRange → All, Frame → True, Axes → False, FrameLabel →
    {"Probe Detuning (Hz)", "Transmission (arb. u.)"}, BaseStyle → Medium};
```

4-level Hamiltonian

Number of levels

```
n = 4;
```

User-entered 4 level Hamiltonian. Here, the Rabi frequency Ω is $\frac{\mu E_0}{\hbar}$.

$$H = \frac{\hbar}{2}\begin{pmatrix} 0 & \Omega p & 0 & 0 \\ \Omega p & -2\Delta 1 & \Omega c & 0 \\ 0 & \Omega c & -2(\Delta 1+\Delta 2) & \Omega rf \\ 0 & 0 & \Omega rf & -2(\Delta 1+\Delta 2+\Delta 3) \end{pmatrix};$$

Decay operators

ρ[i,j] is used for the density matrix elements ρ_{ij}. Thus, we cannot use ρ to refer to the full matrix, so we will use $\rho\rho$

```
ρρ = Table[ρ[i, j], {i, 1, n}, {j, 1, n}]
```

```
{{ρ[1, 1], ρ[1, 2], ρ[1, 3], ρ[1, 4]}, {ρ[2, 1], ρ[2, 2], ρ[2, 3], ρ[2, 4]},
 {ρ[3, 1], ρ[3, 2], ρ[3, 3], ρ[3, 4]}, {ρ[4, 1], ρ[4, 2], ρ[4, 3], ρ[4, 4]}}
```

Define unit vectors

```
e[i_] = Table[{KroneckerDelta[i, j]}, {j, 1, n}];
```

Define the projection matrices σ, see Fleischhauer et al, Rev. Mod. Phys. **77**, 633 (2005), eq. 9.

```
σ[i_, j_] = e[i].e[j]^T;
```

Test that σ works

```
σ[2, 2] // MatrixForm
```

$$\begin{pmatrix} 0 & 0 & 0 & 0 \\ 0 & 1 & 0 & 0 \\ 0 & 0 & 0 & 0 \\ 0 & 0 & 0 & 0 \end{pmatrix}$$

Following are the "decay operators," see Fleischhauer et al, Rev. Mod. Phys. **77**, 633 (2005), eq. 9. Γ_{ij} is the decay rate due to spontaneous emission of level i (into level j). The total decay rate of a level due to spontaneous emission is $\Gamma_i := \sum_j \Gamma_{ij} = \frac{1}{\tau}$, where τ is the $\frac{1}{e}$lifetime of state i. The case of equal indices in a decay operator (L[i,i]) corresponds to an additional dephasing rate of level i, labelled γ_i. These rates are labelled γ_i instead of Γ_{ii} to not confuse them with the total decay rate of a state, Γ_i. γ_i are optional additional dephasing rates affecting only the coherences. γ_i could be due to collisions, laser phase jitter, or other sources of decoherence. These additional dephasing rates are labelled $\gamma_{i\,\mathrm{dephas}}$ in Fleischhauer's review.

Use γ_i instead of Γ_{ii}.

```
Γ[i_, i_] = γ[i];
```

Define the decay/decoherence operators L[i,j].

```
L[i_, j_] = Γ[i, j]/2 (2 σ[j, i].ρρ.σ[i, j] - σ[i, i].ρρ - ρρ.σ[i, i]);
```

Differential equations, steady state

User-entered time evolution $\frac{d\rho}{dt} = -\frac{i}{\hbar}\left[\hat{H}, \hat{\rho}\right] + \hat{L}$

```
ρdot = -(i/ħ) (H.ρρ - ρρ.H) + L[3, 2] + L[2, 1] + L[4, 3];
```

Format the differential equations to be solved and add the condition that all population remains in the system.

```
eqns = Apply[And,
   Append[
      Table[
       0 == ρdot[[i, j]],
       {i, 1, n}, {j, 1, n}
      ],
      1 == Plus @@ Table[ρ[i, i], {i, 1, n}]
     ] /.
     {ρ[i_, j_] :> ToExpression["ρ" <> ToString[i] <> ToString[j]]} // Flatten];

solutionsWanted = Table[ρ[i, j], {i, 1, n}, {j, 1, n}] /.
   {ρ[i_, j_] :> ToExpression["ρ" <> ToString[i] <> ToString[j]]} // Flatten
```

```
{ρ11, ρ12, ρ13, ρ14, ρ21, ρ22, ρ23, ρ24, ρ31, ρ32, ρ33, ρ34, ρ41, ρ42, ρ43, ρ44}
```

Comparison of 2-level, 3-level, and 4-level absorption spectra

Numerical Parameters in SI units

```
myParams = {
   Γ[2, 1] → 1/(26 × 10^-9),
   Γ[3, 2] → 1/(78 × 10^-6),
   Γ[4, 3] → 1/(78 × 10^-6),
   ħ → PlanckConstantReduced 1./(Joule Second),
   Ωp → 2 π 10^6 0.1,
   Ωc → 2 π 1 × 10^6,
   Ωrf → 2 π 0.16 × 10^6,
   Δ1 → 0,
   Δ2 → 0,
   Δ3 → 0
  };
```

Solve the steady state equations for different probe detunings Δ1

Compile results as a table of probe absorption versus probe detuning. The absorption is proportional to Im[ρ21].

Only probe light

```
sols2Level = Table[{δ/(2π), Im[ρ21]} /.
    Solve[eqns /. {Δ1 → δ, Ωc → 0., Ωrf → 0.} /. myParams, solutionsWanted],
   {δ, -2π 5×10^6, 2π 5×10^6, 2π 0.01×10^6}] // Flatten[#, 1] &;
```

Probe and coupling light

```
sols3Level = Table[{δ/(2π), Im[ρ21]} /.
    Solve[eqns /. {Δ1 → δ, Ωrf → 0.} /. myParams, solutionsWanted],
   {δ, -2π 5×10^6, 2π 5×10^6, 2π 0.01×10^6}] // Flatten[#, 1] &;
```

Probe light, coupling light, and microwaves

```
sols4Level =
  Table[{δ/(2π), Im[ρ21]} /. Solve[eqns /. {Δ1 → δ} /. myParams, solutionsWanted],
   {δ, -2π 5×10^6, 2π 5×10^6, 2π 0.01×10^6}] // Flatten[#, 1] &;
```

■ Plot results

When the probe light is on and all other fields are off, we get only the probe absorption peak.

```
ListPlot[sols2Level, plotOptions]
```

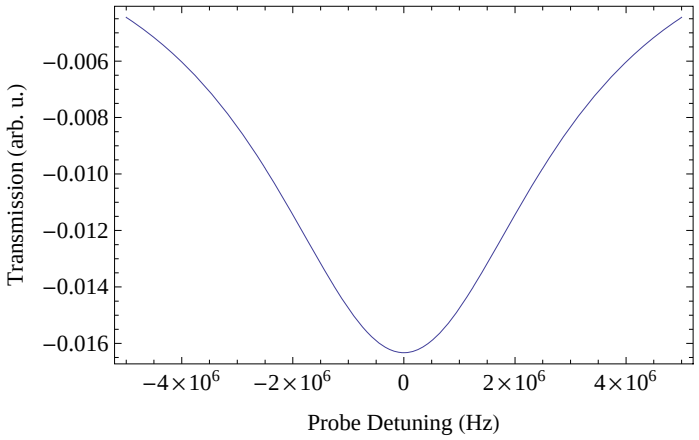

When the probe and coupling light fields are on, we get the EIT peak in the absorption line.

```
ListPlot[sols3Level, plotOptions]
```

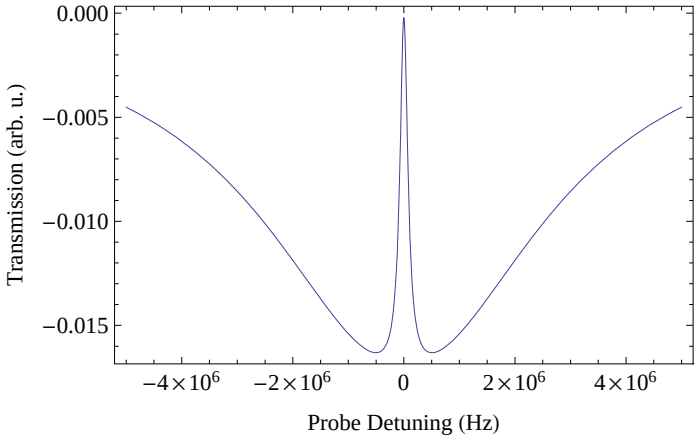

When the probe light, the coupling light and the microwaves are on, we see the EIT peak in the absorption line, just as in a 3-level system. However, there is now an additional narrow region of opacity in the center. This is caused by the coupling of the 3rd to the 4th level, and is unique to the four-level system.

```
ListPlot[sols4Level, plotOptions]
```

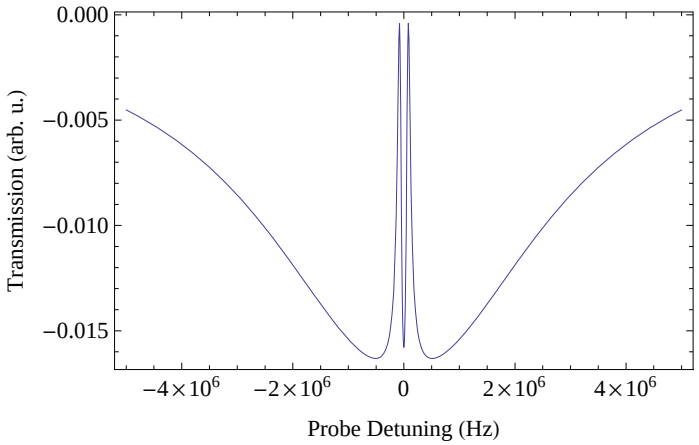

■ Export data

Export the data to ASCII files

```
Export["sols2Level.dat", formatParamsForOutput[myParams] ~
   Join ~ {"#Delta1 Transmission"} ~ Join ~ sols2Level, "Table"];
```

```
Export["sols3Level.dat", formatParamsForOutput[myParams] ~
   Join ~ {"#Delta1 Transmission"} ~ Join ~ sols3Level, "Table"];
```

```
Export["sols4Level.dat", formatParamsForOutput[myParams] ~
   Join ~ {"#Delta1 Transmission"} ~ Join ~ sols4Level, "Table"];
```

Changing parameters (Cs system)

■ Numerical Parameters in SI units

```
myParams = {
   Γ[2, 1] → 1/(30.405 × 10^-9),
   Γ[3, 2] → 1/(75.0 × 10^-6),
   Γ[4, 3] → 1/(68.3 × 10^-6),
   ħ → PlanckConstantReduced 1./(Joule Second),
   Ωp → 2 π 10^6 0.1,
   Ωc → 2 π 1 × 10^6,
   Ωrf → 0.990 × 10^6,
   Δ1 → 0,
   Δ2 → 0,
   Δ3 → 0
  };
```

■ Solve 4-level EIT for different parameters

Changing probe power (probe Rabi Frequencies defined in units of 2π MHz)

```
myProbeFreqs = {0.2, 0.4, 0.6, 0.8, 1.0, 1.2};
```

```
(solsProbe =
    Table[Table[{δ/(2 π), Im[ρ21]} /. Solve[eqns /. {Δ1 → δ, Ωp → Ω} /. myParams,
          solutionsWanted], {δ, -2 π 1 × 10^6, 2 π 1 × 10^6, 2 π 0.005 × 10^6}] //
      Flatten[#, 1] &, {Ω, 2 π 10^6 myProbeFreqs}
    ];) //
 Timing
```

```
{9.172, Null}
```

Changing coupling power (coupling Rabi Frequencies defined in units of 2π MHz)

```
myCouplingFreqs = {0.25, 0.5, 1.0, 2.0, 4.0, 8.0};
```

```
(solsCoupling =
    Table[Table[{δ/(2 π), Im[ρ21]} /. Solve[eqns /. {Δ1 → δ, Ωc → Ω} /. myParams,
          solutionsWanted], {δ, -2 π 1 × 10^6, 2 π 1 × 10^6, 2 π 0.001 × 10^6}] //
      Flatten[#, 1] &, {Ω, 2 π 10^6 myCouplingFreqs}
    ]; ) //
 Timing
```

```
{43.25, Null}
```

Changing microwave power (microwave Rabi Frequencies defined in units of 2π MHz)

```
myRFFreqs = {0.01, 0.16, 0.32, 0.64};
(solsRF =
    Table[Table[{δ/(2 π), Im[ρ21]} /. Solve[eqns /. {Δ1 → δ, Ωrf → Ω} /. myParams,
          solutionsWanted], {δ, -2 π 1 × 10^6, 2 π 1 × 10^6, 2 π 0.001 × 10^6}] //
      Flatten[#, 1] &, {Ω, 2 π 10^6 myRFFreqs}
    ]; ) //
 Timing
```

```
{30.109, Null}
```

Changing Rydberg level lifetime (decay rates defined in units of 2π MHz)

```
myRydbergDecayrates = {0.002, 0.02, 0.05, 0.1, 0.2, 0.5};
(solsLifetime = Table[Table[{δ/(2 π), Im[ρ21]} /.
        Solve[eqns /. {Δ1 → δ, Γ[3, 2] → γ, Γ[4, 3] → γ} /. myParams,
         solutionsWanted], {δ, -2 π 1 × 10^6, 2 π 1 × 10^6, 2 π 0.005 × 10^6}] //
      Flatten[#, 1] &, {γ, 2 π 10^6 myRydbergDecayrates}
    ]; ) //
 Timing
```

```
{8.922, Null}
```

Normalize solutions for clarity

```
normalize[sols_] := Table[
   sols[[k]] /. {i_, j_} → {i, j / Abs[Min[sols[[k, 1 ;;, 2]]]]},
   {k, 1, Length[sols]}
  ];
solsProbe = normalize[solsProbe];
solsCoupling = normalize[solsCoupling];
solsRF = normalize[solsRF];
solsLifetime = normalize[solsLifetime];
```

■ Plot results

Increasing probe power

```
ListPlot[solsProbe, plotOptions]
```

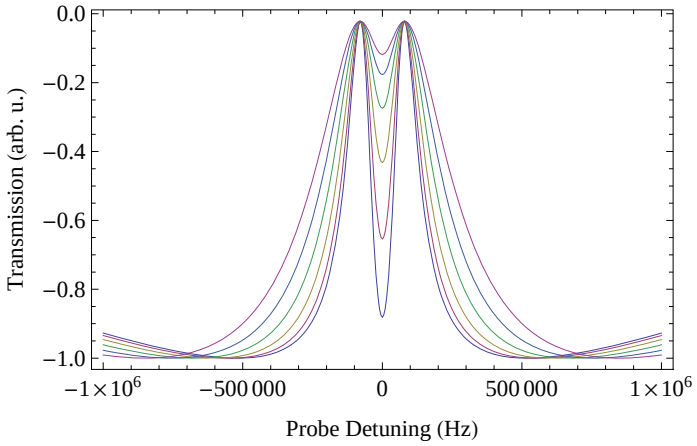

Increasing coupling power

```
ListPlot[solsCoupling, plotOptions]
```

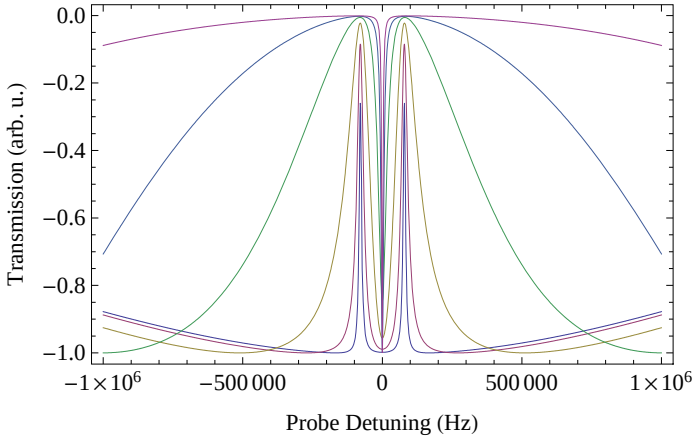

Increasing microwave power

```
ListPlot[solsRF, plotOptions]
```

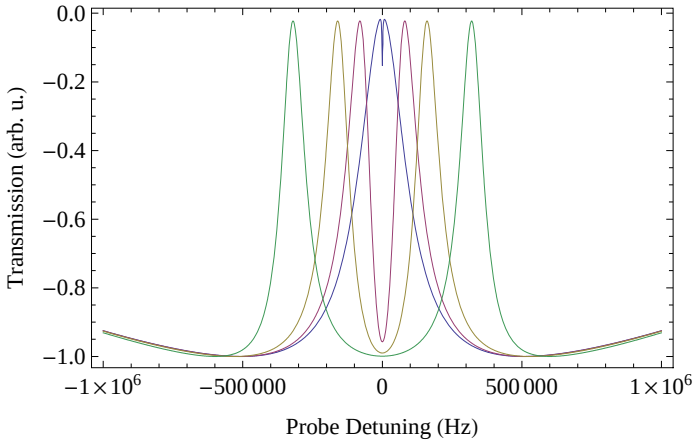

Decreasing Rydberg lifetime

```
ListPlot[solsLifetime, plotOptions]
```

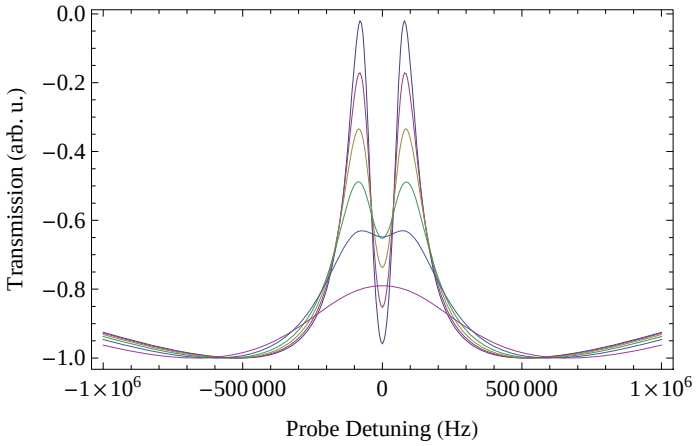

■ Export data

Define a function that formats the data for easy plotting in Origin

```
formatForExport[sols_] := Flatten[
   Table[
    {Join[sols[[1, i]], sols[[2 ;;, i, 2]]}, {i, 1, Length[sols[[1]]]}], 1];
```

Save the data

```
Export["solsProbePower",
 formatParamsForOutput[myParams] ~ Join ~ {{"#Delta1 "} ~ Join ~ myProbeFreqs} ~
  Join ~ formatForExport[solsProbe], "Table"]
```

```
solsProbePowerRF_Cs_forThesis_n_59.dat
```

```
Export["solsCouplingPower", formatParamsForOutput[myParams] ~
  Join ~ {{"#Delta1 "} ~ Join ~ myCouplingFreqs} ~
  Join ~ formatForExport[solsCoupling], "Table"]
```

solsCouplingPowerRF_Cs_forThesis_n_59.dat

```
Export["solsRFPower", formatParamsForOutput[myParams] ~ Join ~
  {{"#Delta1 "} ~ Join ~ myRFFreqs} ~ Join ~ formatForExport[solsRF], "Table"]
```

solsRFPowerRF_Cs_forThesis_n_59.dat

```
Export["solsRydbergLifetime.dat", formatParamsForOutput[myParams] ~
  Join ~ {{"#Delta1 "} ~ Join ~ myRydbergDecayrates} ~
  Join ~ formatForExport[solsLifetime], "Table"]
```

solsRydbergLifetimeRF_Cs_forThesis_n_59.dat

Rb microwave experiment with thermal averaging

- **Numerical Parameters in SI units**

```
myParams = {
    Γ[2, 1] → 1 / (26 × 10^-9),
    Γ[3, 2] → 1 / (136 × 10^-6),
    Γ[4, 3] → 1 / (166 × 10^-6),
    ħ → PlanckConstantReduced 1. / (Joule Second),
    Ωp → 2 π 10.4 × 10^6,
    Ωc → 2 π 0.160 × 10^6,
    Ωrf → 2 π 12.0 × 10^6,
    Δ1 → 0,
    Δ2 → 0,
    Δ3 → 0
  };
```

- **Run EIT for different microwave powers and include the thermal averaging**

RMS velocity for the Rubidium vapor cell temperature of 90 degrees Celsius

```
rmsvelSI = Sqrt[2 k T / m] Second / Meter /. {k → BoltzmannConstant, T → 363.15 Kelvin,
    m → ElementData["Rubidium", "AtomicMass"] AMU} // Convert[#, 1] &
```

265.812

These are the effective microwave Rabi frequencies used in the Rb experiment. They are calculated

for the $53\,D_{5/2}\ F = 4,\ m_F = 4 \to 54\,P_{3/2}\ F = 3,\ m_F = 3$ Rydberg-to-Rydberg transition, using the known microwave intensity at the center of the vapor cell.

```
rabiFreqsUsedInExperiment =
 2 π {623.1265981340391`, 2.6277030762647158`*^6, 3.504098369560496`*^6,
   4.672790276217482`*^6, 6.231265981340391`*^6, 8.309526735627638`*^6,
   1.1080931993093599`*^7, 1.4776660301134573`*^7, 1.970499320735991`*^7,
   2.627703076264716`*^7, 3.5040983695604965`*^7, 4.6727902762174815`*^7,
   6.231265981340391`*^7, 8.30952673562764`*^7, 1.10809319930936`*^8}
```

$$\{3915.22,\ 1.65103\times10^{7},\ 2.20169\times10^{7},\ 2.936\times10^{7},\ 3.91522\times10^{7},\ 5.22103\times10^{7},\ 6.96235\times10^{7},\ 9.28445\times10^{7},\ 1.2381\times10^{8},\ 1.65103\times10^{8},\ 2.20169\times10^{8},\ 2.936\times10^{8},\ 3.91522\times10^{8},\ 5.22103\times10^{8},\ 6.96235\times10^{8}\}$$

Solve the 4-level EIT system, including the average over thermal velocities.

```
sols =
  Table[
   Table[
    {δ/(2 π),
     Sum[2401/(u Sqrt[π]) Im[ρ21] e^(-v^2/u^2) /. {u → rmsvelSI} /.
       Quiet[Solve[eqns /. {Δ1 → k1 v, Δ2 → δ - k2 v, Ωrf → rfRabi} /.
           myParams /. {u → rmsvelSI, k1 → 2 π/(780. × 10^-9), k2 → 2 π/(480. × 10^-9)},
         solutionsWanted]], {v, -600, 600, 0.5}]} // Flatten,
    {δ, -2 π 120. × 10^6, 2 π 120. × 10^6, 2 π 0.25 × 10^6}], {rfRabi,
    rabiFreqsUsedInExperiment}];
```

■ Plot the Doppler averaged results

```
ListPlot[sols, Joined → True,
 PlotRange → {{-60 10^6, 60 × 10^6}, All}, plotOptions]
```

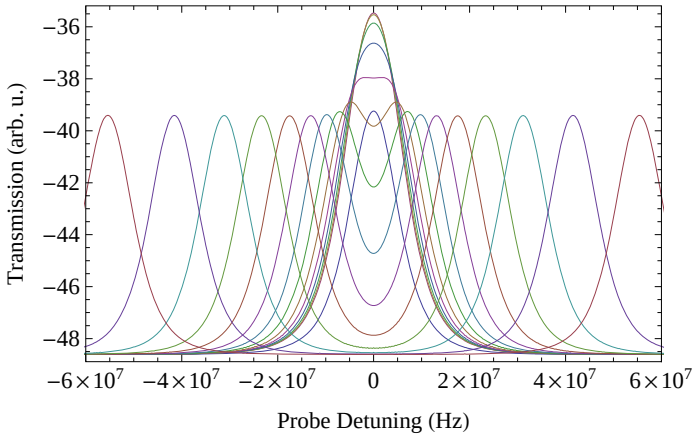

■ Export data

Save the parameters and results to a file.

```
baseFileName = "dopplerbroadenedEIT";

sols >> baseFileName;

rabiFreqsUsedInExperiment >> (baseFileName <> "_RabiFreqs")
```

Create a table of microwave powers used in the experiment. Here, x is the dB(m) setting on the front panel of the microwave generator. The 3.5 dBm loss is from the microwave assembly (isolator + directional coupler).

```
powersUsed =

  Table[{x, 10^(-3.5/10) 10^(x/10)/1000}, {x, {-110, -37.5, -35, -32.5, -30, -27.5, -25,
      -22.50, -20, -17.5, -15, -12.5, -10, -7.5, -5}}] //
   TableForm[#, TableHeadings → {{}, {"x (dBm)", "P (W)"}}] &
```

x (dBm)	P (W)
−110	4.46684×10^{-15}
−37.5	7.94328×10^{-8}
−35	1.41254×10^{-7}
−32.5	2.51189×10^{-7}
−30	4.46684×10^{-7}
−27.5	7.94328×10^{-7}
−25	1.41254×10^{-6}
−22.5	2.51189×10^{-6}
−20	4.46684×10^{-6}
−17.5	7.94328×10^{-6}
−15	0.0000141254
−12.5	0.0000251189
−10	0.0000446684
−7.5	0.0000794328
−5	0.000141254

Save the data in a format that can be easily imported into Origin, using a separate file for each microwave power.

```
Module[{fileName, power, rabiFreq},
 Do[
  power = {-110, -37.5, -35, -32.5, -30, -27.5,
     -25, -22.50, -20, -17.5, -15, -12.5, -10, -7.5, -5}[[i]];
  fileName = baseFileName <> "_" <> ToString[InputForm[power]] <> "_dBm.dat" //
    StringReplace[#, "*" → "_10"] &;
  Export[fileName, sols[[i]], "Table"];
  Print[fileName],
  {i, 1, Length[sols]}
 ]
]
```

```
dopplerbroadenedEITSmallRFDecayForThesis_-110_dBm.dat
dopplerbroadenedEITSmallRFDecayForThesis_-37.5_dBm.dat
dopplerbroadenedEITSmallRFDecayForThesis_-35_dBm.dat
dopplerbroadenedEITSmallRFDecayForThesis_-32.5_dBm.dat
dopplerbroadenedEITSmallRFDecayForThesis_-30_dBm.dat
dopplerbroadenedEITSmallRFDecayForThesis_-27.5_dBm.dat
dopplerbroadenedEITSmallRFDecayForThesis_-25_dBm.dat
dopplerbroadenedEITSmallRFDecayForThesis_-22.5_dBm.dat
dopplerbroadenedEITSmallRFDecayForThesis_-20_dBm.dat
dopplerbroadenedEITSmallRFDecayForThesis_-17.5_dBm.dat
dopplerbroadenedEITSmallRFDecayForThesis_-15_dBm.dat
dopplerbroadenedEITSmallRFDecayForThesis_-12.5_dBm.dat
dopplerbroadenedEITSmallRFDecayForThesis_-10_dBm.dat
dopplerbroadenedEITSmallRFDecayForThesis_-7.5_dBm.dat
dopplerbroadenedEITSmallRFDecayForThesis_-5_dBm.dat
```

C.3 52-level Rydberg EIT notebook

The polarization effects in 52-level Rydberg EIT spectra that are shown in Section 6.3.3 were calculated on a cluster computer. The Mathematica code that was used is reproduced on the following pages.

52-level Rydberg atom EIT

by Arne Schwettmann for James P. Shaffer Lab

This notebook computes the transmission spectrum of the 52-level ladder-type Rydberg EIT system subject to 2 laser light fields and microwave radiation, including the average over the thermal velocities of the atoms. The microwaves couple two Rydberg levels coherently. The resulting transmission lineshape depends on the polarizations of all three fields. The notebook has to be run separately for each combination of polarizations. The calculation is done by numerical time evolution of the density matrix into the steady state regime (t~μs). The calculation is run on a cluster computer, because it is extremely computation heavy. For example, the computation of a single polarization combination using this notebook took ~16 hours to complete when it was run on 240 Intel Xeon E5405 cpu cores (30 compute nodes with 8 cpu cores each).

Init for cluster

The following lines are used to initialize 240 parallel *Mathematica* kernels on the cluster computer.

```
Needs["SubKernels`RemoteKernels`"]
```

```
LaunchKernels[RemoteMachine/@StringSplit[Environment["LSB_HOSTS"]]];
```

Init

Load in physical constants and units

```
<< PhysicalConstants`
<< Units`
```

Set the output directory

```
SetDirectory[NotebookDirectory[]];
```

Format parameters to use as header lines in the data files

```
formatParamsForOutput[params_] := params /.
  (a_ → b_) :> "#" <> StringReplace[ToString[a], {"Δ" → "Delta", "Ω" → "Omega",
      "Γ" → "Gamma", "ħ" → "hbar"}] <> " = " <> ToString[InputForm[N[b]]]
```

```
$HistoryLength = 0
```

```
0
```

52-level Hamiltonian

■ Quantum numbers

Define the state quantum numbers in a list, each entry contains n,L,J,F,mF

```
groundStates = Table[
    {5, 0, 1 / 2, 2, mF}, {mF, -2, 2}
  ];
excitedStates = Table[
    {5, 1, 3 / 2, 3, mF}, {mF, -3, 3}
  ];
DStates = Table[
     {53, 2, 5 / 2, F, mF}, {F, 1, 4}, {mF, -F, F}
   ] // Flatten[#, 1] &;
PStates = Table[
     {54, 1, 3 / 2, F, mF}, {F, 0, 3}, {mF, -F, F}
   ] // Flatten[#, 1] &;
stateLabel = Join[groundStates, excitedStates, DStates, PStates];
```

Number of levels

```
n = Length[stateLabel]
```

```
52
```

■ Angular factors

Following are the definitions of angular factors. For transverse (x), longitudinal (z) linear, the Rabi frequency Ω=Ω0 × $\Omega_{x,z}$ where Ω0 = $\frac{E}{\hbar}$ < nL | er | $n' L'$ > , and the integral has no angular part to it - it is just the radial wavefunction. For RHC (σ^+) circular polarization the matrix element <1|μ · E|2> = Ωminus[1,2] Ω0[1,2], if 1 is the lower and 2 is the higher state, and <2| μ· E|1> = -Ωplus[2,1] Ω0[1,2]. Those two matrix elements are the same, because -Ωplus[2,1]=Ωminus[1,2].

```
Ωx[{L_, J_, F_, mF_}, {Lp_, Jp_, Fp_, mFp_}] :=
  (-1)^(J+Fp+Jp+F) (-1)^mF Sqrt[(2 Fp + 1) (2 F + 1)] Sqrt[(2 Jp + 1) (2 J + 1)]
   Sqrt[(2 L + 1) (2 Lp + 1)] SixJSymbol[{J, F, 3 / 2}, {Fp, Jp, 1}]
   SixJSymbol[{L, J, 1 / 2}, {Jp, Lp, 1}] ThreeJSymbol[{L, 0}, {1, 0}, {Lp, 0}]
   1/Sqrt[2] (ThreeJSymbol[{F, -mF}, {1, -1}, {Fp, mFp}] -
     ThreeJSymbol[{F, -mF}, {1, +1}, {Fp, mFp}]);
Ωz[{L_, J_, F_, mF_}, {Lp_, Jp_, Fp_, mFp_}] :=
  (-1)^(J+Fp+Jp+F) (-1)^mF Sqrt[(2 Fp + 1) (2 F + 1)] Sqrt[(2 Jp + 1) (2 J + 1)]
   Sqrt[(2 L + 1) (2 Lp + 1)] SixJSymbol[{J, F, 3 / 2}, {Fp, Jp, 1}]
   SixJSymbol[{L, J, 1 / 2}, {Jp, Lp, 1}] ThreeJSymbol[{L, 0}, {1, 0}, {Lp, 0}]
   ThreeJSymbol[{F, -mF}, {1, 0}, {Fp, mFp}];
```

```
Ωplus[{L_, J_, F_, mF_}, {Lp_, Jp_, Fp_, mFp_}] :=
  (-1)^(J+Fp+Jp+F) (-1)^mF Sqrt[(2 Fp + 1) (2 F + 1)] Sqrt[(2 Jp + 1) (2 J + 1)]
   Sqrt[(2 L + 1) (2 Lp + 1)] SixJSymbol[{J, F, 3 / 2}, {Fp, Jp, 1}]
   SixJSymbol[{L, J, 1 / 2}, {Jp, Lp, 1}] ThreeJSymbol[{L, 0}, {1, 0}, {Lp, 0}]
   ThreeJSymbol[{F, -mF}, {1, +1}, {Fp, mFp}];
Ωminus[{L_, J_, F_, mF_}, {Lp_, Jp_, Fp_, mFp_}] :=
  (-1)^(J+Fp+Jp+F) (-1)^mF Sqrt[(2 Fp + 1) (2 F + 1)] Sqrt[(2 Jp + 1) (2 J + 1)]
   Sqrt[(2 L + 1) (2 Lp + 1)] SixJSymbol[{J, F, 3 / 2}, {Fp, Jp, 1}]
   SixJSymbol[{L, J, 1 / 2}, {Jp, Lp, 1}] ThreeJSymbol[{L, 0}, {1, 0}, {Lp, 0}]
   ThreeJSymbol[{F, -mF}, {1, -1}, {Fp, mFp}];
```

■ Rabi frequencies

Define the Rabi frequencies between state i and j. I use ν for the principal quantum number, because n is already in use. The Rabi frequencies depend on the polarization combination. This notebook is run separately for each polarization combination.

```
(* Sigma Plus, Sigma Minus *)
Ω0[{5, 0}, {5, 1}] = Ω0[{5, 1}, {5, 0}] = Ωp;
Ω0[{5, 1}, {53, 2}] = Ω0[{53, 2}, {5, 1}] = Ωc;
Ω0[{53, 2}, {54, 1}] = Ω0[{54, 1}, {53, 2}] = Ωrf;
Ω0[_, _] = 0;
Ω[{ν_, L_, J_, F_, mF_}, {νp_, Lp_, Jp_, Fp_, mFp_}] :=
 Which[
  {ν, L, νp, Lp} == {5, 0, 5, 1},
  -Ωplus[{L, J, F, mF}, {Lp, Jp, Fp, mFp}] Ω0[{ν, L}, {νp, Lp}],
  {ν, L, νp, Lp} == {5, 1, 5, 0},
  Ωminus[{L, J, F, mF}, {Lp, Jp, Fp, mFp}] Ω0[{ν, L}, {νp, Lp}],
  {ν, L, νp, Lp} == {5, 1, 53, 2},
  Ωminus[{L, J, F, mF}, {Lp, Jp, Fp, mFp}] Ω0[{ν, L}, {νp, Lp}],
  {ν, L, νp, Lp} == {53, 2, 5, 1},
  -Ωplus[{L, J, F, mF}, {Lp, Jp, Fp, mFp}] Ω0[{ν, L}, {νp, Lp}],
  {ν, νp} == {53, 54} ⋁ {ν, νp} == {54, 53},
  Ωz[{L, J, F, mF}, {Lp, Jp, Fp, mFp}] Ω0[{ν, L}, {νp, Lp}],
  True, 0
 ]
```

```
(* Sigma Minus, Sigma Plus
  Ω0[{5,0},{6,1}]=Ω0[{5,1},{5,0}]=Ωp;
Ω0[{5,1},{53,2}]=Ω0[{53,2},{5,1}]=Ωc;
Ω0[{53,2},{54,1}]=Ω0[{54,1},{53,2}]=Ωrf;
Ω0[_,_]=0;
Ω[{ν_,L_,J_,F_,mF_},{νp_,Lp_,Jp_,Fp_,mFp_}]:=
 Which[
  {ν,L,νp,Lp}=={5,0,5,1},
  Ωminus[{L,J,F,mF},{Lp,Jp,Fp,mFp}] Ω0[{ν,L},{νp,Lp}],
  {ν,L,νp,Lp}=={5,1,5,0},
  -Ωplus[{L,J,F,mF},{Lp,Jp,Fp,mFp}] Ω0[{ν,L},{νp,Lp}],
  {ν,L,νp,Lp}=={5,1,53,2},
  -Ωplus[{L,J,F,mF},{Lp,Jp,Fp,mFp}] Ω0[{ν,L},{νp,Lp}],
  {ν,L,νp,Lp}=={53,2,5,1},
  Ωminus[{L,J,F,mF},{Lp,Jp,Fp,mFp}] Ω0[{ν,L},{νp,Lp}],
  {ν,νp}=={53,54}⋁{ν,νp}=={54,53},
  Ωx[{L,J,F,mF},{Lp,Jp,Fp,mFp}] Ω0[{ν,L},{νp,Lp}],
  True,0
 ] *)
(* x, x, z
  Ω0[{5,0},{5,1}]=Ω0[{5,1},{5,0}]=Ωp;
Ω0[{5,1},{53,2}]=Ω0[{53,2},{5,1}]=Ωc;
Ω0[{53,2},{54,1}]=Ω0[{54,1},{53,2}]=Ωrf;
Ω0[_,_]=0;
Ω[{ν_,L_,J_,F_,mF_},{νp_,Lp_,Jp_,Fp_,mFp_}]:=
 Which[
  {ν,L,νp,Lp}=={5,0,5,1},Ωx[{L,J,F,mF},{Lp,Jp,Fp,mFp}] Ω0[{ν,L},{νp,Lp}],
  {ν,L,νp,Lp}=={5,1,5,0},Ωx[{L,J,F,mF},{Lp,Jp,Fp,mFp}] Ω0[{ν,L},{νp,Lp}],
  {ν,L,νp,Lp}=={5,1,53,2},Ωx[{L,J,F,mF},{Lp,Jp,Fp,mFp}] Ω0[{ν,L},{νp,Lp}],
  {ν,L,νp,Lp}=={53,2,5,1},Ωx[{L,J,F,mF},{Lp,Jp,Fp,mFp}] Ω0[{ν,L},{νp,Lp}],
  {ν,νp}=={53,54}⋁{ν,νp}=={54,53},
  Ωz[{L,J,F,mF},{Lp,Jp,Fp,mFp}] Ω0[{ν,L},{νp,Lp}],
  True,0
 ] *)
```

```
(* Sigma Plus, Sigma Plus
  Ω0[{5,0},{5,1}]=Ω0[{5,1},{5,0}]=Ωp;
Ω0[{5,1},{53,2}]=Ω0[{53,2},{5,1}]=Ωc;
Ω0[{53,2},{54,1}]=Ω0[{54,1},{53,2}]=Ωrf;
Ω0[_,_]=0;
Ω[{ν_,L_,J_,F_,mF_},{νp_,Lp_,Jp_,Fp_,mFp_}]:=
 Which[
  {ν,L,νp,Lp}=={5,0,5,1},
  -Ωplus[{L,J,F,mF},{Lp,Jp,Fp,mFp}] Ω0[{ν,L},{νp,Lp}],
  {ν,L,νp,Lp}=={5,1,5,0},
  Ωminus[{L,J,F,mF},{Lp,Jp,Fp,mFp}] Ω0[{ν,L},{νp,Lp}],
  {ν,L,νp,Lp}=={5,1,53,2},
  -Ωplus[{L,J,F,mF},{Lp,Jp,Fp,mFp}] Ω0[{ν,L},{νp,Lp}],
  {ν,L,νp,Lp}=={53,2,5,1},
  Ωminus[{L,J,F,mF},{Lp,Jp,Fp,mFp}] Ω0[{ν,L},{νp,Lp}],
  {ν,νp}=={53,54}⋁{ν,νp}=={54,53},
  Ωx[{L,J,F,mF},{Lp,Jp,Fp,mFp}] Ω0[{ν,L},{νp,Lp}],
  True,0
 ]*)
(* Sigma Minus, Sigma Minus
  Ω0[{5,0},{5,1}]=Ω0[{5,1},{5,0}]=Ωp;
Ω0[{5,1},{53,2}]=Ω0[{53,2},{5,1}]=Ωc;
Ω0[{53,2},{54,1}]=Ω0[{54,1},{53,2}]=Ωrf;
Ω0[_,_]=0;
Ω[{ν_,L_,J_,F_,mF_},{νp_,Lp_,Jp_,Fp_,mFp_}]:=
 Which[
  {ν,L,νp,Lp}=={5,0,5,1},
  Ωminus[{L,J,F,mF},{Lp,Jp,Fp,mFp}] Ω0[{ν,L},{νp,Lp}],
  {ν,L,νp,Lp}=={5,1,5,0},
  -Ωplus[{L,J,F,mF},{Lp,Jp,Fp,mFp}] Ω0[{ν,L},{νp,Lp}],
  {ν,L,νp,Lp}=={5,1,53,2},
  Ωminus[{L,J,F,mF},{Lp,Jp,Fp,mFp}] Ω0[{ν,L},{νp,Lp}],
  {ν,L,νp,Lp}=={53,2,5,1},
  -Ωplus[{L,J,F,mF},{Lp,Jp,Fp,mFp}] Ω0[{ν,L},{νp,Lp}],
  {ν,νp}=={53,54}⋁{ν,νp}=={54,53},
  Ωz[{L,J,F,mF},{Lp,Jp,Fp,mFp}] Ω0[{ν,L},{νp,Lp}],
  True,0
 ]*)
```

■ Detunings

Define the detunings

```
Δ[{ν_, L_, J_, F_, mF_}] =
  Switch[{ν, L}, {5, 0}, 0, {5, 1}, Δ1, {53, 2}, Δ1 + Δ2, {54, 1}, Δ1 + Δ2 - Δ3];
```

■ Generate the Hamiltonian

Automatically generate the 52-level Hamiltonian. This Hamiltonian is in the interaction picture, after application of RWA and another rotation to eliminate time dependences of the form $e^{i\delta t}$.

```
H = ħ/2 Quiet[
    Table[
     If[i == j,
      -2 Δ[stateLabel⟦i⟧],
      Ω[stateLabel⟦i⟧, stateLabel⟦j⟧]
     ], {i, 1, n}, {j, 1, n}
    ]
   ];
```

Decay Operators

We use ρ[i,j] for the density matrix elements ρ_{ij}. That way, we cannot use ρ to refer to the full matrix, so we will use $\rho\rho$

```
ρρ = Table[ρ[i, j], {i, 1, n}, {j, 1, n}];
```

Define unit vectors

```
e[i_] = Table[{KroneckerDelta[i, j]}, {j, 1, n}];
```

Define the projection matrices σ, see Fleischhauer et al, Rev. Mod. Phys. **77**, 633 (2005), eq. 9.

```
σ[i_, j_] = e[i].e[j]^T;
```

Following are the "decay operators," see Fleischhauer et al, Rev. Mod. Phys. **77**, 633 (2005), eq. 9. Γ_{ij} is the decay rate due to spontaneous emission of level i (into level j). The total decay rate of a level due to spontaneous emission is $\Gamma_i := \sum_j \Gamma_{ij} = \frac{1}{\tau}$, where τ is the $\frac{1}{e}$lifetime of state i. The case of equal indices in a decay operator (L[i,i]) corresponds to an additional dephasing rate of level i, labelled γ_i. These rates are labelled γ_i instead of Γ_{ii} to not confuse them with the total decay rate of a state, Γ_i. γ_i are optional additional dephasing rates affecting only the coherences. γ_i could be due to collisions, laser phase jitter, or other sources of decoherence. These additional dephasing rates are labelled $\gamma_{i\,\text{dephas}}$ in Fleischhauer's review.

Define the decay/decoherence operators L[i,j].

Use γ_i instead of Γ_{ii}.

```
Γ[i_, i_] := γ[i];
```

Add a dephasing of the Rydberg levels.

```
γ[{ν_, L_, J_, F_, mF_}] := Which[
  ν == 53, 2 γRy,
  ν == 54, 2 γRy,
  True, 0
 ]
```

```
L[i_, j_] := If[Γ[stateLabel[[i]], stateLabel[[j]]] === 0,
    0, Γ[stateLabel[[i]], stateLabel[[j]]]
                                                    2
      (2 σ[j, i].ρρ.σ[i, j] - σ[i, i].ρρ - ρρ.σ[i, i])];
```

Define B[α',α], the branching ratio to decay from level α' to level α.

```
B[{νp_, Lp_, Jp_, Fp_, mFp_}, {ν_, L_, J_, F_, mF_}] :=
 Which[
  Abs[Fp - F] > 1 ⋁ Abs[mFp - mF] > 1, 0,
  {ν, L} == {νp, Lp}, 0,
  True, (ThreeJSymbol[{F, -mF}, {1, mF - mFp}, {Fp, mFp}]
       √((2 Fp + 1) (2 F + 1)) SixJSymbol[{J, F, 3 / 2}, {Fp, Jp, 1}])^2 (2 Jp + 1)
 ]
```

Define the decay operator.

```
Γ[{ν_, L_, J_, F_, mF_}, {νp_, Lp_, Jp_, Fp_, mFp_}] :=
 Which[
  Abs[Fp - F] > 1 ⋁ Abs[mFp - mF] > 1, 0,
  {ν, L, νp, Lp} == {5, 1, 5, 0},
  Γeg B[{ν, L, J, F, mF}, {νp, Lp, Jp, Fp, mFp}],
  {ν, L, νp, Lp} == {53, 2, 54, 1},
  Γryry B[{ν, L, J, F, mF}, {νp, Lp, Jp, Fp, mFp}],
  {ν, L, νp, Lp} == {53, 2, 5, 1},
  Γrye B[{ν, L, J, F, mF}, {νp, Lp, Jp, Fp, mFp}],
  {ν, L, νp, Lp} == {54, 1, 5, 1},
  Γrye B[{ν, L, J, F, mF}, {νp, Lp, Jp, Fp, mFp}],
  {ν, L, νp, Lp} == {53, 2, 5, 0},
  Γryg B[{ν, L, J, F, mF}, {νp, Lp, Jp, Fp, mFp}],
  {ν, L, νp, Lp} == {54, 1, 5, 0},
  Γryg B[{ν, L, J, F, mF}, {νp, Lp, Jp, Fp, mFp}],
  True, 0
 ]
```

Define the extra dephasing operator due to laser linewidths.

```
Ld := Table[
  If[γL[stateLabel[[i]], stateLabel[[j]]] === 0, 0,
   -γL[stateLabel[[i]], stateLabel[[j]]] ρρ[[i, j]]], {i, 1, n}, {j, 1, n}
 ]
```

```
γL[{ν_, L_, J_, F_, mF_}, {νp_, Lp_, Jp_, Fp_, mFp_}] :=
 Which[
  {ν, L, νp, Lp} == {5, 1, 5, 0} ⋁ {ν, L, νp, Lp} == {5, 0, 5, 1},
  If[Ω[{ν, L, J, F, mF}, {νp, Lp, Jp, Fp, mFp}] ≠ 0, γp, 0],
  {ν, L, νp, Lp} == {53, 2, 5, 1} ⋁ {ν, L, νp, Lp} == {5, 1, 53, 2},
  If[Ω[{ν, L, J, F, mF}, {νp, Lp, Jp, Fp, mFp}] ≠ 0, γc, 0],
  {ν, L, νp, Lp} == {53, 2, 54, 1} ⋁ {ν, L, νp, Lp} == {54, 1, 53, 2},
  If[Ω[{ν, L, J, F, mF}, {νp, Lp, Jp, Fp, mFp}] ≠ 0, γrf, 0],
  {ν, L, νp, Lp} == {53, 2, 5, 0} ⋁ {ν, L, νp, Lp} == {5, 0, 53, 2}, γp + γc,
  {ν, L, νp, Lp} == {54, 1, 5, 1} ⋁ {ν, L, νp, Lp} == {5, 1, 54, 1}, γc + γrf,
  {ν, L, νp, Lp} == {54, 1, 5, 0} ⋁ {ν, L, νp, Lp} == {5, 0, 54, 1}, γp + γc + γrf,
  True, 0
 ]
```

Add all decay terms up to find the total decay operator.

```
Ltotal = Sum[L[i, j], {i, 1, n}, {j, 1, n}] + Ld;
```

Differential equations

User-entered time evolution $\frac{\mathrm{d}\rho}{\mathrm{dt}} = -\frac{i}{\hbar}\left[\hat{H},\, \hat{\rho}\right] + \hat{L}$

```
ρdot = -(i/ħ) (H.ρρ - ρρ.H) + Ltotal;
```

Format the differential equations to be solved and include the initial condition where all population starts in the ground state.

We convert the generated expressions from the previous section into an index-less, time-dependent form so that they can be understood by NDSolve. This includes a change of notation, replacing ρ[i,j] with ρij[t].

```
eqns = Table[
      {
       ρ[i, j]'[t] == (ρdot[[i, j]] /. {ρ[i_, j_] :> ρ[i, j][t]}),
       If[(i == 1 ⋀ j == 1) ⋁ (i == 2 ⋀ j == 2) ⋁ (i == 3 ⋀ j == 3) ⋁
          (i == 4 ⋀ j == 4) ⋁ (i == 5 ⋀ j == 5), ρ[i, j][0] == 1 / 5, ρ[i, j][0] == 0]
      },
      {i, 1, n}, {j, 1, n}
     ] /. {ρ[i_, j_] :> ToExpression["ρ" <> ToString[i] <> "a" <> ToString[j]]} //
   Flatten;

solutionsWanted = Table[ρ[i, j], {i, 1, n}, {j, 1, n}] /. {ρ[i_, j_] :>
       ToExpression["ρ" <> ToString[i] <> "a" <> ToString[j]]} // Flatten;
```

Define quantities that are proportional to the susceptibilities on each transition, see C. S. Adams et al., J. Phys. B: At. Mol. Opt. Phys. **44** (2011) 184020, Eq. 8 and 9: $\chi = \frac{-2\,N\,(d_{21})^2}{\hbar\,\epsilon_0\,\Omega}\,\rho_{21}$. So the susceptibility is proportional to the transition dipole moment divided by the electric field of the probe, in my case, this is $\propto \Omega_{ij} / {\Omega_p}^2$

```
(* probeAbsorptionMatrixElements=
 Cases[
    Table[
      {ρ[i,j][t],Ω[stateLabel⟦j⟧,stateLabel⟦i⟧]},
      {i,Flatten[Position[stateLabel,{5,1,_,_,_}]]},
      {j,Flatten[Position[stateLabel,{5,0,_,_,_}]]}
     ]//Flatten[#,1]&,
    {a_,coupling_}/;Not[coupling===0]→a
   ]/.ρ[i_,j_]:↦ToExpression["ρ"<>ToString[i]<>"a"<>ToString[j]]//
  Flatten *)
probeSusceptibilityMatrixElements =
 Cases[
    Table[
      {- Ω[stateLabel⟦j⟧, stateLabel⟦i⟧] / Ωp^2 ρ[i, j][t],
       Ω[stateLabel⟦j⟧, stateLabel⟦i⟧]},
      {i, Flatten[Position[stateLabel, {5, 1, _, _, _}]]},
      {j, Flatten[Position[stateLabel, {5, 0, _, _, _}]]}
     ] // Flatten[#, 1] &,
    {a_, coupling_} /; Not[coupling === 0] → a
   ] /. ρ[i_, j_] :↦ ToExpression["ρ" <> ToString[i] <> "a" <> ToString[j]] //
  Flatten
```

Numerical integration and thermal averaging

Numerical Parameters in SI

```
myParams = {
    Γeg → 1. / (26 × 10^-9),
    Γrye → 1. / (136 × 10^-6),
    Γryry → 1. / (166 × 10^-6),
    Γryg → 0 1. / (78 × 10^-6),
    γp → 2 π 1 × 10^6,
    γc → 2 π 1 × 10^6,
    γrf → 0,
    γRy → 0 × 2 π 0.1 × 10^6,
    Ωp → 2 π 8.34 × 10^6,
    ħ → PlanckConstantReduced / (Joule Second),
    Ωc → 2 π 1.41 × 10^6,
    Ωrf → 2 π 78.3 × 10^6,
    Δ1 → 0.,
    Δ2 → 0.,
    Δ3 → 0.
   };
```

Define the thermal rms velocity, for a cell temperature of 90 degrees Celsius.

```
rmsvelSI = Sqrt[2 k T / m] Second / Meter /. {k → BoltzmannConstant, T → 363.15 Kelvin,
    m → ElementData["Rubidium", "AtomicMass"] AMU} // Convert[#, 1] &
```

```
265.812
```

The quantities we want to output are the total dispersion $\propto \mathrm{Re}\{\chi\}$, the total absorption $\propto \mathrm{Im}\{\chi\}$, and, for reference, the dispersion and absorption on each allowed probe transition

```
probeSusceptibility[t_] =
 Join[{Total[Re /@ probeSusceptibilityMatrixElements]},
   {Total[Im /@ probeSusceptibilityMatrixElements]},
   Re /@ probeSusceptibilityMatrixElements,
   Im /@ probeSusceptibilityMatrixElements] /. myParams
```

Run the 52-level EIT calculation with Doppler integration. It is faster to solve the time dependent problem than to find the steady state solution.

Final time

```
t1 = 64 × 10^-6
```

Define the method to do the time evolution of the system. The commented-out method was slower but used a lot less memory in initial tests.

```
(* myMethod={"Extrapolation",
   Method->"ExplicitModifiedMidpoint","StiffnessTest"→False}; *)
myMethod =
  {"ExplicitRungeKutta", "DifferenceOrder" → 4, "StiffnessTest" -> False};
```

Define a base filename to use.

```
baseFileName = "52LevelEIT_20111209_006"
```

Save the parameters to a file.

```
Put[myParams, baseFileName <> "_params"]
```

Use NDSolve to numerically evolve the system for one combination of polarizations. The calculation is done twice, once for the experimental parameters, and once for zero coupling power. The results can later be subtracted to simulate the lock-in detection used in the experiment. The Doppler averaging is done in parallel, using the command “ParallelSum.”

Solve the system for the experimental parameters, coupling light on.

```
myProbeSusceptibility[ProbeDetuning_?NumericQ,
  CouplingDetuning_?NumericQ] := probeSusceptibility[t1] /.
  NDSolve[eqns /. {Δ1 → ProbeDetuning, Δ2 → CouplingDetuning} /. myParams,
    solutionsWanted, {t, 0, t1}, MaxSteps → 100 000, Method → myMethod][[1]]
```

```
sols = Table[
   Join[{δ/(2 π)}, ParallelSum[1201/(u √π) myProbeSusceptibility[δ + k1 v, -k2 v] e^(-v^2/u^2) /.
      {u → rmsvelSI, k1 → 2 π/(780. × 10^-9), k2 → 2 π/(480. × 10^-9)}, {v, -600, 600, 1.0},
     Method → "FinestGrained"]], {δ, -2 π 40 × 10^6, 2 π 40 × 10^6, 2 π 1 × 10^6}];
```

Export data (coupling light on)

```
Export[baseFileName <> ".dat", sols, "Table"]
```

```
Put[sols, baseFileName]
```

Solve the system again for the experimental parameters, this time with the coupling light off.

```
myProbeSusceptibilityOnlyProbe[
  ProbeDetuning_?NumericQ, CouplingDetuning_?NumericQ] :=
 probeSusceptibility[t1] /. NDSolve[eqns /. {Δ1 → ProbeDetuning,
       Δ2 → CouplingDetuning, Ωc → 2 π 0.0 × 10^6, Ωrf → 2 π 0.0 × 10^6} /. myParams,
    solutionsWanted, {t, 0, t1}, MaxSteps → 100 000, Method → myMethod][[1]]
```

```
solsOnlyProbe = Table[Join[{δ/(2 π)},
    ParallelSum[1201/(u Sqrt[π]) myProbeSusceptibilityOnlyProbe[δ + k1 v, -k2 v] E^(-v^2/u^2) /.
      {u → rmsvelSI, k1 → 2 π/(780. × 10^-9), k2 → 2 π/(480. × 10^-9)}, {v, -600, 600, 1.0},
     Method → "FinestGrained"]], {δ, -2 π 40 × 10^6, 2 π 40 × 10^6, 2 π 1 × 10^6}];
```

Export data (coupling light off)

```
Export[baseFileName <> "_bg.dat", solsOnlyProbe, "Table"]
```

```
Put[solsOnlyProbe, baseFileName <> "_bg"]
```

Appendix D

Publications

D.1 Introduction

This Appendix contains lists of my publications and presentations.

D.2 Publications

Following is a list of peer-reviewed journal articles that I was author or co-author on, in reverse chronological order.

11. A. Schwettmann, J. Sedlacek, and J. P. Shaffer, "Field-programmable gate array based locking circuit for external cavity diode laser frequency stabilization," Rev. Sci. Instrum. **82**, 103103 (2011).

10. J. S. Cabral, J. M. Kondo, L. F. Gonçalves, V. A. Nascimento, L. G. Marcassa, D. Booth, J. Tallant, A. Schwettmann, K. R. Overstreet, J. Sedlacek and J. P. Shaffer, "Effects of electric fields on ultracold Rydberg atom interactions," J. Phys. B: At. Mol. Opt. Phys. **44**, 184007 (2011).

9. K. R. Overstreet, A. Schwettmann, J. Tallant, D. Booth and J. P. Shaffer, "Observation of electric-field-induced Cs Rydberg atom macrodimers," Nature Physics **5**, 581 - 585 (2009).

8. V. A. Nascimento, L. L. Caliri, A. Schwettmann, J. P. Shaffer, and L. G. Marcassa, "Electric Field Effects in the Excitation of Cold Rydberg-Atom Pairs," Phys. Rev. Lett. **102**, 213201 (2009).

7. A. Schwettmann, K. R. Overstreet, J. Tallant, and J. P. Shaffer, "Analysis of long-range Cs Rydberg potential wells," J. Mod. Opt. **54**, 2551-2562 (2007).

6. K. R. Overstreet, A. Schwettmann, J. Tallant, and J. P. Shaffer, "Photoinitiated collisions between cold Cs Rydberg atoms," Phys. Rev. A **76**, 011403(R) (2007).

5. A. Schwettmann, C. McGuffey, S. Chauhan, K. R. Overstreet, and J. P. Shaffer, "Tunable four-pass narrow spectral bandwidth amplifier for use at ∼508 nm," Appl. Opt. **46**, 1310-1315 (2007).

4. A. Schwettmann, J. Crawford, K. R. Overstreet, and J. P. Shaffer, "Cold Cs Rydberg-gas interactions," Phys. Rev. A **74**, 020701(R) (2006).

3. J. Tallant, K. R. Overstreet, A. Schwettmann, and J. P. Shaffer, "Sub-Doppler magneto-optical trap temperatures measured using Rydberg tagging," Phys. Rev. A **74**, 023410 (2006).

2. K. Overstreet, P. Zabawa, J. Tallant, A. Schwettmann, and J. P. Shaffer, "Multiple scattering and the density distribution of a Cs MOT," Optics Express **13**, 9672 (2005).

1. A. Schwettmann, J. Franklin, K. R. Overstreet, and J. P. Shaffer, "Stark slowing asymmetric rotors: Weak-field-seeking states and nonadiabatic transitions," J. Chem. Phys. **123**, 194305 (2005).

D.3 Presentations

Following is a list of presentations that I gave or contributed to, in reverse chronological order.

21. A. Schwettmann, J. Sedlacek, C. Gentry, and J. P. Shaffer, "Probing RF electric fields with Rydberg atoms," DAMOP, Atlanta, GA (2011). (Talk)

20. J. Sedlacek, A. Schwettmann, and J. P. Shaffer, "Generation of 480 nm cw light for Rydberg excitation of Rb," DAMOP, Atlanta, GA (2011). (Poster)

19. A. Schwettmann, J. Sedlacek, L. Trafford, and J. P. Shaffer, "Atom-chip trap for Rydberg atom experiments," DAMOP, Houston, TX (2010). (Poster)

18. J. Tallant, D. Booth, A. Schwettmann, and J. P. Shaffer, "Rydberg tagging time-of-flight imaging: An improved apparatus for studying many-body processes," DAMOP, Houston, TX (2010). (Poster)

17. D. Booth, J. Tallant, A. Schwettmann, J. P. Shaffer, J. Cabral, J. Kondo, L. Gonçalves, and L. Marcassa, "Electric field effects on decay of Rb Rydberg atom pairs," DAMOP, Houston, TX (2010). (Talk)

16. A. Schwettmann, J. Tallant, D. Booth, C. E. Savell and J. P. Shaffer, "Decoherence of a Rb BEC caused by stray magnetic fields and surface effects," DAMOP, Charlottesville, VA (2009). (Poster)

15. D. Booth, A. Schwettman, J. P. Shaffer, J. S. Cabral, L. F. Gonçalvez, L. G. Marcassa, "Electric field effects on cold Rydberg atom nD-nD pair collisions," DAMOP, Charlottesville, VA (2009). (Poster)

14. A. Schwettmann, K. R. Overstreet, J. Tallant, D. Booth and J. P. Shaffer, "Observation of Cs Rydberg atom macrodimers," DAMOP, Charlottesville, VA (2009). (Talk)

13. J. Tallant, A. Schwettmann, D. W. Booth, and J. P. Shaffer, "Rydberg tagging time-of-flight imaging to study 3-body recombination," DAMOP, Charlottesville, VA (2009). (Poster)

12. A. Schwettmann, V. A. Nascimento, L. L. Caliri, J. P. Shaffer, and L. G. Marcassa, "Electric field effects on cold Rydberg atom pair excitation," DAMOP, State College, PA (2008). (Talk)

11. K. R. Overstreet, A. Schwettmann, J. Tallant, and J. P. Shaffer, "Long Range, Cold Cs Rydberg Atom-Rydberg Atom Molecules," DAMOP, State College, PA (2008). (Talk)

10. J. Tallant, K. R. Overstreet, A. Schwettmann, and J. P. Shaffer, "Dipole-Dipole Interactions in a Cold Cs Rydberg Gas," DAMOP, State College, PA (2008). (Talk)

9. A. Schwettmann, K. R. Overstreet, J. Tallant, and J. P. Shaffer, "Long-range Cs Rydberg molecules," DAMOP, Calgary, CA (2007). (Talk)

8. K. R. Overstreet, A. Schwettmann, J. Tallant, and J. P. Shaffer, "Resonant collision processes in a Cs Rydberg gas," DAMOP Calgary, CA, (2007). (Talk)

7. J. Tallant, K. R. Overstreet, A. Schwettmann, and J. P. Shaffer, "Rydberg tagging time-of-flight imaging to study ultracold collisions," DAMOP, Calgary, CA (2007). (Poster)

6. A. Schwettmann, J. Crawford, K. R. Overstreet, and J. P. Shaffer, "Rydberg Atom - Rydberg Atom Interaction Potentials," DAMOP, Knoxville, TN (2006). (Talk)

5. K. R. Overstreet, P. Zabawa, J. Tallant, A. Schwettmann, J. Crawford, and J. P. Shaffer, "Abel Inversion for study of multiple scattering in a Cs magneto-optical trap," DAMOP, Knoxville, TN (2006). (Poster)

4. A. Schwettmann, J. Franklin, K. R. Overstreet, J. Tallant, and J. P. Shaffer, "Stark Slowing Asymmetric Rotors," DAMOP, Knoxville, TN (2006). (Talk)

3. J. Tallant, K. R. Overstreet, A. Schwettmann, and J. P. Shaffer, "Temperature Measurements Using Rydberg Tagging," DAMOP, Knoxville, TN (2006). (Poster)

2. A. Schwettmann, J. Franklin, K. R. Overstreet, J. Tallant, J. Crawford, and J. P. Shaffer, "Stark Slowing Asymmetric Rotors: Weak Field Seeking States and Nonadiabatic Transitions," DAMOP, Lincoln, NE (2005). (Poster)

1. K. R. Overstreet, J. Tallant, J. Crawford, A. Schwettmann, and J. P. Shaffer, "Cold Cs Rydberg Atom Collisions: Line Shifts, Broadening and Inelastic Collisions," DAMOP, Lincoln, NE (2005). (Talk)